DESIGN AND DEVELOPMENT OF NOVEL RADIO FREQUENCY SENSORS BASED ON FAR-FIELD AND NEAR-FIELD PRINCIPLES

A Dissertation
Presented to
The Academic Faculty

by

Trang Thuy Thai

In Partial Fulfillment
of the Requirements for the Degree
Doctor of Philosophy
in
Electrical and Computer Engineering

School of Electrical and Computer Engineering
Georgia Institute of Technology
December 2013

DESIGN AND DEVELOPMENT OF NOVEL RADIO FREQUENCY SENSORS BASED ON FAR-FIELD AND NEAR-FIELD PRINCIPLES

Approved by:

Dr. Manos Tentzeris, Advisor
School of ECE
Georgia Institute of Technology

Dr. Gerald DeJean, Co-Advisor
Microsoft Research
School of ECE
Georgia Institute of Technology

Dr. Andrew Peterson
School of ECE
Georgia Institute of Technology

Dr. Edward Conrad
School of Physics
Georgia Institute of Technology

Dr. Gregory Durgin
School of ECE
Georgia Institute of Technology

Dr. Herve Aubert
Institut National Polytechnique,
Toulouse, France

Date Approved: September 30, 2013

"The essential in the existence of a man like me is what he thinks and how he thinks,

not what he does or suffers." – Albert Einstein

To my parents,

whose suffering and sacrifice have made this education possible to me.

ACKNOWLEDGEMENTS

First and foremost, I would like to express my deepest gratitude for my advisor, Professor Manos Tentzeris. Dear Manos, you did not only help me through my undergraduate years with your guidance and research opportunities leading me to a fruitful academic direction, but also encourage and inspire me to embark on this journey of a PhD that changed the course of my life. Without your constant support financially, intellectually, and mentally, I could hardly imagine what I have achieved today. I have learnt that despite great challenges that life may bring, you showed me that hard work and perseverance would pay off. Secondly, I am eternally grateful to my co-advisor, Dr. Gerald DeJean. Dear Gerald, the impact of your awesome mentorship and generous patience for me in the past five years has shaped my character and my life in many ways. I was lucky enough to have Manos put me to work with you when I first joined ATHENA in 2006, our research group. As you said before, you and Manos have helped to transform me into a mature researcher both academically and socially, who you would be proud of. I cannot thank you enough for your presence in my career. Thirdly, my research work owes its significant value to Professor Herve Aubert. Dear Herve, the opportunities that I had at LAAS in Toulouse in the past years had marked a turning point to my PhD career. Your vision in the field, your knowledge, your teaching, and your patience have paved the way for my research to flourish. Without your support, my research would have been shaken and not completed by now. Your sense of humor also enlightened the difficult times I faced.

I would like to extend my gratitude to the thesis reading committee members including Professor Andrew Peterson and Professor Gregory Durgin for the comments and feedback that are valuable to my current and future work. I would also like to thank Professor Edward Conrad for his participation on my defense committee, and Professor F. Levent Degertekin for his practical suggestions during my thesis proposal. I am thankful to Dr. Darko Kirovski and Dr. Ran Gilad-Bachrach at Microsoft Research for their guidance during my internships there.

Additionally, I owe the successful results in my work largely to the assistance of my dear colleagues at LAAS, Toulouse including Dr. Franck Chebila, Professor Hamida Hallil, Tonio Idda, and Dr. Mehdi Jatlaoui. Dear all, our wonderful friendships have broadened my horizon and reminded me that our scientific work was and would always be about and for the people. I also owe my academic success to my dear colleagues and friends I met in Atlanta including Dr. Daniela Staiculescu, Dr. Luca Aluigi, Dr. Giulia Orecchini, Dr. Vasileios Lakafosis, Dr. Amin Rida, Rushi Vyas, Dr. Li Yang, and Taoran Le. Dear all, your support have carried me through this roller coaster ride and brought me joy in those long years. Thank you so much. I also want to thank all the ATHENA members for making our lab an enjoyable environment, and all the staff of GEDC and ECE office for their excellent assistance.

Furthermore, I would like to acknowledge the financial support of the Georgia Electronic Design Center and the Microsoft Research PhD Fellowship throughout my doctorate program.

Finally and most importantly, I am in endless debt to my beloved family. My sister, Rachel Thai, you have never stopped being the big sister who I can always lean on.

My brother, Binh Thai, you are always there when I need and you have inspired me intellectually. And words cannot describe enough the immensurable significance of my mother, Nguyen Thi Nga, and my father, Thai Kien Dinh, in my life. Dear mom and dad, I owe what I am today to you for my entire education, my health, my integrity, my discipline, and my success. You have made constant and tremendous sacrifices for your children to have the best and to be the best of what we can, and to let us fly high and far even if it means that you would lose sight of us. This PhD is for you, and yet it is only a fraction of what you deserve. Being far away from you, in every step of my life, I will continue to cultivate more knowledge, wisdom, kindness, and happiness so that I may refine myself and continue the work that you started 29 years ago.

16 October 2013

Trang T.

TABLE OF CONTENTS

LIST OF TABLES

LIST OF FIGURES

LIST OF SYMBOLS AND ABBREVIATIONS

°	degree
3D	Three dimensional
ADS	Advanced Design System
ASK	Amplitude shift keying
BW	Bandwidth
C	Capacitor
CNT	Carbon Nanotube
CPW	Coplanar Waveguide
CW	Continuous Wave
dB	decibels
dBc	decibels relative to the carrier
dBi	dB isotropic
DC	Direct Current
E-field	Electric field
EM	Electromagnetic
FMCW	Frequency Modulated Continuous Wave
ε_o	Permittivity of free space
ε_r	Dielectric constant
ε_{eff}	Effective dielectric constant
f	Frequency
GHz	Giga Hertz

H-field	Magnetic field
HF	High Frequency
IC	Integrated Circuit
ID	Identification
IDT	Interdigital Transducer
λ	wavelength (Greek lambda)
L	Inductor
LF	Low Frequency
LNA	Low Noise Amplifier
μ_o	Permeability of free space
NF	Noise Figure
Ω	Ohm
PCB	Printed Circuit Board
Q	Quality factor
RCS or σ	Radar Cross Section
RF	Radio Frequency
RFID	Radio Frequency Identification
SAR	Synthetic Aperture Radar
SAW	Surface Acoustic Wave
SNR	Signal to Noise Ratio
SRR	Split Ring Resonator
TDD	Time Domain Division
TDS	Time Domain Sampling

TEM	Transverse Electromagnetic
TM	Transverse Mode
TRL	Thru-Reflect-Line
tanδ	loss tangent
UWB	Ultra Wide band
VNA	Vector Network Analyzer
VCO	Voltage Controlled Oscillator

SUMMARY

The objective of this work is to enhance and advance sensing technologies with the design and development of novel radio frequency (RF) sensors based on far-field and near-field principles of the electromagnetic (EM) resonances. In the first part of this thesis, original design and development of a passive RF temperature sensor, a passive RF strain sensor, and a passive RF pressure sensor are presented. The RF temperature sensor is presented in Chapter 3. It is based on split ring resonators loaded with bimorph cantilevers. Its operating principles and equivalent circuits are discussed in Chapter 4, where the design concept is illustrated to be robust and highly adaptable to different sensing ranges, environments, and applicable to other type of sensing beyond temperatures. The passive RF strain sensor, based on a patch antenna loaded with a cantilever-integrated open loop, is presented in Chapter 5, where it is demonstrated to have the highest strain sensitivity in the same remote and passive class of sensors in the state-of-the-art. Chapter 6 describes the passive RF pressure sensor, which is based on a dual-band stacked-patch antenna that allows both identification and sensing to be embedded in its unique dual resonant responses.

In the second part of this thesis, an original and first-of-its-kind RF transducer is presented that enables non-touch sensing of human fingers within 3 cm of proximity (based on one unit sensor cell). The RF transducer is based on a slotted microstrip patch coupled to a half-wavelength parallel-coupled microstrip filter operating in the frequency range of 6 – 8 GHz. The sensing mechanism is based on the EM near-field coupling between the resonator and the human finger. Fundamentally different from the electric

field capacitive sensing, this new method of sensing, the first of its kind, based on near-field interference that produces a myriad of nonlinearities in the sensing response, can introduce new capabilities for the interface of electronic displays (the detection is based on pattern recognition). What set this sensor and its platform apart from previous proximity sensors and microwave sensing platforms is the low profile planar structure of the system, and its compatibility with mobile applications.

The thesis provides both breadth and depth in the proposed design and development and thus presenting a complete research in its contributions to RF sensing.

Chapter 1.

Introduction

1.1. Concept of Radio Frequency Transduction

Sensing technologies are critical across different industries and everyday life aspects of consumers. Sensing devices are widely exploited in many domains from micro-machined silicon devices to the wireless integrated micro-sensors such as wireless capacitive devices hermetically sealed at wafer level. They transform mechanical, chemical or thermal events into electrical signals,. Sensing is particularly important to robot control, machine-to-machine networks, human-computer interface for ubiquitous computing, mobile devices, and medical systems. Today, substantial development of microwave circuits allows the integration of sensors into wireless devices that further advance sensing applications.

Radio frequency (RF) probing, or microwave remote sensing, has been around as early as 100 years ago when radar was invented [1.1 – 1.2]. The development of radar in the early days focused on detection and measurements of RF reflective objects (by means of backscattered signals) to extract information such as the presence of the objects, their locations, their velocity, and their material properties including surface roughness. Synthetic aperture radar (SAR), microwave scatterometers, and radar altimeters are examples of classic microwave remote sensors. Those applications use antennas whose sources are in the far field, defined as a spatial region that is further than a distance of $2D^2/\lambda$ away from the radiating source, where D is the aperture of the antenna and λ is the free-space wavelength [1.3]. Thus, sensing mechanism is based on far-field

characteristics of the electromagnetic (EM) radiation. Those far-field probing techniques provide sensing signals with low spatial resolution and lack detail physical properties. Later in the 1970s, microwave sensing techniques based on near-field (the region whose radius smaller than $2D^2/\lambda$) were developed such as microwave radiometry [1.4], or microwave imaging in the past two decades [1.5 – 1.6]. Microwave radiometry refers to the detection of the emitted microwave radiation of the objects in proximity. The detection is performed by means of the antennas based on their near-field radiation patterns according to the reciprocal principle [1.3 – 1.4, 1.7]. Microwave imaging relies on the penetration of the electromagnetic (EM) waves in the objects (such as human tissues in the case of breast cancer screening), and the images are re-constructed based on the reflected and transmitted waves of the probing antennas (300 MHz – 30 GHz) [1.5]. These near-field sensing platforms operate in short range (less than 100 cm) and require heavy signal processing. They are large in physical size (usually consisting of large arrays) applicable to clinical setting only (in the case of medical applications), and not applicable to low cost or ubiquitous applications.

Due to the continuing advances in radar and RF communications, wireless data capturing techniques such as RF identification (RFID) systems were developed also in the 1970s mostly emerged from the need of tracking and inventory of industries [1.8]. A typical RFID platform consists of a reader (similar to a radar), and a transponder (in the form of a tag with minimal electronics) that has the capacity to perform data transmission with the reader through the wireless RF channel. Therefore, this platform can be considered as a hybrid of the conventional radar probing platform (a single transceiver on one end of the data channel) and the telecommunication platform (two transceivers on

two ends of the data channel). The advantages of RFID systems include mobile, ubiquitous, and low cost tags that can be identified at a distance from the reader in non-line-of-sight operations.

In recent decades, demands for low cost and ubiquitous sensing platforms have stimulated the transformation of the RFID tags into sensors that are automatically inherent of the same advantages. In an RFID sensing platform, the tags have the capacity to monitor certain physical parameters such as temperature, pressure, or stress/strain of its surrounding environment. They encode the change of these physical parameters into their backscattered signals that are received by the reader. At the center of the sensing mechanism is the sensing element, i.e. the transducer, which transforms a change of a physical quantity into a change in the electric signal (such as a change in resistance, capacitance, or induced voltage). In active RFID tags, a power source (on-board battery or scavenging electronics) is required to operate the transducers (such as a thermistor), and to enable the tags to transmit sensing data back to the reader. In passive RFID tags, the RF transduction is performed without additional electronic medium, i.e. to transform the physical quantity into the backscattered signal by means of EM principles without active components. Such transducers are defined here as RF transducers. Thus, such RF transducers, which are constructed based on the EM resonators, distinctively depart from conventional transducers. In general, passive EM sensing devices, or RF transducers, convert the variation of a physical quantity (such as, e.g., pressure, temperature or gas concentration) into a known/specific variation of a given EM wave descriptor. For example, an RF pressure transducer converts the variation of an applied pressure into a variation of the resonant frequency of its resonator. Unlike surface acoustic wave (SAW)

sensors, RF transducers do not require EM-to-acoustic wave conversion and consequently avoid high losses due to this conversion especially in long rang remote probing. In this thesis, the term 'RF sensing' always refers to wireless sensing based on RF transducers without active circuit elements. In this thesis, the term "passive sensors" always refers to chipless sensors unless noted otherwise.

1.2. Background and Motivations

The innovation of RF transducers from the conventional microwave sensors is the integration of the sensing element together with the resonators (usually antennas) in the form of mobile and ubiquitous tags/cells. At the same time, their operating principles should be compatible with low cost and ubiquitous sensing platforms. Constructed based on EM resonators, RF transducers can utilize both far-field and near-field resonant behaviors to acquire unique sensing capabilities.

1.2.1. Far-Field based RF Sensing

In general, multi-node wireless remote sensing in RFID platforms can be classified into active and passive categories based on the construction of the sensor tags. Active sensors require a DC power source and an integrated circuit (IC) on board. Active sensors platforms, such as Berkeley Motes [1.9] or BTnodes [1.10], have been well developed with features like time history of data, real-time updates, and alarm triggering. They are power intensive, require sophisticated electronics, have high cost and low service life. Some other semi-active sensing platforms such as Intel WISP [1.11] allow the RF signals to be harvested and converted to DC power for the on-board electronics to operate, thus they eliminate the need for battery and increase the unit life time.

Meanwhile, passive sensors require no DC power or IC and they are operated entirely based on the incident EM waves and EM backscattering. Recently, a large demand for wireless and passive sensors has grown significantly due to their attractive capabilities. Those capabilities include operations in harsh environments such as in extremely high temperature and high radiation, having low-cost fabrication and long-term measurement stability.

In long range remote sensing, there are two essential factors that are required for any interrogation platform: a detectable sensing signal, and an ID for each sensor node. These factors are especially challenging in passive sensing, where both ID and sensing signals must be encoded and decoded only via the backscattered signals. The signal interrogation of a passive sensing platform is illustrated in Figure 1.1. [1.12]. Existing wireless passive sensors can be classified into two groups based on the response signals received from the sensor: time domain signature, and frequency domain signature. Time domain signature refers to sensors whose responses are differentiated from other signals by a separation in time such as the signals are received at the reader such as the one in Figure 1.1c. Frequency domain signature refers to sensors whose responses are differentiated from other signals by their distinct frequency band such as the one in Figure 1.1b, which can be identified after a Fourier transform performed at the reader. Each signature response then has three main modulation schemes that include amplitude, frequency, and phase modulation. For example, SAW based RFID sensors operate with time domain signature and have their ID encoded in the unique reflected pulse pattern like a bar code. Then the sensing signal is encoded in either the change of the signal levels of the different pulses (amplitude modulation), or in the relative position of the

pulses (phase modulation) (see Section 2.2 of Chapter 2). Another example of a frequency domain signature passive sensor is an inkjet- printed RFID tag for gas sensing [1.13]. It is based on a bowtie antenna loaded with ink-jet printed carbon nanotubes (CNTs) loaded at the antenna's terminals. As the gas (ammonia) concentration surrounding the CNTs changes then the load impedance is modified, thus the reflected power level is modulated. In this case, if the reader monitors the response signal of the tag by its backscattered power in a narrow frequency band, then it is implementing amplitude modulation. If the reader scans the response signal of the tag in a wide frequency band, then the notch frequency of the received power can be tracked, i.e. frequency modulation for the sensing signal.

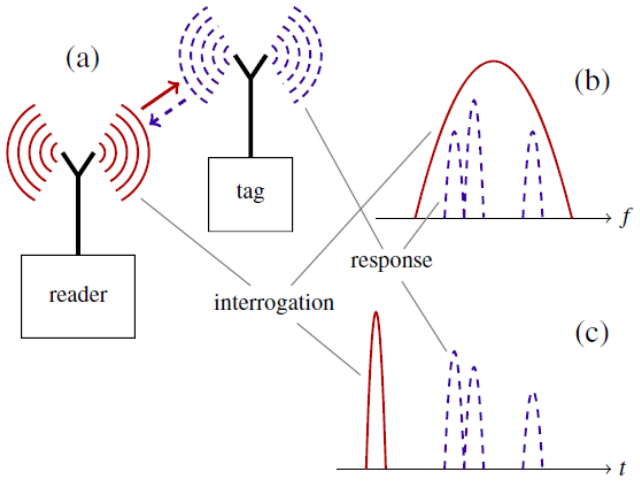

Figure 1.1. Frequency and time-domain data encoding/transfer principle of passive chipless wireless tags with a) System overview, b) example frequency-domain coding scheme, and c) example time-domain coding scheme. [1.12]

Among many advantages of remote passive sensing, one major advantage is the promise of their implementation in harsh environments where chip-based (referring to semiconductor elements) or wired sensors have failed. Recent developments of remote passive sensors such as temperature, stress/strain, gas sensors have demonstrated and captured many such advantages [1.12, 1.13 – 1.16]. However, whether based on conventional RFID, SAW, or the newly emerging RF transducers, the existing designs yield limited sensitivity and limited capacity to operate in extremely high temperature environments (above 1000 ^{o}C). The reasons are usually due to limitations of their operating principles and their material requirements. Therefore, the objectives of this thesis are the design and development of chipless RF sensors, which not only embrace the advantages of remote passive sensing but also enable sensing to be performed in extremely high temperature environments (not limited by their operation principles or material requirements) by means of original and novel design concepts.

1.2.2. Near-Field based RF Sensing

As discussed in Section 1.1, near-field sensing is essentially based on the response of the radiating EM resonators in the near-field region. Usually, near-field sensing operates in short range (less than 100 cm), therefore the need for identification of the sensor node is not applicable. Different from the conventional near-field sensing techniques such as microwave radiometry or microwave imaging, both of which usually employ ultra wideband (UWB) antennas, the concept of near-field RF sensing means that the change of the surrounding in proximity (for example, an approaching object) alters the radiation pattern of the resonators in their near-field region of their operation such that their resonant behavior is altered (usually in the form of a resonant frequency shift).

Consequently, the RF transducers employed here should have narrow bandwidth and thus are high quality factor resonators. The sensing mechanism is essentially based on the non-linearity of the near-field radiation of the transducers. In a near-field RF sensing platform, passive sensing is defined by a condition in which the objects under sensing is not instrumented. However, to stay coherent with the development for RFID systems driven by the demand for low cost, mobile, and ubiquitous sensing, the platform for near-field RF sensing should also be made low cost, mobile, and ubiquitous. To pioneer such development along this direction, where no other work has been seen in literature, an original proximity RF sensor is presented in the second part of this thesis.

1.3. References

[1.1] M. I. Skolnik, "Fifty years of radar," in *Proc. IEEE*, vol. 73, no. 2, pp. 182 – 197, Feb. 1985.

[1.2] M. I. Skolnik, *Introduction to Radar Systems*, 3rd ed. New York: Mc- Graw-Hill, 2001.

[1.3] C. Balanis, *Antenna Theory: Analysis and Design*. New York, NY: John Wiley & Sons, Inc, 1997.

[1.4] K. Carr, "Microwave radiometry: Its importance to the detection of cancer," *IEEE Trans. Microw. Theory Tech.*, vol. 37, no. 12, pp. 1862 – 1869, Dec. 1989.

[1.5] E. C. Fear, P. M. Meaney, M. A. Stuchly, "Microwaves for breast cancer detection?," *IEEE Potentials*, vol. 22, no. 1, pp. 12 – 18, Feb.- Mar. 2003.

[1.6] A. Hassan, M. El-Shenawee, "Review of Electromagnetic techniques for breast cancer detection," *IEEE Reviews in Biomed. Eng.*, vol. 4, pp. 103 – 118, Sept. 2011.

[1.7] K. D. Stephan, J. A. Pearce, "Antennas and Reflectors for Near-Field radiometric remote sensing of temperature in industrial applications," in *IEEE Ant. Prop. Soc. Int. Symp.*, vol. 4, 2002, pp. 302 – 305.

[1.8] M. Roberti (2005 Jan. 16). *The history of RFID technology* [Online]. Available: http://www.rfidjournal.com/articles/view?1338 (Accessed: 2013, July 27).

[1.9] N. Kurata, B. F. Spencer Jr., M. R. Sandoval, "Risk monitoring of buildings with wireless sensor networks," *Struct. Control Health Monitoring*, vol. 12, no. 3 – 4, pp. 315 – 327, 2005.

[1.10] J. Beutel, M. Dyer, M. Hinz, L. Meier, M. Ringwald, "Next-generation prototyping of sensor networks," in *Proc. 2nd Int. Conf. Embedded Netw. Sensor Syst.*, New York, 2004, pp. 291 – 29.

[1.11] A. P. Sample, D. J. Yeager, P. S. Powledge, A. V. Mamishev, J. R. Smith, "Design of an RFID-based battery-free programmable sensing platform," *IEEE Trans. Instrum. Meas.*, vol. 57, no. 11, pp. 2608 – 2615, Nov. 2008.

[1.12] C. Mandel, B. Kubina, M. Schüßler, R. Jakoby, "Metamaterial-inspired passive chipless radio-frequency identification and wireless sensing," *Ann. Telecommun*., Springer-Verlag, vol. 68, no. 7 – 8, pp. 385 – 399, Aug. 2013.

[1.13] L. Yang, R.Zhang, C.P.Wong, M.M.Tentzeris, "A Novel Conformal RFID-Enabled Module Utilizing Inkjet-Printed Antennas and Carbon Nanotubes for Gas-Detection Applications," *IEEE Antennas and Wireless Propagation Letters*, vol. 8, pp. 653 – 656, June 2009.

[1.14] S. Preradovic, N. C. Karmakar, "Chipless RFID: Bar code of the future," *IEEE Microwave Mag.*, pp. 87 – 97, Dec. 2010.

[1.15] H. Aubert, F. Chebila, M. Jatlaoui, T. Thai, H. Hallil, A. Traille, S. Bouaziz, a. Rifai, P. Pons, P. Menini, M. Tentzeris, "Wireless sensing and identification based on radar cross section variability measurement of passive electromagnetic sensors," *Ann. Telecommun., Springer-Verlag*, pp. 1 – 11, June 2013.

[1.16] R. Bhattacharyya, C. Floerkemeier, S. Sarma, "Low-cost, ubiquitous RFID-tag-antenna-based sensing," in *IEEE Proceedings*, vol. 98, no. 9, pp. 1593 – 1600, Sept. 2010.

PART I.

RF SENSING BASED ON FAR FIELD

Chapter 2.

Overview on RF Sensing Platforms

In the current state-of-the-art remote passive sensing, there are three major platforms that have been introduced. Radio frequency identification (RFID) platforms have been maturely developed for decades. A surface acoustic wave (SAW) platform is actually a subcategory of the RFID platform. However it employs a completely distinct sensing mechanism at the tags. Both technologies have been made available commercially. Another platform, operated based on frequency modulation continuous wave (FMCW) radar and the generated beat frequency, was proposed only in recent years. This chapter gives an overview on all three technologies. However, the RF transducers developed in this thesis, which can be employed and incorporated into RFID and SAW based systems, are tested mostly with the FMCW system to embrace the advantages that set it apart from the RFID systems.

2.1. Remote Sensing based on RFID

RFID first appeared in the 1940s along with the development of radio technology and radar systems [2.1]. Then in the 1970s, RFID technology was utilized in industry for tracking and inventory. A typical RFID system consists of a reader or interrogator, an RFID tag or transponder, and an electronic interface to encode and decode the identification data from the reader [2.2]. Based on the information encoded in the tags, RFID systems can be classified into two major groups based on the data transfer between the reader and the tags. The first group comprises 1-bit transponders which indicate only two states: ‘transponders in interrogation zone’ and ‘transponders not in interrogation

zone'. The second group comprises n-bit transponders which allow many distinguishable tags in the same interrogation zone. A summary on different RFID systems is given in Figure 2.1, where different operation principles are listed (more details can be found in Chapter 3 of [2.2]). In multi-node sensing networks, different tags should be identified so only n-bit tags are appropriate for these networks. Furthermore, RFID tags can be broadly classified as either active or passive. The active RFID tags are comprised of an antenna and an integrated circuit (IC), which requires an on-board DC power supply (from the battery) to process the data and communicate with the reader. In semi-active tage, ICs collect power from the interrogation signal emitted by the reader and rectify it into a DC power source. In passive tags, there is no DC power. In general, active tags can allow reading ranges up to 100 m while passive tags offer ranges up to 10 m [2.3], and semi-active tags operate with ranges somewhere in between. Within the passive tag category, surface acoustic wave (SAW) devices are RFID tags that can operate without ICs or chipless. Those SAW devices are the only n-bit and chipless RFID tags currently available commercially [2.4].

Based on the operating frequency of the tags, passive RFID systems can be summarized into the following four categories: low frequency (LF) (125 – 134 kHz), high frequency (HF) (13.56 MHz), ultra high frequency (UHF) (433 MHz and 860 – 956 MHz), and microwave frequencies (2.45 – 5.8 GHz) [2.2, 2.5]. Both LF and HF systems operate based on either inductive coupling or capacitive coupling with large size tags and they are limited to small range (less than 1 m). Systems of UHF and microwave frequencies operate based on electromagnetic (EM) backscattering. A schematic of an EM backscattering RFID system is shown in Figure 2.2, where the chip is powered

remotely from the RF signal transmitted by the RFID reader. The reader sends signals that alternate between a continuous wave (CW) and modulated transmissions. The input impedance of the tag is modulated by the chip, thus the backscattered signal is modulated to encode the data. The tag sends back data during one of the CW periods. The difference in the backscattered signal is represented by a certain radar cross section (RCS). Typical received signal at the reader is shown in Figure 2.3 to illustrate the data exchange between an RFID reader and a tag [2.6]. The modulation scheme often used here is amplitude shift keying (ASK) in which the IC impedance switches between the matched state and the mismatched state.

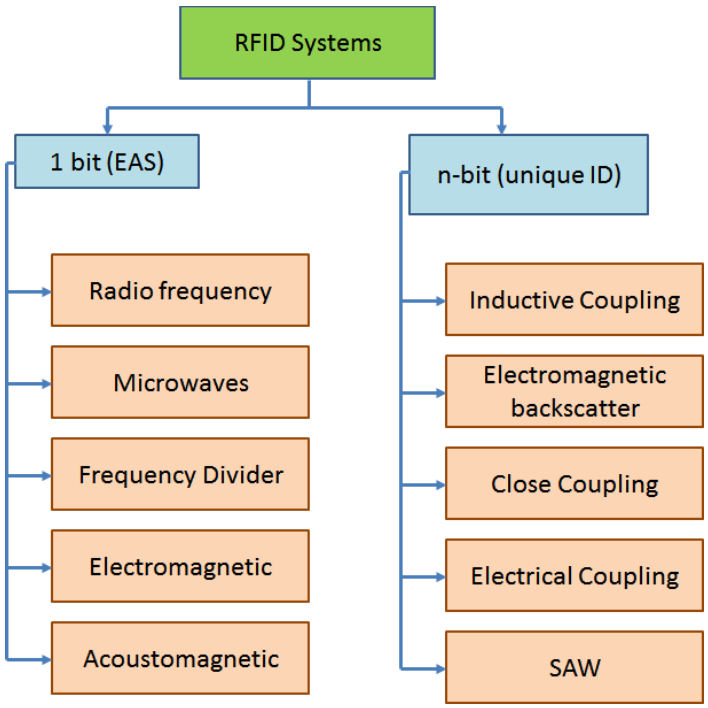

Figure 2.1 Summary of different RFID systems based on their operating principles.

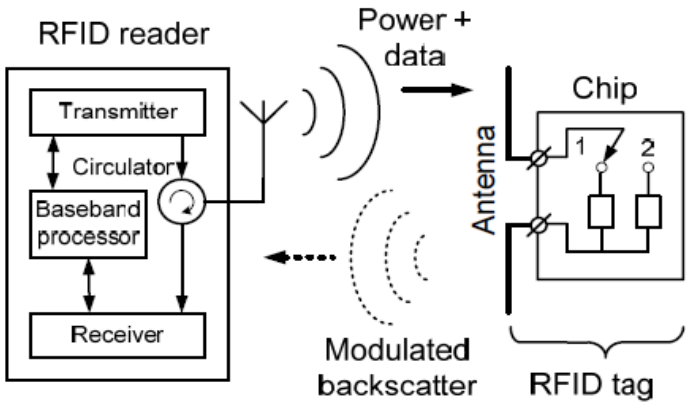

Figure 2.2. RFID system overview. [2.6]

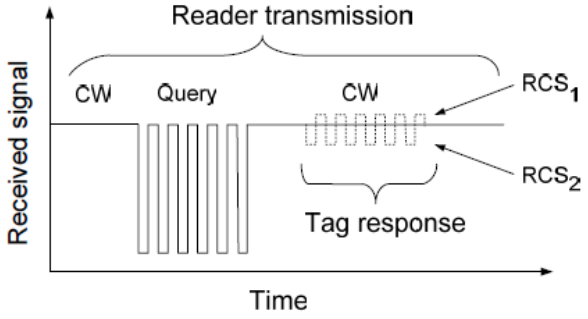

Figure 2.3. Data exchange between an RFID reader and a tag. [2.6]

The schematic of the RFID tag and its equivalent circuit is shown in Figure 2.4. The power reflection coefficient, η, of the RFID antenna can be calculated to evaluate the reflected wave strength according to (2.1), where Z_L and Z_A represent the complex impedance of the load and the antenna terminals, respectively, with its complex conjugate Z_A^* [2.7].

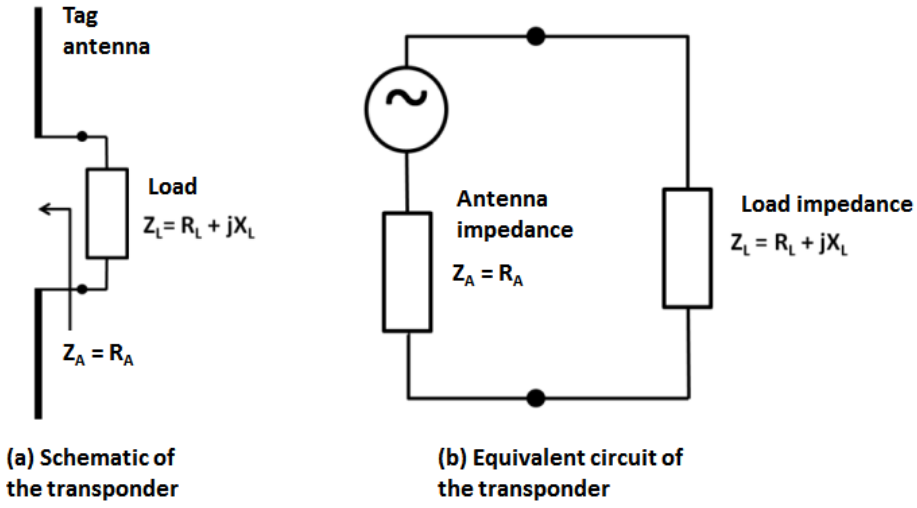

Figure 2.4. The tag with its a) schematic and b) equivalent circuit.

$$\eta = \left|\frac{Z_L - Z_A^*}{Z_L + Z_A}\right|^2 \tag{2.1}$$

The same mechanism can be used to realize RFID-enabled sensor modules. When the power level changes, it means that there is variation in the load impedance. Consequently, when the load impedance is dependent on certain physical quantity in the environment such as temperature, pressure, or strain, then the variation in the load impedance indicates the change in that physical quantity.

The expected power levels of the received signal at the load of the RFID antenna, P_{tag}, can be calculated using the Friis free-space transmission formula, as in (2.2), where P_T is the power fed into the reader antenna, G_T and G_A is the gain of the reader antenna and tag antenna, respectively, λ is the wavelength of the carrier frequency, and d is the distance between the reader and the tag.

$$P_{tag} = P_T G_T G_A \left(\frac{\lambda}{4\pi d}\right)^2 \quad (2.2)$$

Due to the change in the mismatch level between the load and the tag antenna, a changeable portion of the received power would be reflected back, denoted as P_{ref} in (2.3). And as η varies to indicate the change in the physical quantity under sensing, the received power, P_R, at the reader also varies, as in (2.4), assuming no polarization loss and all other values remain constant during the sensing interrogation time.

$$P_{ref} = P_{tag}\eta \quad (2.3)$$

$$P_R = P_{ref} G_T G_A \eta \left(\frac{\lambda}{4\pi d}\right)^2 = P_T {G_T}^2 {G_A}^2 \eta \left(\frac{\lambda}{4\pi d}\right)^4 \quad (2.4)$$

Radar cross section (RCS), σ, can also be calculated from the reflected power, P_{ref}, as defined in (2.5), where S is the power density of the EM wave incident on the RFID tag. Thus, RCS of an RFID tag can be written as in (2.7), showing its dependence on the load impedance of the tag (R_A is the real part of Z_A) [2.8].

$$\sigma = \frac{P_{ref}}{S} \quad (2.5)$$

$$S = \frac{P_T G_T}{4\pi d^2} \quad (2.6)$$

$$\sigma = \frac{\lambda^2 G_A^2 R_A^2}{\pi |Z_A + Z_L|^2} \quad (2.7)$$

Consequently, the RCS can also be written in terms of the return loss, S_{11}, where the magnitude of S_{11} is estimated as in (2.8) [2.6]. Then RCS can be expressed as in (2.9).

$$|S_{11}|^2 \approx \frac{P_R}{P_T} \tag{2.8}$$

$$\sigma = |S_{11}|^2 \frac{(4\pi)^3 r^4}{G_T^2 \lambda^2} \tag{2.9}$$

In passive remote sensing, identification of the sensor can be constructed in either time domain signature or in frequency domain signature (refers to Chapter 1). In the time domain signature, identification is constructed with delay lines for both amplitude modulation [2.9, 2.10] or for phase modulation [2.11]. The delay lines were constructed with metamaterial-based transmission lines to reduce the size of the tag. Those in [2.9 – 2.10] operate at 3.4 GHz and 4.2 GHz, while the one in [2.11] operates at 2.2 GHz as shown in Figure 2.5. For frequency domain signature, interrogation is possible only if the reflections from the environment are negligible and not mixed with the signals from the sensors. Consequently, applications that require sensors positioned next to large metallic surfaces cannot utilize a frequency domain signature platform. In this platform, the sensors are identified based on their operating frequencies. For amplitude modulation, sensing is based on the RCS variation of the RFID tags as reported in [2.12]. For frequency modulation, sensing is based on tracking the resonant frequency shift of the RFID tags as in [2.7]. Note that if the sensing element is not integrated with a high gain antenna in this platform, the interrogation range is highly limited because path loss as reflected in (2.4) would apply.

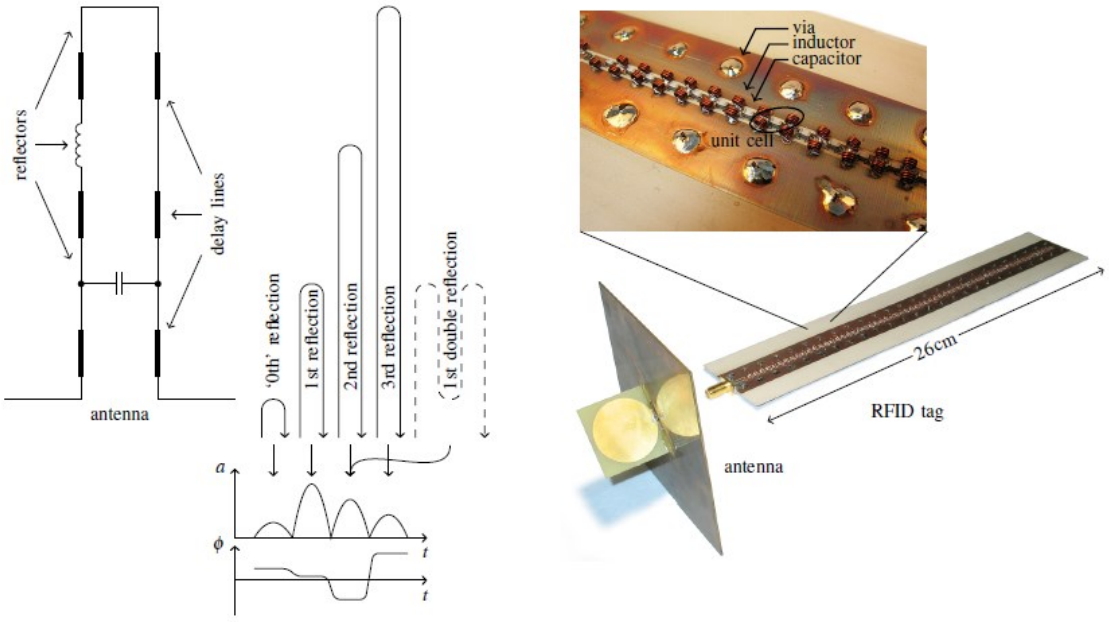

(a) Operating principles of the passive RFID tag using delay lines

(b) Prototype of the passive RFID tag using delay lines at 2.2 GHz

Figure 2.5. Phase modulation of digital ID of an RFID tag using metamaterial delay lines. [2.11]

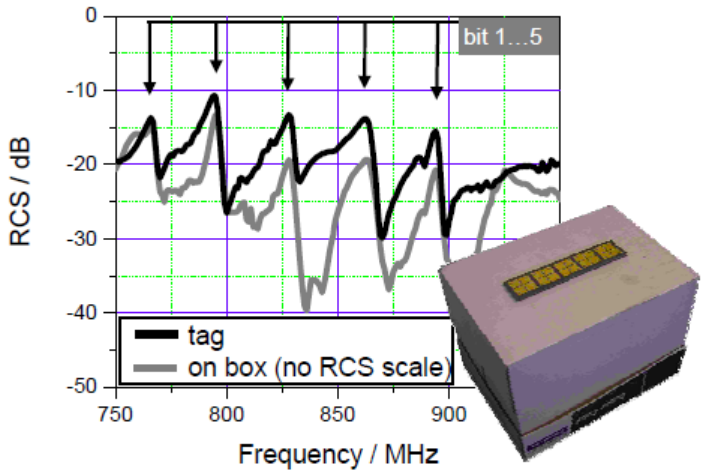

Figure 2.6. RCS of resonators based on microstrip patch antenna (finite ground) measured in free space and on top of a carton box. [2.12]

2.2. Passive Remote Sensing based on SAW

A major advantage of SAW RFID tags is that they are chipless and operating in long range (up to 20 m) [2.13]. SAW devices are based on the piezoelectric effect and on the surface-related dispersion of elastic waves at low speed [2.2]. The substrate used is a piezoelectric single crystal, which generates surface charges when it is elastically deformed in certain direction. The effect is also reversible, where the surface waves are generated when there are charges accumulated. Figure 2.7 shows the schematic of a passive SAW RFID tag. In an RFID system, a high frequency EM wave emitted from the interrogation unit is received by the antenna of the SAW transponder. The interdigital transducer (IDT) that is connected to the tag antenna transforms the RF signal (RF pulses) into an SAW by the inverse piezoelectric effect. The SAW then propagates on the crystal toward the reflectors. The reflectors are positioned in certain pattern such that they reflect the SAW back to the IDT in a series of echoes like bar code signals. These echoes are converted back into EM waves at the IDT by the piezoelectric effect and transmitted back to the RFID reader through the tag antenna. The echo pulses received at the reader are delayed from the interrogation pulse and the pulse collection allows for identification of the tag.

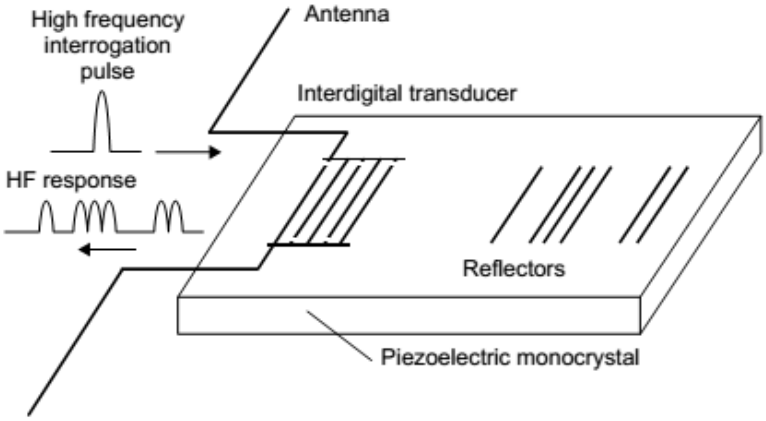

Figure 2.7. Diagram of a SAW transponder under interrogation. [2.2]

The interrogation range, *d,* of the SAW system can be determined by (2.10), which can be derived from the radar equations in Section 2.1. It includes the integration time, t_i, noise figure, *F*, signal-to-noise ratio, *SNR* (typically required to be 10 dB), and insertion loss, *IL*. [2.2, 2.14]

$$d = \sqrt[4]{\frac{P_T G_T^2 G_R^2 t_i \lambda^4}{k T_o F(SNR) IL}} \tag{2.10}$$

In SAW based RFID sensors, the physical quantity to be monitored has to act on the path of the SAW. For example, the change in temperature, pressure, or stress/strain alters the length of the acoustic path and the elastic constants of the substrate material, thus changing the velocity of the SAW. There are four main types of passive SAW sensors: SAW delay lines, SAW dispersive lines, one-port SAW resonators, and two-port SAW load impedances [2.2, 2.14, 2.15]. Sensing in SAW delay lines is based on the

phase change (due to, for example, the temperature, stress/strain effects on the substrate) in the SAW propagation time $T_D = L/v_{SAW}$, the ratio of acoustical length and SAW velocity. In dispersive SAW sensors, dispersive properties of the substrate depend on the physical quantity under sensing, causing a Doppler shift that yields a time shift of the compressed impulse similar to the Doppler shift of an FMCW radar system [2.14 – 2.15]. A one-port resonator SAW tag consists of acoustic resonators (constructed by finger electrodes as shown in Figure 2.8), where received energy is stored in the resonators, delayed and then reflected back to the tag antenna [2.2]. Multiple reflections due to the resonators yield a longer acoustic path therefore a longer delay time. To eliminate the interrogation signal and echoes from the environment, the first 1 to 2 μs of the reflected signals are gated in the time domain. In two-port impedance SAW sensors (Figure 2.9), an IDT is used as a reflector that is loaded by a varying impedance element, which can be a switch or an external sensor. The variation of the load impedance (dependent on a physical quantity) changes the acoustic transmission and reflection properties of the IDT [2.2, 2.14].

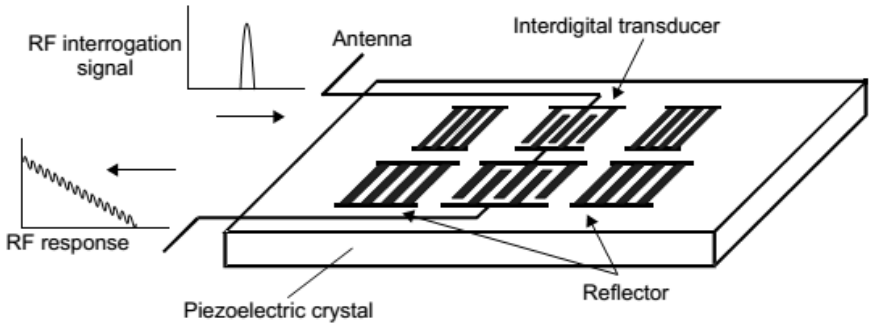

Figure 2.8 One-port resonator SAW sensor. [2.2]

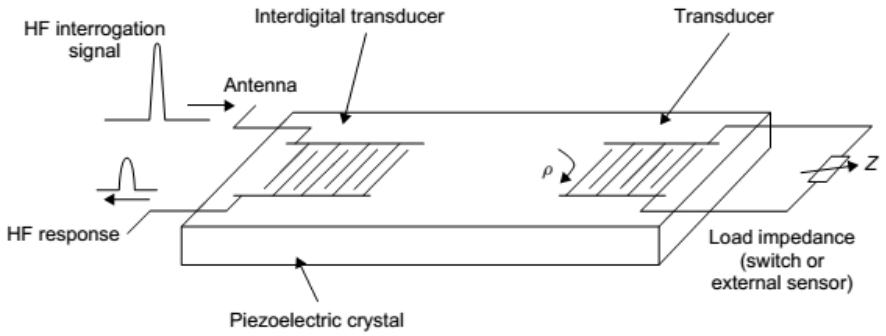

Figure 2.9 Two-port impedance SAW sensor. [2.2]

In general, the uplink and downlink (transmitted and echoed signals respectively) have to be separated. In passive SAW RFID sensors, a separation in time, i.e. time domain division (TDD) is necessary. Then the interrogation is based on either time domain sampling (TDS) as in radar, or frequency domain sampling (FDS) as in vector network analyzer (VNA). In TDS, the transmitted signals from the reader cover the total system bandwidth at once (wideband sampling). The whole sensor response can be recorded in one single scan of the interrogation cycle. A diagram of the TDS system is shown in Figure 2.10 [2.15]. This system gives fast access to the sensor information and requires low energy contents with fast switching in the transmitter and fast data acquisition in the receiver. In FDS, the interrogation is performed by scanning step-by-step small intervals of frequency (the resolution bandwidth) in the frequency domain to cover the total bandwidth (narrowband sampling). The sensor response is measured for a certain total number of scans at the center frequency, and the fast Fourier transform algorithms are performed at the receiver. A schematic of this system is shown in Figure 2.11. Therefore, interrogation in a SAW system can be performed with pulses or continuous waves (with wideband chirps especially for dispersive SAW sensors) [2.15].

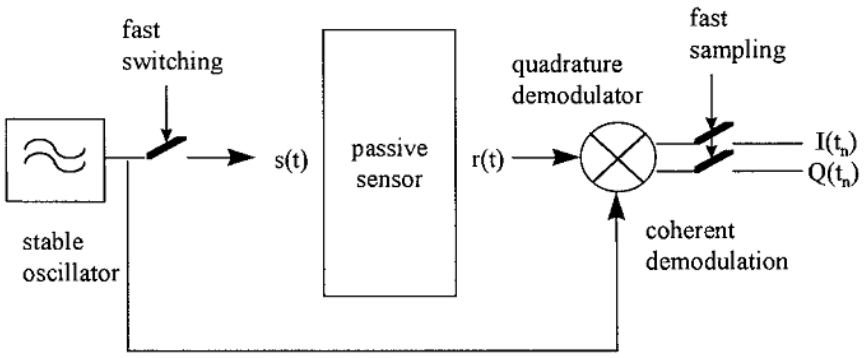

Figure 2.10. Time domain sampling transmitter and receiver principle. [2.14]

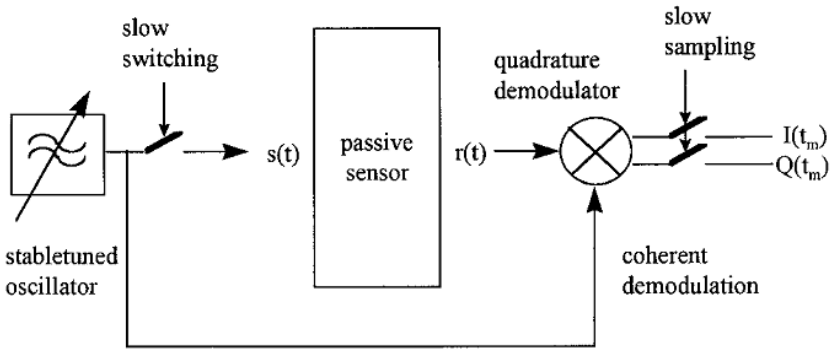

Figure 2.11. Frequency domain sampling transmitter and receiver principle. [2.14]

These devices operate at 2.45 GHz, which is known as IMS band (allocated for industrial, medical and scientific use). Due to the damping factor of the acoustic wave on the piezoelectric materials, the SAW RFID sensors cannot operate at higher frequencies such as those in millimeter waves. Most common materials that enable SAW devices are quartz (SiO_2), lithium-niobate ($LiNbO_3$), and lithiumtantalate ($LiTaO_3$). Recently, high temperature materials applicable up to 1000 ^oC have been introduced such as berlinite ($AlPO_4$), lithium tetraborate ($Li_2B_4O_7$), langasit ($La_3Ga_5SiO_{14}$), and gallium

orthophosphate ($GaPO_4$) [2.15]. Those substrates potentially enable SAW based sensors to be deployed in harsh environments such as aircraft engines, space shuttles, and space applications.

2.3. Passive Remote Sensing based on the Beat Frequency of an FMCW Radar

Recently, a new and original wireless sensing platform was introduced in which the identification is constructed in the beat frequency of the FMCW radar [2.16 – 2.17], in which different sensors give different time arrivals of multiple echoes due to delay lines (a time domain signature platform). The load (the sensor element) is connected to a high gain antenna with a delay line. Fundamentally, delay lines are utilized to separate the structural mode from the antenna mode in the backscattered signals. Sensing is achieved with the variation in RCS level from the target (amplitude modulation) due to the variation in the load impedance. Note that the system parameters here can be estimated by the same set of equations as in (2.1) to (2.7). The advantage of this platform is the elimination of ultra-wideband (UWB) reader utilized in the conventional RFID systems. It was demonstrated for passive sensors in long range (up to 30 m) for carrier frequency at 30 GHz [2.18 -2.19], although potentially platforms based on work in [2.9 – 2.12] may achieve similar range in theory. Furthermore, because the identification is based on beat frequency, it may tolerate lower SNR especially in long range interrogation. Low power on the receive channel of the reader with less signal processing also allows for better SNR. The FMCW radar offers advantages of lower power output and ease of implementation compared to the pulse radar.

2.3.1. Frequency Modulation

In an FMCW radar system, the frequency of the transmitted signal is modulated as a function of time (linear sawtooth or triangular signal modulation). In the triangular modulation, moving targets are easier to be detected based on double Doppler measurement that gives both velocity and range information [3.20]. The reflected signals consist of a replica of the transmitted waveform, delayed by the two-way propagation delay, $\tau = 2d/c$, where d is the distance and c is the propagation velocity. The beat frequency, f_b, is calculated as in (2.11) and illustrated in Figure 2.12a, where the transmitted signal is the solid black line and the received signal is the dotted black line for stationary targets. In the case of moving targets, the received signal suffers a Doppler frequency shift, $f_{Doppler}$, as illustrated in the blue line of Figure 2.12a and can be calculated as in (2.12). Depending on the direction of the movement (whether the target is moving toward or away from the radar), the beat frequency becomes either f_b^+ or f_b^- as in (2.13) and (2.14), respectively. The effects of the Doppler shifts on the beat frequency are illustrated in Figure 2.12b. In sensing applications, to isolate the Doppler effects from the beat frequency, which carries the ID of the sensor, is to have a reference (EM) reflective node that is immune to the change in the physical quantity under sensing and undergoing the same frequency variations due to Doppler effects [2.16]. Therefore, Doppler effects can be derived and accounted for when calculating the ID beat frequency of the sensor situated on the moving target.

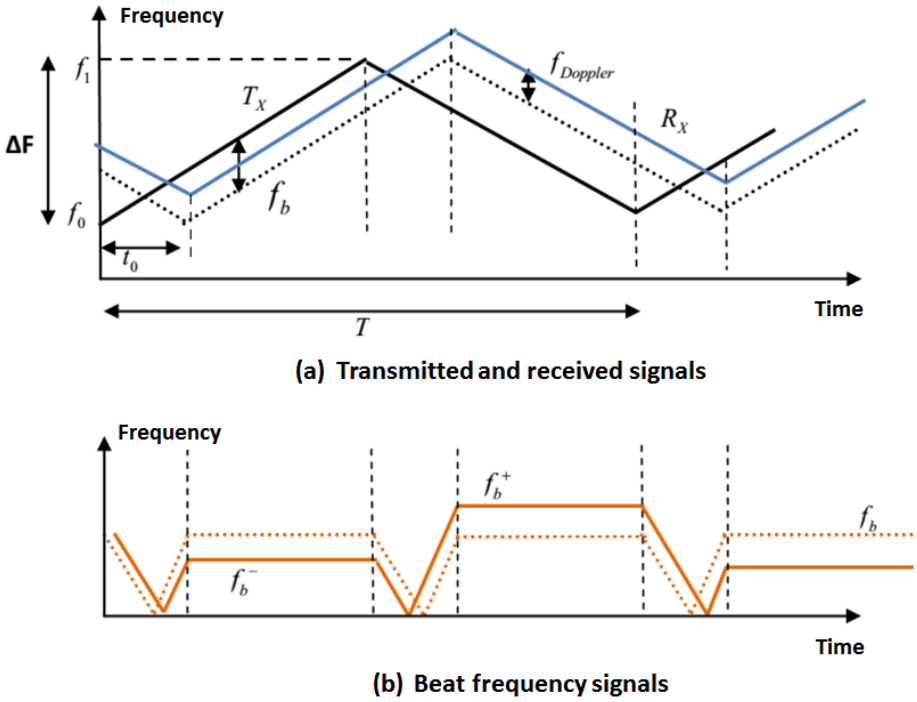

Figure 2.12. Signals obtained at the FMCW radar with a) the transmitted and received signal and b) the beat frequency signals. [2.16]

$$f_b = 2\,\frac{\Delta F}{T} t_o \tag{2.9}$$

$$f_{Doppler} = 2\,\frac{\upsilon}{\lambda} \tag{2.10}$$

$$f_b^- = 4\,\frac{\Delta F}{T} - f_{Doppler} \tag{2.11}$$

$$f_b^+ = 4\,\frac{\Delta F}{T} + f_{Doppler} \tag{2.12}$$

Sensing here relies on the resonant frequency shift of the load, from which shift the RCS variation is detected in certain bandwidth (Figure 2.13). Note that the scattering parameter, S_{11}, is equals to the reflection coefficient, Γ, that depends on the antenna and the load impedance as in (2.13) (recall Figure 2.4).

$$\Gamma = \frac{Z_A - Z_L}{Z_A + Z_L} \tag{2.13}$$

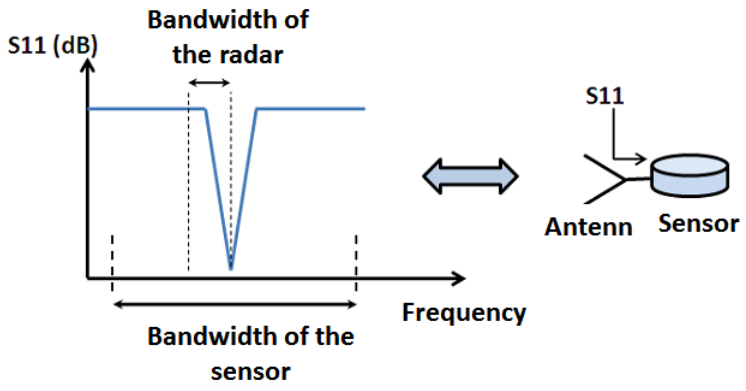

Figure 2.13. Interrogation bandwidth of the radar relative to the sensor. [2.16]

The interrogation bandwidth generated by the radar should cover the operation bandwidth of the sensor. There are two methods of modulation to cover the operating bandwidth of the sensor. In the first method, the modulation frequency bandwidth can be varied from *ΔF1*, to *ΔF2* and *ΔF3* with the center frequency *F0* fixed (Figure 2.14). This method applies to monitoring the RCS level of the sensor at a fixed center frequency (direct amplitude reading). The smaller band ΔF1 enables RCS reading with high accuracy provided by the high sensitivity of the sensor, while increasing larger

modulation bandwidth can accommodate large sensing dynamic range of the sensor. In the second method, the modulation frequency bandwidth is offset in fixed intervals across the operating bandwidth of the sensor in order to track the resonant frequency of the sensor, i.e. the RCS notch in the frequency domain (Figure 2.15).

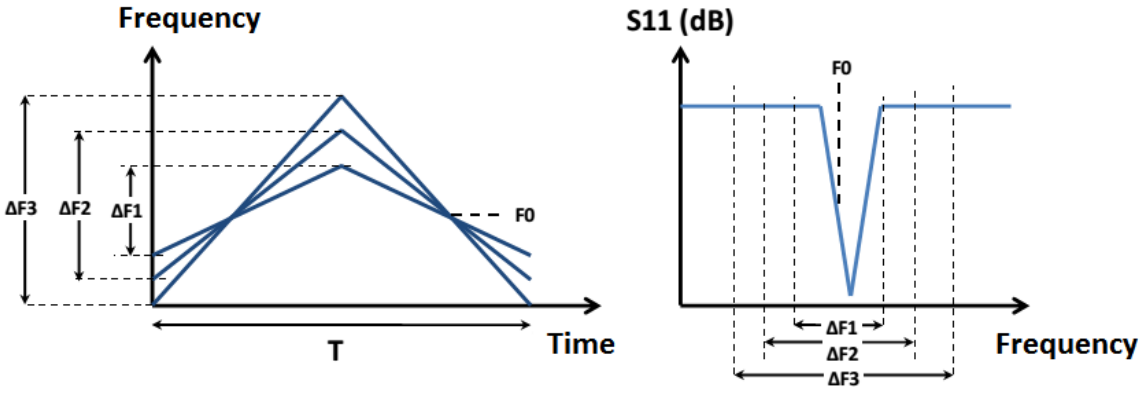

Figure 2.14. Modulation with variable frequency bandwidth. [2.16]

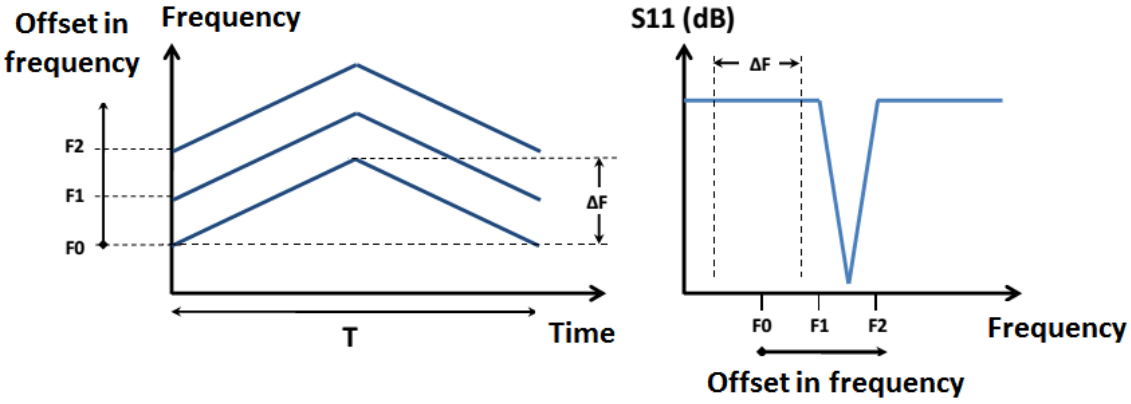

Figure 2.15. Modulation with stepped frequency bandwidth. [2.16]

2.3.2. Detection and Sensitivity of RCS

Simulations and measurements to estimate the level of threshold power for the maximum range of the FMCW radar system were investigated by F. Chebila in [2.16] for a system at 3 GHz and another at 30 GHz. The bistatic radar transmitting and receiving antennas, each with 14 dBi gain. The output power is 13 dBm for a target of gain 0 dBi. The plot of the threshold power is shown in Figure 2.16. Here, threshold power refers to the received power with the threshold SNR of 10 dB, Consequently, as the tag antenna is implemented, for example with a 15 dBi gain, it allows an SNR of about 10 dB at 20 m for the 30 GHz system in an outdoor environment (the noise floor is about – 80 dBm). Sensitivity of the RCS in this platform can be estimated as in (2.16), which is derived based on (2.7) and Figure 2.4. Equation (2.16) relates the change in the load impedance (sensitivity with respect to the physical quantity) to the change in RCS [2.16].

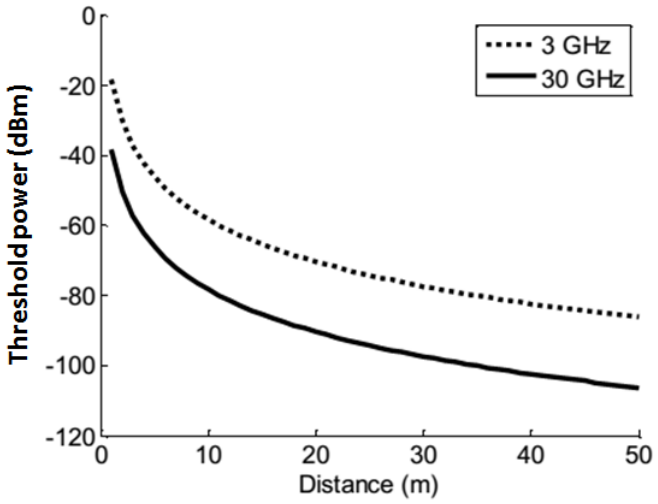

Figure 2.16. Threshold power depending on the distance. [2.16]

$$\frac{\Delta\sigma}{\sigma} = \frac{2(R_A+R_L)R_L}{(R_A+R_L)^2+X_L^2}\frac{\Delta R_L}{R_L} + \frac{2X_L^2}{(R_A+R_L)^2+X_L^2}\frac{\Delta X_L}{X_L} \quad (2.16)$$

2.3.3. Problems and Solutions of the Delay Lines

As discussed in Section 2.1, the delay lines are important when the sensor (refers to both the sensor element and the communicating antenna) is placed on a large metallic surface, a situation common in aircraft and space applications. This problem is common to both conventional RFID systems and the beat-frequency detection radar system in passive remote sensing, and is further discussed here. The problem that necessitates and is solved by the delay lines is illustrated in Figure 2.17. The structural mode and the antenna mode signal (in terms of RCS) are overlapped at the same beat frequency, while the two modes are separated into different beat frequencies with the use of the delay line.

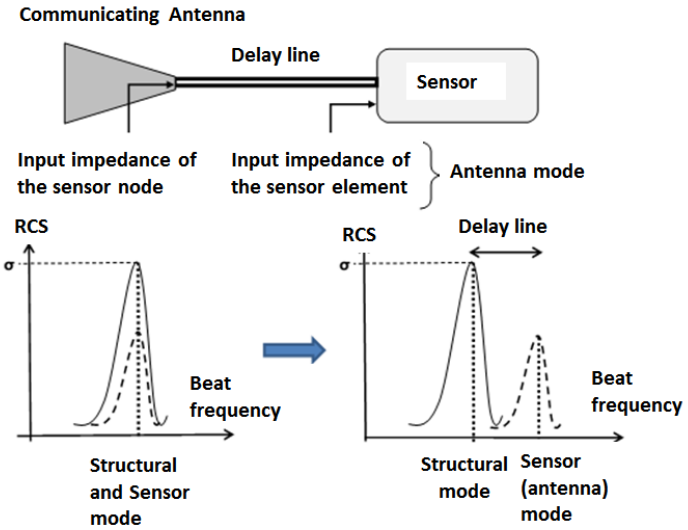

Figure 2.17 Structural mode and the sensor (antenna) mode in the beat frequency domain. [2.16]

The presence of the delay lines introduces loss and large area to the sensor element, but they can be mitigated with several techniques. The size of the delay lines can be minimized with techniques such as microstrip meanderline topology [2.21 – 2.23]. An example of such a line is shown in Figure 2.18. The loss of the delay lines can be minimized with the use of metamaterial resonators [2.11, 2.24], which also shorten the physical length of the line due to the slow wave behavior in the resonant frequency band of the resonators while keep the electrical length the same.

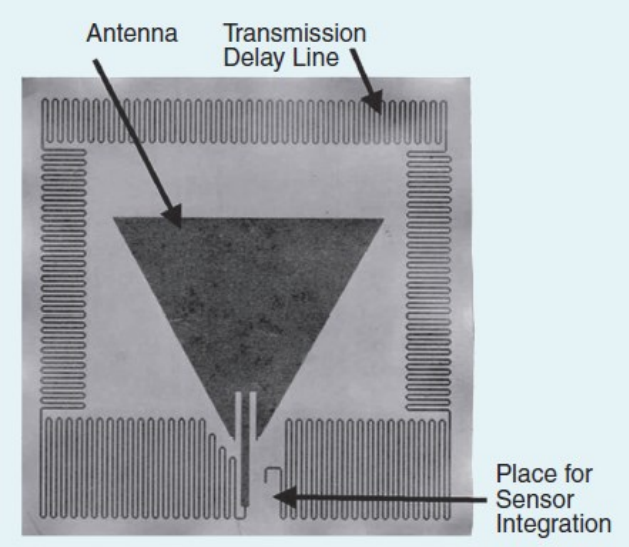

Figure 2.18. Chipless RFID tag with patch antenna and delay line. [2.23]

2.3.4. Multi-node Passive Sensing Networks

With the delay lines, each sensor node can be identified in the beat frequency domain with their own frequency peak associated with their own delay line (electrical)

length. An example of such a network applicable to an aircraft wing is shown in Figure 2.19 [2.16], where different sensors give different distinct beat frequencies. The different changes in the level of the radar signal at these beat frequencies indicate different changes due to the physical quantity occurring at different sensors distributed on the wing. The capacity of the radar to differentiate between several sensors in this network relies on the minimum delay between different sensor mode signals. This minimum delay, Δd, is the same as the depth resolution of the radar, and it can be estimated according to (2.17), where ΔF is the modulation bandwidth and c is the velocity of light. Consequently, the beat frequency separation, Δf, can be estimated according to (2.18) [2.17], where T is the modulation period (chirp signal) and ε_r is the relative permittivity of the transmission line.

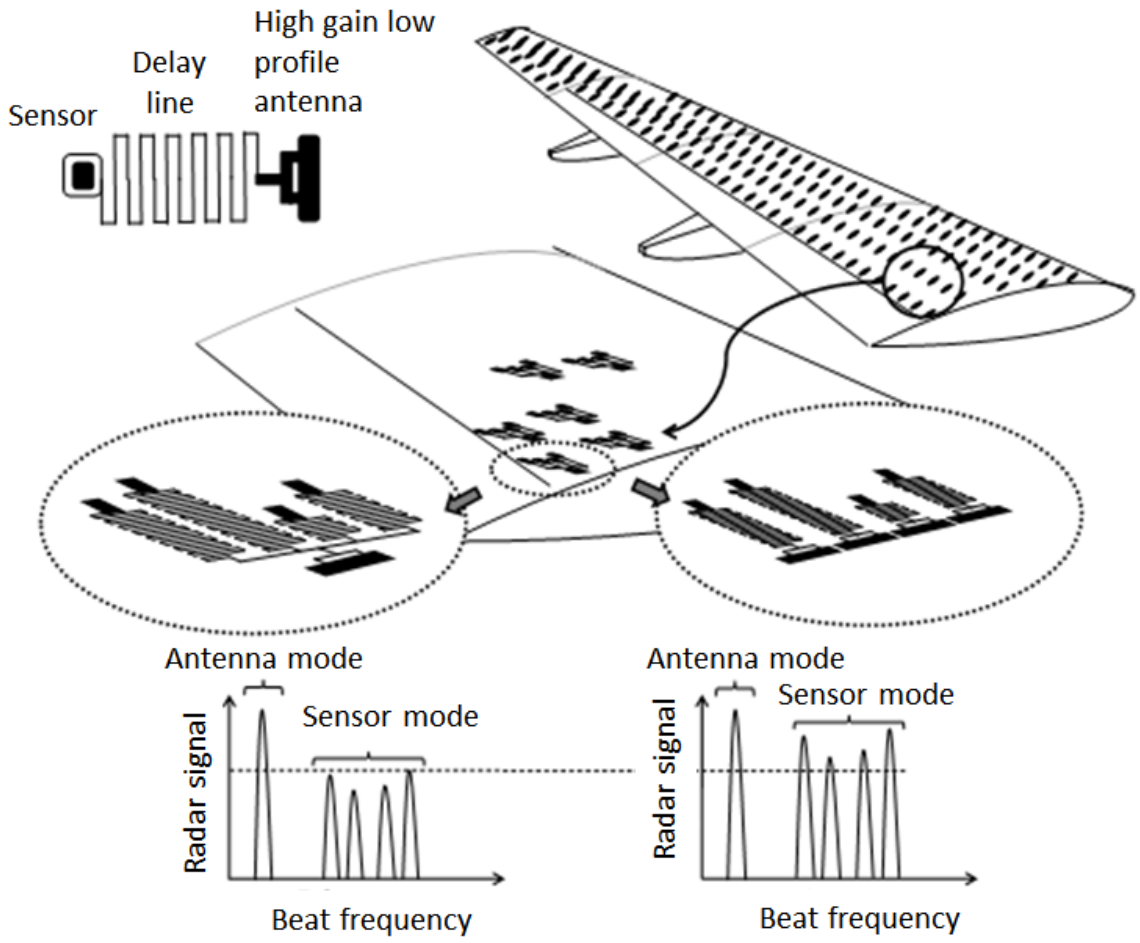

Figure 2.19. Example of passive sensor network based on beat frequency implemented on an aircraft wing.

$$\Delta d = \frac{c}{2\Delta F} \tag{2.17}$$

$$\Delta f = 4\frac{\Delta F}{T}\frac{\Delta d\sqrt{\varepsilon_r}}{c} \tag{2.18}$$

A proof-of-concept measurement of this network was demonstrated for a system at 30 GHz (ΔF = 700 MHz, T = 1 ms) by Chebila [2.17, 2.24]. The experiment setup is

shown in Figure 2.20, where two horn antennas were positioned at distances R_1 (1 m) and R_2 (2.5 m) away from the radar. The delay lines L_1 (30 cm), L_2 (75 cm), and L_3 (75 cm) are based on coaxial line (50 Ω, ε_r = 1.7) with 2 dB/m of loss. The three different loads Z_1, Z_2, and Z_3 are arranged according to the sketch in Figure 2.20. Four different load configurations of (Z_1,Z_2,Z_3) were tested: (∞,∞,∞), (50 Ω, ∞, ∞), (∞, 50 Ω, ∞), and (∞,∞, 50 Ω). Depending on different load configurations, the echoed signals of different scatterers are shown in Figure 2.21 in the beat frequency domain [2.17, 2.24], where five distinct echoes were detected. This experiment is to demonstrate the feasibility of the passive sensor network based on beat frequency identification, not to include the signal variation based on the small variation of the load impedance. Here, the minimal physical length of L_{min} = 50 cm (propagation delay of $L\sqrt{\varepsilon_r}/c \approx 2\ ns$) is required for neighboring non-overlapping distinct echos. Correspondingly, the depth resolution in terms of beat frequency separation can be estimated according to (2.18) to be 6 kHz [2.17].

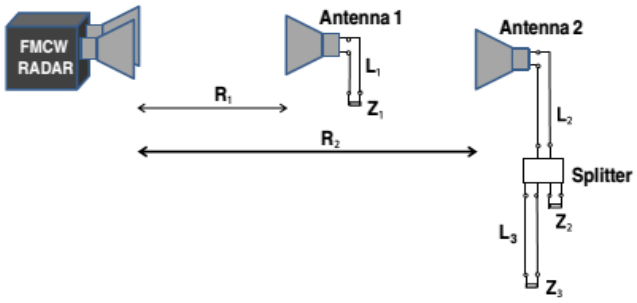

Figure 2.20. Sketch of the proof-of-concept experiment for multi-node passive sensing network based on beat frequency identification. [2.17]

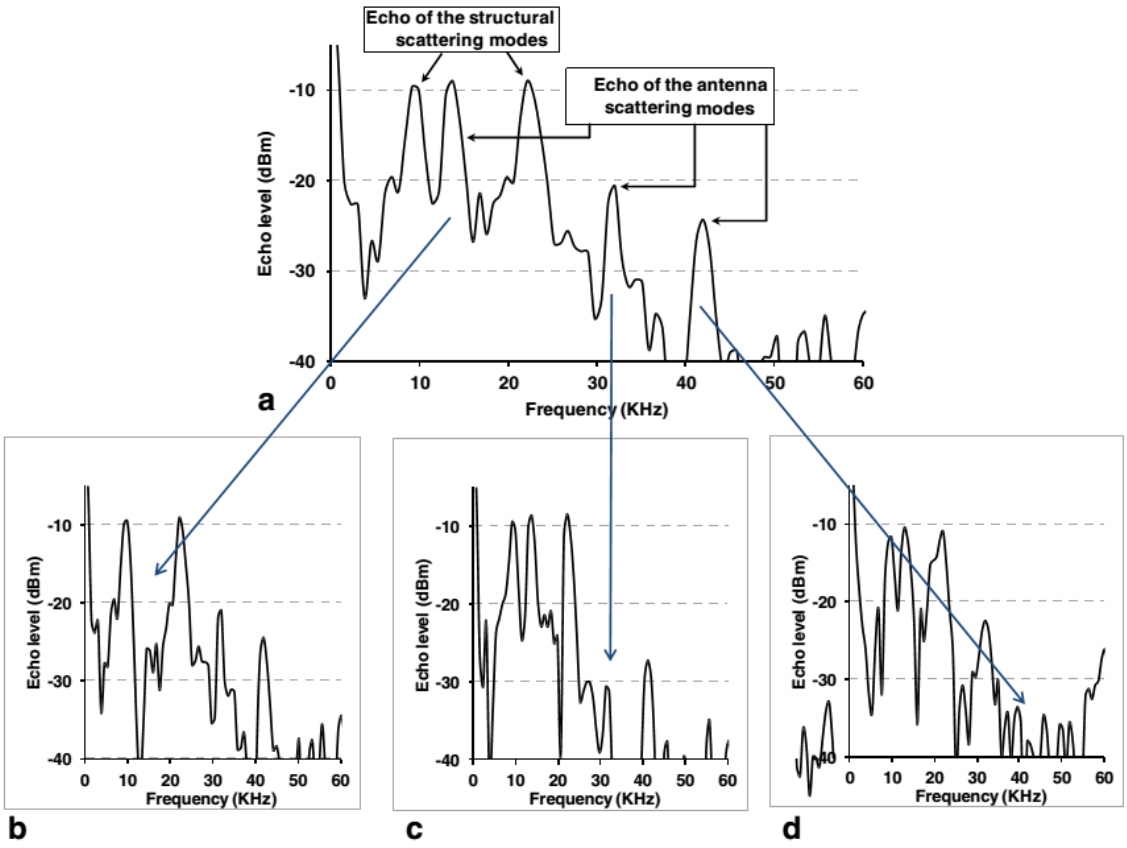

Figure 2.21. Beat frequency spectrum measurement by the FMCW radar reader for (Z1,Z2,Z3) of a) (∞,∞,∞), b) (50 Ω, ∞, ∞), c) (∞, 50 Ω, ∞), and d) (∞,∞, 50 Ω). [2.17]

2.4. References

[2.1] J. Landt, "The history of RFID," *IEEE Potentials*, vol. 24, no. 4, pp. 8 – 11, 2005.

[2.2] K. Finkenzeller, *RFID Handbook*, 2nd ed. New York: Wiley, 2003.

[2.3] S. Preradovic, N. Karmakar, I. Balbin, "RFID transponders," *IEEE Microwave Mag.*, vol. 9, no. 5, pp. 90 – 103, Oct. 2008.

[2.4] C. S. Hartmann, "A global SAW ID tag with large data capacity," in *Proc. IEEE Ultrasonics Symp.*, Munich, Germany, Oct. 2002, vol. 1, pp. 65 – 69.

[2.5] B. Violino (2005 Jan.). *A Summary of RFID Standards*, RFID Journal [Online]. Available: http://www.rfidjournal.com/article/view/1335/3 (Accessed: 21 July 2013).

[2.6] P. V. Nikitin, K. V. S. Rao, "Theory and measurement of backscattering from RFID tags," *IEEE Antennas and Propagation Mag*., vol. 48, no. 6, pp. 212 – 218, Dec. 2006.

[2.7] T. T. Thai, L. Yang, G. R. DeJean, M. M. Tentzeris, "Nanotechnology enables wireless gas sensing," *IEEE Microwave Mag*., vol. 12, no. 4, pp. 84 – 95, June, 2011.

[2.8] K. Penttila, M. Keskilammi, L. Sydanheimo, M. Kivikoski, "Radar cross-section analysis for passive RFID systems", *IEE Proceedings on Microwaves Antennas and Propagation*, vol. 153, no. 1, pp. 103 – 109, Feb. 2006.

[2.9] M. Schüßler, C. Damm, R. Jakoby, "Periodically LC loaded lines for RFID backscatter applications," in *Metamaterials*, Rome, Italy, Oct. 2007.

[2.10] M. Schüßler, C. Damm, M. Maasch, R. Jakoby, "Performance evaluation of left-handed delay lines for RFID backscatter applications," in *IEEE MTT-S Int. Microw. Symp.*, Atlanta, GA, June 2008, pp. 177 – 180.

[2.11] C. Mandel, M. Schüßler, M. Maasch, R. Jakoby, "A novel passive phase modulator based on LH delay lines for chipless microwave RFID applications," in *IEEE MTT-S Int. Microwave Workshop on Wireless Sens. Local Pos. and RFID*, Cavtat, Croatia, 2009, pp. 1 – 4.

[2.12] M. Schüßler, M. Maasch, C. Damm, R. Jakoby, "Compact microstrip patch antennas for passive RFID backscatter tags," in *Euro. Microw. Conf.*, Rome, Italy, Sept. – Oct. 2009, pp. 1101 – 1104.

[2.13] J. Dowling, M. M. Tentzeris, N. Beckett, "RFID-enabled Temperature Sensing Devices: A major Step Forward for Energy Efficiency in Home and Industrial Applications?," in *IEEE MTT-S Int. Microwave Workshop on Wireless Sens. Local Pos. and RFID*, Cavtat, Croatia, Sept. 2009, pp. 1 – 4.

[2.14] L. Reindl, G. Scholl, T. Ostertag, H. Scherr, U. Wolff, F. Schmidt, "Theory and Application of Pasisve SAW Radio Transponders as Sensors," *IEEE Trans. Ultra. Ferro. Freq. Contrl.*, vol. 45, no. 5, pp. 1281 – 1292, Sept. 1998.

[2.15] A. Pohl, "A review of wireless SAW sensors," *IEEE Trans. Ultra. Ferro. Freq. Contrl.*, vol. 7, no. 2, pp. 317 – 332, Mar. 2000.

[2.16] F. Chebila, "Lecteur Radar pour Capteurs Passifs à Transduction Radio Fréquence," Ph.D. dissertation, University of Toulouse, Toulouse, France, Mar. 2011.

[2.17] H. Aubert, F. Chebila, M. Jatlaoui, T. Thai, H. Hallil, A. Traille, S. Bouaziz, A. Rifai, P. Pons, P. Menini, M. Tentzeris, "Wireless sensing and identification based on radar cross section variability measurement of passive electromagnetic sensors," *Ann. Telecommun., Springer-Verla*g, vol. 68, no. 7 – 8, pp. 425 – 435, June 2013.

[2.18] M. Jatlaoui, F. Chebila, P. Pons, H. Aubert, "New microsensors identification techniques based on reconfigurable multiband scatterers," in *Asia-Pacific Microw. Conf.*, Singapore, Dec. 2009, pp. 968 – 971.

[2.19] M. Jatlaoui, F. Chebila, T. Idda, P. Pons, H. Aubert, "Phenomenological theory and experimental characterizations of passive wireless EM pressure micro-sensor prototype," in *IEEE Conf. Sensors*, Waikaloa, Hawaï, Nov. 2010, pp. 1 – 4.

[2.20] H. D. Griffiths, "New ideas in FM radar," *Elect. & Comm. Eng. J.*, pp. 185 – 194, Oct. 1990.

[2.21] A. Chamarti, K. Varahramayan, "Transmission delay line based ID generation circuit for RFID applications," *IEEE Microw. Wireless Comp. Lett*., vol. 16, no. 11, pp. 588 – 590, Nov. 2006.

[2.22] J. Vemagiri, A. Chamarti, M. Agarwal, K. Varahramyan, "Transmission line delay-based radio frequency identification (RFID) tag," *Microw. Opt. Technol. Lett*., vol. 49, no. 8, pp. 1900 – 1904, 2007.

[2.23] S. Shretha, J. Vemagiri, M. Agarwal, K. Varahramyan, "Transmission line reflection and delay-based ID generation scheme for RFID and other applications," *Int. J. Radio Freq. Identi. Tech. Appl*., vol. 1, no. 4, pp. 401 – 416, 2007.

[2.24] M. Jatlaoui, F. Chebila, S. Bouaziz, P. Pons, H. Aubert, "Original identification technique of passive EM sensors using loaded transmission delay lines," in *Euro. Microw. Conf.*, Paris, France, Sept. 2010, pp. 1106 – 1109.

Chapter 3.

Radio Frequency Temperature Sensor

3.1. Introduction

A wireless, passive temperature transducer is a device without internal power placed at the monitored site that can transform the local temperature into an output signal that can be read wirelessly by a control system located remotely from the monitored site. Some techniques for temperature measurements include those based on thermoelectricity, temperature dependent variation of the resistance of electrical conductors, fluorescence and spectral characteristics [3.1]. However, most existing temperature sensors require a power source, and those with high sensitivity suffer from performance degradation above 130 ^{o}C [3.2 – 3.5]. In the class of passive RF sensors, a capacitively-loaded MEMS (micro-electromechanical systems) slot element for wireless temperature sensing demonstrated up to 300 ^{o}C was introduced [3.5] but had a low sensitivity of about 580 kHz/^{o}C (operating around 19.4 GHz), i.e. 0.003 % of frequency shift per ^{o}C. This sensor operates based on multimorph cantilevers where the deflection of the cantilevers alters the slot capacitance, thus shifting the slot resonant frequency. The sensitivity here is inherently limited by the resonant principle of the sensor design.

The work in this chapter introduced a new wireless, passive, and ultrasensitive temperature transducer. The following discussions and results are based on [3.6]. The RF transducer consists of split ring resonators (SRRs) integrated with bi-layer micro-cantilevers. The bimorph cantilevers consist of layers of different thermal expansive coefficients that cause them to bend as temperature changes. Utilizing MEMS allows

devices to have low costs, small form factors, and ease of fabrication and integration. The SRRs can potentially operate up to millimeter-wave frequencies above 30 GHz. The micro-cantilevers are placed over split gaps of the SRRs. As the cantilevers deflect in response to temperature changes, the resonant frequencies of the SRR are shifted. The bimorph material choices can be varied and adapted for various temperature ranges desired for different applications while requiring little design modification; thus it allows for sensing in an extreme temperature environment potentially up to 1600 ^{o}C. Further illustration of such an application with respect to state-of-the-art sensors will be discussed later in this chapter. Without loss of generality, a prototype scaled up in size with operating frequency of 4.7 GHz is presented in this chapter to demonstrate the proof-of-concept. To perform remote interrogation on the sensor, the radar technique discussed in Section 2.3 of Chapter 2 was utilized to perform measurements on the temperature prototypes. The radar system was developed by Herve Aubert, Franck Chebila, and co-authors [3.7 – 3.11]. The communication is based on the reading/monitoring of the RCS level of loaded multi-band scatterers by an FMCW radar as discussed in Chapter 2. The RCS measurements of the temperature prototypes were performed to illustrate a possible implementation of the transducer in passive, wireless sensing nodes in remote sensing networks. A more detailed evaluation of the performance of this sensor design and its remote interrogation compared to other existing remote sensors and systems are discussed at the end of this chapter.

3.2. Designs and Simulations

3.2.1. Designs

The transducer consists of double split rings positioned on a dielectric substrate. The slits of the rings are covered with bimorph micro-cantilevers whose layers are made from two different materials, gold (Au) with a thermal coefficient of 14.1 (10^{-6} K^{-1}) and silicon (Si) with a thermal coefficient in the range of 4.7 – 7.6 (10^{-6} K^{-1}) [3.12]. The design of the SRRs integrated with cantilevers is shown in Figure 3.1. The dimensions of the split rings are as follows: r_{int} = 230 μm, c = 120 μm, d = 50 μm, and s = 45 μm. The substrate is made of glass with dielectric constant ε_r = 4.82, and a thickness of 150 μm. The cantilevers have a length, *Lcant*, of 130 μm , and *dcap* is a variable parameter that symbolizes the air gap between the cantilever tip and the ring surface which is the same as the anchor's thickness in simulations. Both thicknesses of the Au and Si layers are 0.5 μm.

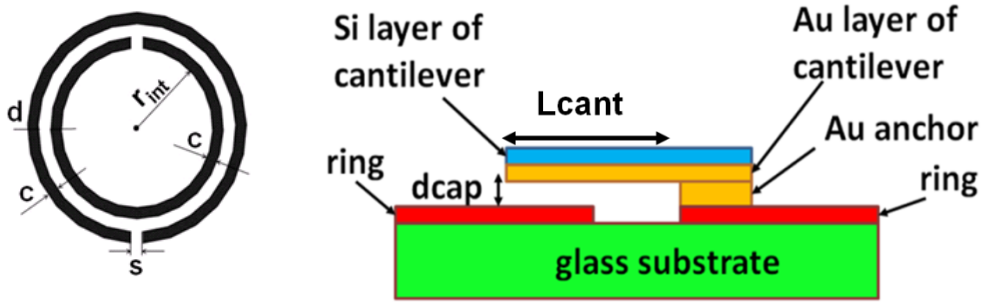

Figure 3.1. Topology of the SRRs and bimorph cantilevers.

The SRRs of the sensor can be excited by two distinct methods. In the first method, a plane wave is incident on the face of the SRRs as illustrated in Figure 3.2. It should be noted that an incident field EM wave must excite the magnetic resonance of the SRR through magnetic coupling in which the external magnetic field (H-field) should be polarized perpendicular to the SRR plane, i.e. the direction of propagation should be parallel to the SRR. However, if the direction of propagation is normal to the SRR plane and the incident electric field (E-field) is parallel to an imaginary line crossing the slits (Figure 3.2), the E-field coupling can induce the magnetic resonance of the SRR [3.13]. In the second approach, a coplanar waveguide (CPW) is placed on the other side of the substrate, and the slits of the SRR, denoted by *s*, are aligned to a gap between the signal line and the ground plane as illustrated in Figure 3.3. Thus, the SRRs can be excited by the fringing field that travels along the CPW, which has an impedance of 50Ω.

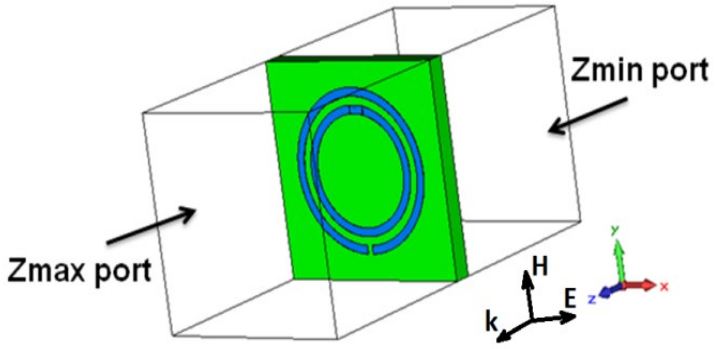

Figure 3.2. The setup of the first approach to excite the SRRs.

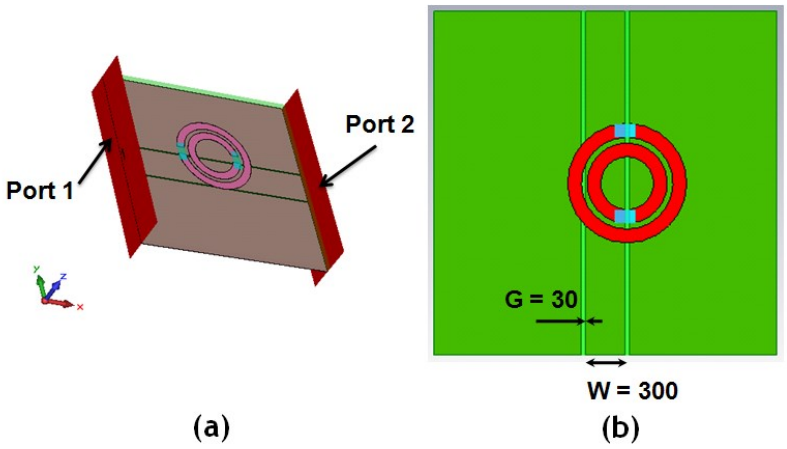

Figure 3.3. The setup of the second approach to excite the SRRs with (a) the three dimension view and (b) the top view of the circuit with substrate not shown and dimensions indicated in micron.

3.2.2. Simulation Results

Since the EM fields of the cantilevers are mostly concentrated in the air region sandwiched between the cantilevers and the metal rings, the deflection of the micro-cantilevers is approximated with a uniform deflection across the whole length of the cantilevers in simulations and measurements. The relationship between the deflection of the cantilever tip and temperature is shown in (3.1) (see [3.12] for details), where δ denotes the deflection, α_1 and α_2 denote thermal expansion coefficients of the two layers, t_1 and t_2 denote the thicknesses of the two layers and ΔT denotes the temperature change. From (3.1), the design of cantilevers presented in Figure 3.1 is estimated to have a sensitivity of 0.19 μm/^{o}C.

$$\delta = \frac{\Delta T(\alpha_1 - \alpha_2)\left(1 + {}^{t_1}/_{t_2}\right) {L_{cant}}^2}{2(t_1 + t_2)} \tag{3.1}$$

The simulation results of the first excitation approach, as presented in Figure 3.2, are shown in Figure 3.4. In this model, only one cantilever is implemented per SRR, which is positioned over the split of the inner rings. The two resonance modes observed in this frequency range (between 20 – 40 GHz) are excited by the two rings in this structure. Observed from Figure 3.4, the highest sensitivity is shown to be 1.41 GHz/μm, corresponding to 268 MHz/^{o}C using Au-Si bimorph cantilevers.

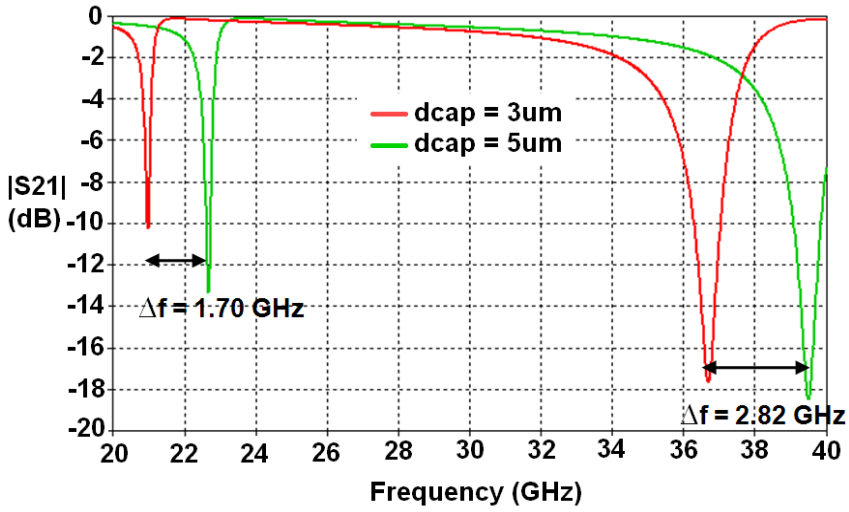

Figure 3.4. Magnitude of transmission coefficient S_{21} of the sensor in the first excitation configuration with incident plane waves.

The simulation results of the second excitation approach, as presented in Figure 3.3, are shown in Figure 3.5. In this model, two cantilevers are implemented per SRR, one is positioned over the inner ring split, and the other is placed over the outer ring split. The resonances in Figure 3.4 are different from those observed in Figure 3.3 because the

effective impedance in this structure is different from that presented in Figure 3.2. From Figure 3.5, the sensitivity is recorded as 2.62 GHz/μm, corresponding to 498 MHz/^{o}C, i.e. 1.6% frequency shift per ^{o}C, more than 2 orders of magnitude higher than the sensitivity reported in [3.5]. In [3.5], the cantilevers of the slot antenna deflect from 200 μm to a flat position, corresponding to a temperature range of 25^{o}C to 300^{o}C.

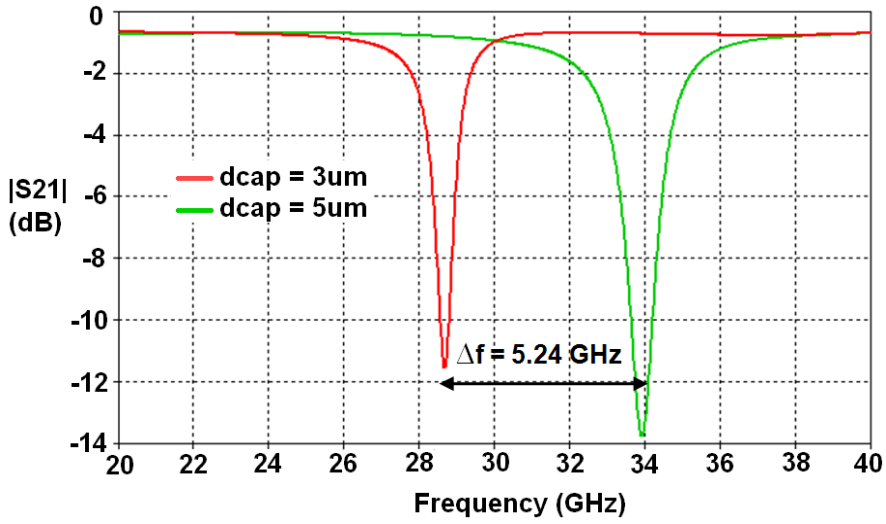

Figure 3.5. Magnitude of transmission coefficient S_{21} of the sensor in the second excitation configuration with CPW coupling.

3.3. Principles of Operation

The temperature sensing mechanism of the transducer is based on two uncoupled principles: 1) deflection of bimorph cantilevers in response to temperature change, and 2) resonant frequency shifts in response to deflection of cantilevers. Since they are two independent physical phenomena, they can be optimized separately.

3.3.1. Mechanical Response - Cantilever Deflection versus Temperature

The deflection is caused by the difference in thermal expansion coefficients of the two materials that constitute the two different layers of the cantilevers. This mechanism is well-known and has been utilized widely in numerous applications [3.12, 3.14]. As temperature changes the length of each cantilever layer expands at different rates. Since the two layers are bonded together, the cantilevers are bent in order to accommodate the different rates of change in the length of their layers. The deflection can be estimated utilizing (3.1). The bimorph cantilevers can realize various operating ranges depending on the material choices given that they provide the linear mechanical deflection within the temperature range of interest. Despite extended thermal cycling, the bimorph cantilevers are robust, and they reliably return to the same position at a given temperature as long as they are operated within the range limits for a particular material choice [3.12]. In the fabrication of bimorph micro-cantilevers, the tips of the cantilevers are usually deflected, referred to as initial deflection, which is due to the stress and strain during different MEMS processes. The initial deflection is in equilibrium at room temperature; then, it changes in response to temperature change. As a result, this initial deflection determines the resonances of the sensor at room temperature, which can be controlled to within an acceptable tolerance. The discussion of this tolerance limit is not within the scope of this thesis.

3.3.2. RF Response - Resonant Frequency shift versus Cantilever Deflection

The split ring structure became well-known from [3.15] and has attracted a growing interest since then. Many variations of SRRs have been proposed to realize materials with negative values of magnetic permeability also known as metamaterials. The metamaterials based on SRRs are highly frequency selective suggesting the SRR elements have a very high quality factor ($Q > 600$) [3.16 – 3.17]. When the SRRs are excited, an electromotive force is induced around the rings. However, due to the slits on each ring, displacement currents flow from one ring to another across the slot between them, thus the SRRs effectively inherit a distributed capacitance. As a result, the field at the slit on each ring has high intensity, which suggests that for any modification of the capacitance of these slots, the currents on the rings can be influenced significantly. Therefore, such change in the currents may induce a significant shift in the resonant frequencies. In the design proposed in Figure 3.1, the metal layer (Au) of the cantilever constitutes the lower layer of the bimorph cantilever, which is supported by a gold anchor that shorts the bimorph cantilever to one end of the split ring. The free end of the bimorph cantilever effectively forms a parallel plate capacitance with the other end of the split ring, making the split gap capacitance sensitive to the deflection of the bimorph cantilever. Note that the split gap capacitance also influences the distributed capacitance formed by the two concentric split rings.

In most applications of the SRRs, the split capacitances are relatively small and can be neglected. However, in the temperature sensor proposed here, where the splits are loaded with cantilevers, the significant values of the split gap capacitances cause large

shifts of the resonant frequencies as the displacement *dcap* changes due to the deflection of the bimorph cantilevers. This is because these capacitances can be estimated approximately as $(\varepsilon_o c\Delta x \,/\, dcap)$ where *c* is the width of the ring strip and the cantilever, *Δx* is the overlap length of the cantilevers and the rings, and *dcap* is the height of the cantilevers with respect to the ring surface. Therefore, as *dcap* increases, the effective capacitance of the resonator decreases, thus the resonant frequencies increase according to (3.2). To further understand how the frequency shift of the SRRs corresponds to the deflection of the cantilevers, a thorough study on the equivalent circuits of the split rings loaded with cantilevers is discussed in Chapter 4.

$$f = \frac{1}{2\pi\sqrt{(L_{eff}C_{eff})}} \tag{3.2}$$

Observe that the rate of change of capacitance is proportional to $(1/dcap^2)$, which would give a higher sensitivity as *dcap* decreases. On the other hand, if the cantilever gap *d* decreases below certain limit, the circuit would appear as a short circuit to the operating frequency. Therefore, to give the sensor a good dynamic range for a given sensitivity, the initial gap should be chosen appropriately given the limitations of the fabrication technology. Once the applications specify the temperature operating range, the choice of the materials, which is limited by the working environment, should produce the largest difference between the thermal expansion coefficients of the two layers that constitute the bimorph cantilevers. Next, the desired sensing range (deflection

induced by temperature change) should operate in the linear range of the EM response of the sensor, which is a strong dependence on the choice of the initial deflection.

3.4. Fabrications and Measurements of Proof-of-concept Prototypes

As discussed earlier, the operation of the first principle is independent from that of the second principle; hence, these two uncoupled mechanisms can be optimized separately. As a result, the sensitivity and the upper and lower limits of the temperature sensing range are determined mostly by the choice of materials utilized in the bimorph cantilevers. To demonstrate the proof-of-concept of the proposed temperature transducer, lower frequency prototypes were constructed for use at 3 – 5 GHz due to fabrication limitations. The size of the cantilevers was scaled up so they could be fabricated with quick and manual processes. Prototypes of both excitation methods (Figs. 3.2 – 3.3) were constructed. It should be noted that in the first prototype design (Figure 3.2), only one cantilever is loaded, while two cantilevers are loaded on the second prototype design (Figure 3.3).

3.4.1. Fabrication and Characterization of Cantilevers

In the low frequency prototypes, the cantilevers were made from a 100 μm thick Al sheet (thermal coefficient of 22.2 $x10^{-6}K^{-1}$) and a 50 μm thick PET (Polyethylene terephthalate, thermal coefficient of 59.4 $x10^{-6}K^{-1}$) sheet [3.12]. The anchor of the cantilever is also made of PET with different thicknesses (50 and 150 μm). The cantilevers were fabricated in the following steps. First, the 50 μm thick PET sheet is laminated to one side of the Al sheet. A smaller sheet of PET of either 50 μm or 150 μm

thickness, which is the anchor layer, is laminated onto the other side of the Al sheet. Then, the three laminated sheets (PET-Al-PET) were diced to leave 1mm x 1mm on the area of PET-Al-PET formation and 1.5 mm x 1 mm on the area of Al-PET formation to produce cantilevers with attached anchor. The results were 2.5 mm long cantilevers assembled with PET anchors that had preset thicknesses (Figure 3.6). The cantilevers were then stamped onto the SRR, over the splits, and mechanically stabilized with conductive epoxy at one end. The conductive epoxy also serves to short the cantilevers to the rings (Figure 3.6). The air gaps between cantilevers and rings, denoted as *dcap* in Figure 1, were measured with an optical scanner (a profilometer) after the assembly. Two samples with different anchor heights were fabricated to emulate the uniform deflection of the cantilevers. When SRRs are loaded with these cantilevers, without inducing temperature change, the frequency measurements on these samples could validly demonstrate the second operation principle (the EM responses for a given deflection) of the sensor. Note that although this formation of the cantilevers for prototypes operating in the 4 – 6 GHz range utilizes different materials from the cantilever formation shown in Figure 3.1 (PET and aluminum instead of silver and silicon in the respective order), loading the split ring structures in Figure 3.2 – 3.3 with the bimorph cantilevers of Al-PET does not alter their circuit operation. Recall that the operation of the sensor is based on two independent operating principles (Sect. 3.3), in which the mechanical principle (deflection versus temperature) is well-known. Thus, the proof-of-concept prototypes presented in the subsections 3.4.2 – 3.4.3 seek to validate the EM principles, from which the frequency shifts occur as observed in the thermally static RF simulations. The order of the bimorph cantilever layers would only affect the deflection direction of the

cantilevers (up or down) for a given temperature change (increased or decreased) but not the range of the deflection. In all the thermally static RF simulations presented in this chapter, the deflection direction of the cantilevers does not influence the frequency shifts – only the range of the deflection does. An optical measurement capture is shown in Figure 3.7 where the surface height is coded in color. Different reflecting points along the red line in Figure 3.7 are plotted in Figure 3.8, where the cantilever in the measurement is shown to slightly deflect upwards after the assembly and annealing processes.

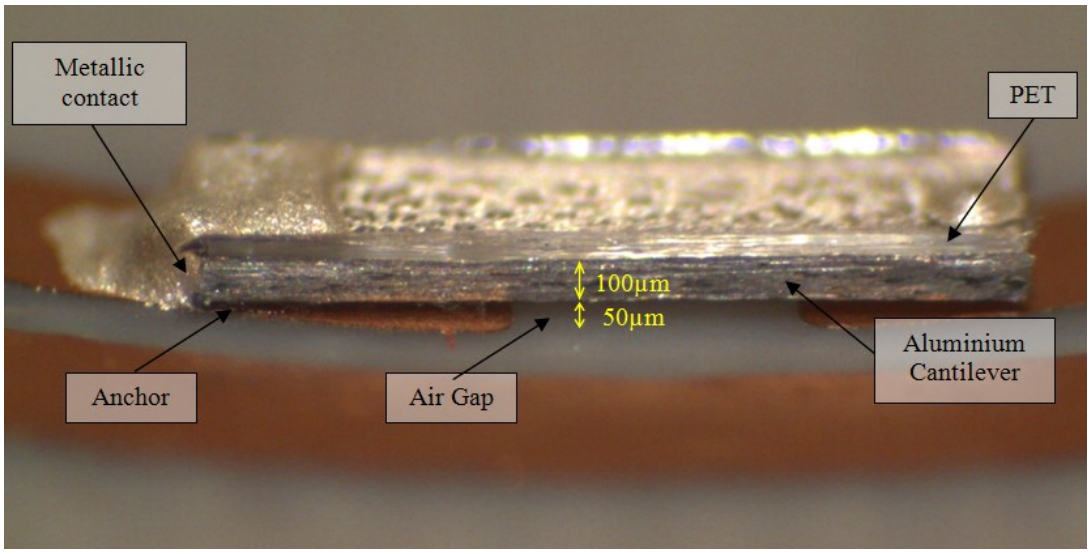

Figure 3.6. An Al-PET bimorph cantilever under microscope with PET anchor.

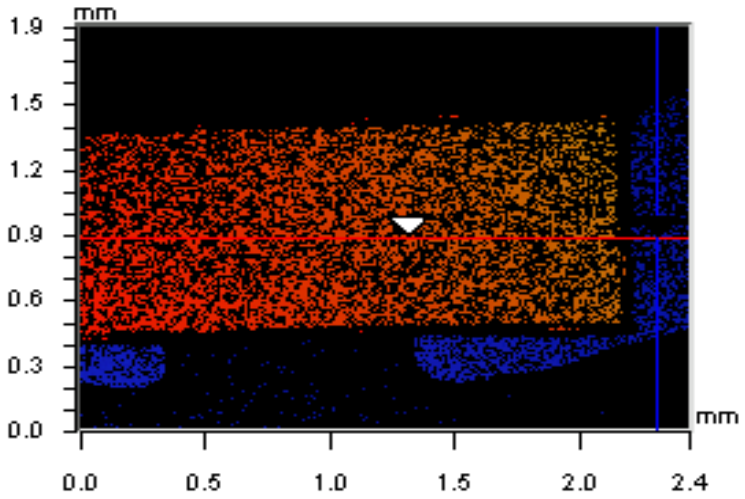

Figure 3.7. Top view capture of a cantilever from optical scan.

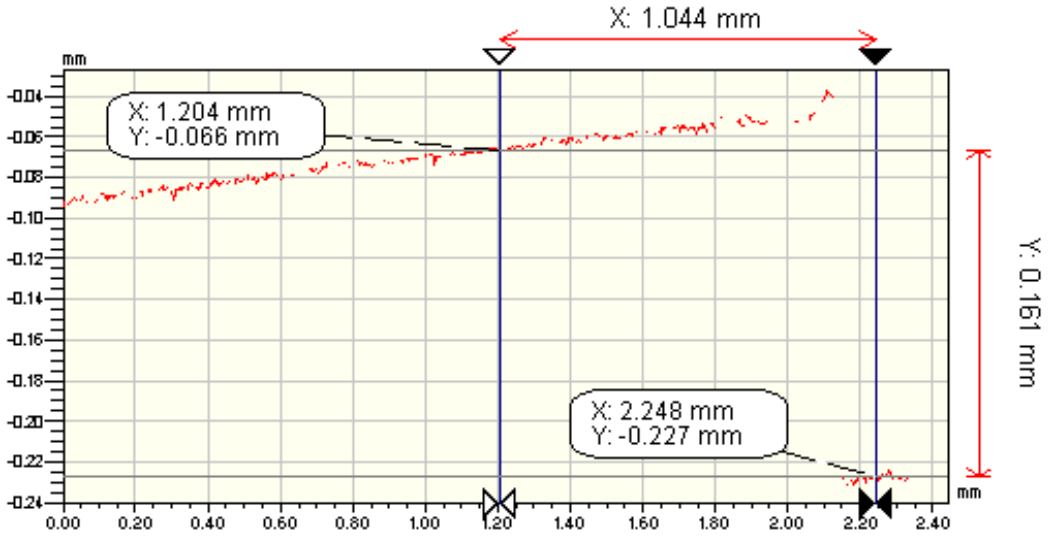

Figure 3.8. Optical surface scan along the long-axiscenter of the cantilever and ring.

3.4.2. Fabrication and Measurements of the Sensor: Incident Wave Excitation

Four SRRs, each loaded with one cantilever, were fabricated into a 2x2 array configuration as shown in Figure 3.9 without a ground plane. The substrate was RT5870 by Rogers Corporation [3.18] (ε_r = 2.33, substrate thickness = 787 μm). The dimensions of the SRRs are as follows: r_{int} = 3.5 mm, c = 1.0 mm, d = 0.5 mm, and s = 1.0 mm.

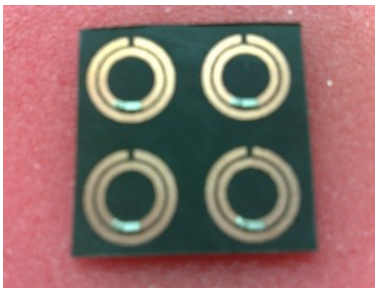

Figure 3.9. Array of 4 SRRs loaded with bimorph cantilevers.

The measurements were performed with a horn antenna and a vector network analyzer (VNA). Reflection-only calibration was performed using short, open, and load standards. To obtain temperature measurements, a horn antenna was directed at the sample as shown in the setup (Figure 3.10). The sample was attached onto a foam mat, and the temperature probe was placed next to the sample. The horn antenna was connected to the VNA for a 1-port measurement and S_{11} was recorded. At first, the temperature surrounding the sample was heated up to about 100 ^{o}C with a lamp. Since this was an open environment so the heated air was diffused quickly away from the

heated sample. Consequently, it was difficult to obtain a thermal steady state for each temperature point. Therefore, the temperature was allowed to cool down until the reading on the thermometer became relatively stable. Also, because of the open environment and limitations in the test conditions, an array of 4 ring sets was chosen in this test to achieve relatively uniform temperature induced by the lamp. Then the temperature and S_{11} result could be recorded. With such a measurement setup, only two data sets corresponding to two temperature points of 60 ^{o}C and 32 ^{o}C could be validly recorded in which the temperature appeared to be relatively stable with a tolerance of about +/- 5 ^{o}C. However, in this demonstration only the difference in temperature is important. The plot of this measurement is shown in Figure 3.11, which shows a resonant frequency shift of 70 MHz, from 4.77 GHz to 4.70 GHz, corresponding to a sensitivity of 2.5 MHz/^{o}C, i.e. 0.05 % of frequency shift per degree based on the center operating frequency of 4.735 GHz . In comparison to the sensitivity of 580 kHz/^{o}C as reported in [3.5], i.e., 0.003 % of frequency shift per degree based on a center operating frequency of 19.36 GHz (Figure 3.7 in [3.5]), the transducer prototype at 4.7 GHz reported here is 17 times more sensitive. The sensitivity achieved on this prototype is not proportional to that reported in the millimeter wave model in terms of dimension ratio because it is largely limited by the thermal-mechanical response of Al-PET bimorph cantilevers to temperature change. Note that the fabricated Al-PET bimorphs were estimated to have a deflection of 0.8 μm/^{o}C. In this setup, the positions of the cantilevers cannot be recorded during measurements, so the sensitivity in terms of frequency shift per deflection unit is not reported. Due to limitations in fabrication and measurements, the linearity of this sensor prototype is not addressed. In order to investigate the linearity of the sensor, a better controlled

environment for temperature measurements was constructed for the second prototype that is excited by the CPW coupling.

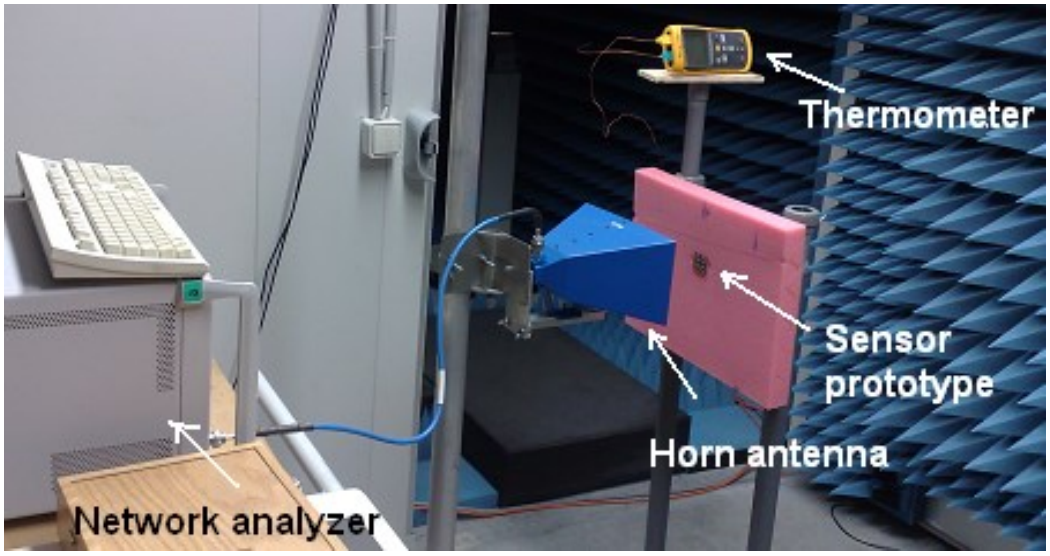

Figure 3.10. The temperature measurement setup.

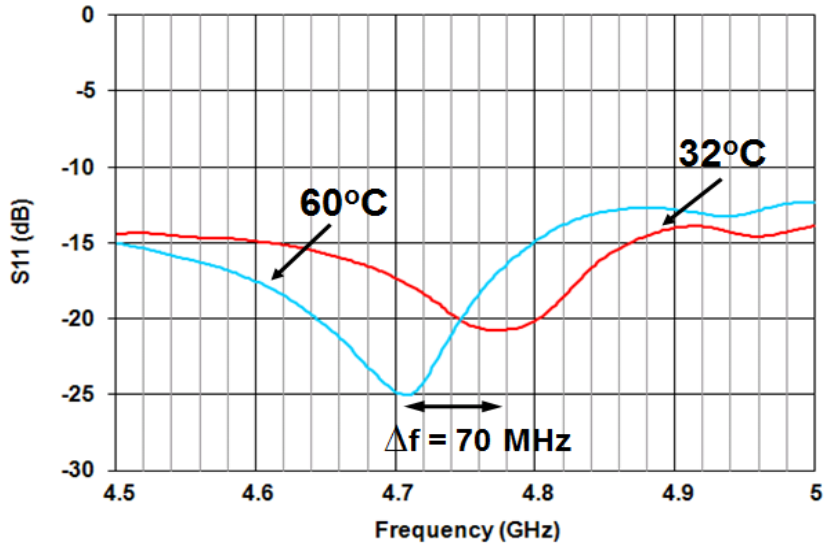

Figure 3.11. Frequency response for two different temperatures of the prototype with four SRR array loaded with cantilevers.

3.4.3. Fabrication and Measurements of the Sensor: CPW Coupling Excitation

In this configuration, the SRRs are loaded with two bimorph cantilevers and are excited by the traveling field of the CPW printed on the other side of the substrate (Figure 3.12). The prototype was realized on Neltec N9217 substrate (ε_r = 2.17, substrate thickness = 787 μm). The dimensions of the SRRs in this model are as follows: r_{int} = 2.5 mm, c = 1.0 mm, d = 0.5 mm, and s = 1.0 mm. The width of the signal line is 4 mm (50 Ω of the impedance) and the ground-signal separation is 150 μm. Since there is little control over this process of fabrication (discussed in Section 3.4.1), the cantilevers assembled on the same prototype have different initial deflections. Two prototypes were built, and the average heights (*dcap*) of the cantilevers are approximately 128 μm and 101 μm (relative to the top surface of the ring) for each pair of the cantilevers that were assembled on the two prototypes.

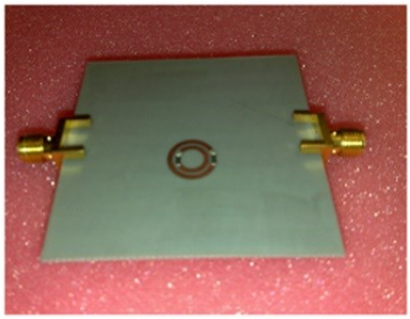

Figure 3.12. Sensor prototype with CPW excitation.

A. Frequency responses at room temperature for the thermally static cantilevers

The measurements for two prototypes of Figure 3.12 were performed in a thermally static setting with a VNA at room temperature. The simulated and measured results for the prototypes are shown in Figure 3.13. The sensor prototype with *dcap* of 101 μm is denoted as *S101*, while the one with *dcap* of 128 μm is denoted as *S128*. The simulations presented in Figure 3.13 were set up with the same configuration, materials, and dimensions of the prototype shown in Figure 3.12. Note that after the optical characterization step was performed to evaluate the heights of the cantilevers, the measured height values (measured *dcap*) were applied in the simulations. The simulations were performed with the actual *dcap* values obtained from the profilometer measurements (Figure 3.8) of the sensor prototypes. As a result, the simulated parameters corresponded closely to those of the physical prototypes. The plots in Figure 3.13 show good correlation between simulations and measurements for the resonant frequency peaks. This consistency validates the EM principles behind the frequency shifts of the SRRs that correlate to the deflection of the cantilevers. Here, the thermal responses and the uniform deflections of the bimorph cantilevers are assumed, i.e. constant and thermally static *dcap* values of the two separate prototypes represented different deflections of the cantilevers. Furthermore, because the prototypes at low frequencies (Figure 3.12) share the same electromagnetic circuit topology with the high frequency designs in the Section 3.2, the results in Firgure 3.13 also indirectly validate the EM simulations shown in Figure 3.4 – 3.5.

On the other hand, the low value of S_{21} in the measurements seen in Figure 3.13 reflects a high insertion loss due to the transition between CPW and coaxial cable. Unfortunately, due to limitations of fabrication, errors were introduced. There were gaps

between the SMA connectors and the CPW signal line, and the SMA outer radius was also slightly smaller than the width of the CPW signal line that caused reflection as the signal was launched into the CPW. However the negative effect has little significance concerning the proof-of-concept. A frequency shift of about 800 MHz is observed for the prototypes S101 and S128 (from 4 GHz to approximately 4.8 GHz, respectively). This shift gives a sensitivity of about 30 MHz/μm, approximately 2 orders of magnitude higher than the sensitivity of 700 kHz/μm as reported in [3.5] (based on a 19 GHz resonating slot). Note that this comparison refers to the RF transduction principles, i.e. how well the resonator is designed to transform the temperature change into the frequency shift, whereas thermal-mechanical response is another independent principle.

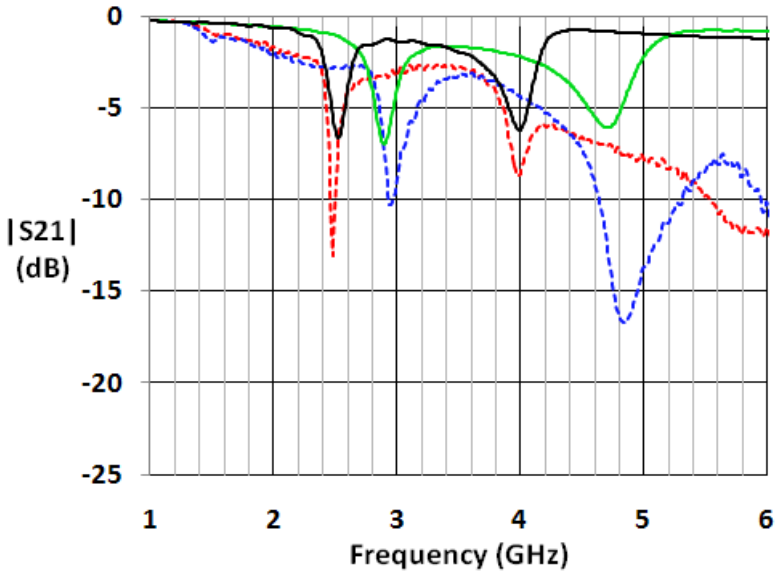

Figure 3.13. Magnitude of S_{21} for the CPW SRR sensor prototype with the simulated results of *S101* in solid black and *S128* in solid green, the measured results of *S101* in dash red and *S128* in dash blue.

B. Frequency response measurements corresponding to different temperatures

In this measurement, a close environment surrounding the transducer prototype was constructed. The prototype was housed in a plastic enclosure having two coaxial cables connected to the CPW device through the sides of the box as shown in Figure 3.14. The openings, where the cables access the device, were shielded with rubber to isolate the device. The reference temperature probe was inserted next to the SRRs for temperature monitoring. The prototype and the air inside the box were heated to 100 ^{o}C with a lamp and then allowed to cool down. It should be noted that the lamp was kept at a constant distance *d* from the plastic container to maintain constant illumination of the thermal flux as illustrated in Figure 3.15. Thus, at any given temperature, distance *d* could be adjusted so the temperature inside the container could be brought into thermal equilibrium with the outside region illuminated by the lamp. This configuration also allowed for the profilometer measurements of the cantilevers (their tip positions relative to the ring) while the prototypes were kept inside the transparent container. The captured image shown in Figure 3.16 presents the actual setup showing the VNA and SMA connectors. The lamp was removed after heating to avoid interference with the RF reading during the cool down process. The temperature readings from the reference probe decreased at a much slower rate because they reflected the heat diffusion instead of the air diffusion. As a result, the temperature reading was obtained in the range of 54^{o}C to 20^{o}C with a smaller temperature error of about +/- 1^{o}C. Note that it took about 10 – 15 minutes for each temperature point in this measurement, and about an hour and a half for temperature to be heated up to 100 ^{o}C and then cooled down to about 27 ^{o}C. The

prototype was allowed to cool down overnight, and the measurement at room temperature (recorded to be 20 ^{o}C) was performed approximately 24 hours later. The measurement results are shown in Figure 3.17, where six different temperature responses were recorded. Figure 3.18 shows the resonant frequency plotted against the temperature, where a relatively linear response of the frequency shifts is observed, i.e. from 4.85 GHz at 47 ^{o}C to about 4.80 GHz at 20 ^{o}C with a sensitivity of 1.85 MHz/^{o}C or 0.04 % frequency shift per ^{o}C. This sensitivity is slightly lower than the prototype reported in Section 3.4.2 with 0.05 % of frequency shift per ^{o}C. The responses at 54 ^{o}C appear to be nonlinear reflecting the limit of the linear region of operation. In practice, to identify the linear operation limits of the sensor, each operating principle, the mechanical-EM response and the thermal-mechanical response, should be characterized to obtain the overall linear response for the sensor in terms of frequency shift versus temperature change.

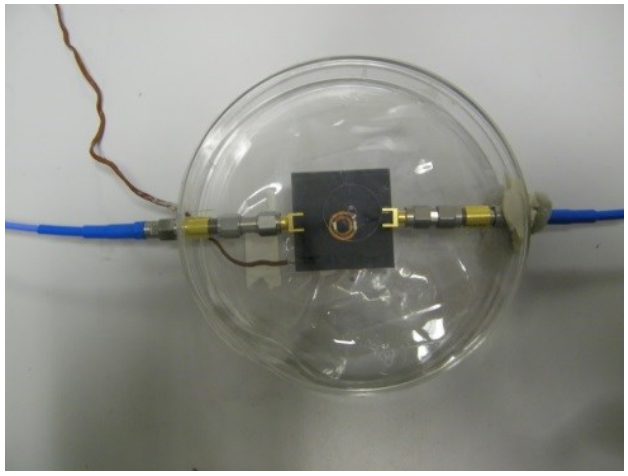

Figure 3.14. Plastic enclosure for direct temperature measurements of the CPW SRR sensor prototype.

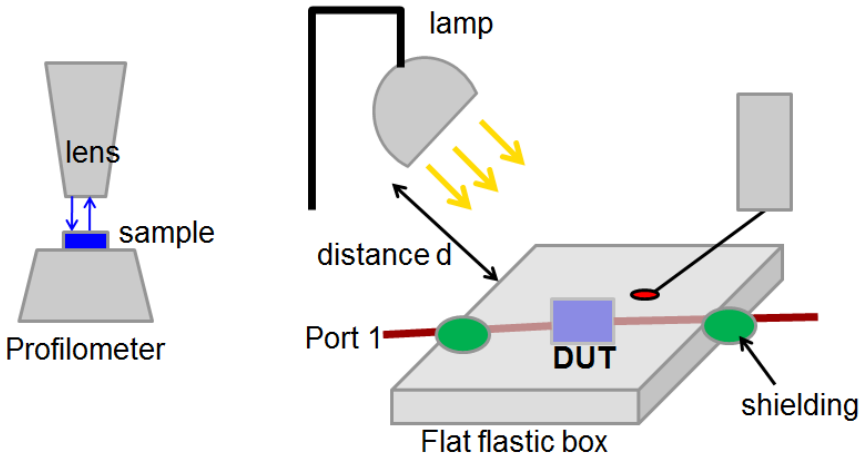

Figure 3.15. Temperature measurement setup.

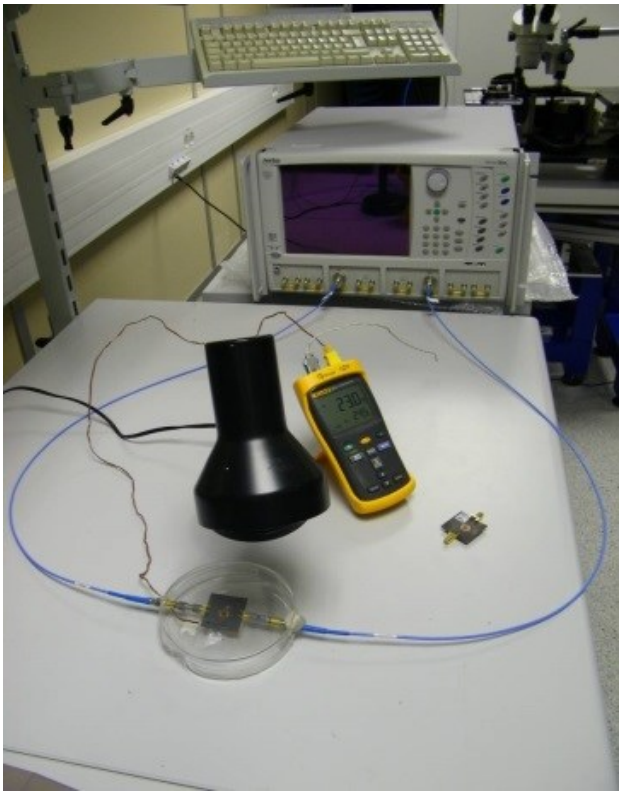

Figure 3.16. The temperature measurement setup with VNA (the blue cables) and the reference temperature probe inserted inside the plastic container (the brown wire).

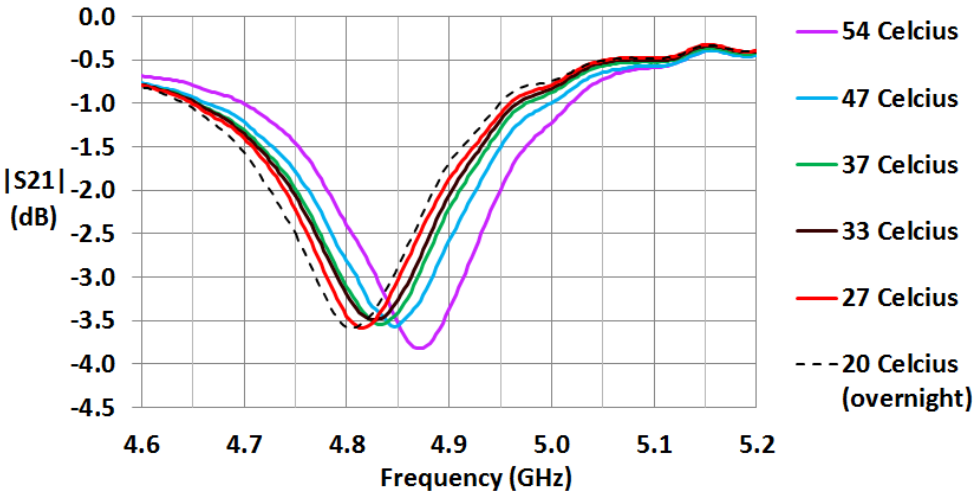

Figure 3.17. Frequency response of the temperature sensor prototype excited with CPW at different temperatures.

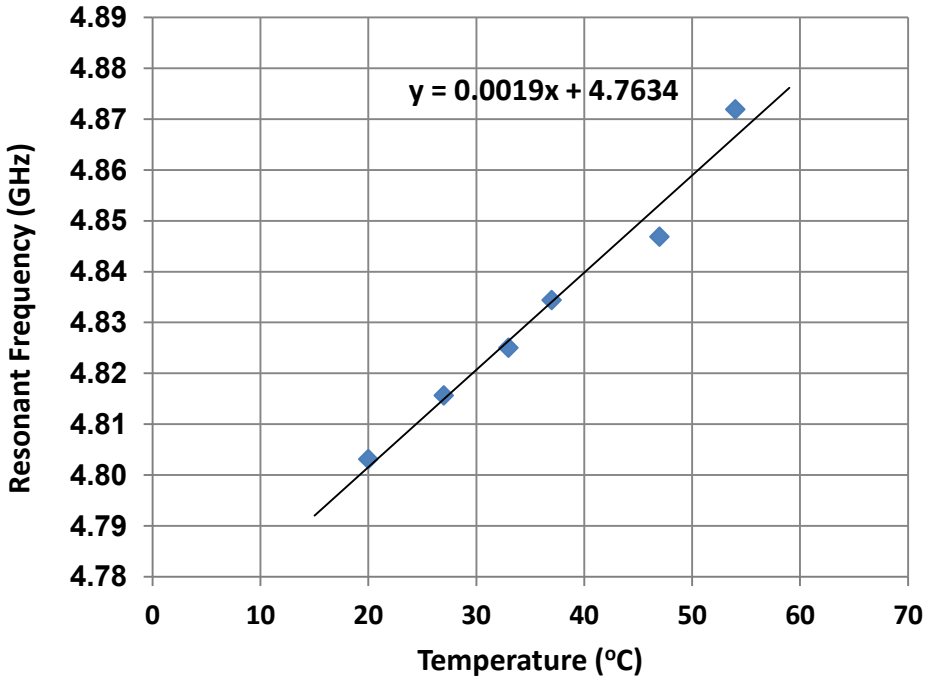

Figure 3.18 Resonant frequency versus temperature of the CPW SRR sensor prototype.

3.5. Remote Sensing Implementation

As demonstrated in Section 3.4.2, the sensor array of four elements (as designed in Figure 3.2) was interrogated remotely by incident waves in short range (20 – 30 cm). However, to enable long range interrogation, the surrounding environment of the sensor has to be considered. In applications where the sensor is not placed on metallic surfaces or surrounded closely by metallic objects, CPW excitation design (Figure 3.3) can be integrated, as a load, with a typical RFID tag antenna. Then, it can be interrogated by an UWB (ultra wideband) reader, which can track the resonant frequency of the sensor tag. However, in applications where the sensor is required to be surrounded by metallic objects, the FMCW radar system as discussed in Chapter 2 providing the beat frequency to decode both identification and sensing signals of the sensor is required. This platform allows a ground plane to be in the proximity or as part of the sensor, and the ground plane helps to reduce interferences from the half space surrounding the sensor. This section investigates the performance of the sensor implemented in the beat frequency based platform for long range interrogation.

3.5.1. Beat Frequency Interrogation System

A. The Radar and the Reading Platform

An FMCW radar with carrier frequency operating around 3 GHz was utilized as an interrogation device in the communication system illustrated in Figure 3.19 – 3.20. The radar system utilized in this measurement was built and operated by Franck Chebila [3.11]. Each of the two sensor prototypes of Figure 3.12 (measurement results in Figure

3.13) was terminated with a 50 Ω load on one end and connected to a horn antenna (also referred to as communication antenna) on the other end via a long coaxial cable (characteristic impedance of 50 Ω). In this technique of remote identification and data acquisition [3.7 – 3.11] (see Section 2.3 of Chapter 2), the transmitted signal has a linear sawtooth variation of frequency with time, i.e. chirp tuned linearly by a voltage-controlled oscillator (VCO). As the chirp signal is emitted from the radar antenna, it is backscattered by objects and received at the radar as an attenuated replica of the chirp delayed by the two-way propagation time of $\Delta t = 2R/c$, where R is the range between the radar antenna and the sensor loaded antenna, and c is the speed of light. The instantaneous frequency difference between the chirp and its delayed replica is given by $2\frac{\Delta F}{T_R}\Delta t$, where ΔF is the bandwidth of the chirp (2.85 GHz – 3.1 GHz) with the center frequency, f_c, of 2.975 GHz, and T_R is the sawtooth modulation period of 1 ms. The echoed signal is then mixed with the transmitted chirp to produce the beat frequency. Here, the radar has two identical horn antennas, one of which is the transmitter with gain G_T and the other is the receiver with gain G_R. The radar block diagram is shown in Figure 3.21 [3.11].

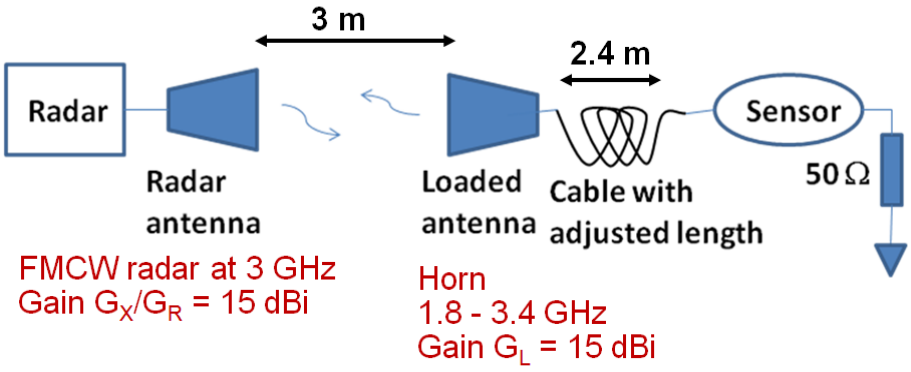

Figure 3.19. RCS measurement system for remote sensing and identification.

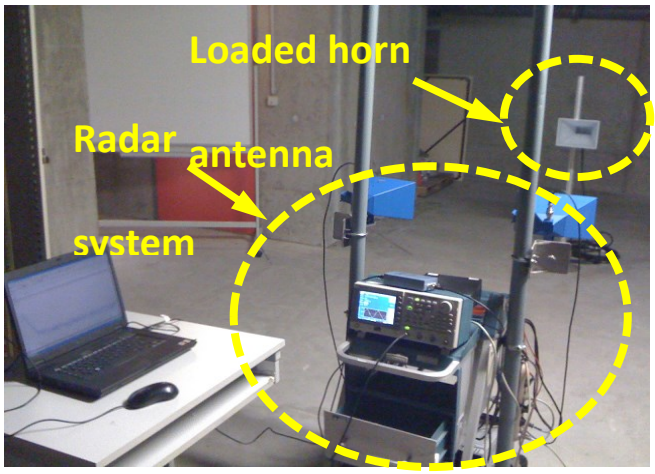

Figure 3.20. Captured image of RCS measurement system.

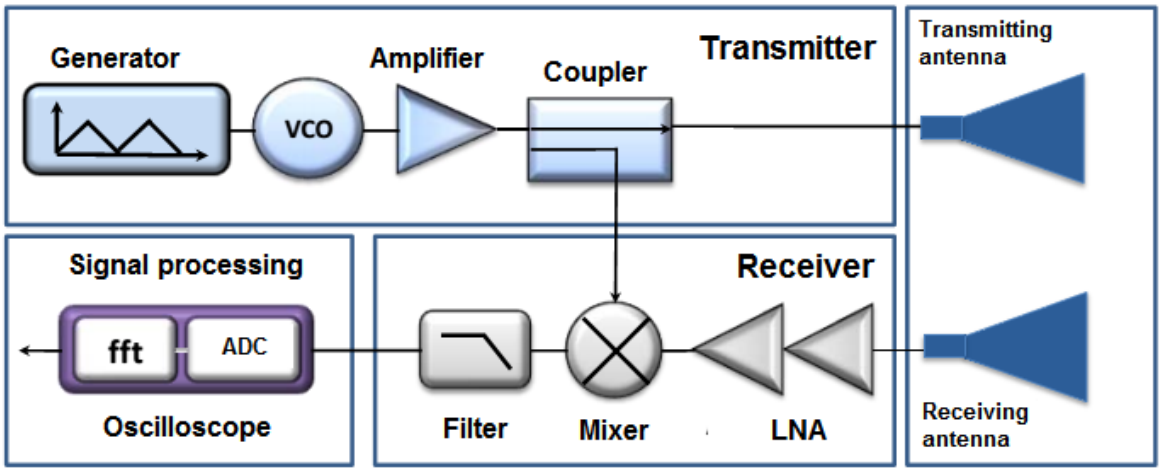

Figure 3.21 Block diagram of the interrogation radar. [3.11]

There are two important beat frequencies to be observed in the setup of Figure 3.19 – 3.20. The backscattered signal by the sensor-loaded antenna, with gain G_A, gives the first beat frequency, which can be estimated from (3.3), i.e. the structural mode. The second important beat frequency to be identified is the backscattered signal that travels

along the delay cable to the loading sensor (terminated with a 50 Ω) and is reflected. This beat frequency can be estimated from (3.4), where L is the cable length and ε_r is the cable dielectric constant [3.19].

$$f_{b1} \approx 2\frac{\Delta F}{T_R}\frac{2R}{c} \tag{3.3}$$

$$f_{b2} \approx 2\frac{\Delta F}{T_R}\frac{2(R+L\sqrt{\varepsilon_r})}{c} \tag{3.4}$$

There are advantages and disadvantages for different frequency ranges of the carrier frequency of the FMCW radar. Higher frequencies such as millimeter-wave frequencies allow miniaturization of the antennas and the sensors, high gain antennas and beam-steering capability. In high frequencies, the physical distance becomes longer electrically and thus the noise level caused reflection and multipaths due to nearby objects is reduced. Furthermore, the antenna impedance matching is also less influenced by the surrounding. However, the signals attenuated by a factor of $(f_H/f_L)^2$ for the high frequency, f_H, compared to the lower frequency, f_L. In terms of detection range, given the same transmitted effective isotropic radiated power (EIRP), the same receiving antenna gain G_R, and the same received back scattered power, P_R, for both frequency f_H and f_L when interrogating a scatterer of a given effective area, S, the detection ranges, R_H, at f_H and R_L at f_L, are the same. Such conclusions can be inspected in (3.5 – 3.8) [3.19].

$$P_R = \sigma\frac{\lambda^2 G_R}{(4\pi)^3 R^4}EIRP \tag{3.5}$$

$$\Rightarrow \qquad \frac{\sigma_H}{f_H^2 R_H^2} = \frac{\sigma_L}{f_L^2 R_L^2} \tag{3.6}$$

and $$\sigma_H \approx 4\pi(\frac{S}{\lambda_H})^2 \quad (3.7)$$

$$\sigma_L \approx 4\pi(\frac{S}{\lambda_L})^2 \quad (3.8)$$

The output power of the VCO (Hittite HMC416LP4) around the center frequency is between 2.0 dBm and 2.4 dBm [3.11], with a voltage tuning response reported in Figure 3.22 [3.11]. The VCO response shows a potential for a radar bandwidth from 2.7 GHz to 3.2 GHz, however the frequency band of 2.85 GHz – 3.10 GHz was chosen because it covers the frequency shifts of the first resonant frequency of the two samples under test. The loaded horn antenna, located 3 m away from the terminal of radar system, operates in the band of 1.8 GHz to 3.4 GHz with a gain, G_A, of 15 dBi. The sensor prototype is treated as a load of the target horn antenna of the system and is terminated with a 50 Ω load when connected to the 2.4 m long cable. Based on the total travel distance of the signals, each load target with their corresponding range gives a different beat frequency with a different received power level, thus a different RCS value. Table 3-1 gives a summary of different parameters.

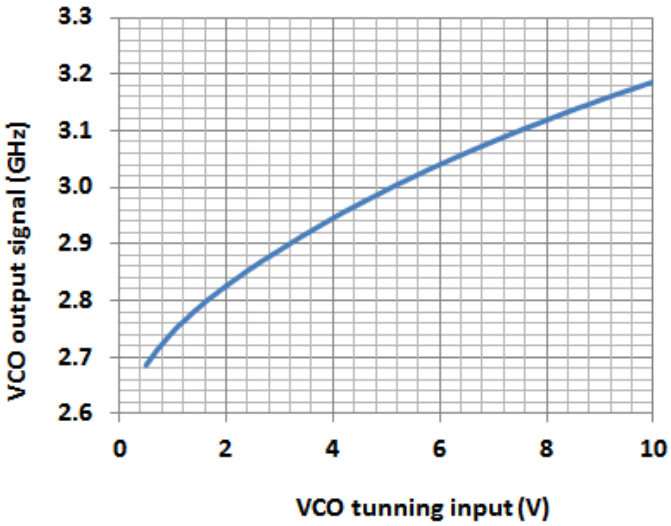

Figure 3.22. Output signals of the VCO.

TABLE 3-1

Summary of the Radar System Parameters

ΔF	250 MHz
T_R	1 ms
fc	2.975 GHz
VCO at f_c	2.3 dBm
R	3 m
L	2.4 m
Cable ε_r	2.25
G_R	15 dBi
G_T	15 dBi
G_L	15 dBi

Assuming no significant loss due to the attenuation of the signal in the delay line cable (Figure 3.19), the power received at the radar can be estimated according to (3.9) (see Section 2.3 of Chapter 2 for derivations), where P_R and P_T are the transmitted and

received power at the radar respectively, λ is the wavelength of the signal, R is the distance between the horn antennas of the radar to the loaded target antenna (connected to the sensor), G_T and G_R are the gain of the transmitting and received horn antennas of the radar respectively, G_A is the gain of the loaded horn antenna, R_A is the resistance of the loaded horn antenna (its reactance is zero), and R_S and X_S are the resistance and reactance of the sensor seen by the loaded horn antenna (including the 50 Ω termination). In (3.9), the delay line cable is not accounted for.

$$P_R = P_T \times 4\left(\frac{\lambda}{R}\right)^4 \frac{G_T G_R G_A^2}{(4\pi)^4} \frac{{R_A}^2}{(R_A+R_S)^2+X_S^2} \tag{3.9}$$

B. The Interrogated Sensor Samples

To estimate the received power, P_R, resulted from the two prototypes illustrated in Figure 3.12 (prototypes *S101* and *S128* with two average *dcap* values of 101 μm and 128 μm respectively), their input impedances (R_S and X_S) were extracted from the measurements of their *S* parameters using ADS simulations (Figure 3.23). Note that the measurement setup here is thermally static, because the analysis in this section investigates the feasibility of remote sensing based on the EM responses of the sensor. Recall that the thermal-mechanical response is an independent and well-known principle in the operating principles of the proposed sensor. The resistance and reactance of the two samples from ADS simulations are shown in Figure 3.24. Assuming transmitted power, P_T, to be 0 dBm, then the received power, P_R, in (3.9) can be estimated for *S101*

and *S128* (based on the plots in Figure 3.24) and shown in Figure 3.25. The power difference for the two prototypes is shown in Figure 3.26.

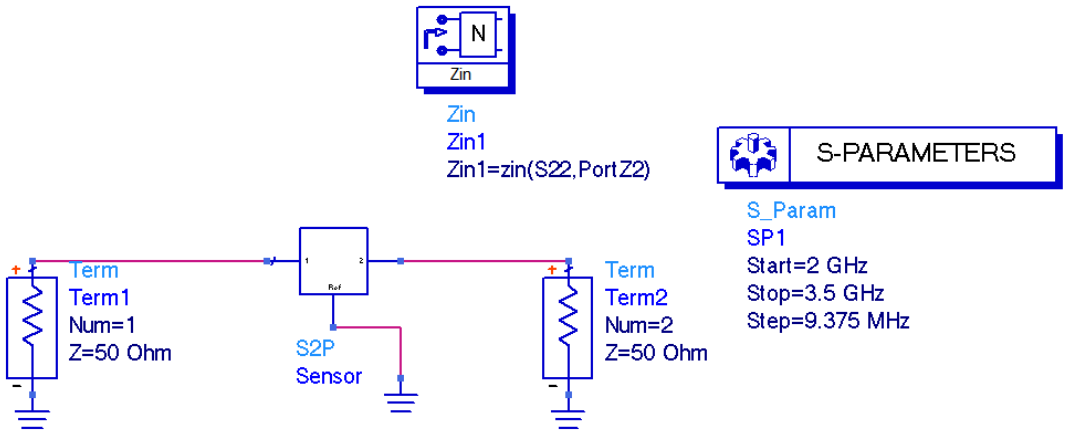

Figure 3.23. ADS simulations of the sensor impedance.

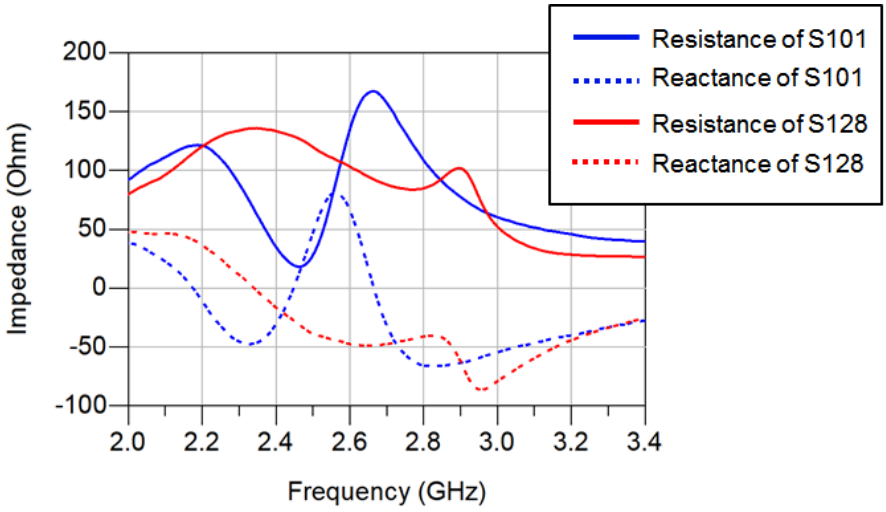

Figure 3.24. Impedance of sample *S101* and *S128* obtained from ADS simulations.

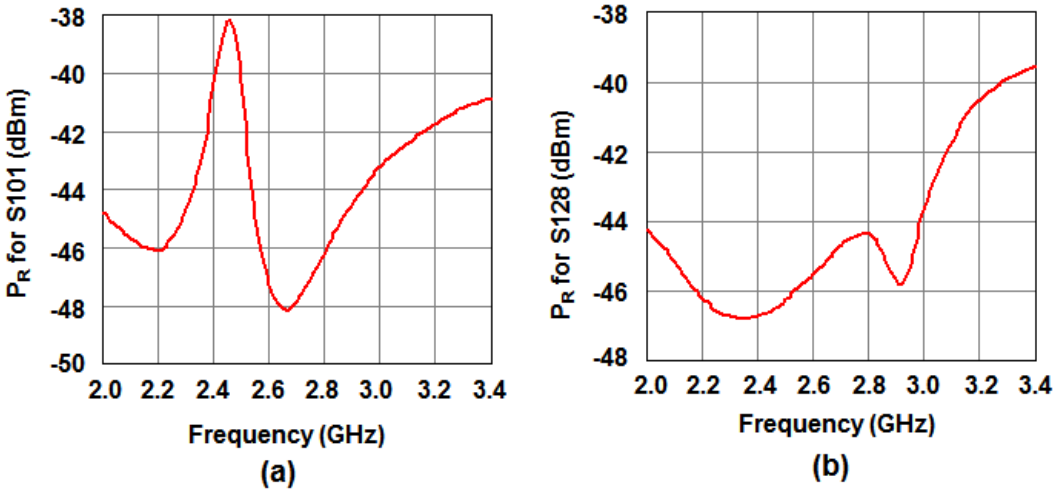

Figure 3.25. Calculated received power for prototypes a) S101 and b) S128.

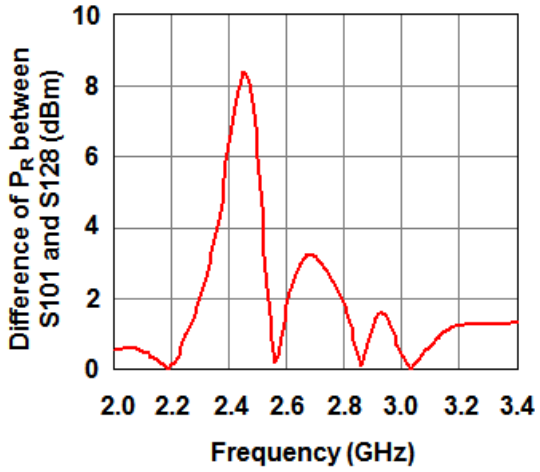

Figure 3.26. The variation in the received power between prototypes S101 and S128.

3.5.2. Radar Echo Measurement Results

The beat frequency power received at the radar of Figure 3.19 was measured and plotted against the beat frequency domain in Figure 3.27. The corresponding beat

frequency for the sensor prototypes is estimated to be 22 kHz from (3.4) based on the signal path length, while the beat frequency of the structural mode of the loaded target antenna is about 9 kHz. Other detected peaks between 9 kHz and 22 kHz are contributed by the reflections from the room walls because the room is approximately 5 x 10 m^2 (Figure 3.20). The first power peak at 10 kHz is approximately -12 dBm corresponding to the structural mode, and the power level of the antenna mode at the peak of 22 kHz is approximately -35 dBm and -32 dBm corresponding to prototypes *S101* and *S128* respectively. The output power, P_T, is about 10 dBm after amplification. Consequently, the variation of the power level at the beat frequency between the two thermal static prototypes S101 and S128 is 3 dB given a difference of 127 μm between their cantilever tip gaps (*dcap*), i.e. 0.024 dB/μm of sensitivity for the mechanical-EM response of the sensor design. Note that this RF response can be improved further when operating at higher frequency such as 30 GHz to give a larger dB per micron of the cantilever deflection. Given the fabricated Al-PET bimorph cantilevers having a thermal-mechanical response of 0.8 μm/^{o}C, the temperature sensitivity of the prototypes here can be estimated to be 0.03 dB/^{o}C. Recall that the thermal response can be improved with a different set of bimorph cantilevers without altering the RF responses of the sensor. For example, if 10 μm thick Pt (platinum) layer replaces the 50 μm thick Al layer, 100 μm PET layer replaces 50 μm PET layer, and the cantilever is made 0.5 mm longer (a total length of 3.5 mm instead of 3 with the anchor base of 0.5 mm), then the thermal-mechanical response is 10 μm/^{o}C, i.e. 0.24 dB/^{o}C for the sensor in the beat frequency domain.

Meanwhile, in the frequency band of 2.85 GHz – 2.90 GHz of the plot in Figure 3.26, the calculated received power variation (implying the RCS variation) between the two sensor prototypes, *S101* and *S128*, is approximately 2 dB, while the power difference observed in measurements is approximately 3 dB (Figure 3.27). Furthermore, note that in calculations the peak of the power difference is also around 3 dB in the frequency band of 2.6 – 2.8 GHz. The observed discrepancy between the calculated and measured values of the power variation with its corresponding frequency band may be attributed to the absence of the cable in calculations. With its non-zero inductance and capacitance (acting as an impedance transformer), the cable can alter the impedance seen by the target antenna (looking toward the loading sensor), resulting in lower R_S and X_S or equivalently a higher back scattered power according to (3.9). On the other hand, in calculations (Figure 3.26) the largest power fluctuation of about 8 dB is observed around 2.5 GHz. This result is consistent with the plots of Figure 3.13, where the largest variation of $|S_{21}|$ between two samples, *S101* and *S128*, also occurs around 2.5 GHz. Potentially, with a different radar system optimized for the 2.5 GHz frequency band, the power fluctuation (thus RCS sensitivity) can be as high as 8 dB given the same sensor prototypes built here.

In Figure 3.27, the peak power level of the echoed signals from the sensor is close to -35 dBm, while the noise level is around -55 dBm, i.e. a SNR of 20 dB. This SNR reflects all the noises in the system and from the environment. Although multipath reflections are possible, their signal level is negligibly low (close to noise level). Furthermore, the measurements were performed indoor, therefore the noise level and multipath signals for outdoor environment are expected to be less than the measured results observed from this experiment. The measurement variation (3 data points) for

each prototype is shown in Figure 3.28, illustrating an error margin of approximately 0.7 dB at around -34.5 dBm for the prototype *S101* and 0.25 dB at around -31.5 dBm for the prototype *S128*.

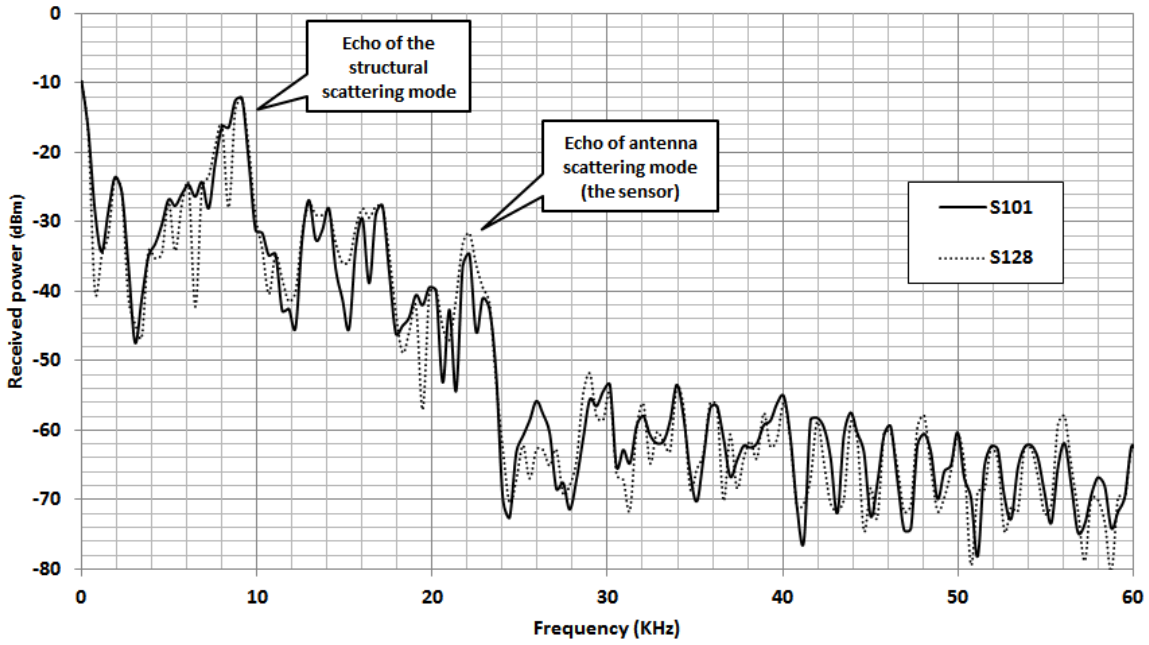

Figure 3.27. Beat frequency power level for the two low frequency prototypes S101 with dcap of 101 μm (solid line) and S128 with dcap of 128 μm (dash line).

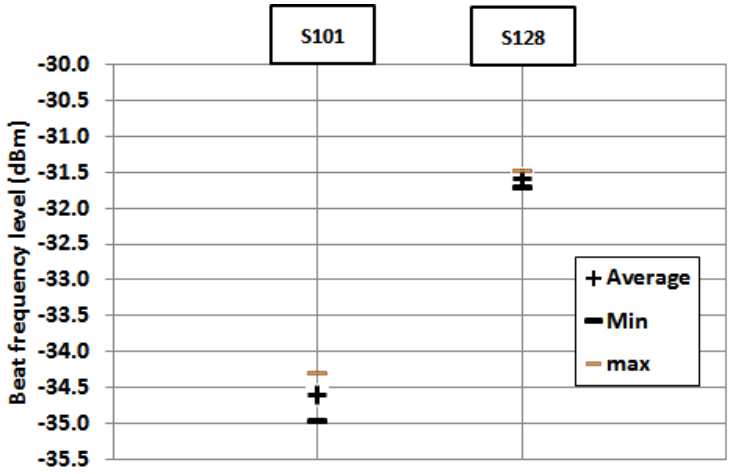

Figure 3.28 Measurement variation for the beat frequency level of sample S101 and S128.

3.5.3. Performance Analysis of the Sensor Design

The maximum potential of the sensor design, based on the same interrogation platform described in Figure 3.19, is further investigated in this section. Simulations of the design in Figure 3.3 were performed with a slightly different set of parameters: r_{int} = 2.5 mm, c = 1 mm, d = 0.5 mm, and s = 0.5 mm (see Figure 3.1). The substrate was RT5870 (ε_r = 2.33, substrate thickness = 787 µm). The difference in this study is that the cantilever is made of only 1 metallic layer that forms a parallel plate capacitance with the ring with the overlap area of 1 mm x 1 mm. The cantilever in this study is not bimorph because the dielectric layer in the bi-layer cantilever has little influence on the frequency response of the sensor with respect to the cantilever deflection (refers to Chapter 4 for the operating principles). The simulations were performed with different dcap values ranging from 20 µm to 200 µm. Magnitude of S_{21} of the sensor is shown in Figure 3.29 for *dcap* from 20 µm to 100 µm with steps of 10 µm. The greater frequency shift in the upper

frequency band (3.5 GHz – 5 GHz) presents a best sensitivity given a *dcap* variation, i.e. the cantilever deflection, hence this upper resonant frequency is chosen as an example for the best performance evaluation.

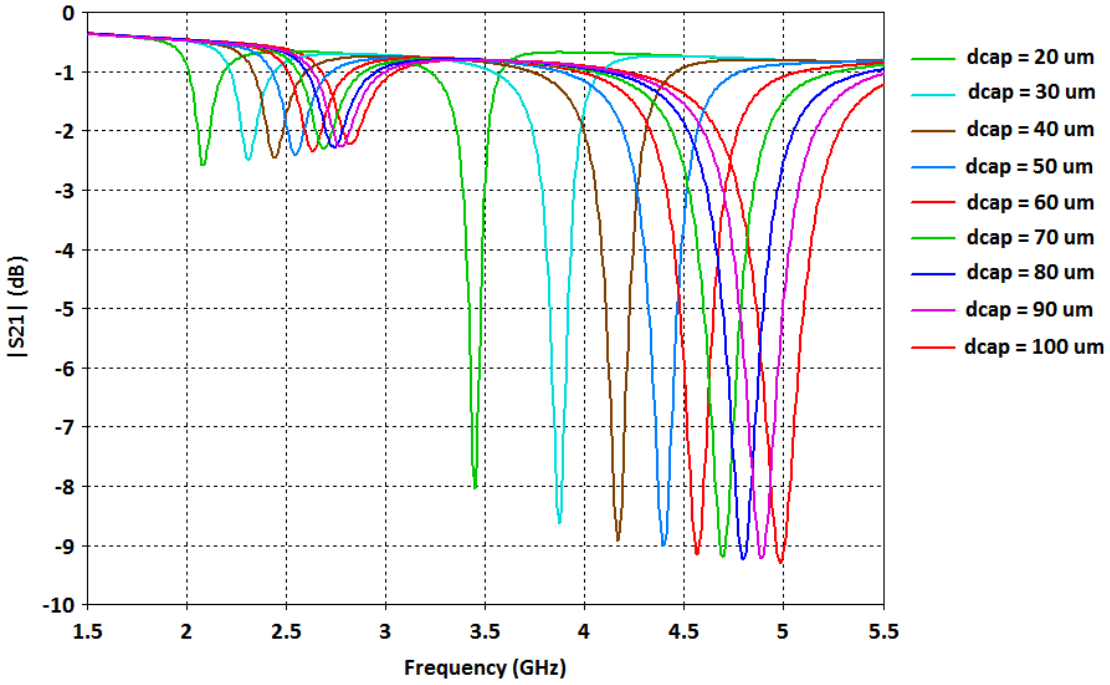

Figure 3.29. Magnitude of S21 of the simulated sensor design with CPW coupling.

Using ADS simulations (as in Figure 3.23) to extract the complex impedance of the CPW SRR sensor models simulated in Figure 3.29, the received power level (with P_T set to 0 dBm) is plotted in Figure 3.30 based on (3.9) for different *dcap* values from 20 µm – 200 µm with steps of 20 µm. |S21| responses of smaller variations of *dcap* are shown in Figure 3.31. Note that if a P_T of 10 dBm is assumed (the same as the calculations performed in the previous section), the received power in Figure 3.30 – 3.31

would be raised by 10 dB. Therefore, it would result in a SNR of about 15 dB given an outdoor noise level of approximately -60 dB [3.11] (although the power level discussed here is applied to a carrier frequency around 3.5 – 5 GHz, it shares similar system parameters with the 3 GHz band radar discussed earlier). Observe that the frequency shift of the sensor is not linear across the large range of *dcap*. The shifts of the frequency at the notch power (corresponding to the resonant frequency of the sensor) are shown in Figure 3.32, where two linear regions can be identified (two different slopes, i.e. two different sensitivities). Recall that there are two methods to interrogate the sensor with the FMCW as suggested in Figure 2.15 of Section 2.3.1. One approach is to sweep the chirp in a narrow bandwidth and read the power fluctuation at a constant beat frequency. The second approach is to sweep the chirp in adjacent intervals of a frequency band such that different beat frequencies can be used to track the frequency shift of the notch power received at the radar. The frequency shift of the notch power can be tracked with a sufficiently small bandwidth of the chirp modulation, although the processing time would take longer. However, the more dominant limiting factor in the detectable spectral resolution is the minimum detectable power change of the radar. Results in Figure 3.28 suggests that a minimum detectable power difference is 1 dB, therefore a spectral resolution of 25 MHz (the bandwidth of 1 dB above the notch power level) can be applied to track the notch power such as the variations seen in Figure 3.31. The phase noise of the radar system (Figure 3.21) is below -100 dBc/Hz for both the VCO and the oscillator [3.11], which is sufficient to accommodate this spectral resolution. For *dcap* variations from 100 μm to 200 μm, a spectral resolution of about 100 MHz would apply.

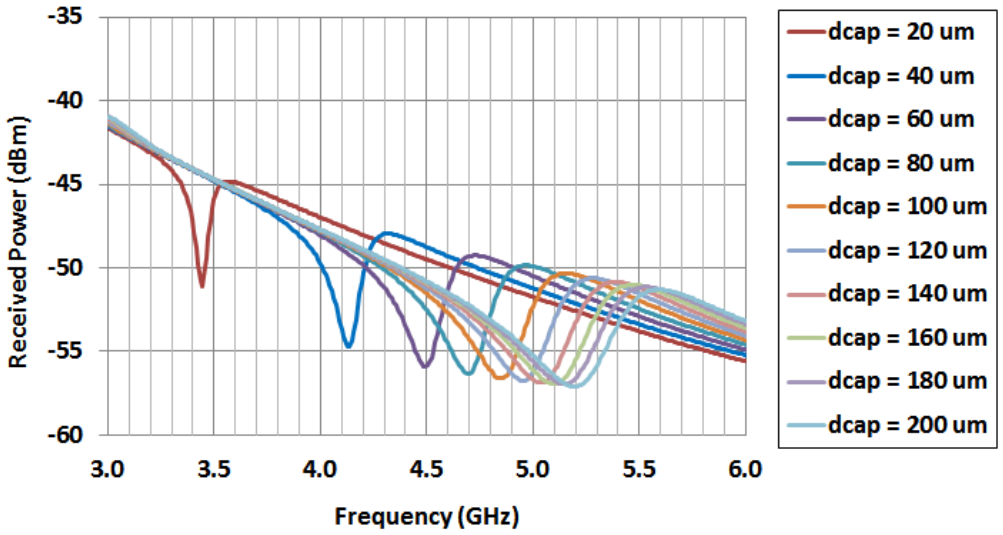

Figure 3.30. Received power estimated for the simulated sensor models with different *dcap* values from 20 µm to 200 µm with steps of 20 µm.

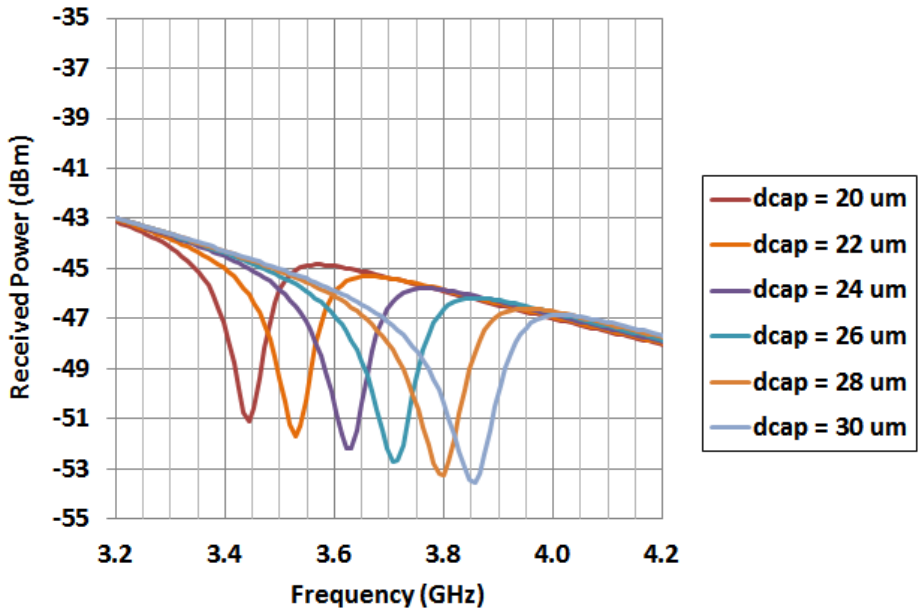

Figure 3.31. Received power estimated for the simulated sensor models with different dcap values from 20 µm to 30 µm with steps of 10 µm.

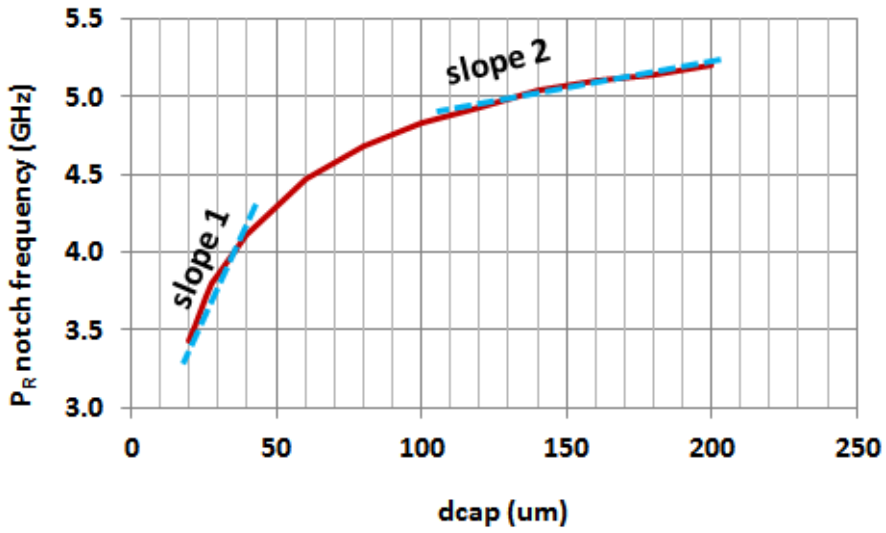

Figure 3.32. The frequency of the notch power in the signals of the sensor as received by the radar.

Taking the power level obtained from the simulation for *dcap* of 20 μm to be the reference, the power fluctuation for the received power of different *dcap* values compared to the reference are shown in Figure 3.33. Considering the power leve at 5.6 GHz, there exists a relatively linear response for the power of *dcap* values from 20 μm (the zero level in Figure 3.33) to 140 μm. In this case, a single chirp sweep in a narrow frequency band can be used to read the received power fluctuation corresponding to the cantilever deflection. Again, Figure 3.28 suggests a minimum detectable power level to be 0.7 dB. Table 3-2 gives a summary of the estimated performance parameters for the sensor. The column "RCS" indicates performance when scanning with a fixed frequency band and the column "Frequency Scan" indicates performance when scanning with multiple adjacent frequency bands. Note that %f is calculated as a ratio of the frequency shift over the carrier frequency for 1 μm of the cantilever deflection. The dynamic range

here is the ratio between the deflection limits in decibels (the upper and lower limits in the linear range).

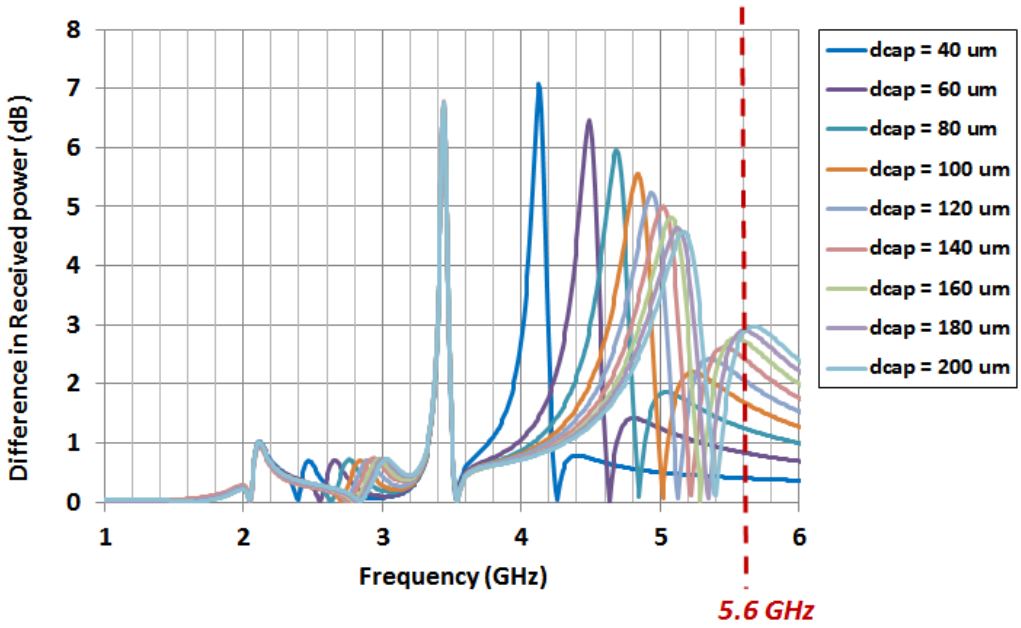

Figure 3.33. The estimated power fluctuation of the sensor when loaded in the radar interrogation system with dcap of 20 μm as the reference power level.

TABLE 3-2.

Summary of the Estimated Performance Parameters of the Sensor Design

Interrogation	RCS	Frequency Scan	
Output power (P_T)	10 dBm	10 dBm	
SNR	15 dB	15 dB	
Sensitivity	0.035 dB/μm	1.2 %f/μm	0.07 %f /μm
Reference carrier frequency	5.6 GHz	3.45 GHz	5 GHz
Detection resolution	0.5 dB	25 MHz	100 MHz
Linear range	20 - 140 μm	20 - 30 μm	100 - 200 μm

The substrate used in this study, RT5870 by Rogers Corporation [3.18], has a coefficient of thermal expansion of 40 ppm/^{o}C from 0 ^{o}C to 150 ^{o}C [3.20], which is negligible to circuit dimensions at 3 GHz. Its dielectric constant increases less than 0.5 % from -50 ^{o}C to 150 ^{o}C [3.20]. Therefore, it can be considered that the frequency response of the sensor is independent from the temperature effects applied to the substrate within -50 ^{o}C and 150 ^{o}C. Consequently, the frequency response of the sensor is only influenced by the construction of the bimorph cantilevers. To correspond the performance parameters in Table 3-2 to the thermal responses of the sensor, two different material pairs (Al-PET and Ti-PET) are used in the calculations. Each material pair gives a different deflection sensitivity for a given temperature change according to (3.1). The temperature sensing performance of the SRR sensor utilizing the two material pairs are estimated and summarized in Table 3-3 and Table 3-4 (%f refers to percent of the frequency shift with respect to the reference operating frequency). The estimations are based on cantilevers of 3 mm long and 50 μm thick for each material layer. The pair Al-PET gives a thermal sensitivity of 3.2 μm /^{o}C, while Titanium and PET gives a sensitivity of 4.5 μm/^{o}C. Table 3-3 and Table 3-4 show that the performance of the sensor can be optimized for different desired temperature accuracy and dynamic range and easily adapted to different applications.

In an outdoor environment, the radar interrogation system at 3 GHz was estimated to give a beat frequency signal of the structural mode at -30 dBm for a range of 30 m with a noise floor level of -80 dBm [3.11]. The beat frequency of the sensor (the antenna mode) with loss due to the delay line was estimated to be around -40 dBm to -50 dBm, resulting in a SNR above 20 dB. As long as the SNR and the read power resolution are

maintained, the performance parameters of the sensor estimated in Table 3-2, 3-3, 3-4 would apply. Chebila also demonstrated a radar system of 30 GHz (P_T = 13 dBm, and a bandwidth of 700 MHz) in the same remote interrogation method for a target at a distance up to 30 m. At 30 GHz, the antenna gains of the transmitter and receiver are 35 dBi and 14 dBi for, respectively [3.11]. The read power threshold (the radar sensitivity) was reported to be –77 dBm. The beat frequency signals for both the structural and scattering modes were in the range -10 dBm to -50 dBm with a noise level of about -60 dBm (the delay line used was 1 m). A resolution of about 1 dB was achieved. Here, the implication is that such a system allows the chipless sensor design proposed in Sect 3.2 to be implemented in a remote sensing platform for a long range potentially up to several decameters.

TABLE 3-3.

Estimated Performance Parameters for Al-PET Bimorph Cantilevers

Material	$\alpha_{Al} = 24\ (10^{-6}\ K^{-1})$, $\alpha_{PET} = 59.4\ (10^{-6}\ K^{-1})$		
Interrogation	RCS	Frequency Scan	
Output power (P_T)	10 dBm	10 dBm	
SNR	15 dB	15 dB	
Sensitivity	0.064 dB/^{o}C	3.84 %f/^{o}C	0.22 %f /^{o}C
Reference carrier frequency	5.6 GHz	3.45 GHz	5 GHz
Temperature accuracy	8 ^{o}C	0.2 ^{o}C	8 ^{o}C
Maximum linear range	380 ^{o}C	30 ^{o}C	320 ^{o}C
Linear dynamic range	depends on initial cantilever position		

TABLE 3-4.

Estimated Performance Parameters for Ti-PET Bimorph Cantilevers

Material	$\alpha_{Ti} = 8.9\ (10^{-6}\ K^{-1})$, $\alpha_{PET} = 59.4\ (10^{-6}\ K^{-1})$		
Interrogation	RCS	Frequency Scan	
Output power (P_T)	10 dBm	10 dBm	
SNR	15 dB	15 dB	
Sensitivity	0.09 dB/^{o}C	5.4 %f/ ^{o}C	0.315 %f / ^{o}C
Reference carrier frequency	5.6 GHz	3.45 GHz	5 GHz
Temperature accuracy	6 ^{o}C	0.1 ^{o}C	6 ^{o}C
Maximum linear range	540 ^{o}C	45 ^{o}C	450 ^{o}C
Linear dynamic range	depends on initial cantilever position		

3.5.4. Extreme Temperature Applications

In harsh environments with extremely high temperature (500 ^{o}C to 1500 ^{o}C) that typical occur in the space shuttle, rotating bearings of an aircraft engine, disc brakes, or jet engines, existing temperature sensors have been very limited in their performance. Some thermocouple sensors can measure up to 2300 ^{o}C with high accuracy (0.1 ^{o}C). They are based on Seebeck effect of a pair of metals (for example, platinum and rhodium). But they are easy to be contaminated, the wire is rated for operation at much lower temperature (contact with the target), the signal output is weak, easily affected by common mode noises [3.21]. Optical fiber based thermal probes have operation range up to 1400 ^{o}C with high accuracy (0.1 ^{o}C) but also requires direct contact with the target [3.22 – 3.23]. Non-contact thermal platforms such as optical thermometry can measure high temperature by detecting the thermal radiation emitted by the object, and the change in the optical path length of objects made of material whose thermal expansion

coefficient and refractive index change as a function of temperature up to 1500 ^{o}C . However, these optical based sensors are limited in sensitivity, accuracy, and range (about 200 – 300 mm) and they require line-of-sight in measurements [3.24 – 3.25]. Some SAW sensors have been shown to operate up to 1000 ^{o}C [3.26 – 3.29]. Although SAW tags can be interrogated up to several meters [3.26], but for very high temperature SAW sensors, the system is limited to 15 cm [3.26] and the sensitivity has low accuracy of around 40 ^{o}C (due to the constraint by the pulse width and the measurable temperature-dependent delay, 10 dBm power output, and a SNR of 10 dB). SAW based sensors operate based on the reflective acoustical delay line which is modified by the physical quantity under sensing. The major limitations of SAW in high temperature sensing are the piezoelectric substrate materials that are required to be stable up to 1000 ^{o}C or above. The temperature influences the acoustic path of the substrate together with the elastic constant of the substrate material. Hence, the velocity of the surface waves is altered results in a change in the delayed reflected signals. Consequently, the newly developed Pt/Rh/ZrO_2 thin-film electrodes and langasite substrate ($La_3Ga_5SiO_4$) can enable SAW sensors up to 1000 ^{o}C but the sensitivity based on SAW operating principles is inherently limited [3.26 – 3.29]. Furthermore, SAW based sensors are limited to low frequency (around 3 GHz) due to the fabrication difficulties in shrinking the electrode fingers of the IDT. Given the same dimensions and output power, the antenna gain is limited at low frequencies therefore the range is limited. On the contrary, at high frequencies, especially in millimeter waves supported by the operation of the EM sensors, the interrogation range for the EM sensors can be extended by the high gain small size

antennas (for example, dish antennas with 20 – 30 cm in diameter) and the data bandwidth is also larger.

Beside the bimorph microcantilever integrated slot reported in [3.5] as discussed earlier in this chapter, recently another wireless passive sensor based on a slot resonator (operating around 5 GHz) was reported that can perform temperature sensing up to 1000 ^{o}C utilizing temperature-dependent dielectric constant of alumina [3.30]. However, both designs in [3.5, 3.30] have very low sensitivity, 0.008 % f/ ^{o}C in [3.29] and 0.003 %f/^{o}C in [3.5] and the accuracy of both is above 50 ^{o}C. Detection is performed with incident waves emitted by a transmitting antenna, and the reflected signals from the slots are directly detected with a time gating window reader. This interrogation method is the same as reported in [3.5] and also investigated in Section 3.5.2 of this chapter for the SRR sensor design reported in this thesis. Recall that in this direct incident and reflected wave interrogation method, the SRR based design presented in this thesis offers a sensitivity of 0.05 %f/^{o}C with an estimated accuracy of 10^{o}C. Note that this method of interrogation is itself very limited in range. As seen in [3.5, 3.29] and Figure 3.11, the reading range is less than half a meter. Although the materials utilized in the proof-of-concept prototypes (Figure 3.9) cannot operate up to 1000 ^{o}C, the materials can be replaced by alumina for the substrate and platinum (Pt) for the electrodes. The main advantage of the SRR design is that its operating principles are inherently not limited to materials and the design can be easily adapted to different frequencies. The high sensitivity is achieved through the efficient conversion of the gap capacitance into the frequency shifts, where the gap capacitance is modified by the temperature-dependent cantilever displacement.

In terms of remote long range interrogation based on an FMCW radar(as described in Section 3.5.2), recently two new passive remote temperature sensors were also reported [3.31 – 3.32]. The sensor in [3.31] utilizes liquid metal (Galinstan) housed in a microfluidic channel across a gap positioned at the middle of the dipole antenna. The dipole is open at the reference temperature and is closed as the volume of the Galinstan expands across the dipole gap. The sensor comprises of a number of such antenna elements operating close to 30 GHz. The temperature-dependent volume of the liquid metal would alter the linear array, which results in a change in the RCS level of the backscattered signals. The temperature range is probed at discrete levels. Although potentially this sensor can be used in extreme temperature environment because Galinstan (Ga/In/Sn) exists in liquid form from -20 ^{o}C to 1300 ^{o}C, the sensor has a limited tunable temperature range (20 ^{o}C). This is because probing temperature in discrete intervals with a resolution of about 4 ^{o}C corresponds to a change of 1.8 dBsm in the RCS of the array. The temperature resolution potentially can be made smaller but the number of antenna elements would need to increase to maintain the same temperature sensing range, thus also limits the special resolution. The sensor in [3.32] utilizes a water micro-fluidic channel situated between capacitive planar plates of a 2-port transmission line operating around 30 GHz. The capacitance of the gap changes with the temperature as the water level moves across the plates, thus altering the characteristics of the transmission line. The sensitivity was shown to be 0.4 dBm/^{o}C in a limited measurable range of 10 ^{o}C. It demonstrated a long range cost effective design but it cannot be applied to extreme temperature environments.

To enable sensing above 1000 ^{o}C for the SRR CPW sensor design (Figure 3.3), alumina (as the dielectric material) and Pt (as the metal) can be used to fabricate the split rings as well as the bimorph cantilevers. Alumina has a melting point of 2000 ^{o}C, and Pt has a melting point of 1768 ^{o}C. In fact, alumina (Al_2O_3) was identified to be a robust material for harsh environment applications by NASA Glen Research Center [3.33]. Its dielectric constant properties were reported in [3.33] and are shown in Figure 3.34 – 3.35. The SRR resonator design can be easily scaled for the alumina substrate. The monotonic and linear change of the dielectric constant of the alumina can shift the resonant frequency of the SRR resonator but the shift is much lower than the shifting effect caused by the gap capacitance change due to the cantilevers of the design. For example, with a thickness of 50 μm for each layer and a cantilever length of 3 mm, the bimorph cantilever deflection sensitivity of alumina with thermal coefficient of 5.4 (10^{-6} K^{-1}) and Pt with thermal coefficient of 9 (10^{-6} K^{-1}), is 0.3 μm/^{o}C. Since the mechanical strength (based on Young's modulus) of alumina is about 10 times higher than that of PET, and the mechanical strength of Pt is twice that of Al [3.34 – 3.35], the bimorph cantilevers can be made 5 mm long and the Pt layer can be made 10 μm thick and it is still mechanically stable. And it gives a temperature response of 4.5 μm/^{o}C, from which the performance of the sensor can be estimated from Table 3-4. Note that the length of the cantilevers does not necessarily influence the parallel plate overlap area between the cantilevers and the rings. This overlap area is the key parameter in the RF responses of the SRR sensor. Consequently, in theory, as opposed to the existing sensors limited by their operating principles, the robust design of the SRR based sensor illustrated in this chapter can allow

high sensitive and long range passive wireless sensing for temperatures up to 1600 ^{o}C using the beat frequency detection radar system for interrogation.

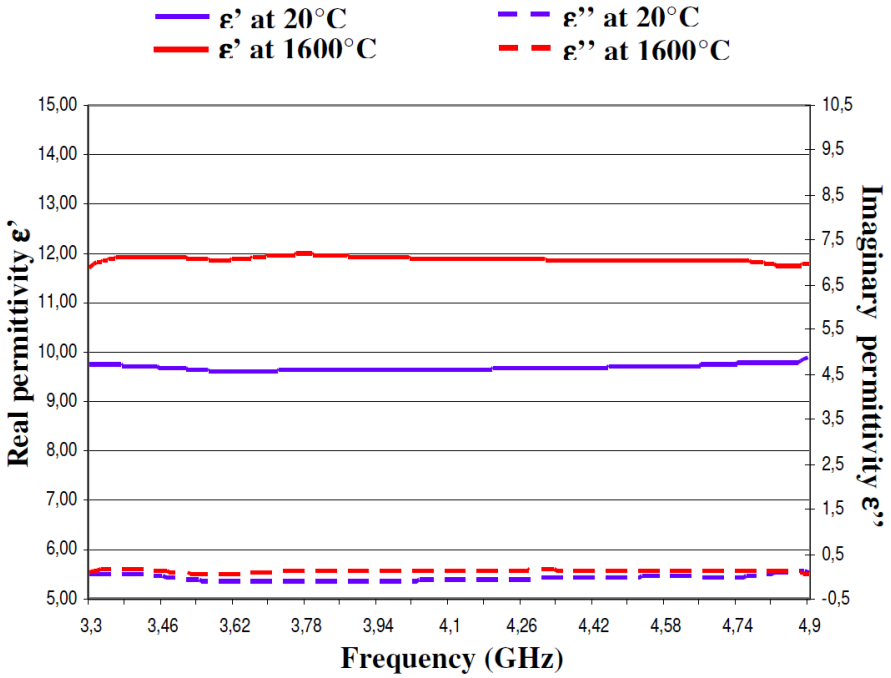

Figure 3.34. Real and imaginary permittivity of alumina at 20 oC and at 1600 oC. [3.33]

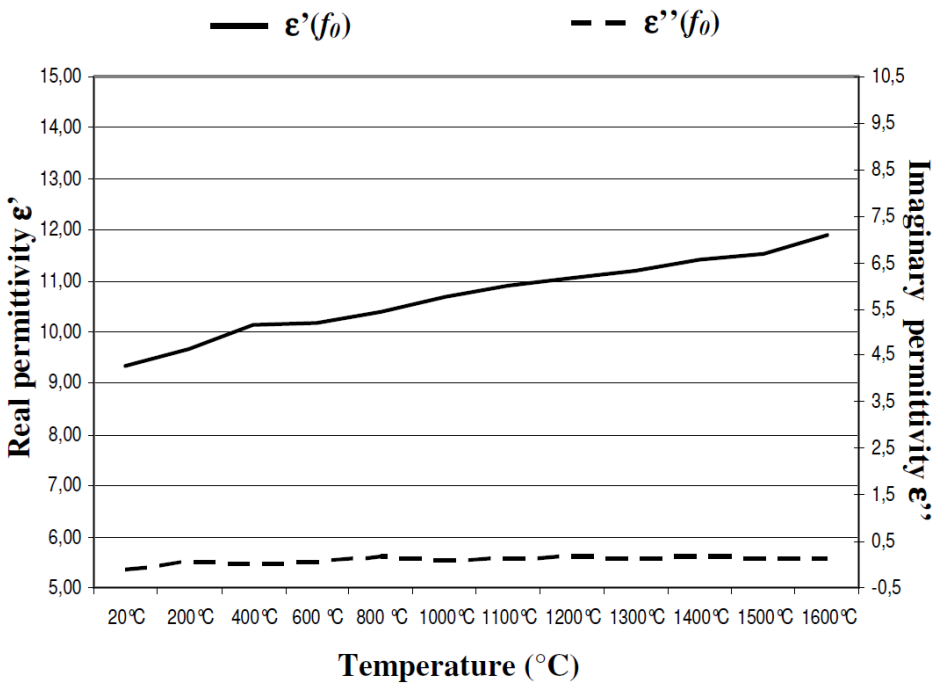

Figure 3.35. Real and imaginary permittivity of alumina versus temperature. [3.33]

In harsh environments such as aircraft engines, the mechanical vibration would be a major perturbation to the operation of the sensor. The mechanical stability of the Pt-Al_2O_3 bimorph cantilevers in the example described earlier can be evaluated in terms of their natural mechanical resonant frequencies. The fundamental natural frequency, f_n, is given in (3.10) below [3.36], where n denotes the order of the mechanical resonant mode, E is the Young's modulus of the material, I is the moment of inertia of the rectangular cross section of the cantilever, m is the total uniformly distributed mass, and L is the cantilever length. For a cantilever with one end clamped and the other end free, β has the following values: $\beta_1 L = 1.8751$, $\beta_2 L = 4.6941$, $\beta_3 L = 7.8548$ [3.36]. The Young's modulus (or tensile modulus) of the bilayer cantilever can be estimated according to (3.11), where

t_1 and t_2 denote the thickness of each material layer, and E_1 and E_2 denotes the Young's modulus of each material [3.37]. The moment of inertia, I, is calculated according to (3.12), where w denotes the width of the cantilever and t is total thickness of the cantilever [3.36]. Table 3-5 gives a summary of the calculations. The first mechanical resonant frequency of the bimorph cantilever of 50-um thick alumina and 10-um thick Pt is 1.3 kHz, which is an order of magnitude above the vibration frequency of the typical aircraft engine [3.38] (Figure 3.36). Table 3-5 also illustrates how the tip deflection sensitivity of the cantilever can be improved while keeping the natural vibrational frequencies of the cantilevers well above the harsh environment mechanical noise.

$$f_n = \frac{1}{2\pi}\sqrt{\beta_n^4 \frac{EI}{m/L}} \tag{3.10}$$

$$E_{bilayer} \approx \frac{E_1 t_1 + E_2 t_2}{(t_1 + t_2)} \tag{3.11}$$

$$I = \frac{1}{12} w t^3 \tag{3.12}$$

TABLE 3-5.

Natural oscillation frequencies of the cantilevers

$t_{alumina}$ (μm)	50	150
t_{Pt} (μm)	10	10
Lcant (mm)	5	7
w (mm)	1	1
f_1 (kHz)	1.3	1.58
f_2 (kHz)	8.1	9.9
f_3 (kHz)	22.7	27.7
Tip deflection (μm /^{o}C)	4.5	8.8

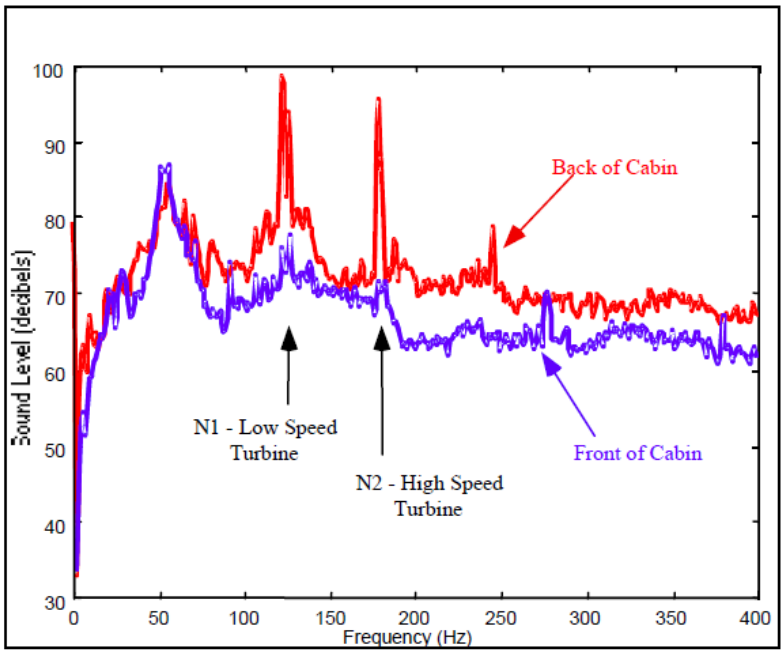

Figure 3.36. Typical internal cabin (measured data) noise spectrum of an aircraft with fuselage mounted engines. [3.38]

3.6. Limitations and Future Work

The operation of the proposed SRR based sensor relies on the operation of the bimorph cantilevers. In this thesis, the reliability of the Al-PET cantilevers in the proof-of-concept prototypes has not been investigated. Nevertheless, the thermal response of the bimorph cantilevers has been studied extensively in the literature. RF switches of Au-SiN bimorphs have been tested up to 1 billion thermal actuation cycles [3.39]. Bimorphs made of Al-SiO_2 were demonstrated to work after 10 million thermal actuation cycles at 3 kHz [3.40]. The Al-SiO_2 bimorphs of the slot based temperature sensor in [3.5] were shown to function with negligible fatigue past a billion thermal cycles [3.41]. Future work of this thesis should consist of fabrication and tests on different bimorph formations integrated with the split ring circuit.

The suspended cantilevers of the design can impose a major drawback to the performance of the sensor in harsh environments where not only high temperature above 1000 ^{o}C occurs but also strong vibrational noises are present. However, as Chapter 4 illustrates, the operating principles of the sensor are not limited to the use of cantilevers but any temperature-dependent capacitance change at the SRR gaps would allow a large frequency shift. Potentially, temperature-dependent capacitive microfluidic channels similar to the one proposed in [3.32] may replace the cantilevers in the SRR design utilizing Galinstan instead of water for extreme temperature applications.

To enable multi-node sensing networks, different lengths of the delay lines connecting between the sensor nodes to the target antenna (the loaded antenna) may be used. Different sensor nodes may be identified by different beat frequencies and their sensing information may be encoded in the received power fluctuation at the beat

frequencies (or RCS levels). Note that in the proof-of-concept measurements in Section 3.5.2, the horn antenna was conveniently used as the target antenna. In practice, it could be replaced by low profile highly directive antenna arrays such as a highly compact Yagi-type array of patch antennas [3.42 – 3.43].

In the interrogation method of the FMCW radar, the required delay lines present a challenge in the layout of a multi-node sensor network. As seen in Figure 3.27, the antenna mode is only required to be separated from the structural mode by the width of the peak (where 1 dB difference in power level can be read between peaks), i.e. a spacing of about 2 kHz in the beat frequency domain. This minimum spacing corresponds to about two free-space wavelengths of the carrier frequency at 3 GHz, which is a determining factor on the length of the delay lines. This same limit can also be used as a reference to separate different sensor nodes in a network (see Section 2.3). Potentially, this sensor operating based on load impedance modulation can be integrated with a SAW sensor architecture such as the two-port impedance SAW sensors (Figure 2.9), where the slow travelling acoustic wave can act as a miniaturized delay line (refers to Section 2.3). Future work of the RF SRR sensor should include a complete integration of the sensor, the delay line, and the loaded antenna fabricated on an alumina substrate with Pt electrodes and to be tested for operation above 1000 ^{o}C.

3.7. References

[3.1] P. R. N. Childs, J. R. Greenwood, C. A. Long, "Review of temperature measurement," *Rev. Sci. Instrum*., vol. 71, no. 8, pp. 2959 – 2978, Aug. 2000.

[3.2] J. Goetz, "Sensors that can take the heat," *Sensors*, pp. 20 – 38, June 2000.

[3.3] O. J. Gregory, T. You, “Ceramic Temperature Sensors for Harsh Environments,” *IEEE Sensor J.*, vol.5, no. 5, pp.833 – 838, Oct. 2005.

[3.4] L. Toygur, “Interface Circuits in SOI-CMOS for High-temperature Wireless Micro Sensors,” Ph.D. Dissertation, Case Western Reserve University, Cleveland, OH, Jan. 2004.

[3.5] S. Scott, D. Peroulis, “A capacitively-loaded MEMS slot element for wireless temperature sensing of up to 300 ^{o}C,” in *IEEE Int. Microw. Symp.*, Boston, MA, June 2009. pp. 1161 – 1164.

[3.6] T. T. Thai, J. M. Mehdi, F. Chebila, H. Aubert, P. Pons, G. R. DeJean, M. M. Tentzeris, R. Plana, “Design and Development of a Novel Passive Wireless Ultrasensitive RF Temperature Transducer for Remote Sensing,” *IEEE Sensors J.*, vol. 12, no. 9, pp. 2756 – 2766, Sept. 2012.

[3.7] M. M. Jatlaoui, F. Chebila, P. Pons, H. Aubert , "New Micro-sensors Identification Techniques Based on Reconfigurable Multi-band Scatterers," in *Asia-Pacific Microw. Conf.*, Singapore, Dec. 2009, pp. 968 – 971.

[3.8] M. M. Jatlaoui, F. Chebila, P. Pons, H. Aubert, “Wireless Interrogation Techniques for a Passive Pressure Micro-sensor using an EM Transducer,” in *Euro. Microw. Conf.*, Rome, Italy, Sept. – Oct. 2009, pp. 53 – 56.

[3.9] F. Chebila, M. M. Jatlaoui, P. Pons, H. Aubert, “Pressure Measurement from the Radar Interrogation of Passive Sensors,” in *IEEE Ant. Prop. Soc. Int. Symp*, Toronto, ON, July 2010, pp. 1 – 4.

[3.10] Aubert H, Pons P, Chebila F, Jatlaoui M, “Measurement device comprising an electromagnetic diffuser,” W.O. Patent 2010/136388, May 29, 2009.

[3.11] F. Chebila, “Lecteur Radar pour Capteurs Passifs à Transduction Radio Fréquence,” Ph.D. Dissertation, University of Toulouse, Toulouse, France, Mar. 2011.

[3.12] R. J. Stephenson, A. M. Moulin, M. E. Welland, “Bimaterials thermometers,” in *The Measurement Instrumentation and Sensors Hanbook,* Chemical Rubber, Boca Raten, FL, 1999.

[3.13] K. Aydin, A. O. Cakmak. L. Sahin, Z. Li, F. Bilotti, L. Vegni, E. Ozbay, “Split-Ring-Resonator-coupled enhanced transmission through a single subwavelength aperture,” *Appl. Phys. Lett*., vol. 102, no. 1, pp. 013904/4, Jan. 2009.

[3.14] C.-Y. Lee, C.-H. Tsai, L.-W. Chen, L.-M. Fu, Y.-C. Chen, "Elastic-plastic modeling of heat-treated bimorph micro-cantilevers," *Microsystem Technologies*, vol. 12, no. 10 – 11, pp. 979 – 986, Aug. 2006.

[3.15] J. B. Pendry, A. J. Holden, D. J. Ribbins, W. J. Stewart, "Magnetism from conductors and enhanced nonlinear phenomena," *IEEE Trans. Microw. Theory Tech*., vol. 47, no. 11, pp. 2075 – 2084, Nov. 1999.

[3.16] D. Smith, W. J. Padilla, D. C. Vier, S. C. Nemat-Nasser, S. Schultz, "Composite Medium with Simultaneously Negative Permeability and Permittivity," *Phys. Rev. Lett*., vol. 84, no. 18, pp. 4184 – 4187, May 2000.

[3.17] R. Marques, F. Mesa, J. Martel, F. Medina, "Comparative analysis of edge- and broadside-coupled split ring resonators for metamaterial design - theory and experiments," *IEEE Trans. Ant. and Prop*., vol. 51, no. 10, pp. 2572 – 2581, Oct. 2003.

[3.18] Rogers Corporation [Online]. Available: http://www.rogerscorp.com/index.aspx (Accessed: 21 July 2013).

[3.19] H. Aubert, F. Chebila, M. Jatlaoui, T. Thai, H. Hallil, A. Traille, S. Bouaziz, a. Rifai, P. Pons, P. Menini, M. Tentzeris, "Wireless sensing and identification based on radar cross section variability measurement of passive electromagnetic sensors," *Ann. Telecommun., Springer-Verlag*, vol. 68, no. 7 – 8, pp. 425 – 435, June 2013.

[3.20] P. Bratt (Mar. 2010). *Properties of Low Dielectric Constant Laminates* [Online]. Available: http://www.rogerscorp.com/documents/1798/acm/articles/Properties-of-Low-Dielectric-Constant-Laminates.pdf (Accessed: 21 July 2013).

[3.21] R. E. Bentley, "Temperature and humidity measurement", in *Handbook of temperature measurement*, vol.1*,* New York, Springer: New York, 1998.

[3.22] T. Wei, X. Lan, H. Xiao, Y. Han, H-L. Tsai, "Optical fiber sensors for high temperature harsh environment sensing," in *IEEE Inst. Meas. Tech. Conf.*, Binjiang, China, May 2011, pp. 1 – 4.

[3.23] Luna Inc. (2013). *Extreme Temperature Thermal and Pressure Sensors* [Online]. Available: http://lunainc.com/technology-development/materials/extreme-range-temperature-sensor/ (Accessed: 14 Oct. 2013).

[3.24] A. B. Murphy, "Laser-scattering temperature measurements of a free burning arc in nitrogen," *J. Phys. D: Appl. Phys*., vol. 27, no. 7, pp. 1492 – 1498, July 1994.

[3.25] M. R. Jones, D. G. Barker, Dept. of Mech. Eng., Brigham Young Uni. *Use of blackbody optical fiber thermometers in high temperature environment*s [Online]. Available: http://tfaws.nasa.gov/TFAWS01/NASA/13Spacecr/kJONES.PDF (Accessed: 2013 July 21).

[3.26] R. Fachberger, G. Bruckner, R. Hauser, L. Reindl, "Wireless SAW based high-temperature measurement systems," in *IEEE Int. Frq. Contrl. Symp. Expo*., Miami, FL, June 2006, pp. 356 – 367.

[3.27] A. Canabal, P. M. Davulis, G. M. Harris, M. Pereira da Cunha, "High-temperature battery-free wireless microwave acoustic resonator sensor system," *Elec. Lett*., vol. 46, no. 7, pp. 471 – 472, April 2010.

[3.28] M. Pereira da Cunha, T. Moonlight, R. Lad, G. Bernhardt, D. J. Frankel, "Enabling Very High Temperature Acoustic Wave Devices for Sensor & Frequency Control Applications," in *IEEE Int'l Ultrason. Symp*, New York, NY, Oct. 2007, pp. 2107 – 2110.

[3.29] A. Canabal, P. M. Davulis, E. Dudzik, and M. Pereira da Cunha, "CDMA and FSCW surface acoustic wave temperature sensors for wireless operation at high temperatures," in *IEEE Int'l Ultrason. Symp.*, Rome, Italy, Sept. 2009, pp. 807 – 810.

[3.30] H. Cheng, S. Ebadi, X. Gong, "A low-profile wireless passive temperature sensor using resonator/antenna integration up to 1000 ^{o}C," *IEEE Ant. Wireless Prop. Lett*., vol. 11, pp. 369 – 372, April 2012.

[3.31] A. Traille, S. Bouaziz, S. Pinon, P. Pons, H. Aubert, A. Boukabache, M. Tentzeris, "A wireless passive RCS-based temperature sensor using liquid metal and microfluidics technologies," in *Euro. Microwave Conf*., Manchester, UK, Oct. 2011, pp. 45 – 48.

[3.32] S. Bouaziz, F. Chebila, A. Traille, P. Pons, H. Aubert, M. Tentzeris, "A new millimeter-wave micro-fluidic temperature sensor for wireless passive radar interrogation," in *IEEE Sensors*, Taipei, Taiwan, Oct. 2012, pp. 1 – 4.

[3.33] S. Fargeot, D. Guihard, and P. Lahitte, "Dielectric characterization at high temperature (1600 ^{o}C) for space applications," in *IEEE Int. Conf. Microw. Technol. Comput. Electromagn*., Beijing, China, May 2011, pp. 48 – 50.

[3.34] *Elastic Properties and Young Modulus for some materials* [Online]. Available: http://www.engineeringtoolbox.com/young-modulus-d_417.html (Accessed: 2013 July 21).

[3.35] *Aluminum Oxide (Al_2O_3) Properties* [Online]. Available: http://aries.ucsd.edu/LIB/PROPS/PANOS/al2o3.html (Accessed: 2013 July 21).

[3.36] *PDHengineer* [Online]. Available: http://www.pdhengineer.com/courses/s/S-3001.pdf (Accessed : 2013 July 22)

[3.37] J. Murin, V. Kutis, "An effective solution of the composite (FGM'S) beam structures," *Eng. Mech*., vol. 15, no. 2, pp. 115 – 132, 2008.

[3.38] J. DePriest (2001). *Aircraft Engine Attachment and Vibration Control* [Online]. Available: Lord Library of Technical Articles, LL-6505, Lord Corporation http://mutualhosting.com/~lordfulfillment/upload/LL6505.pdf (Accessed: 2013 July 22).

[3.39] P. Robert, D. Saias, C. Billard, S. Boret, N. Sillon, C. Maeder-Pachurka, P. Charvet, G. Bouche, P. Ancey, and P. Berruyer, “Integrated RF-MEMS switch based on a combination of thermal and electrostatic actuation,” in *Int. Conf. Transducers, Solid-State Sens., Actuators Microsyst*., Boston, MA, June 2003, vol. 2, pp. 1714 – 1717.

[3.40] Y. Liu, X. Li, T. Abe, Y. Haga, and M. Esashi, “A thermomechanical relay with microspring contact array,” in *IEEE Int. Conf. MEMS*, 2001, pp. 220–223.

[3.41] S. Scott, J. Katz, F. Sadeghi, D. Peroulis, “Highly reliable MEMS Temperature Sensors for 275 oC Applications – Part 2: Creep and Cycling Performance,” *J. MEMS Sys*., vol. 22, no. 1, pp. 236 – 243, Feb. 2013.

[3.42] T. T. Thai, G. R. DeJean and M. M. Tentzeris, "Design and development of a novel compact softsurface structure for the front-to-back ratio improvement and size reduction of microstrip Yagi antenna arrays," in *Proc. of the 2007 IEEE Ant. Prop. Soc. Int. Symp*., Honolulu, Hawaii, June 2007, pp.1193 – 1196.

[3.43] G. R. DeJean, T. T. Thai, S. Nikolaou and M. M. Tentzeris, "Design and analysis of microstrip bi-Yagi and quad-Yagi antenna arrays for WLAN applications," *IEEE Antennas and Wireless Propagation Letters*, vol.6, pp. 244-248, April 2007.

Chapter 4.

Equivalent Circuits of the SRR-based RF sensors

4.1. Introduction

A new ultrasensitive RF temperature sensor was proposed in Chapter 3. The sensor is based on split ring resonators loaded with cantilevers, where the sensing mechanism is based on a resonant frequency shift caused by the deflection of the bimorph cantilevers as they respond to a temperature change. The operation of the sensor was investigated with a brief introduction on an equivalent circuit, yet a design circuit model was not included. This chapter aims in presenting a methodology to extract an equivalent circuit model for the design and optimization of such structures for different applications.

Since their first introduction in 1999 [4.1], SRRs have been extensively studied in terms of both their physics and equivalent circuit models [4.1 – 4.13]. There are two major approaches in modeling the SRRs. The first approach derives analytical expressions for the SRRs and their variations based on polarizability and magnetic dipoles (current and field calculations), and then an expression for the resonant frequency [4.1 – 4.10]. The second approach is based on a transmission line model with distributed-circuit elements to calculate the SRR resonant frequency [4.11 – 4.12]. Those approaches derive the inductance and capacitance values from the physical dimensions of the SRRs. Although they could predict the resonant behavior of the SRRs well and they could offer valuable insight into the physics of the SRRs, such approaches are based on lengthy calculations with multiple parameters before deriving a simple and effective *LC* circuit (an inductor-capacitor tank) and consequently, they are ineffective in driving the designs

and in directly assisting optimization. Most of the electrical circuit models are also limited to only the lowest (or fundamental) resonant mode of the SRRs. A compact circuit model was introduced in [4.10] but the capacitive circuit elements were not estimated in a systematic way. A circuit extraction based on scattering parameters was introduced in [4.13] but the method was applied to a network of SRRs coupled to planar transmission lines rather than the SRRs themselves, which were also represented by the complex analytical method. All previous works including [4.10] could not provide a straightforward connection between the resonant behavior of the SRRs and the circuit view of only two equivalent lumped elements L and C. If the mode of a resonator can be described with an effective inductor and an effective capacitor that correspond to certain desired physical parameters of the resonator, then designers have direct access to its inductive and capacitive behavior to intuitively manipulate and optimize sensors operated based on the resonant frequency of the resonator. Furthermore, the circuit extraction method presented in this chapter can model a large resonant frequency shift of up to 25 % of the operating frequency; at the same time, it can produce circuits that capture 2 – 3 resonant modes spanning a large range of frequency (20 – 90 GHz) making it highly adaptable to wideband applications. In general, circuits accounting for higher modes of a resonator can enhance the accuracy in modeling the lower modes. In particular, the first two modes (slightly coupled since both are influenced by the split gaps) of a double split ring resonator are highly sensitive to its split gap capacitances, which are the critical factors in sensing. Therefore, it is important in the perspective of design to separate those modes and capture their changing behaviors with the inclusion of the next higher mode, the third mode, for high accuracy. On the other hand, while most of the proposed models

were concerned with metamaterial applications, the tuning range limits of the resonant frequencies of individual SRRs in terms of their split gap capacitance were not addressed. Such sensitivity and their dynamic range in terms of frequency shifts present a great potential in sensing applications. To assist the optimization and the derivation of automated design rules for sensing applications, specifically applied to the sensing principles of the SRR based RF temperature proposed in Chapter 3, this chapter introduces a simple and systematic approach to extract lumped circuit elements modeling different resonant modes of the split rings loaded with cantilevers. This work presents the first effort to model the variation of the resonant frequencies of the split rings in terms of the variation of the split gap capacitance based on a simple circuit extraction method in a comprehensive study. Each resonant mode is modeled by an *LC* pair in series in which the capacitance is shown to correspond directly to the split gap capacitance made tunable by the embedded cantilevers. In particular, rather than concerning with the quality factor of the resonator or the physical basis of the effective lumped circuit elements, the scope of the method focuses on the relationship between the split gap capacitance and the resonant frequencies and their shifts in the operation of the sensor (see Chapter 3). The study of the double split rings loaded with cantilevers (DSRRC) proceeds from the study of double closed-loop rings (DCRR), which is built upon the investigation of a single closed-loop ring and a single open ring. The discussion of mode modeling based on the series circuit topology of a closed-loop ring (CRR) and an open ring loaded with a cantilever (ORRC) are provided in Section 4.2, which also illustrates the circuit extraction method. It is followed by the investigation on the DCRR and the DSRRC in

Section 4.3. Finally, discussion on the inductance variations and conclusions are presented in Section 4.4 and Section 4.5, respectively.

4.2. Single Split Ring loaded with a Cantilever

4.2.1. Mode Analysis

As the first step for the derivation of an equivalent circuit model, full-wave CST electromagnetic simulations [4.14] are set up for a typical CRR (Figure 4.1a) centered on top of a substrate backed by a ground plane. It is excited by a normally incident plane wave with only an x-component of the electric field (E-field) and a y-component of the magnetic field (H-field). The complete schematic diagram of the problem geometry is shown in Figure 4.2, and its dimensions are provided in Table 4-1 (consistent with the dimensions reported in Chapter 3). Note that all the ring widths and split gaps of the resonators in Figure 4.1 are identical. To remain consistent with the designs proposed in the previous chapter, glass is utilized as the substrate (dielectric constant, ε_r, of 4.82). The backside of this substrate is metallized. Without loss of generality, and for the proof of concept, all metallic objects are considered to be perfect electric conductors with thickness, t. The waveguide, extended continuously from the plane wave port to the ground plane, with a square cross section with a side dimension, L_{sub}, is constructed with perfect electric walls (PEC) on the x-faces ($E_{tangent} = 0$), and perfect magnetic walls (PMC) on the y-faces ($H_{tangent} = 0$). The waveguide is thus equivalent to a parallel plate waveguide with no cutoff frequency for the Transverse ElectroMagnetic (TEM) fundamental mode ($E_Z = 0$ and $H_Z = 0$) and with cutoff frequencies (determined by L_{sub}) for non-TEM modes. The air region has the length, L_x, and the substrate region has the

length, h. Then the CRR is replaced by an open ring with a split gap (Figure 4.1b) loaded with a cantilever (Figure 4.3). Note that the cantilever used here is slightly different from what was presented in [14] because the support in a conventional cantilever is replaced by a bonding wire. The replacement allows the parallel plate capacitance of the cantilever to be isolated from the fringing effect of the anchor support. The reference plane for the input impedance evaluation is set to the same plane as that of the ring resonator. Theoretically, the input impedance is purely imaginary because the system is assumed completely lossless. Note that the polarization of the incident E-field is tangential to the ring at its split gap. Ring resonators can be excited by either normal H-field (to induce a magnetic dipole hence an electromotive force voltage) or a tangential E-field (to induce a current). In the case of ORRC and DSRRC (discussed in Section 4.3), the appropriate polarization (tangential) of the incident E-field relative to their split gaps excites the fundamental mode of the open/split rings, which is the mode of interest.

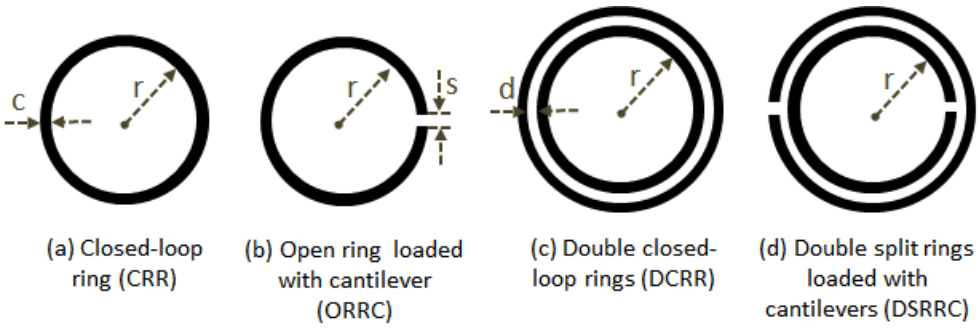

Figure 4.1. Different topologies of closed-loop and split ring resonators where the loaded cantilevers at the split gaps are not shown.

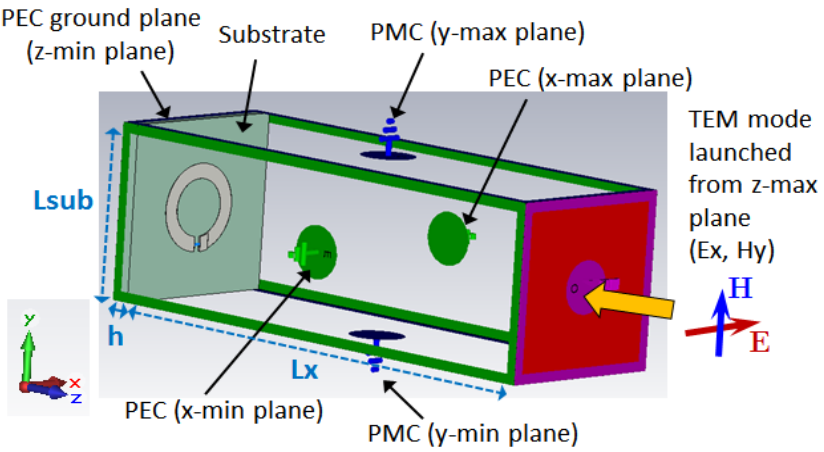

Figure 4.2. CST simulation setup for the closed rings and split rings resonators.

TABLE 4-1

Dimensions of the Problem Geometry

Full-wave electromagnetic simulation parameters	
r	230 μm
c	120 μm
s	45 μm
d	50 μm
L_x	5000 μm
L_{sub}	1400 μm
h	150 μm
t	1 μm
ε_r	4.82

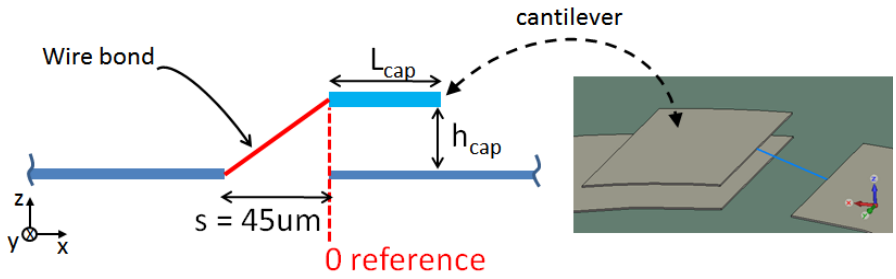

Figure 4.3. Diagram of the parallel plate cantilever loaded on the split rings.

The input impedance (imaginary part or *reactance*) of the CRR and the ORRC is shown in Figure 4.4. The reactance of the ORRC is presented for L_{cap} of 80 µm and different h_{cap} values (6, 10, and 14 µm) (see Figure 4.3). In the efforts of building circuit models for the sensor designs proposed in Chapter 3, the same dimensions are utilized here for the rings and their cantilevers. While all resonators share the same mode at 86 GHz, observe that the resonant mode around 30 – 40 GHz is not present in the CRR. Due to the rotational symmetry of the ORRC, the current distribution at the lowest resonant mode must represent one wavelength. More specifically, the free space wavelength at 86 GHz is 3488 µm. The effective dielectric constant, ε_{eff}, is in the range of 2.91 – 4.82 (the lower limit comes from the mean dielectric constant of air and glass), which results in an effective TEM guided-wavelength, $(\frac{c_o}{f_r\sqrt{\varepsilon_{eff}}})$, of 1589 – 2045 µm approximately where c_0 denotes the vacuum velocity of light. Meanwhile, the mean circumference of the ring is 1822 µm, which is within the estimation of one full guided-wavelength at the resonant frequency of the CRR. Furthermore, observe that only the first resonant frequency of the ORRC shifts as h_{cap} varies (e.g., as the split capacitance is varied), because the second mode resembles the fundamental mode of the CRR and thus is not influenced by the split

gap capacitance. The patterns of the electric field distribution (Figure 4.5) of the CRR at its fundamental mode and the ORRC at its first and second modes confirm such effect. Figure 4.5a and 4.5b illustrate the same E-field distribution pattern except that the axis of the minima of the ORRC is rotated due to the slight asymmetry of the cantilever position relative to the split of the ring. The E-field pattern of the first mode of the ORRC (Figure 4.5c) resembles that of a half-wavelength dipole, where the two ends are brought into close proximity with each other fictitiously. However, the resonant frequency is significantly lower than half the resonant frequency of the second mode due to the additional capacitance brought to the resonator by the cantilever. The mode patterns suggest that the equivalent *LC* circuit at 86 GHz extracted from the CRR can also describe the same mode observed in the ORRC.

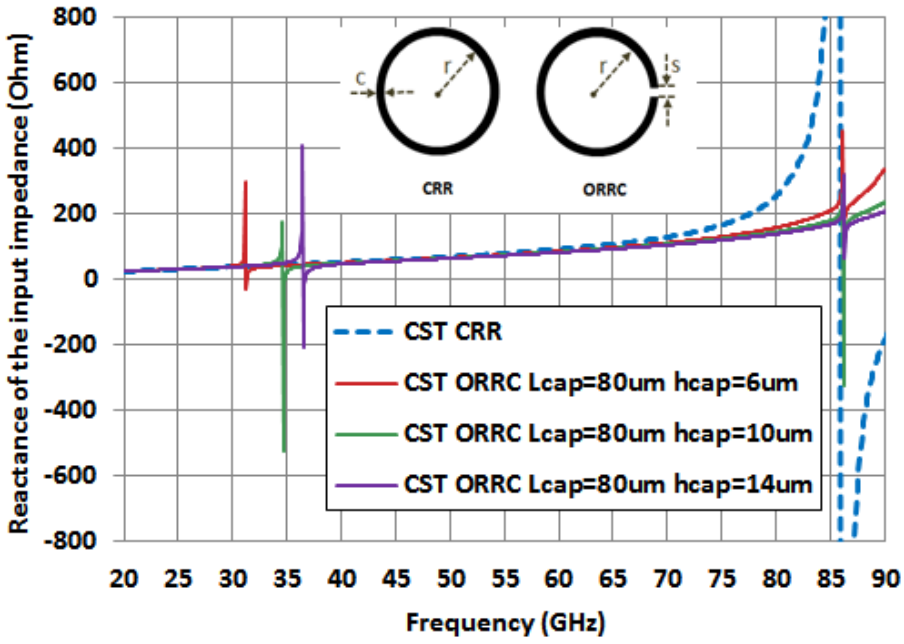

Figure 4.4. Reactance of the CRR and the ORRC.

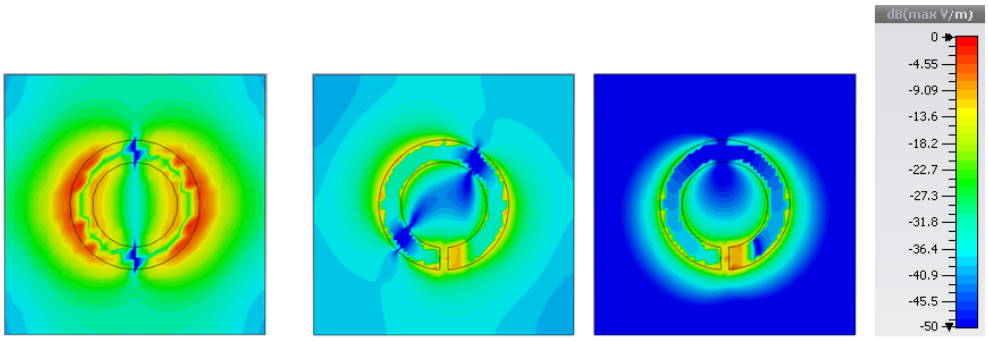

(a) 86 GHz of CRR (b) 86 GHz of ORRC (c) 36 GHz of ORRC

Figure 4.5. Electric field distribution at the reference plane of the CRR at its fundamental resonant mode (86 GHz) and the ORRC at its first mode (36 GHz) and second mode (86 GHz).

4.2.2. Equivalent Circuit Extraction for the CRR

The geometry in Figure 4.2 consists of a transmission line with only the TEM mode (below the cutoff frequency of the first non-TEM mode) incident upon the resonator, continued through the very short transmission line characterized by the substrate and its thickness, finally terminated by the ground plane. Because the waveguide (both air and dielectric regions) and the resonator are excited with the TEM mode only, the physical problem of Figure 4.2 can be approximated with the transmission line circuit shown in Figure 4.6, where the inductance, L_1, and the capacitance, C_1, model the fundamental mode of the CRR and h is the thickness of the substrate. Therefore, the input impedance obtained from CST simulations (Figure 4.7), where the reference plane is moved to the resonator surface, corresponds to the input impedance, Z_{in}, of the transmission line circuit of Figure 4.6. Note that the glass substrate is modeled by a transmission line with length, h_{cap}, and characteristic impedance as the ratio of the air

impedance divided by $\sqrt{\varepsilon_r}$, that is $377/\sqrt{4.82}$. The input admittance (Y_{in} = $1/Z_{in}$ after de-embedding out the air region) is expressed in terms of the transmission line elements (4.1), where Y_0 = (a/b) x $1/377$ S is the characteristic admittance of the transmission line [4.15], a and b denote respectively the width and the height of the TEM waveguide (here $a = b = L_{sub}$). The input admittance is observed to depend on three unknown variables, L_1, C_1, and ω, the radial frequency. The full-wave simulations of the closed-loop ring give a frequency point, ω_{inf} (86 GHz), at which the input impedance is infinite, and another, ω_z (97 GHz), at which the input impedance is zero, i.e., Y_{in} (L_1, C_1, ω_{inf}) = $1/Z_{in}(L_1, C_1, \omega_{inf})$ = 0 and, Z_{in} (L_1, C_1, ω_z) = 0. Therefore, L_1 and C_1 can be found to be 0.76 nH and 3.5 fF, respectively, using the non-linear Levenberg Marquardt method in MathCad [4.16]. The ADS plot of the input reactance of the solution circuit is also shown in Figure 4.7, which appears to match extremely well with the CST full-wave simulated reactance.

Only the appropriate choice of the circuit topology (choice between an LC tank in series or in parallel configurations) would guarantee the existence of a solution. In the series topology, the reactance of $Z_{in} = j\left(\frac{\omega^2 LC-1}{\omega C}\right)$ approaches (ωL) as $\omega \to \infty$, while in the parallel topology, the reactance of $Z_{in} = j\left(\frac{\omega L}{1-\omega^2 LC}\right)$ approaches $(\frac{-1}{\omega C})$ as $\omega \to \infty$. It can be observed in Figure 4.7 that as the frequency increases the reactance approaches a positive value. Therefore, in this extraction approach based on ω_{inf} and ω_z, an LC pair in parallel would not yield solutions.

Based on the parameters of Table 4-1, the waveguide has the cutoff frequency, $f_c = \frac{c_0}{2L_{sub}\sqrt{\varepsilon_r}}$, for the first non-TEM mode at 107 GHz in the air region and at 48.8 GHz in the substrate (glass) region. This indicates that the transmission line model of Figure

4.6 is accurate below 48.8 GHz (Note that at frequencies higher than 48.8 GHz but lower than the cutoff frequency of the second non-TEM mode in the substrate region, this model should incorporate an additional short-circuited transmission line for modeling the standing wave generated by the first non-TEM mode in this region). The inclusion of the substrate is to support the resonances of the rings in the operating frequencies of interests. On a closer look, total attenuation for 48.8 GHz in both air and glass regions is 4.6×10^{-5}, where the attenuation and the coefficient are calculated as $e^{-\alpha_{air}Lx-\alpha_{glass}h}$ and $\alpha = \sqrt{\left(\frac{\pi}{Lsub}\right)^2 - \varepsilon_r \left(\frac{\omega}{c}\right)^2}$ [4.15]. Consequently, non-TEM modes below 48.8 GHz are negligible. Attenuation for 86 GHz in the air region is 0.0014, and this energy portion of the mode continues to propagate through the thin glass layer without further attenuation. Therefore, the resonant frequency found from CST simulations has a certain small error $(86 \pm \Delta)$ GHz. However, this mode is not the shifting mode but rather is included as the higher order factor in the input impedance responses to provide better accuracy in modeling the lower shifting modes. As it will be clarified further in the subsequent sub-sections, such error does not influence the accuracy of the circuit model for the shifting modes (corresponding to the split gap capacitance) that occur below 48.8 GHz.

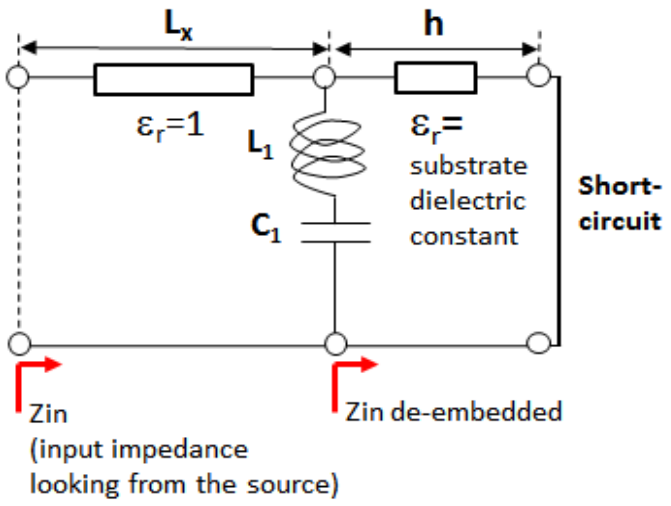

Figure 4.6. Circuit topology of the CRR.

$$Y_{in}(L_1, C_1, \omega) = \left(\frac{1}{jC_1\omega} + jL_1\omega\right)^{-1} - jY_0\sqrt{\varepsilon_r}cot\left(\frac{\omega}{c}\sqrt{\varepsilon_r}h\right) \qquad (4.1)$$

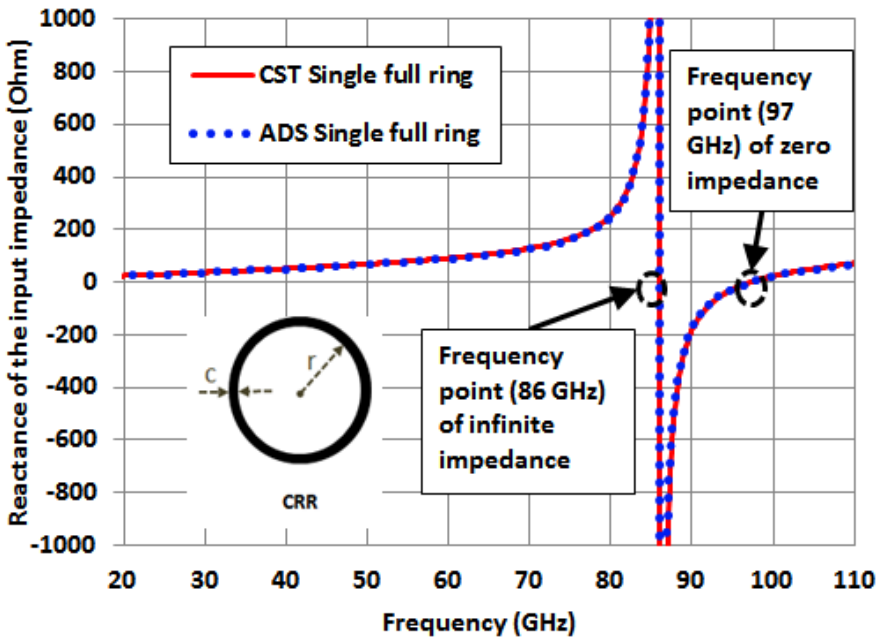

Figure 4.7. Reactance of the CRR.

4.2.3. Split Ring loaded with Discrete Capacitors and Circuit Extraction for the ORRC

To model the lowest resonant mode of the ORRC that does not appear in the CRR, another set of *L*-*C* components in series is added to the above-derived circuit (Figure 4.8). The input impedance becomes (4.2), where Y_{in} depends on L_2, C_2, and ω only since the components L_1 and C_1 that were calculated earlier represent an orthogonal ORRC mode to this one. However, the input reactance responses of the ORRC (with different positions of the cantilever) in Figure 4.4 suggest that the frequency point about the first resonant mode, where the input impedance vanishes, cannot be located reliably unlike how the zero impedance frequency can be located in Figure 4.7. Because the bandwidth of the resonant frequency around 30 – 40 GHz is much smaller than the one around 80 – 90 GHz, the zero impedance frequency point at the lower mode is largely subjected to phase errors in simulation. Rather, only the frequency point where the input admittance vanishes (e.g. infinite or large input impedance) can be identified accurately based on its phase change (e.g. the first derivative of the reactance in the frequency domain is large when approaching from the left and right surrounding the resonant frequency). Therefore, L_2 and C_2 cannot be solved using the same approach applied to L_1 and C_1. On the other hand, when the split gap exists, the split gap modes are mostly due to the gap capacitance [4.5 – 4.12], and other capacitances, such as self-capacitance or distributed capacitance of the ring [4.6], of the ring resonators become negligible. Therefore, the capacitance, C_2, of the ORRC can be approximated by the parallel plate capacitance, C_{2pp}, of the cantilever (see Table 4-1 and Figure 4.3), which can be estimated according to (4.3) with ε_o and ε_r are the free space permittivity and the

dielectric constant of glass, respectively. To estimate the applicability of this assumption, the cantilever of the ORRC is replaced by discrete lumped capacitors (the split gap, *s*, remains unaltered) and simulated with 40 values covering the range of 0.2 – 100 fF. It is then compared with the parallel plate capacitance formed by the cantilever. The lumped capacitors and the parallel plate capacitance are plotted versus the fundamental frequency of the ORRC in Figure 4.9. It shows that the dependence of the resonant frequency on the split gap capacitance is almost the same for the lumped capacitors and the cantilever parallel plate capacitance.

Based on the responses of the fundamental resonant frequency of the ORRC (denoted as f_{res2}) to the lumped capacitors (green curve of Figure 4.9), a fitting 4th order polynomial is found with MathCad for C_2 as a function of f_{res2} as shown in (4.4). Thus, C_2 is easily determined for every f_{res2} located from the CST full-wave simulations, then L_2 is solved from $Y_{in}\ (L_2,\ C_2, f_{res2}) = 1/Z_{in}(L_2,\ C_2, f_{res2}) = 0$.

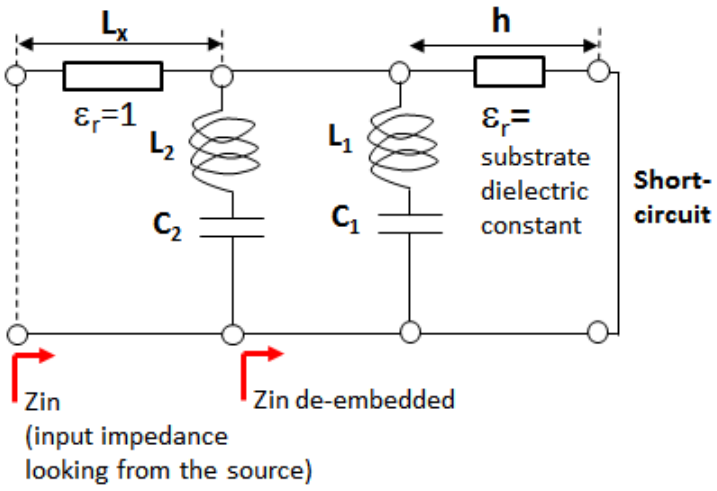

Figure 4.8. Circuit topology of the ORRC.

$$Y_{in}(L_2, C_2, \omega) = \left(\frac{1}{jC_2\omega} + jL_2\omega\right)^{-1} + \left(\frac{1}{jC_1\omega} + jL_1\omega\right)^{-1} - jY_0\sqrt{\varepsilon_r}cot\left(\frac{\omega}{c}\sqrt{\varepsilon_r}h\right) \quad (4.2)$$

$$C_{2pp} = \frac{\varepsilon_0\varepsilon_r L_{cap}c}{h_{cap}} \quad (4.3)$$

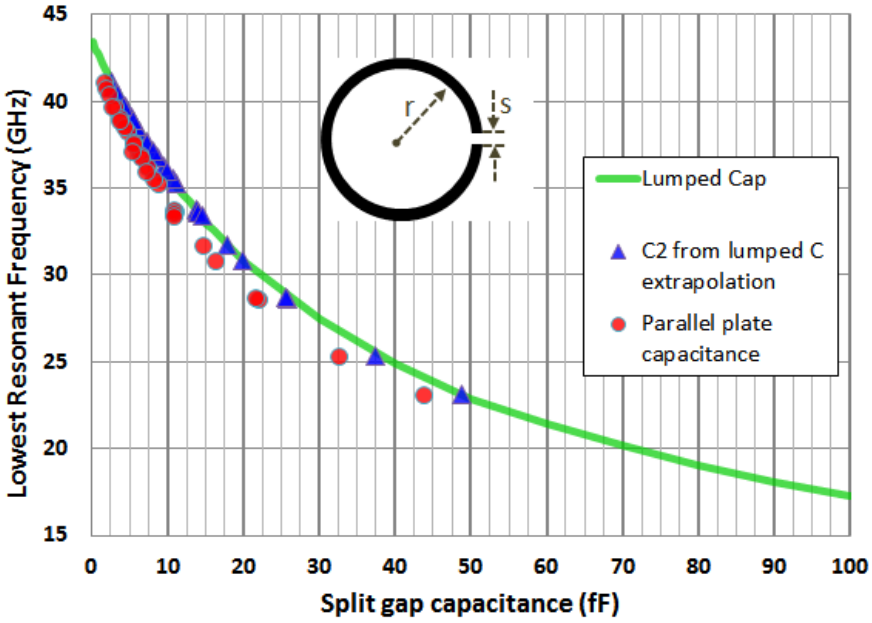

Figure 4.9. Resonant frequency of the ORRC versus split gap capacitances.

$$C_2(f_{res2}) = 664.62 - 62.87f_{res2} + 2.39f_{res2}^2 - 4.20 \times 10^{-2}f_{res2}^3 + 2.81 \times 10^{-4}f_{res2}^4 \quad (4.4)$$

To test the accuracy of the above solutions, various structures of ORRC are simulated with CST for different cantilever conditions, that is, h_{cap} values of 4, 6, 8, 10, 12, and 14 μm and for four different L_{cap} values of 20, 40, 60, and 80 μm (see Figure 4.13). The capacitor C_2 obtained from (4.4) based on those simulations is plotted also in Figure 4.9 and is close to the lumped capacitor curve, as expected. Solutions of L_2 are plotted versus the resonant frequency, f_{res2}, in Figure 4.10. ADS simulations of the circuit in Figure 4.8 using the derived solutions for L_2 *and* C_2 are plotted and compared with CST full-wave simulations in Figure 4.11 – 4.12, where the ADS and CST responses appear to overlap. It can be observed that for various combinations of h_{cap} and L_{cap} values, resulting in different split gap capacitances, the resonant frequency shifts are modeled by the simple lumped circuits with high accuracy (within 1% of error). The solutions of L_2 and C_2 for ADS plots in Figure 4.11 – 4.12 are reported in Table 4-2.

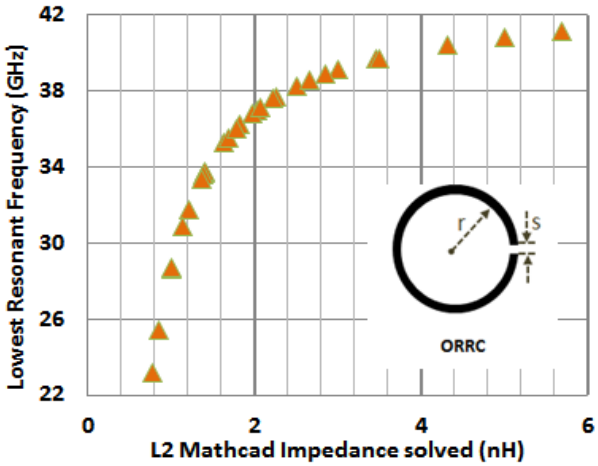

Figure 4.10. Variation of the resonant frequency of the ORRC with respect to L2 solution.

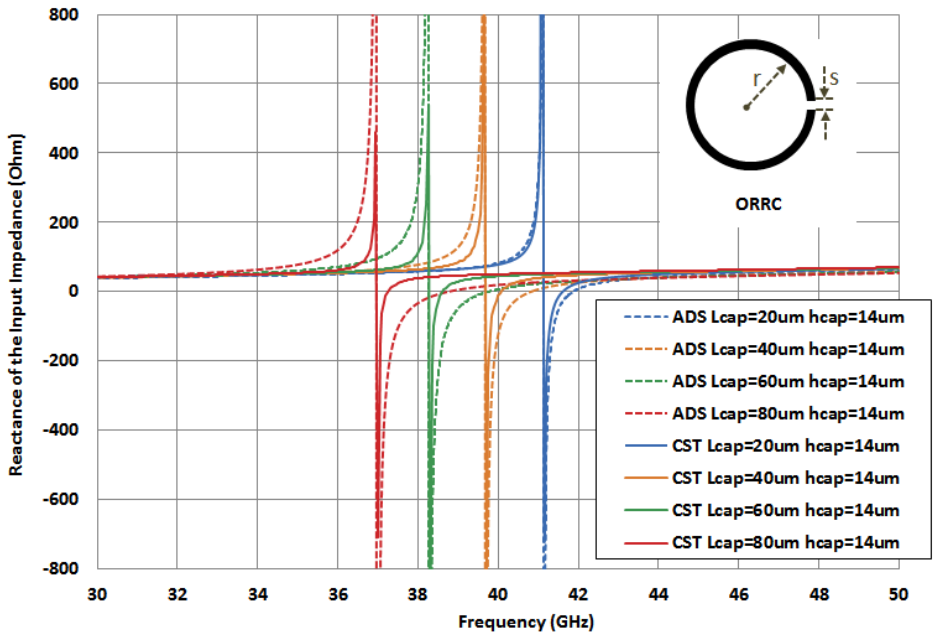

Figure 4.11. Comparison between full-wave CST simulations and ADS simulations of the calculated circuit elements for the ORRC for different cantilever lengths at the same cantilever height of 14 μm.

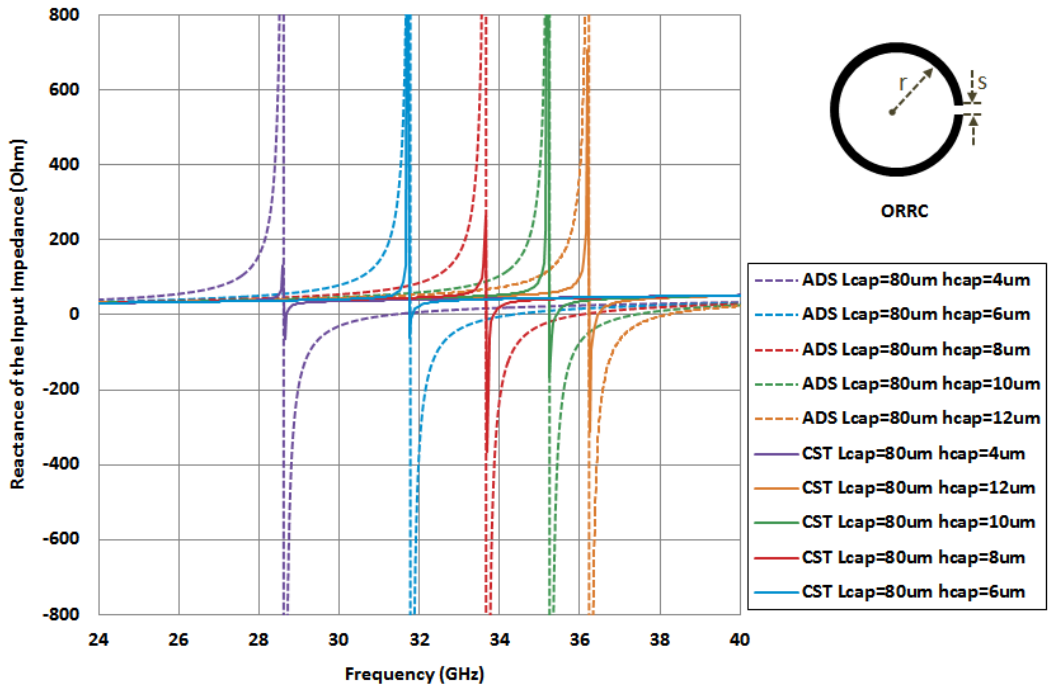

Figure 4.12. Comparison between full-wave CST and ADS simulations of the calculated circuit elements for the ORRC for different cantilever heights at the cantilever length of 80 μm.

TABLE 4-2

Analytical Solutions of Circuit Model of the ORRC

hcap (μm)	Lcap (μm)	C_2 (fF)	L_2 (nH)
14	20	2.54	5.70
14	40	4.38	3.47
14	60	6.36	2.52
14	80	8.33	2.03
12	80	9.50	1.83
10	80	11.15	1.63
8	80	13.98	1.40
6	80	17.85	1.21
4	80	25.74	1.01

4.3. Circuit Extraction of Double Split Rings Loaded with Cantilevers

4.3.1. Mode Analysis

Similar to Section II, the circuit extraction of a DSRRC (Figure 4.1d) starts with the analysis of a DCRR (Figure 4.1c). All simulation setups remain the same as described in Section 4.2. The impedance response of the DCRR follows the same pattern observed with the CRR with the exception of a frequency shift. Therefore, the same circuit topology and solving procedure in Section 4.2.2b can be applied to the DCRR. Figure 4.13 illustrates the behavior of the DCRR with the results from CST and ADS simulations. The resonant frequency observed at 86 GHz in Figure 4.7 is shifted to 54.7 GHz in Figure 4.13. Note that the inner ring of the DCRR has the same dimensions as the CRR, and the outer ring is slightly larger (Figure 4.1, Table 4-1). ADS results in Figure 4.13 are simulated utilizing the L_1 and C_1 solutions for the DCRR (0.5 nH and 12.2 fF in the same circuit as Figure 4.6). The E-field distribution at 54.7 GHz of the DCRR (also in Figure 4.13) shows that the two rings have the same mode pattern as that observed at the fundamental mode of the ORR. At the resonant frequency, the two rings are in phase and the effective current path is longer, shifting the resonant frequency down.

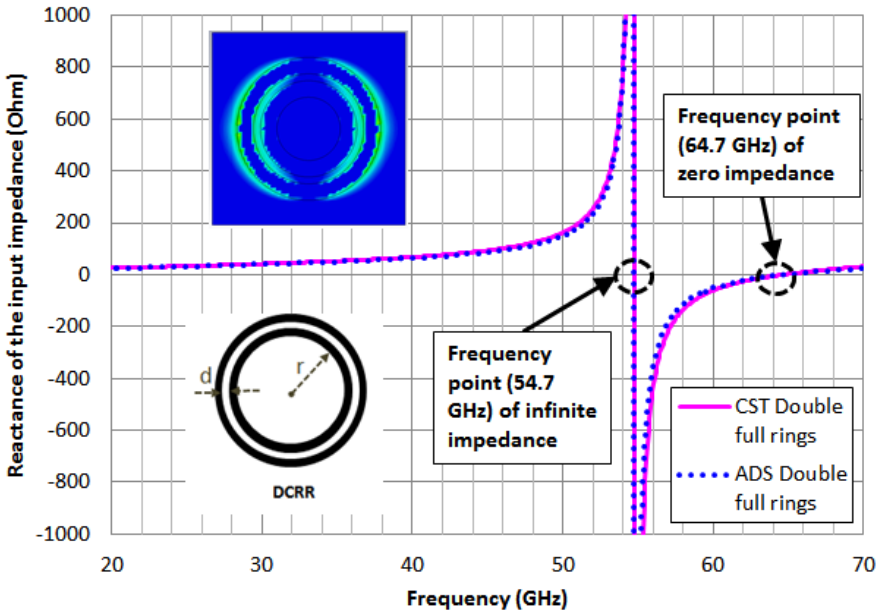

Figure 4.13. Reactance of the DCRR and the electric field distribution at the lowest resonant frequency (54.7 GHz).

On the other hand, the input impedance of the DSRRC deviated significantly from that of the ORRC topology, featuring two shifting modes (instead of one in the ORRC) below the non-shifting mode, which identifies with the fundamental mode of the DCRR. Figure 4.14 shows the CST results of the DSRRC for different cantilever positions (h_{cap} of 6, 10, and 14 μm). Note that the same cantilever setting is applied to both inner and outer rings of the DSRRC. It can be observed that the two lowest modes (at 20 – 25 GHz and 35 – 40 GHz) are shifting as a result of the variation of the split-gap capacitance due to different h_{cap} values. Meanwhile, the third mode around 58 GHz is the same for all three curves. The outer ring with an integrated cantilever (L_{cap} = 80 μm and h_{cap} = 14 μm) at the split gap is individually simulated by itself and presented in Figure 4.14. It can be seen that the mode around 35 GHz is in a similar frequency band with the first mode of

the ORRC shown in Figure 4.4, while the mode around 20 GHz is close to the first mode of the outer ORRC. The observation suggests that the first mode of the DSRRC is mostly due to the outer ring and the second mode is mostly due to the inner ring. However, for the same cantilever setting (L_{cap} = 80 μm, h_{cap} = 14 μm), the resonant frequencies of the first and second modes of the DSRRC are 23 GHz and 40 GHz respectively (Figure 4.14), while the first resonant frequencies of the ORRC with the outer ring radius and the ORRC with the inner ring radius are 24 GHz and 37 GHz respectively (Figure 4.14 and Figure 4.11). The shifts of 1 GHz and 3 GHz between the modes of the DSRRC and their corresponding ORRC are due to the coupling between the individual split rings in the DSRRC. The E-field distributions of those modes also support this observation. Furthermore, the mode pattern of the non-shifting mode (at 56.5 GHz) is the same as the one of the non-shifting mode at the resonant frequency of the ORR.

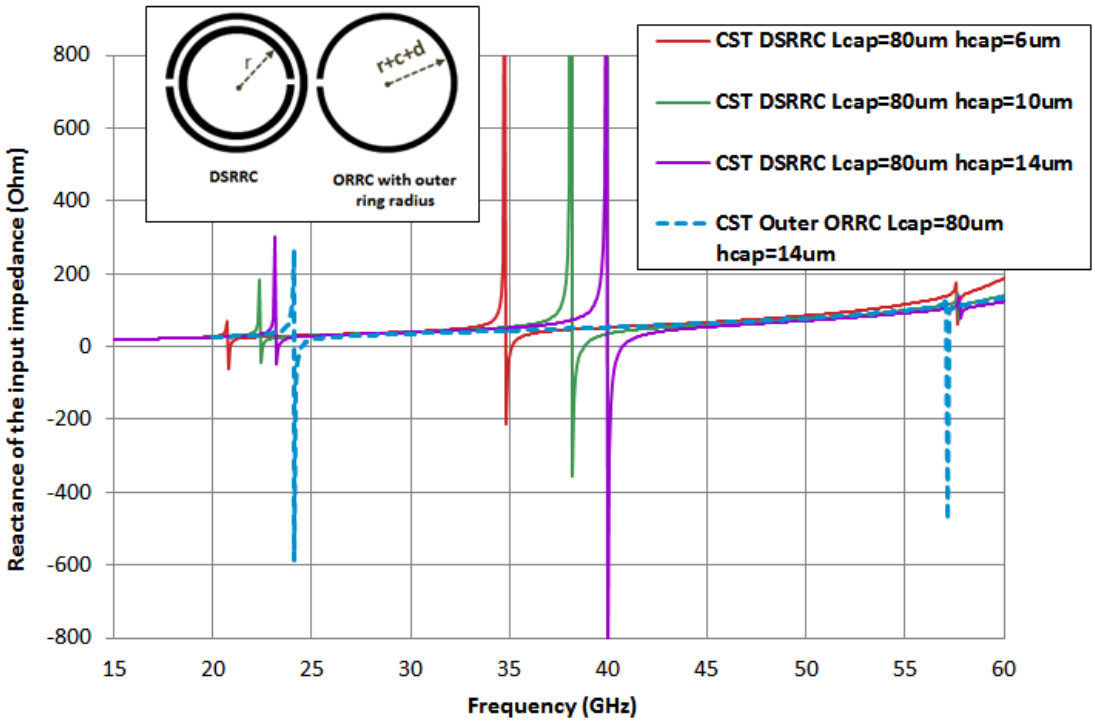

Figure 4.14. Reactance of the DSRRC for selective cantilever settings and the ORRC having dimensions of the outer ring of the DSRRC.

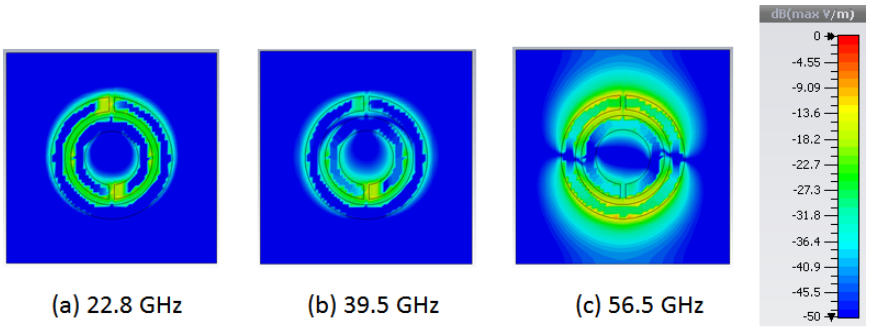

Figure 4.15. E-field distributions at the reference plane for DSRRC with hcap of 14 µm and Lcap of 80 µm.

4.3.2. Split Ring loaded with Discrete Capacitors and Circuit Extraction for the DSRRC

As a result of the accurate performance of the previously developed equivalent circuit, the cantilevers can be replaced by lumped capacitors *Ci* and *Co* on the inner and outer ring, respectively (Figure 4.16). Various *Ci* and *Co* values are simulated and shown in Figs. 4.17 – 4.18. When *Co* is constant, the frequency shift occurs at the second mode for different *Ci* values (Figure 4.17), while the reverse is observed when *Ci* is fixed and *Co* varies (Figure 4.18). Such observation is consistent with the suggested correspondence between the two modes of the DSRRC and those of its individual resonators as discussed in Section 4.2.1. Furthermore, the shift of the second resonant frequency is larger as *Ci* varies (comparison of the frequency shifts between Figure 4.17 and 4.18). This is because the second mode is mostly influenced by the inner ring capacitor (Figure 4.15b) and its effective capacitance comes mostly from the split gap of the inner ring. In the first mode (Figure 4.15a), the uniform E-field distributed across the ring separation (quasi-static) and the equal field intensity of the two split gaps indicate that this mode depends relatively uniformly on the capacitance of both the split gaps and also the ring separation.

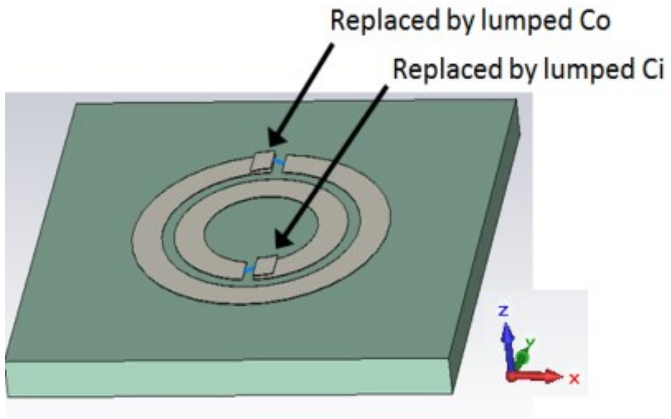

Figure 4.16. Construction of the DSRRC and the replacement of the cantilevers by the lumped capacitors in CST simulations.

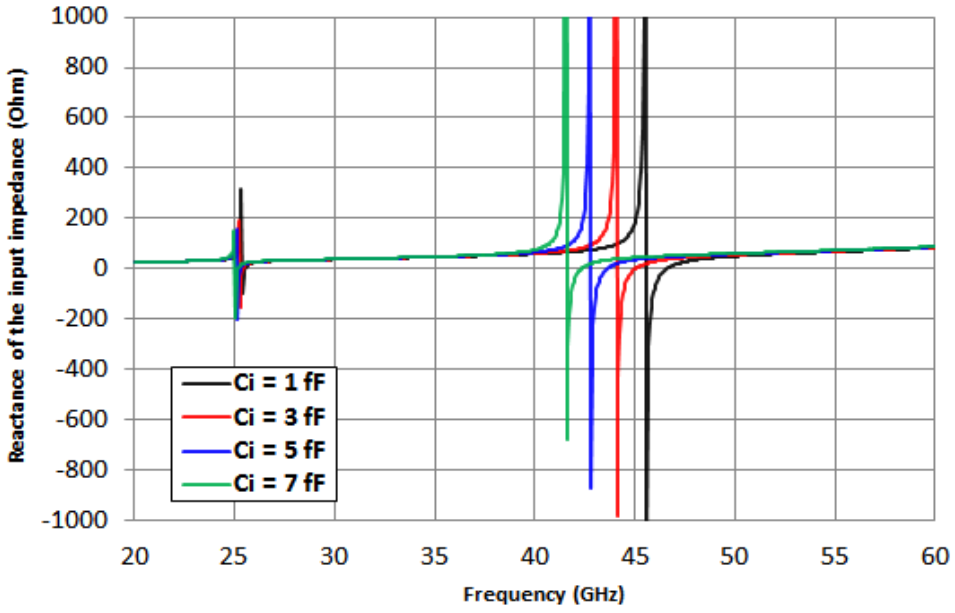

Figure 4.17. Reactance of the input impedance of the double split rings loaded with lumped capacitors Co = 1 fF and various Ci values.

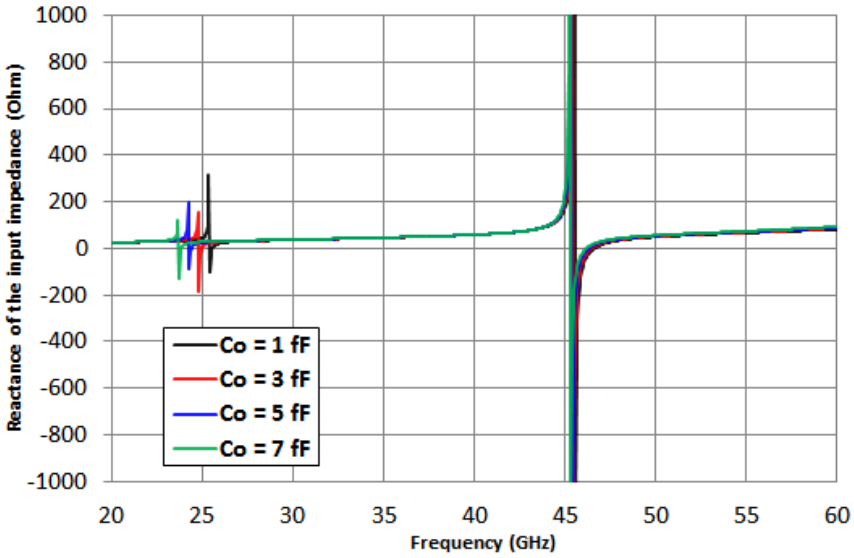

Figure 4.18. Reactance of the double split rings loaded with lumped capacitors Ci = 1 fF and various Co values.

Since the 3 first resonant modes of DSRRC are orthogonal, 2 more sets of series *L*-*C* components are added to the ADS circuit solution presented in the Section 4.3.1 to model the two associated shifting resonant frequencies of the DSRRCs (Figure 4.19). Because the loaded cantilevers of the DSRRC as presented in Chapter 3 were constructed identically (with the same dimensions) and the same variations (in terms of their lengths and heights) were applied to both, i.e. *Ci* and *Co* are set to be the same, denoted as C_L. In practice, it means that the outer and inner cantilevers are assumed to have the same initial conditions and they undergo the same thermal mechanical responses. Note that all capacitance of each individual ring is accounted for in the circuit solely by the split gap, e.g. the parallel plate capacitance of the cantilever. The relevance of this simplification was validated in Section 4.2 (Figure 4.9) within the scope of the circuit model. Hence, similar to (4.2) the input admittance for the DSRRC can be written as in (4.5) with the L_1

and C_1 values calculated previously in Section 4.3.1. The pair L_2-C_2 models the second mode around 30 – 40 GHz (denoted as f_{res2}), while the pair L_3-C_3 models the first mode around 20 – 25 GHz (denoted as f_{res3}). Equivalently, C_2 and C_3 represent *Ci* and *Co*, respectively, and both are also denoted as C_L in the circuit model. Proceeding with the method presented in Section 4.2, 15 different values of C_L in the range 0.2 – 40 fF are simulated in CST. The variation of the lumped capacitor values is plotted versus f_{res2} and f_{res3} in Figure 4.20, where the parallel plate capacitance of the cantilevers is also plotted. The lumped capacitance and the parallel plate capacitance values are in good agreement. This graph contains values of C_L corresponding to two resonant frequencies (f_{res2} and f_{res3}). Therefore, a multivariable 4th order polynomial was found in (4.6) to describe C_L as a function of f_{res2} and f_{res3}, with coefficients solved for by the linear regression method in MathCad (reported in Table 4-3). This formula allows easy calculations of the C_2 values after locating the resonant frequencies f_{res2} and f_{res3} of the DSRRC from CST simulations. The values of C_L, (e.g. C_2 or C_3), are also plotted in Figure 4.20 displaying close patterns to the parallel plate capacitance and the lumped capacitors. For each CST simulation of DSRRC with the calculated C_L value, L_2 and L_3 can be solved simultaneously with the following conditions $1/Z_{in}(L_2, C_L, f_{res2}) = 0$ and $1/Z_{in}(L_3, C_L, f_{res3}) = 0$ utilizing the non-linear Levenberg Marquardt method in MathCad in a way similar to the ORRC calculations discussed in Section 4.2. Figure 4.21 – 4.22 show the CST and ADS simulation results for different cantilever positions, i.e., h_{cap} values of 4, 6, 8, 10, 12, and 14 μm and for four different L_{cap} values of 20, 40, 60, and 80 μm (corresponding to Figure 4.11 – 4.12). The equivalent circuit elements' solutions (reported in Table 4-4) appear to model accurately the resonant frequency and their shifts (again within 1% of

error) corresponding to various cantilever conditions when compared with the full-wave electromagnetic simulations. Figure 4.23 shows the calculated values for L_2 and L_3 versus f_{res2} and f_{res3} and the circuit extraction method is summarized in a diagram shown in Figure 4.24.

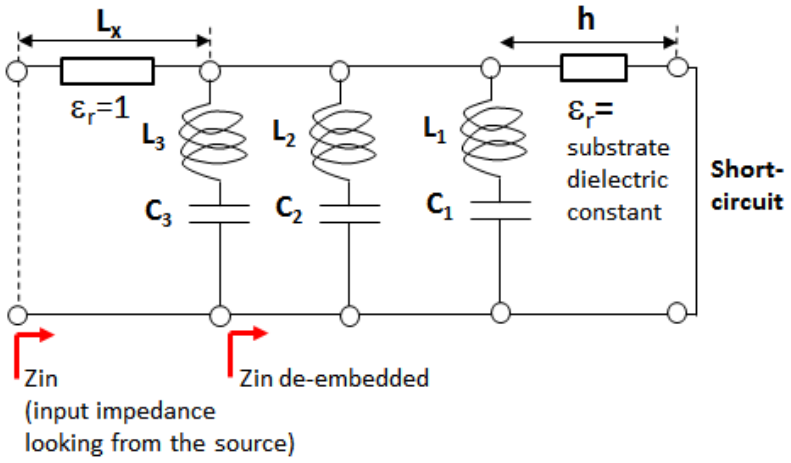

Figure 4.19. Circuit topology of the DSRRC.

$$Y_{in}(L_2, C_2, \omega) = \left(\frac{1}{jC_L\omega} + jL_3\omega\right)^{-1} + \left(\frac{1}{jC_L\omega} + jL_2\omega\right)^{-1}$$

$$+ \left(\frac{1}{jC_1\omega} + jL_1\omega\right)^{-1} - jY_0\sqrt{\varepsilon_r}cot\left(\frac{\omega}{c}\sqrt{\varepsilon_r}h\right) \qquad (4.5)$$

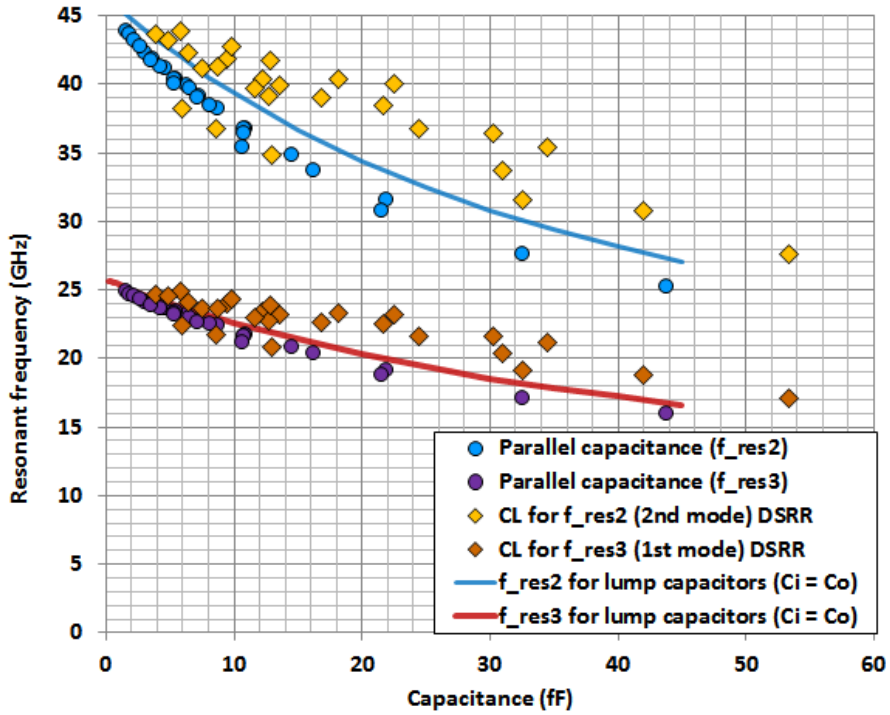

Figure 4.20. Resonant mode frequencies for capacitance values corresponding to the first and second resonant modes of the DSRRC.

$$C_L(f_{res2}, f_{res3}) = \sum_{i=1}^{15}\left(c_i \times {f_{res2}}^{k_{1i}} \times {f_{res3}}^{k_{2i}}\right) \quad (4.6)$$

TABLE 4-3

Coefficients of the Polynomial of C_L

Index i	Term order k_1	Term order k_2	Coefficient c
1	1	3	2.46E+02
2	0	4	-1.35E+02
3	0	3	2.64E+03
4	0	2	-1.83E+04
5	1	2	-3.67E+03
6	2	2	-1.68E+02
7	0	1	5.43E+04
8	1	1	1.71E+04
9	2	1	1.69E+03
10	3	1	5.07E+01
11	0	0	-5.81E+04
12	1	0	-2.55E+04
13	2	0	-3.97E+03
14	3	0	-2.59E+02
15	4	0	-5.72E+00

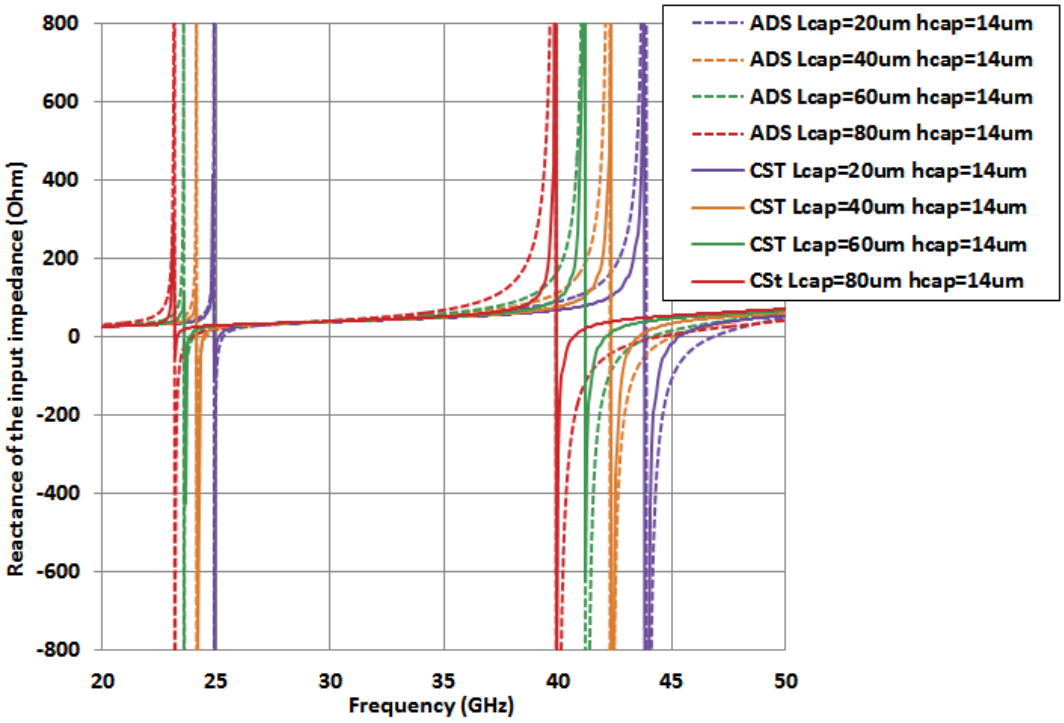

Figure 4.21. Comparison between full-wave CST simulations and equivalent-circuit ADS simulations of the calculated circuit elements for the DSRRC for different cantilever lengths at the cantilever height of 14 μm for both the inner and outer rings.

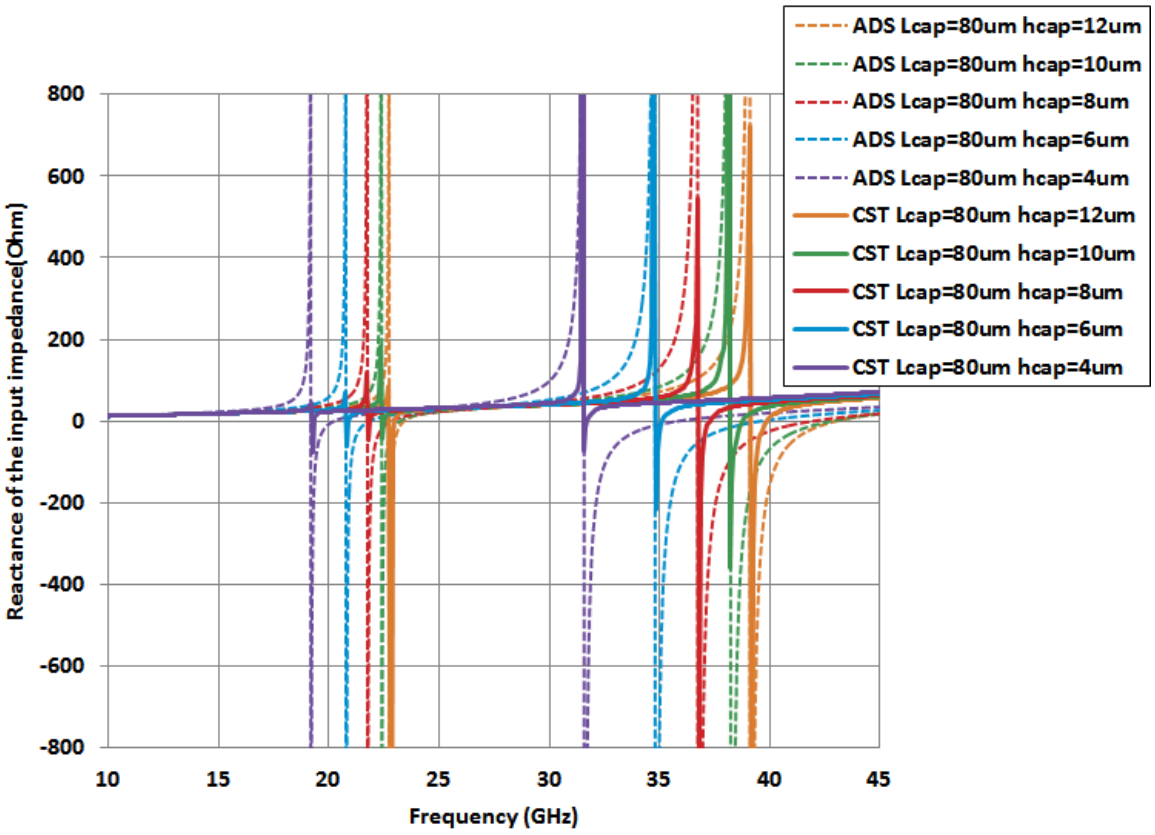

Figure 4.22. Comparison between full-wave CST simulations and equivalent-circuit ADS simulations of the calculated circuit elements for the DSRRC for different cantilever heights at the cantilever length of 80 μm for both the inner and outer rings.

TABLE 4-4

The Analytical Solutions for the Circuit Model of the DSRRC

hcap (μm)	Lcap (μm)	C_L (fF)	L_2 (nH)	L_3 (nH)
14	20	5.78	2.00	6.84
14	40	6.44	1.94	6.53
14	60	7.54	1.73	5.82
14	80	13.51	0.95	3.27
12	80	12.73	1.08	3.63
10	80	16.40	0.84	2.86
8	80	21.67	0.66	2.25
6	80	24.42	0.66	2.18
4	80	30.95	0.64	2.00

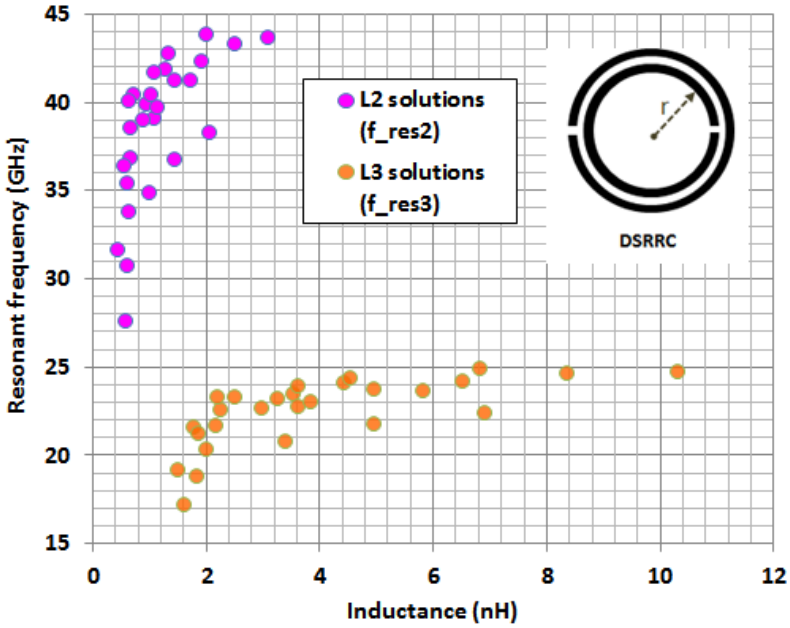

Figure 4.23. Inductance solutions L2 and L3 corresponding with fres2 and fres3 respectively of the DSRRC.

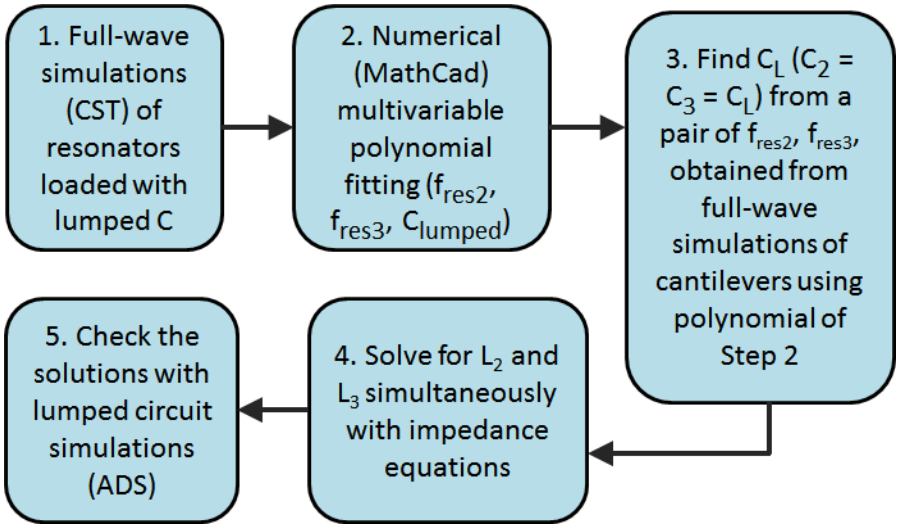

Figure 4.24. Summary of the circuit extraction for the DSRRC.

4.4. Discussions

As shown in previous sections, the proposed equivalent circuits simplified the representation of each resonant mode of the split ring resonator configurations into a series topology of a single lumped inductor and a single lumped capacitor with the capacitor only accounting for the "dominant" split gap capacitance, especially with respect to the accurate calculation of the resonant frequency shifts, which is the most critical factor for the accurate utilization of these structures as wireless sensors. In general, a particular resonant frequency of any resonator can be represented by $\left(1/\sqrt{LC}\right)$, where L and C represent all the effective capacitance and inductance appearing in the resonator. Therefore, with the L's and C's found in the equivalent circuits here, the resonant frequencies are expected to be linearly proportional to the factor $\left(1/\sqrt{LC}\right)$, as it can be clearly seen in Figure 4.25 for an ORRC structure (based on Figs. 4.9 – 4.10). The line is not perfectly linear but slightly curved due to the presence of the short

transmission line representing the substrate used in the model as reflected by the last term in (4.1), (4.2) and (4.4). Since beside the gap capacitance, there exist other capacitance sources, such as surface and stray capacitance (capacitance generated by charges separated at the surface of the same conductor and fringe capacitance generated by charges appear on different conductors), the values of the lumped inductor L_2 effectively account for these capacitance sources [4.9, 4.18]. Figure 4.26 shows the values of L_2 of the ORRC versus the effective wavelength, which is approximated for ε_{eff} of 4.82 (dielectric constant of glass) as in Section 4.2.1. Apparently, this inductance variation (inversely proportional to the effective wavelength) does not directly correspond to the current path, which is proportional to the effective wavelength. As the gap capacitance increases, the resonant frequency decreases (Figure 4.9) with a rather non-linear distribution of the current due to the strong non-uniform perturbation of the loaded cantilever on the E-field. Furthermore, the physical inductance of the ORRC can be approximated with expression (4.7) (applied to low frequency range) [4.18], where l is the physical length of the split ring and other parameters as indicated in Table 4-1. For the designed ORRC in Section 4.2, expression (4.7) gives a value of 5.5 nH, which is the same with the L_2 value at the high frequency limit (Figure 4.10). At low frequencies, the mutual inductance between the currents on the ring and the currents on the ground plane increases. As a result, the self-inductance of the ring is reduced, which also partly contributes to the variation of L_2 observed in Figure 4.26. The inductance variations of the DSRRC in Figure 4.23 have a similar profile with Figure 4.10 although it features a higher dispersion and a lower coherence due to the fact that the element values were

calculated based on the polynomial found in (4.6), where multivariable approximation is less accurate than the single variable one.

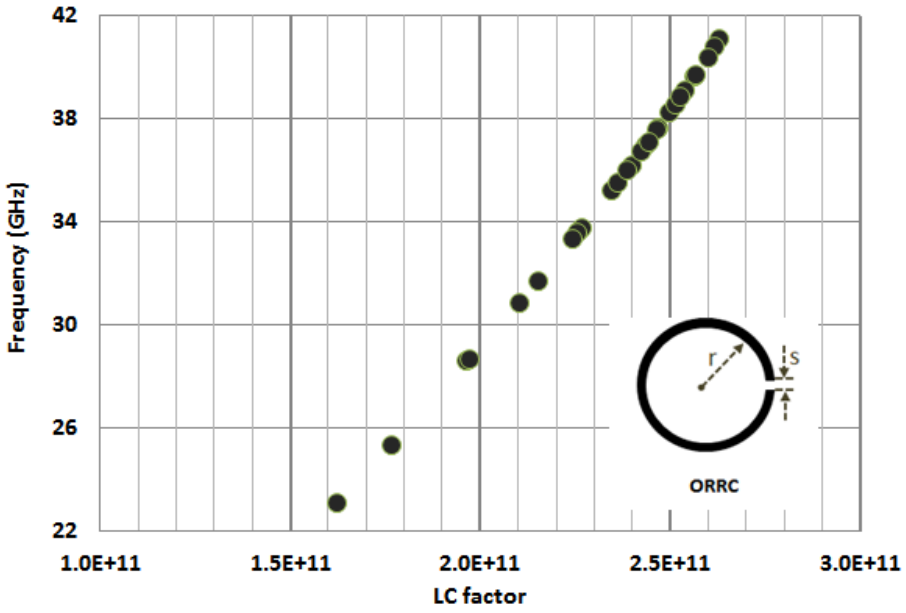

Figure 4.25. Dependence of the resonant frequency on (1/√LC) factor.

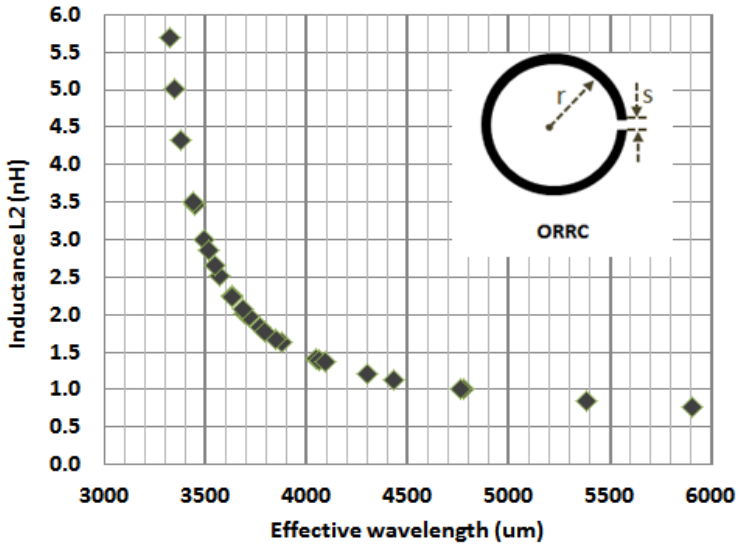

Figure 4.26. Variation of the equivalent circuit inductance L2 as a function of the effective wavelength at the resonant frequencies of the ORRC.

$$L_{eff} \approx \frac{\mu_o}{2\pi} l \left[ln\left(\frac{2h}{c+t}\right) + \frac{3}{2}\right] \quad (4.7)$$

It has to be stressed that the proposed circuits include a short transmission line to account for the effect of the substrate region represented by the last term in (4.1), (4.2), and (4.5). A plot of the reactance of the input impedance of this term is shown in Figure 4.27, where Z_{sub} is the inverse of the transmission line term. The highly linear (relatively constant slope) and positive impedance response in Figure 4.27 suggests that the transmission line element can be replaced with a lumped inductance element that can be calculated from the slope of the curve (equivalent to $2\pi L$). Therefore, over the operating bandwidth of 28 – 88 GHz of the circuit for the ORRC, the inductance value can be approximated by 0.25 nH.

Although the CST simulated geometries of the split ring resonators are completely Ohmic-lossless (conductors are modeled by PEC and dielectric by lossless glass), in practice the resonators carry Ohmic losses in both conductive and dielectric parts. To account for those losses, a resistance in series can be added to each *LC* set modeling each individual mode. Note that in a RLC resonant circuit, the resonant frequency is independent of the resistance and determined by the factor of $\left(1/\sqrt{LC}\right)$. Furthermore, the circuit extraction proposed here is based entirely on the reactance and neglects the resistance of the input impedance. Therefore, it is possible to obtain the equivalent circuits based on lossless assumptions (following the proposed circuit extraction method), then add the series resistance afterwards based on the resistance response of the input impedance. Further investigation of the additional resistance is not within the scope of this work, where the main objective is limited to modeling the

resonant frequencies that are the most important parameters for sensor-related applications. Accounting for the loss effects in the straightforward extracted equivalent circuit that was introduced from the CRR to the ORRC (Figure 4.1a – 4.1b respectively) extended to the DCRR and DSRRC (Figure 4.1c – 4.1d respectively) as illustrated in Section 4.2 – 4.3, the proposed step-by-step procedure using the circuit topology here can be applied to model resonators of multiple closed rings and split rings loaded with arbitrary lumped devices such as resistors, thermistors, or RF switches [4.19] based on their surface impedance.

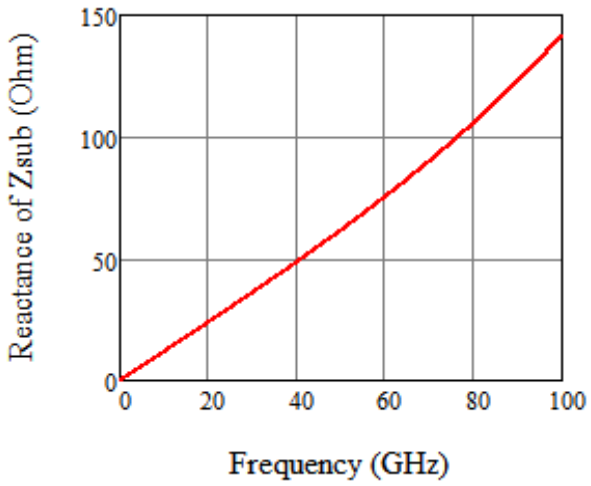

Figure 4.27. Equivalent reactance of the input impedance Zsub of the short-circuited transmission line included in the proposed circuit topology.

4.5. Conclusions

A new equivalent circuit extraction method was introduced and applied successfully to a single closed ring, double closed rings, a single split ring and double split rings both loaded with cantilevers. A thorough study and mode analysis of their

resonant behaviors were also presented. The extracted circuits are composed only of lumped elements of inductors and capacitors except from a short-circuited transmission line representing the wave propagation in the substrate, all derived using a systematic procedure. The circuits are simple utilizing only a series combination of one inductor and one capacitor for each individual resonant mode of the resonators. Although not all lumped elements carry a clear physical significance, the circuits accurately model the resonant frequency shifts corresponding to the loaded capacitance by the cantilevers. Such frequency shifts are crucial to the RF sensor designed introduced in Chapter 3, where the models can be utilized to optimize the sensor design and accurately predict the sensing performance. As an example, the RF temperature sensor in Chapter 3 essentially utilized the change in the parallel plate capacitance of the bimorph cantilevers as it responds to the temperature change to induce measureable resonant frequency shifts. The circuit models here suggest that sensors for other parameters, such as humidity, gas, or temperature can be designed based on the same sensing principles proposed in Chapter 3. Specifically, the bimorph cantilevers can be replaced with fixed cantilevers sandwiching a substrate material whose dielectric constant changes with humidity or gas, or they can be replaced by temperature-dependent capacitive microfluidic channels that were developed in [4.20]. The resonant frequency shifts can be estimated from the change of the dielectric constant, consequently the capacitance of the gap, using the circuit models. The versatility of the extraction method allows circuits to be derived for wide frequency bands. For the cases reported in this chapter, resonant frequency shifts of up to 25 % of the operating frequency (~ 28 – 36 GHz) are accurately represented by the inductance and capacitance equivalent circuit found in the hereby introduced systematic and

straightforward extraction method. The derived equivalent circuits also showed the capability to model up to 3 resonant modes of the split rings covering a wideband from about 20 GHz to 90 GHz. Potentially, the proposed approach can be extended to model many more resonant modes beyond the scope of this thesis. The fitting polynomials provided in this work can assist in various designs of split rings topologies with similar dimensions operating in the same frequency range. The simple topology of the proposed circuits modeling the split ring sensors allows easy integration of the models into larger systems, such as radars or RFID systems having different circuit blocks, remaining valid even for loaded double (or multiple) split rings with resistors, thermistors and RF-MEM switches [4.19].

4.6. References

[4.1] J. B. Pendry, A. J. Holden, D. J. Ribbins, W. J. Stewart, "Magnetism from conductors and enhanced nonlinear phenomena," *IEEE Trans. Microwave Theory Tech*., vol. 47, pp. 2075 – 2084, Nov. 1999.

[4.2] D. Smith, W. J. Padilla, D. C. Vier, S. C. Nemat-Nasser, S. Schultz, "Composite Medium with Simultaneously Negative Permeability and Permittivity," *Phys. Rev. Lett.*, vol. 84, no. 18, pp. 4184 – 4187, May 2000.

[4.3] R. Marques, F. Mesa, J. Martel, F. Medina, "Comparative analysis of edge- and broadside-coupled split ring resonators for metamaterial design- theory and experiments," *IEEE Trans. Antennas and Propagation*, vol. 51, no. 10, pp. 2572 – 2581, Oct. 2003.

[4.4] N. Katsarakis, T. Koschnu, M. Kafesaki, E. N. Economou, C. M. Soukoulis, "Electric coupling to the magnetic resonance of split ring resonators," *Appl. Phys. Lett.*, vol. 84, no. 15, pp. 2943 – 2945, April 2004.

[4.5] B. Sauviac, C. R. Simovski, S. A. Tretyakov, "Double Split-Ring Resonators: Analytical Modeling and Numerical Simulations," *Electromagnetics*, vol. 24, no. 5, pp. 317 – 338, 2004.

[4.6] J. Garcia-Garcia, F. Martin, J. D. Baena, R. Marques, L. Jelinek, "On the resonances and polarizabilities of split ring resonators," *J. Appl. Phys*, vol. 98, no. 3, pp. 033103/9, 2005.

[4.7] J. D. Baena, L. Jelinek, R. Marques, M. Silveirinha, "Unified homogenization theory for magnetoinductive and electromagnetic waves in split-ring metamaterials," *Phys. Rev. A,* vol. 78, no. 1, pp. 013842/5, 2008.

[4.8] O. Sydoruk, E. Tatartschuk, E, Shamonina, L. Solymar, "Analytical formulation for the resonant frequency of split rings," *J. Appl. Phys*., vol. 105, pp. 014903/4, 2009.

[4.9] A. Elhawil, J. Stiens, C. De Tandt, W. Ranson, R. Vounckx, "An Equivalent Circuit Model of Single Circular Open-Ring Resonators," *IEEE J. Selected Topics Quantum Elec*., vol. 16, no. 2, pp. 380 – 385, Mar-April 2010.

[4.10] M. F. Wu, F. Y. Meng, Q. Wu, "A compact equivalent circuit model for the SRR structure in metamaterials," in *Asia-Pacific Conference Proceedings*, vol. 1, no. 4, pp. 4 – 7, Dec. 2005.

[4.11] M. Shamonin, E. Shamonin, V. Kalinin, L. Solymar, "Properties of a metamaterial element: analytical solutions and numerical simulations for a singly split double ring," *J. Appl. Phys*., vol. 95, no. 7, pp. 3778 – 3784, 2004.

[4.12] M. Shamonin, E. Shamonina, V. Kalinin, L. Solymar, "Resonant frequencies of a split-ring resonator: Analytical solutions and numerical simulations," *Microwave Opt. Tech. Lett*, vol. 44, no. 2, pp. 133 – 136, 2005.

[4.13] F. Aznar, M. Gil, J. Bonache, L. Jelinek, J. D. Baena, R. Marques, F. Martin, "Characterization of miniaturized metamaterial resonators coupled transmission lines through parameter extraction," *J. Appl. Phys*., vol. 104, no. 11, pp. 114501/8, 2008.

[4.14] 3D Electromagnetic Simulation Software CST (2013). [Online] Available: http://www.cst.com/ (Accessed: June 2013).

[4.15] D. Pozar, *Microwave Engineering*, 3rd ed., New York, NY, John Wiley & Sons, 2005.

[4.16] Mathematical numerical simulation software MathCad 15. [Online] Available: http://www.ptc.com/products/mathcad/ (Accessed: June 2013).

[4.17] L.-H. Hsieh, K. Chang, "Equivalent Lumped Elements G, L, C, and Unloaded Q's of Closed- and Open-Loop Ring Resonators," *IEEE Trans. Micro.Theo. Tech*., vol. 50, no. 2, pp. 453 – 460, Feb. 2002.

[4.18] F. Leferink, "Inductance Calculations: Methods and Equations," in *IEEE Int. Symp. Electromagnetic Compatibility*, Atlanta, GA, Aug. 1995, pp. 16 –22.

[4.19] D. Dubuc, M. Saadaoui, S. Melle, F. Flourens, L. Rabbia, B. Ducarouge, K. Grenier, P. Pons, A. Boukabache, L. Bary, A. Takacs, H. Aubert, O. Vendier, J.L. Roux, R. Plana, "Smart MEMS concept for high secure RF and millimeterwave communications," *Microelectronics Reliability*, vol. 44, no. 6, pp. 899 – 907, June 2004.

[4.20] S. Bouaziz, F. Chebila, A. Traille, P. Pons, H. Aubert, M. Tentzeris, "A new millimeter-wave micro-fluidic temperature sensor for wireless passive radar interrogation," in *IEEE Sensors*, Taipei, Taiwan, Oct, 2012, pp. 1 – 4.

Chapter 5.

RF Strain Sensor

5.1. Introduction

A crucial factor in many industries ranging from civil infrastructure and mechanical equipment to aerospace and various medical applications is structural health. In measuring the structural health, strain sensing has been the key parameter to monitor civil structures and to address the safety assurance of roads, bridges, and building supports in order to avoid unexpected collapses [5.1]. Strain is a parameter that indicates a physical deformation and mechanical loading. In manufacturing processes and constructions, strain sensing allows the monitoring of vibration, excessive loading, and crack developments to be detected early [5.2 – 5.3]. In medical uses, strain sensing also include implantable sensors for bone, joint healing processes, and bone fracture monitoring [5.4 – 5.5]. In aerospace, strain is especially sensitive for operations of aircraft, including the conditions of wings and blades, and the fatigue of the aircraft body [5.6]. Therefore, strain sensing needs to be accurate, quick, and efficient to allow long term monitoring with little maintenance for public safety and economic and industrial prosperity. However, uses of sensors embedded in structures and machines remain limited.

Strain sensors have been widely developed utilizing different techniques; the most common types are resistive and capacitive gage. Because those sensors typically require wiring and/or complex circuits that expose them to higher chance of failure [5.7], which is highly undesirable, especially for the implementation on aircraft wings or helicopter

blades. Besides those wired sensors, some wireless sensors have been reported [5.8 – 5.9]. They usually include an embedded microprocessor and a radio frequency (RF) module, which is integrated with the transducer. Such a circuit requires battery power (or equivalently harvesting energy module) to operate, has a limited lifetime, and requires more frequent maintenance and replacement. Thus, they are unsuitable for long term monitoring and harsh environment applications such as aircraft engines. Other sensing techniques based on optical fibers are compact, lightweight, and capable to be sensed remotely, but expensive and cannot enable remote long range interrogation [5.6, 5.10]. Therefore, wireless passive strain sensors that can address the aforementioned problems are highly desirable.

The existing designs of remote sensing chipless strain gauges have been limited. In the past, rectangular and circular patch antennas have been utilized as RF strain transducers that operate based on resonant frequency shifts corresponding to the strain-induced dimensional changes of the antennas [5.11 – 5.13]. Other reported designs were metamaterial-based structures that constitute resonant scatterers whose resonant frequencies are also directly dependent on the strain-induced changes in dimensions [5.14 – 5.16]. Although those developments showed the feasibility for wireless and chipless strain sensors, they suffer low sensitivity in terms of resonant frequency shifts for a given strain. The designs in [5.14 – 5.15] are also easily influenced by different application surfaces and the interrogation is limited in range (less than 0.5 m). This chapter introduces a new RF strain transducer that is completely passive and chipless that can enable high sensitivity and long range interrogation. It is based on a patch antenna loaded with open loops integrated with cantilevers. The work in this chapter presents a design

concept that allows very small strain of any surface to be monitored remotely and operation in harsh environment of extremely high temperature. The design was developed from single dimensional sensing to multi-dimensional sensing. The following discussions and results are based on [5.17 – 5.20]. Section 5.2 discusses the designs and the principles of operation. Simulations and modeling are shown in Section 5.3 illustrating how the sensor designs were modeled with respect to the induced strain. Section 5.4 shows benchmarking prototypes and the strain measurements for single dimensional and multi-dimensional sensing. It is followed by Section 5.5, which illustrates an example of remote interrogation based on the FWCW radar platform as discussed in Section 2.3 of Chapter 2 and Section 3.5 of Chapter 3.

5.2. Designs and Principles of Operation

Strain is measured by the deformation of the material volume along the strain direction. It is denoted as $\boldsymbol{\varepsilon_L} = \Delta L/L$. The "zero-strain" length L_o in the stretched direction is deformed into L as in (5.1). Strain is unit-less, and usually measured in % (10^{-2}) or micro-strain (με) which is 10^{-6} of $\Delta L/L$. Therefore, any resonant structure attempting to transform this change directly into a detectable RF signal is inherently limited as the existing designs have shown [5.11 – 5.16]. To resolve this problem, the work in this chapter utilizes a cantilever implemented on each open loop loaded on a patch antenna instead of the patch itself solely as proposed in [5.11 – 5.12]. The patch can have one such loop or two loops positioned on its orthogonal sides.

$$L = (1 + \varepsilon_L)L_o \tag{5.1}$$

Single loop structure of the new RF strain sensor in 3D-view is shown in Figure 5.1, while the two dimensional (2D) sensing design with orthogonal loops is shown in Figure 5.2 with a top view (over the plane of the applied strain). In the 2D design, a rectangular patch is loaded with two stubs, each one located on the radiating edge of the corresponding resonant mode, i.e. two dominant orthogonal modes, induced by orthogonal excitations that apply to two different sides of the patch. Each stub in turn is connected to an open loop whose resonant frequency depends on the open gap capacitance. Specifically, an open loop is loaded along x in order to modify the dominant resonant mode that is induced by the x-polarization excitation. Similarly, another open loop is loaded along y in order to modify the dominant resonant mode that is induced by the y-polarization excitation. The lowest resonant frequency of the open loop, determined by the length of the loop and the gap capacitance, is designed to be close to the dominant resonant frequency of the patch along the x or y direction (Figure 5.2). As a result, for each orthogonal mode of the patch, the structure generates a dual frequency response in which the coupling between the corresponding loop and the patch is strongly influenced by the capacitance of the open ring. The coupling implies that the resonant peaks, especially the one influenced strongly by the open loop, are very sensitive to the capacitance value of the gap for each polarization mode. This is the first of the two operational principles of the new 2D RF strain sensor proposed in this work.

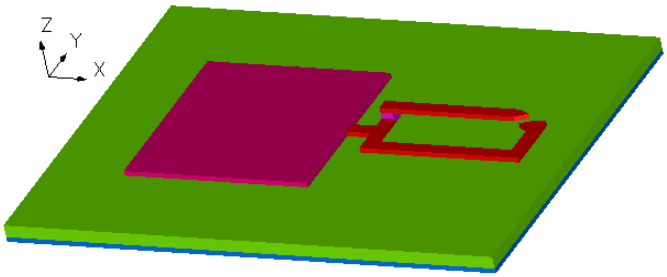

Figure 5.1. 3D-view of the single loop loaded patch RF strain transducer.

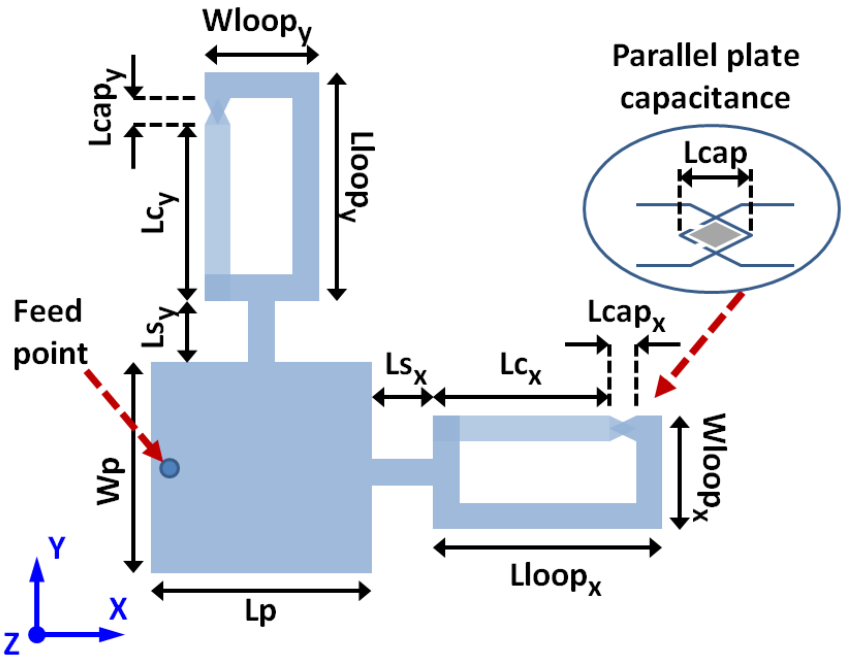

Figure 5.2. Top view of the new design of the RF strain sensor including the zoom-in view of the capacitance gap on the open ring.

Each cantilever is shorted electrically and fixed mechanically at one end of the corresponding open loop, while the free end of the cantilever and the other end of the open loop form a parallel plate capacitor. Thus, the split gap between the two ends of the traditional open ring (Figure 5.3a) is transformed into the separation gap of a parallel

plate capacitor (Figure 5.3b and Figure 5.4). The transformation from the configuration of Figure 5.3a into that of Figure 5.3b allows the capacitance to be tuned non-linearly with respect to the surface strain in the following mechanism. Suppose that a certain *k%* strain is induced on the substrate along the x-direction (Figure 5.4), L_{gap} is increased by ΔL_{gap}, which equals to $k\% \times L_{gap}$. Because the cantilever is fixed to the surface only at one end and the other end is free, its dimension remains unaffected by this strain, and thus, its length, L_c, is constant. Therefore, the entire length deformation ΔL_{gap} is transferred to the change in L_{cap} (Figure 5.4), which is independent from L_{gap}. Consequently, the capacitance is modified by $k\% \times L_{gap}$ instead of $k\% \times L_{cap}$, in which L_{gap} can be made significantly larger than L_{cap} as illustrated in Figure 5.2. The use of triangular tips at the loop gaps further increases the rate of change of the capacitance for a given rate of change of L_{cap} that is induced by a given strain.

(a) Traditional open loop (b) Modified open loop

Figure 5.3. Top view of the traditional and modified loops.

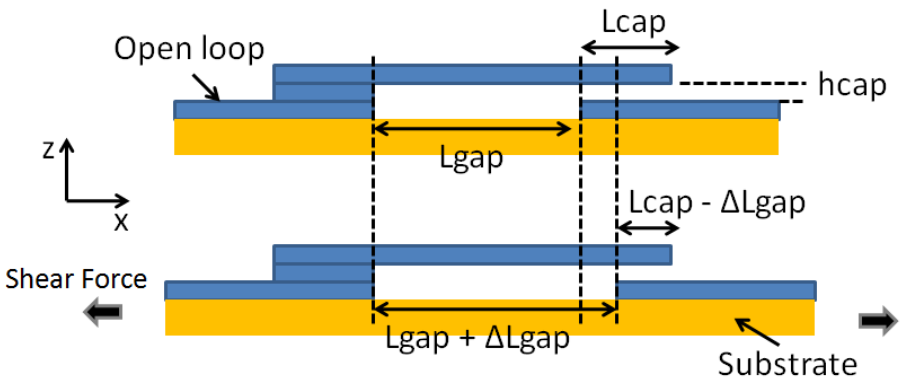

Figure 5.4. Cross section view of a cantilever integrated with an open loop loaded on a patch for the proposed RF strain sensor.

The two inherent independent polarizations of a patch resonator allow independent interrogation of strain in two orthogonal directions, and the strain sensing in one direction is not influenced by the strain in the other. This characteristic of the 2D strain sensor (Figure 5.2) is clarified in Section 5.3. This operating principle lays the foundation for strain sensing in arbitrary directions because of the shear force (applied on the material surface and responsible for the surface deformation) can be decomposed into two orthogonal components (Figure 5.5). This is the second of the two operational principles of the new 2D RF strain sensor proposed in this work.

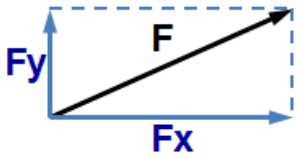

Figure 5.5. Illustration of a force in an arbitrary direction decomposed into orthogonal components.

5.3. Modeling and Simulations

5.3.1. Modeling

As a proof-of-concept, RF strain sensors utilizing one loop and two orthogonal loops were designed and simulated on a Kapton substrate of 100 μm in thickness with a dielectric constant of 3.4 (operating around 3 GHz). An increase of 1% is applied to the length of each parameter along the x-direction only, and RF responses for each polarization of the patch-based sensor were analyzed to show the capability of 2D sensing of the design concept. The applied strain in the x-direction increases the length of the parameters L_p, L_{sx}, and L_{loopx}. Note that L_{loopx} is increased by 1% while L_{cx} remains constant. Consequently, the dimension L_{capx} decreases by 1% of L_{loopx}. Additionally, the substrate under strain also experiences the Poisson effect, which essentially causes a contraction in the direction transverse to the applied strain. Thus, the dimension W_p effectively decreases. The Poisson effect is the ratio of this contraction to the orthogonal expansion caused by the applied strain. The Poisson effect can be calculated as shown in (5.2), in which w denotes the width of the dimension that is transverse to the strain direction, υ_p is Poisson's ratio of the Kapton, and ε_L is the applied strain. Other parameters along the x-direction, such as W_{loopy}, and those under the Poisson effect such as the thickness of the substrate and the width of the open loop, are negligible to the RF responses of the sensor; hence, they are not accounted for. This simplification is justified in the measurement results shown in Section 5.4. In addition, within a few percent (1% – 5%) of the loop width, W_{loop}, the resonant frequency of the open loop is found to be only negligibly influenced.

$$w = (1 + \nu_p \varepsilon_L) w_o \quad (5.2)$$

5.3.2. Analysis of the Open-Loop Cantilever Capacitance

Different L_{cx} values are simulated on the single-loop patch structure (Figure 5.1) to investigate the influence of the loop gap capacitance relative to the resonant frequencies of the loop-loaded patch. For simplicity and without loss of accuracy, the second loop, which is loaded along the y-direction, was not included in the investigation of the loop gap capacitance. In this study, the first operating principle of the RF strain sensor is analyzed with respect to only the x-polarization mode of the patch. It will be illustrated later that this approach is sufficient to address the frequency shifts that occur in the 2D structure in practical measurements (Figure 5.2). Only L_{cx} was varied in those simulations while keeping other values the same for each L_{cx} value, in both non-strain and strain-loading condition. Different L_{cx} values effectively yield different L_{capx} values as illustrated in Figure 5.6. Scattering parameter $|S_{11}|$ simulations results are presented in Figure 5.7 for L_{cx} = 9500 μm, 9750 μm, and 10000 μm. Each L_{cx} value with either zero or 1% strain condition is simulated based on the parameters provided in Table 5-1. Note that the gap between the two parallel surfaces, the lower face of the cantilever free end and the upper face of the open-ended loop, is set to 10 μm. This parameter is highly critical to the sensitivity of the strain transducer because it determines the initial gap capacitance as well as the value of L_{loopx}.

TABLE 5-1

Summary of Simulation Parameters

Dimensions (μm)	No strain	Strain 1%
L_p	26000	26260
W_p	25000	24925
L_{sx}	2000	2020
L_{loopx}	13000	13130
W_{loopx}	5000	5000
L_{sy}	2000	2000
L_{loopy}	13000	13000
W_{loopy}	5000	5000
c (width of stub and loop)	1000	1000
h_{sub} (substrate thickness)	100	100
h_{cap} (gap between the cantilever and loop)	10	10

It is observed from $|S_{11}|$ results in Figure 5.7 that each model has a dual frequency response with two resonant frequencies close to each other. The sensitivity of the RF transducer depends on the value of L_{cx}, which determines the initial capacitance and the rate of change of the capacitance as L_{capx} decreases. Here, the highest sensitivity that can be achieved is found with L_{cx} = 9750 μm, which induces a frequency shift of 125 MHz at 2.72 GHz, or 4.6% frequency shift per 1% strain. This sensitivity is more than 4 times the sensitivity achieved by the rectangular and circular patch antennas previously introduced in the literature, where the change in the dimensions of the patches gave a sensitivity of about 0.9 – 1.0% frequency shift per 1% strain [5.11 – 5.13]. It is observed that as the strain is applied, the resonant frequencies increases due to the resulting decrease in the overall capacitance. Such responses are consistent in all three simulated configurations

(Figure 5.7). Here, the strain is investigated up to 1% because it is the typical level of detection in industrial structures such as bridges and aircrafts. It should be noticed that each set of the curves (blue, black, and red) in Figure 5.7 reflects different L_{cx} values only, while within each set, the difference between the solid and dash line curves reflect the strain simulations in which L_{cx} is constant and the parameters L_p, W_p, L_{sx}, and L_{loopx} are changed according to Table 5-1. It can be observed that the resonator has the largest response for the changes in the set of parameters $\{L_p, W_p, L_{sx}, L_{loopx}\}$ when L_{cx} is around 9750 μm, and this response is altered not in a monotonic way for other values of L_{cx}. This indicates that the two resonant frequencies are responsible by the two impedances coupled through the short stub (L_s), one from the loop and another from the patch, generating a non-linear response as the capacitance of the loop impedance changes.

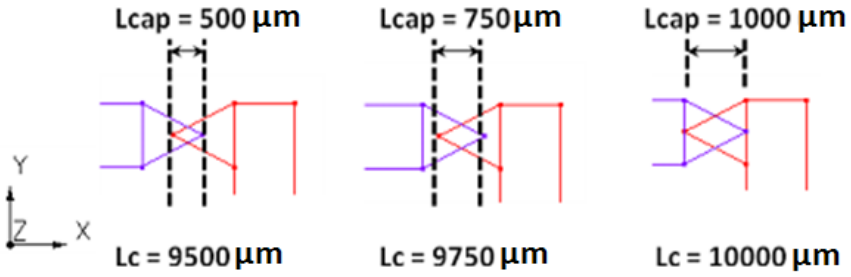

Figure 5.6. Different configurations of the tip capacitance corresponding to different L_c values.

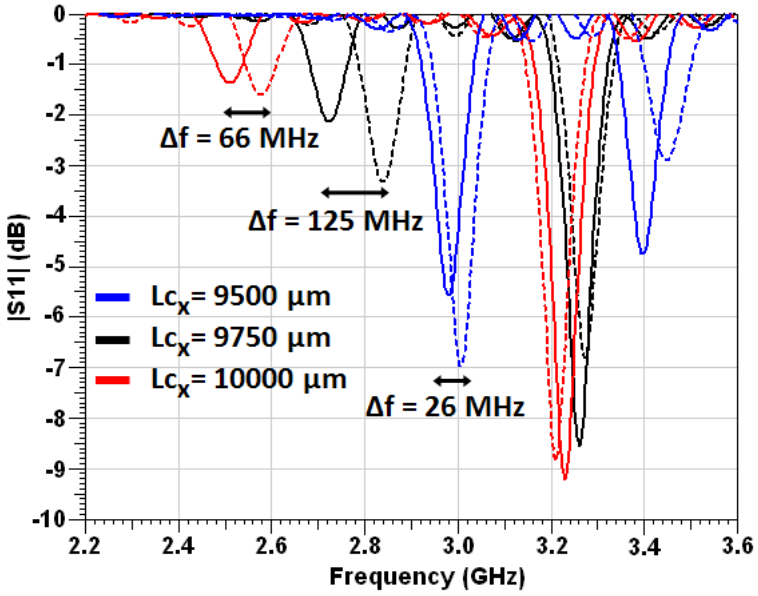

Figure 5.7. Different configurations of the tip capacitance as different L_c values are implemented. The solid lines represent non-strain conditions, and the slash lines represent 1% strain conditions.

In this design, the loop can be considered to be a modified stub that acts as a load of the patch. Based on the stub loading technique, tunable dual and triple resonant frequency patch antennas have been achieved [5.21– 5.22]. The design of the loop here is an effective method to maximize the capacitive change of the load, i.e the open loop, in response to the applied strain. Figures 5.8 and 5.9 show the surface current distributions of the single loop design (as in Figure 5.1) with parameter L_{cx} of 9750 µm for the case of zero strain and 1% strain respectively (the black curves in Figure 5.7). Note that the standing waves that are generated in the loop influence the fundamental mode of the patch, which causes the frequency shift. The patch-loop structure can be considered to have two centers of resonant or standing wave regions, but the patch is still the

effectively dominant radiator from which most radiation occurs. Since $|S_{11}|$ can be written as $|Z_{loop} - Z_{patch}| / |Z_{loop} + Z_{patch}|$, where Z_{loop} and Z_{patch} denote the impedance of the loop and the patch respectively, the rate of change of $|S_{11}|$ with respect to $|Z_{loop}|$, which contains a term of L_{capx}, is observed to be at least a second order dependence. Therefore, such rate of change would have at least a local maximum that is reflected in the non-monotonic sensitivity of different L_{cx} curves. On the other hand, $|S_{11}|$ levels in Figure 5.7 appear to be high indicating an impedance mismatch. Furthermore, from Figure 5.7 the reflection level is observed to be compromised by the sensor sensitivity. For example, the lower resonant frequency of the blue curves (L_{cx} = 9500 μm) has lower $|S_{11}|$ than that of the other curves, but the sensitivity in terms of frequency shift per 1% strain (26 MHz) is lower than others, which yield frequency shifts of 66 MHz and 125 MHz. To reduce the mismatch, additional matching elements can be added. However, to maintain the sensitivity at the same time would require further investigation and optimization of the design. The scope of this thesis was limited to demonstrate the newly proposed principle of the cantilever integrated with a loop and a patch that can significantly improve the frequency shift with respect to the applied strain.

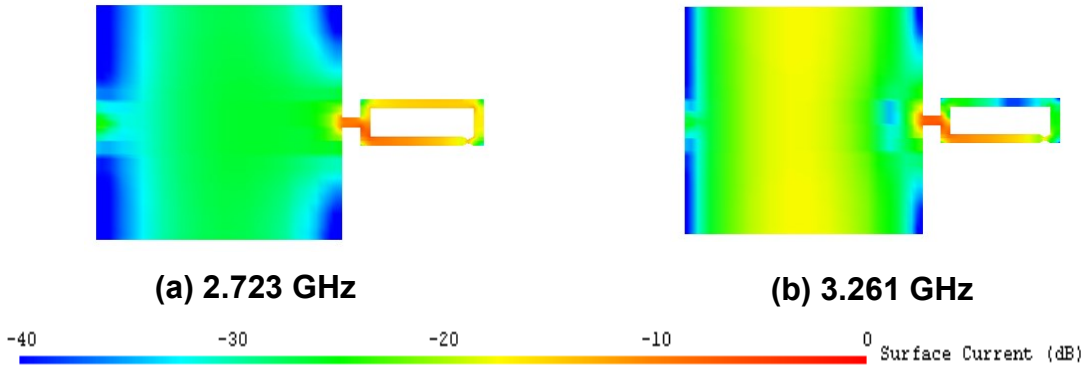

Figure 5.8. Surface current intensity of single loop model with L_{cx} of 9750 µm for the non-strain case at different resonant frequencies (solid black curve in Figure 5.7).

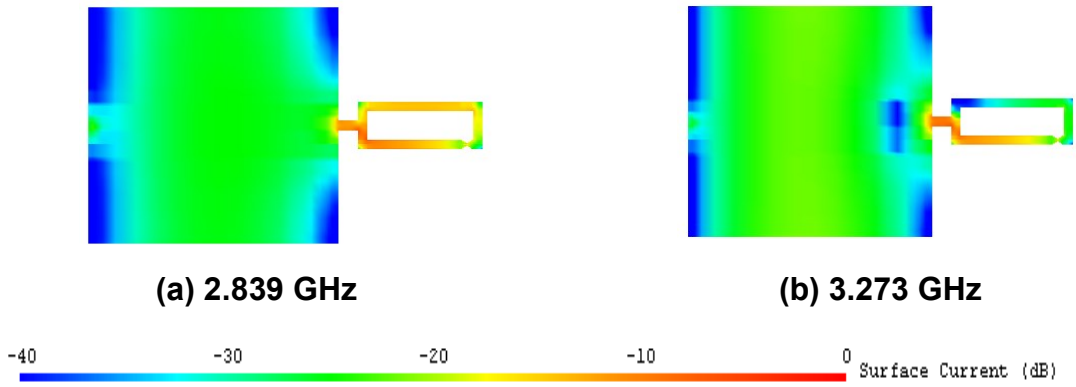

Figure 5.9. Surface current intensity of single loop model with L_{cx} of 9750 µm for the 1% strain case at different resonant frequencies (dash black curve in Figure 5.7).

5.3.3. Resonant Frequency Shifts in Multi-dimensional Sensing

Two different configurations of the structure in Figure 5.2 are set up in order to investigate the responses of the RF strain sensor in different direction/polarization modes. The simulated models are shown in Figure 5.10, where the strain is applied in the x-

direction, while the feeding current of each configuration is orthogonal to each other. The dimensions of the resonators under non-strain and 1% strain conditions are shown in Table 5-1, corresponding to parameters indicated in Figure 5.2. The simulation results of this study are shown in Figure 5.11 with L_{cx} = 9750 μm, in which the solid lines represent the response of the x-polarization excitation and the dashed lines represent the response of the y-polarization excitation. Figure 5.11 shows that around 2.8 GHz when there is strain applied in the x-direction, a significant frequency shift is observed only for the x-polarization mode, while the response in the y-polarization mode stays relatively the same. Consequently, the strain in the x-direction does not influence the frequency response of the y-polarization excitation. Note that the resonant frequency is shifted by 110 MHz (2.75 – 2.86 GHz), similar to the one observed for the simplified single loop structure of Section 5.3.2 (the black curve in Figure 5.7), i.e. the sensitivity remains the same when another loop is orthogonally added. Therefore, the frequency shift observed in the x-polarization excitation can be attributed to the strain in the x-direction only. Since the dimensions L_p and W_p of the patch are slightly different, it can be identified that the x-polarization response has a $|S_{11}|$-peak around 3.3 GHz and y-polarization response has one around 3.4 GHz. These peaks have almost no shift in strain response since they are due to the patch; therefore, they can be used to correspond the frequency shift to the strain direction, i.e. the frequency shift around 2.8 GHz can be identified to be induced by the applied strain in the x-direction if the shift occurs in the curve containing the 3.3 GHz peak or the y-direction if the shift occurs in the curve containing the 3.4 GHz peak. As a result, the strain in x and y can be detected independently with this same RF transducer. Once the strain in x and y directions are obtained, the final strain in an arbitrary direction

can be derived by superposition of these two orthogonal strain responses because the strain parameter is essentially the shear force applied on the surface combining vectorially the two strain components (Figure 5.5). Therefore, this mechanism allows sensing strain in an arbitrary direction.

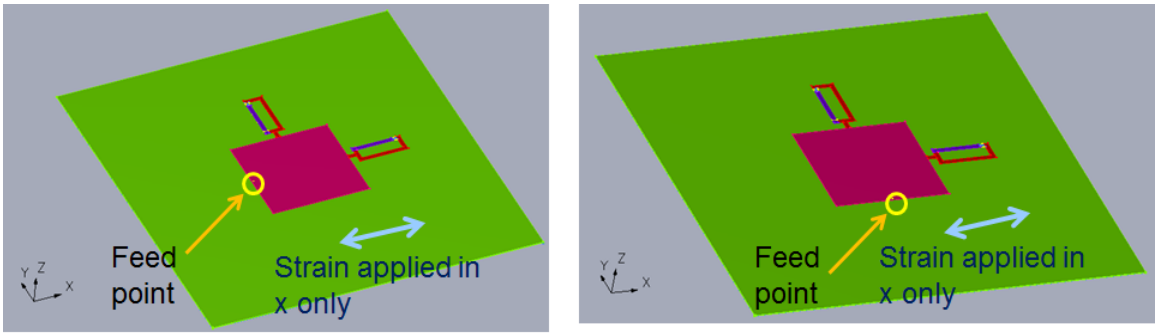

(a) x-polarization excitation. (b) y-polarization excitation.

Figure 5.10. Two configurations to simulate the two orthogonal modes of the ring loaded patch RF transducer.

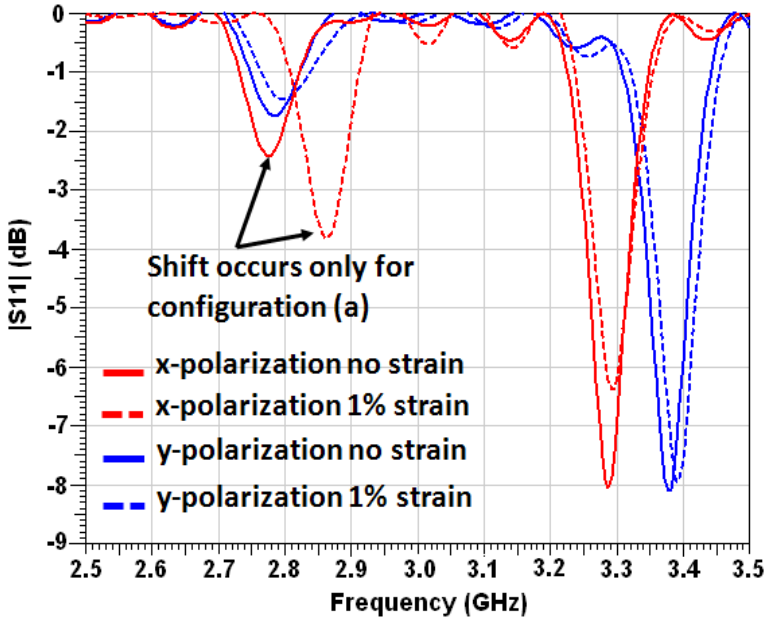

Figure 5.11. Frequency response of the transducer in the two configurations when exciting in two different polarizations under no strain and 1% strain in the x-direction.

Note that the resonant frequency of the ring is not only highly sensitive to the capacitance area (Figure 5.6) but also to the separation distance between the cantilever and the other end of the ring (h_{cap} in Figure 5.4). Results from Figure 5.7 show that mostly the capacitance area determines the sensitivity of the RF transducer in terms of frequency shift for a given strain. To show that the second principle still holds valid regardless of the gap capacitance area (Figure 5.6 illustrated the overlap) or the separation distance (h_{cap} in Figure 5.4), the width of the cantilever is changed to 800 µm instead of 1000 µm, and h_{cap} is changed to 15 µm instead of 10 µm (compared to Table 5-1). The simulation results are shown in Figure 5.12 for the same parameters modeling strain as illustrated in Table 5-1. Although the resonant frequency of the loop is relocated

to around 3.6 GHz instead of 2.8 GHz in Figure 5.7, the same behavior is observed, i.e. a significant shift of about 120 MHz (3.67 – 3.55 GHz), i.e. 3.3%, occurs only in the x-polarization excitation. Observe from Figs. 5.11 that there exists a small shift of a about 20 MHz in the y-polarization excitation (3.61 – 3.63 GHz), i.e. 0.55%. In principle, this small shift can be de-embedded during signal processing.

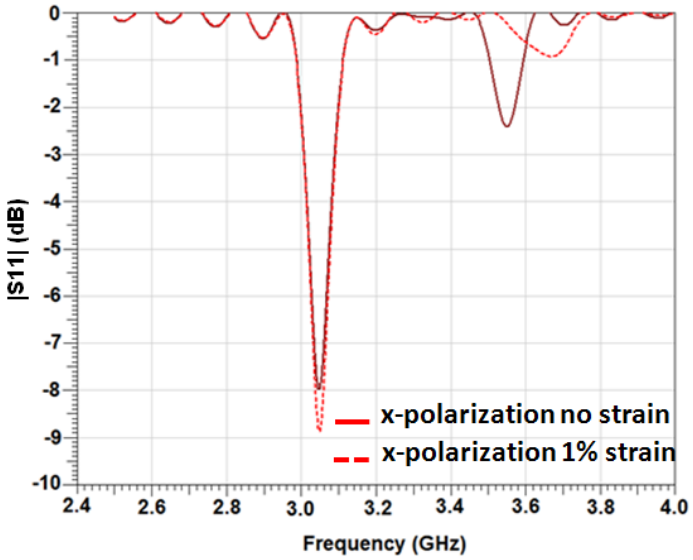

(a)

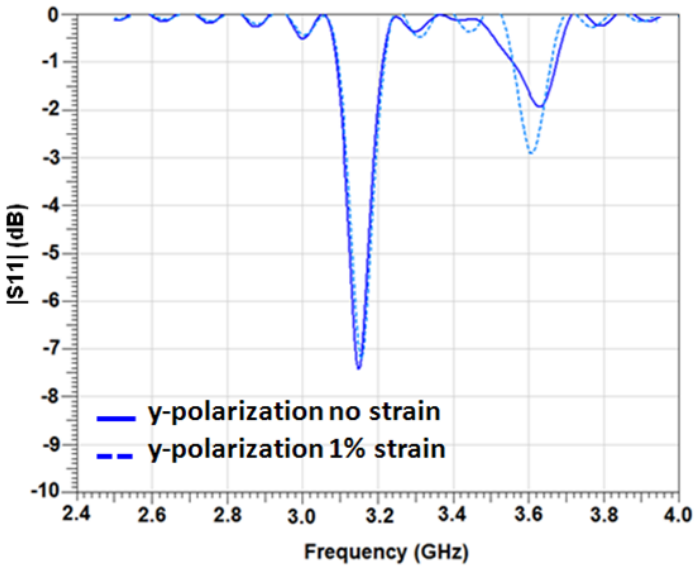

(b)

Figure 5.12. Frequency responses of the multi-dimensional strain transducer for h_{cap} of 15 µm and cantilever width of 800 µm under no strain and 1% strain in the x-direction for: (a) x-polarization excitation and (b) y-polarization excitation.

5.4. Prototypes and Measurements

Proof-of-concept prototypes are presented in this section to illustrate the operating principles discussed in Section 5.3.2 and 5.3.3. First, the patch antenna loaded with a single loop is built and measured with different strain loads to demonstrate the resonant frequency shifts. Then, the prototype of the patch antenna loaded with two orthogonal loops is presented to illustrate the multi-dimensional sensing capability.

5.4.1. One Dimensional Sensing with a Single Loop

The circuit was fabricated in two separate portions as shown in Figure 5.13. The first portion, consist of the patch and the planar open loop (without the cantilever), was fabricated on Kapton substrate with a thickness of 100 μm (Figure 5.13a). The cantilever was fabricated on a separate substrate of Kapton with a thickness of 50 μm (Figure 5.13b). Then the cantilever was manually assembled onto the loop. In the first portion of the circuit (Figure 5.13a), the surface at the tip was cleaned and applied a small amount of transparent adhesive glue spread as thin as possible to create a 10 – 15 μm insulating layer, however not well controlled. As this glue layer was dry, the cantilever patterned on the 50 μm thick Kapton was soldered to the other end of the open loop (Figure 5.14) with the copper layer faced down. Then, to ensure the cantilever tip copper face was in contact with the glue layer in the normal direction but freely to move in the elongate direction, a buffer layer of 127 μm thick Kapton was placed on top of the cantilever and pressed down by Scotch tape. The tape can also prevent the motion in a random arbitrary direction due to mechanical noise. The exerting force can move the cantilever only in the direction of the applied strain. In this configuration, as the open loop was stretched, the

cantilever could still move freely as the solder end of the cantilever pulled on it. This assembling is illustrated in Figure 5.14.

The measurement setup was also illustrated in Figure 5.14, in which the strain was increased as the load was added. Measurements of the RF strain transducer are shown in Figure 5.15 with Figure 5.15a showing two resonant peaks and Figure 5.15b showing more details around 2.9 GHz (a zoom view from Figure 5.15a). Note that the load was added with irregular intervals due to the limited availability of load. Because of such manual process, it was difficult to accurately control the initial gap capacitance of the circuit since the actually L_{cap} could be easily varied between 750 – 1000 μm. Therefore, it was difficult to tune the response of the circuit to the highest sensitivity operation point in fabrication (see plots in Figure 5.7). The resulting strain can be estimated according to (5.3), where P is the load, E is the Young's modulus of Kapton, t is the thickness of Kapton, and W is the total width of the Kapton substrate which was 150 μm.

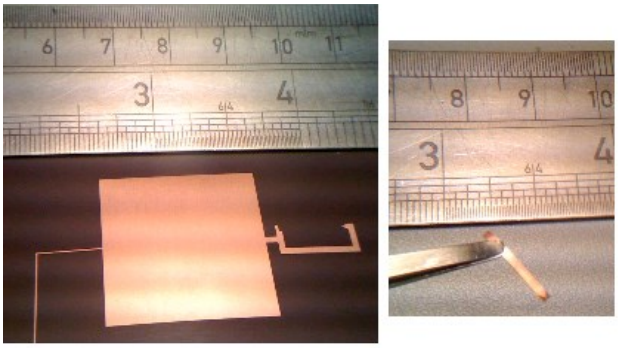

Figure 5.13. Two different fabricated portions of the single loop loaded patch prototype.

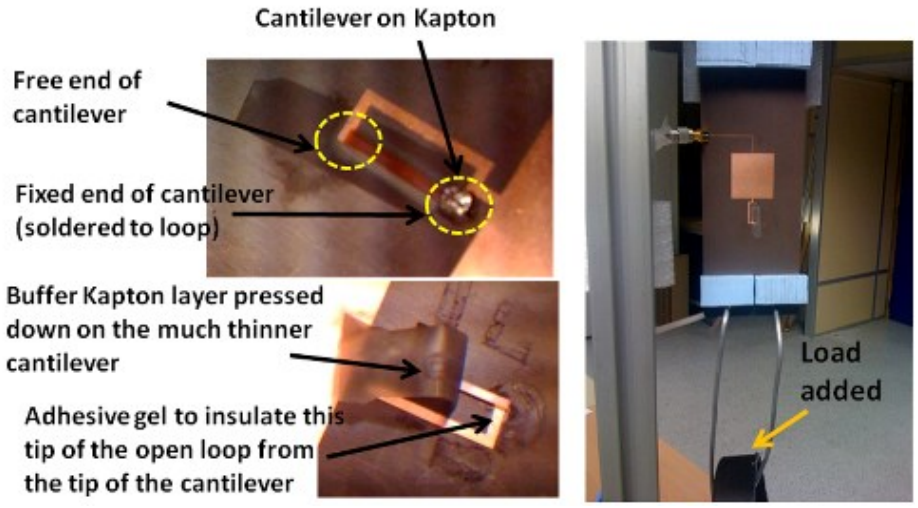

Figure 5.14. The assembled prototype and measurement setup for the single loop loaded patch strain sensor.

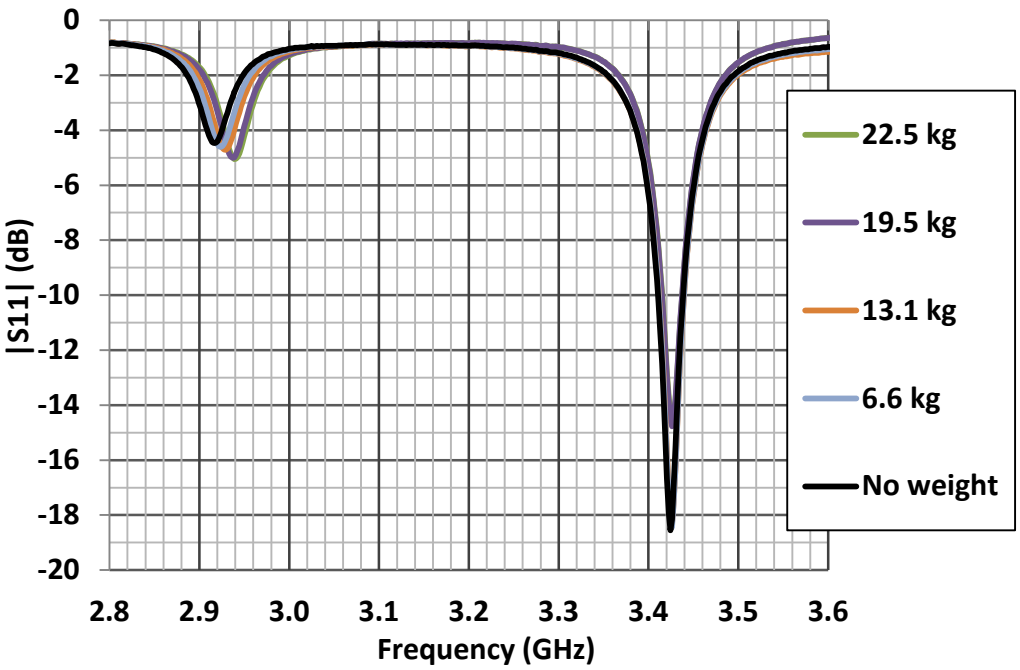

Figure 5.15a. Measurements of |S11| of the fabricated single loop loaded patch prototype subjected to different weights attached.

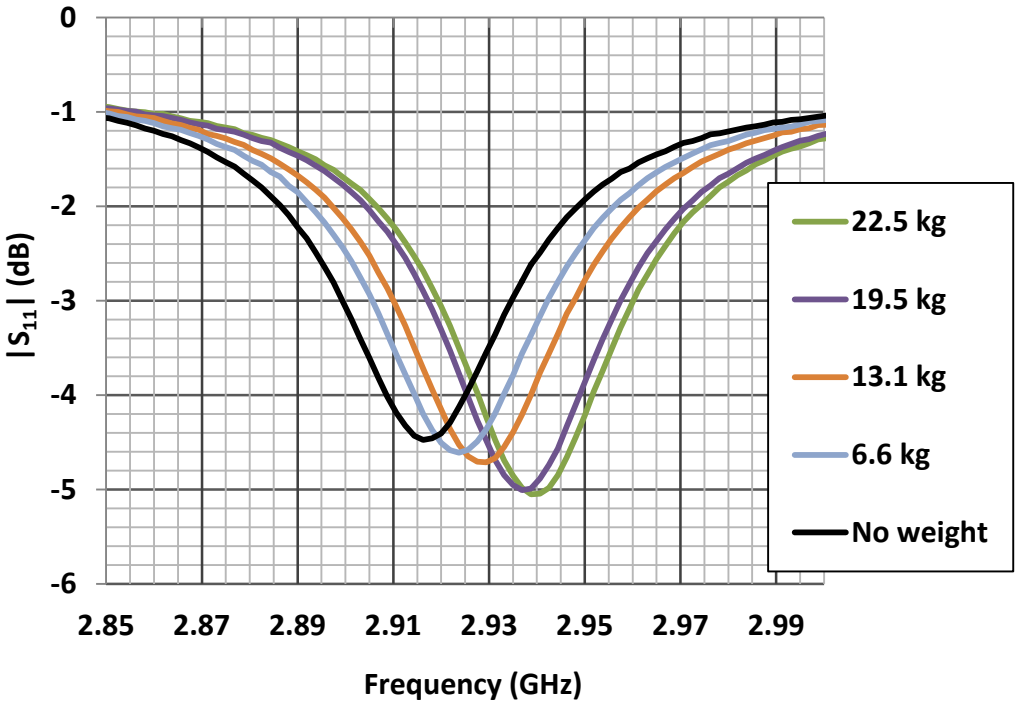

Figure 5.15b. Measurements of |S11| of the fabricated single loop loaded patch prototype subjected to different weights attached around 2.9 GHz.

$$\varepsilon_L = \frac{P}{E \cdot t \cdot W} \times 100\ (\%) \qquad (5.3)$$

Under no load, the two resonant frequencies appearing in Figure 5.15 are 2.9 GHz and 3.4 GHz, which is in excellent agreement with the simulation results in comparison with the blue curve in Figure 5.7 (corresponding to the response of L_c = 9500 μm). Furthermore, a shift of 24 MHz is observed, from 2.914 GHz with no load to 2.938 GHz with 22.5 kg of load, corresponding to 0.645% strain, i.e. 1.26% frequency shift per 1% strain. The plot of the frequency shift (in percent) versus the applied strain (in percent) is shown in Figure 5.15, which indicates an excellent linear response for this strain

transducer prototype within a range of strain of %– 0.7%. Although the prototype was not operating at the most sensitive frequency point as indicated by the black curve in Figure 5.7, the measurements have successfully validated the novel strain sensing concept introduced in this work.

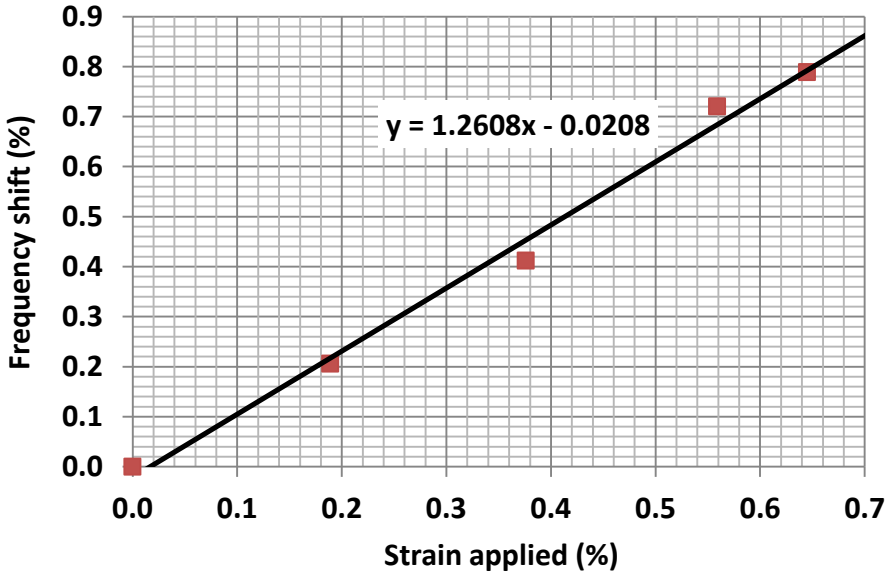

Figure 5.16. Measurements of the proof-of-concept single loop loaded patch prototype.

5.4.2. Two Dimensional Sensing with a Orthogonal Loops

To verify the multi-dimensional sensing capability, two prototypes of the proposed design in Figure 5.2 were fabricated with two different feed positions that excite two orthogonal modes of the patch. The fabrication process was similar to the one described in the previous section. The patch and the flat open ring portion of the circuit

(without the cantilever) were fabricated on Kapton with 100 μm thickness, while the cantilevers were fabricated separately from a 100 μm thick aluminum sheet (Figure 5.17). Then, the cantilever was manually assembled onto the patch circuit. A similar fabrication process performed for the single loop loaded patch was also applied to the patch prototype loaded with orthogonal loops in this section. The assembly details are illustrated in Figure 5.18 and the completed prototypes of the two different excitation polarizations are shown in Figure 5.19.

Figure 5.17. The aluminum cantilever is fabricated separately from the 100 μm thick aluminum sheet.

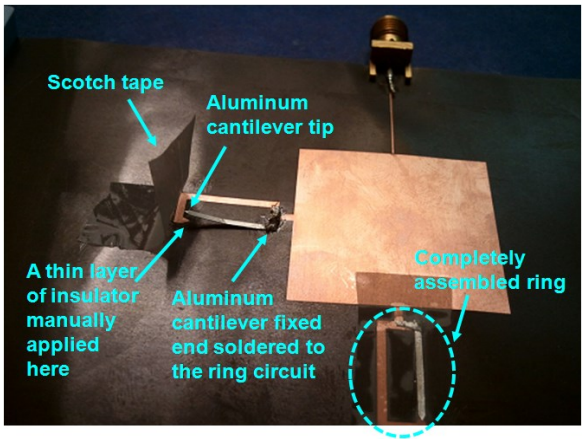

Figure 5.18. The assembly of the aluminum cantilevers onto the patch circuit.

The measurement setup is shown in Figure 5.20. In this figure, the substrate of the modified patch had its top edge mounted to a fixed location on a ladder. The bottom edge of the Kapton substrate was attached to a variable load below. As the load increased when more weights were added, its gravity would pull on the substrate and thus stretching its body in the vertical direction. As the substrate was stretched, the strain was induced on the substrate surface. The sensor was connected to the vector network analyzer (VNA) with a coaxial connector shown near the top left in Figure 5.20. The VNA was calibrated with the standard TRL (thru-reflect-line) procedure. Therefore, the frequency responses of the antenna could be monitored in real time, and they were corresponding to the strain level induced by different loads. Similar to single loop loaded patch measurements, only irregular load increments were implemented. Note that Figure 5.20 illustrates the measurement setup only. The sample that appears in the figure was not a part of the measurements reported in the next section. Instead, each sample presented in Figure 5.19 was subjected to the measurement setup shown in Figure 5.20.

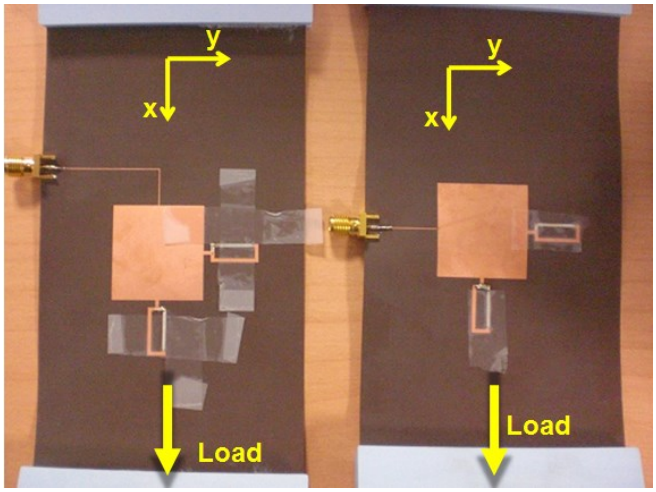

(a) (b)

Figure 5.19. The assembled prototypes for the multi-dimensional strain sensing: (a) x-polarization excitation and (b) y-polarization excitation.

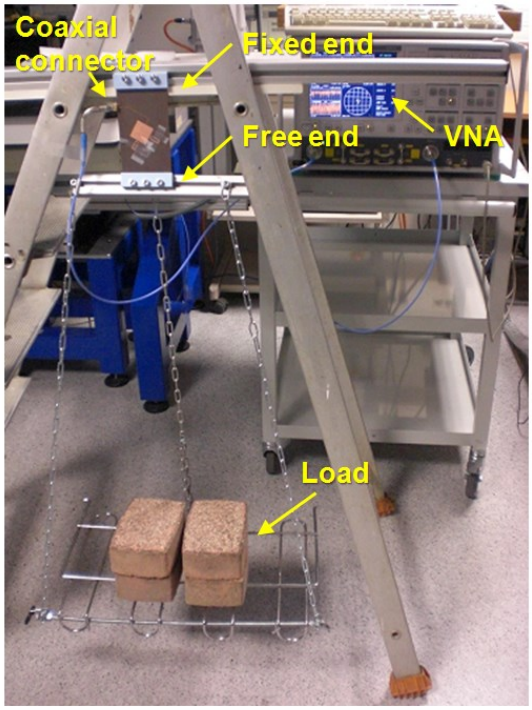

Figure 5.20. Measurement setup for the multi-dimensional strain sensor prototypes.

The measurement results of the two prototypes in Figure 5.19 are shown in Figure 5.21 – 5.22 for different loads corresponding to different strain levels. Figure 5.21 shows the frequency responses of the x-polarization excitation prototype under different loads in x-direction. On the other hand, Figure 5.22 shows the frequency responses of the y-polarization excitation prototype under different loads also in x-direction. Note that those frequency responses appear to resemble the simulation results shown in Figure 5.12, in which a larger *hcap* value was simulated. The correspondence indicates that the adhesive insulator gel layer applied in this assemble of the multi-dimensional strain sensor prototypes was thicker than the gel layer applied to the single loop prototype. Nonetheless, it can be observed that the frequency shifts only occur in the x-polarization excitation prototype, thus validating the multi-dimensional sensing principles as discussed in Section 5.2.

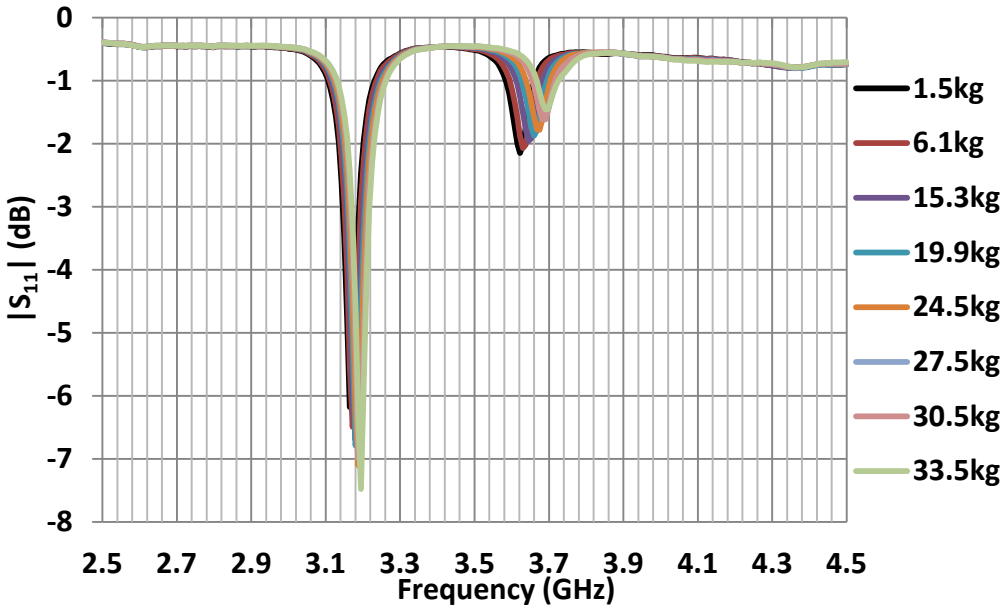

Figure 5.21. Measured $|S_{11}|$ of the fabricated prototype with x-polarization excitation subjected to various attached weights.

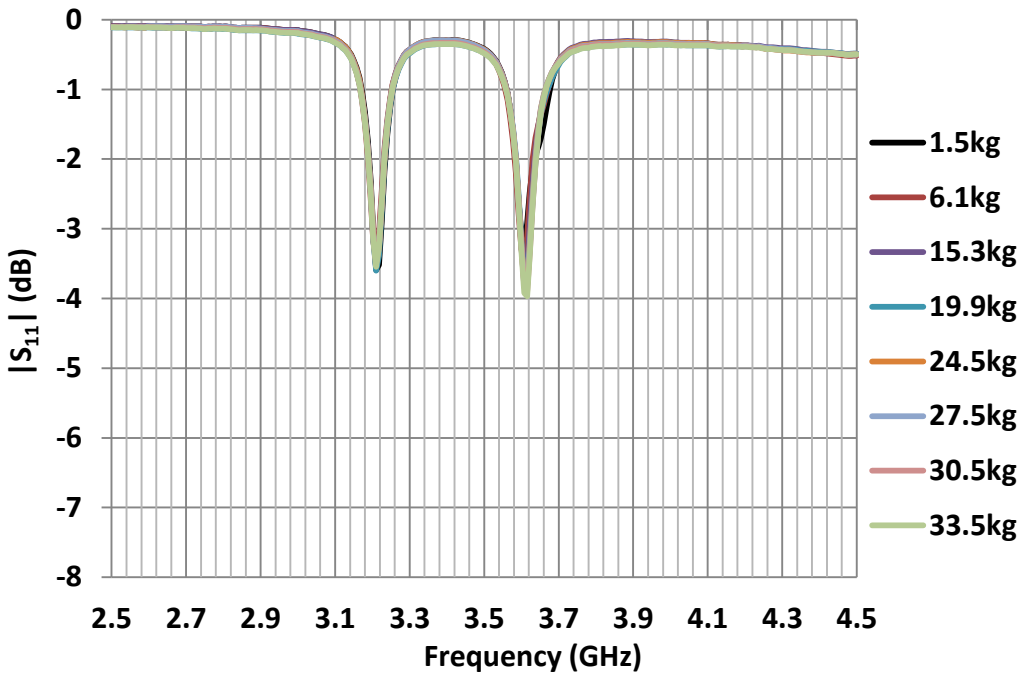

Figure 5.22. Measured $|S_{11}|$ of the fabricated prototype with y-polarization excitation subjected to various attached weights.

A frequency shift of about 70 MHz (3.62 – 3.69 GHz) can be observed in Figure 5.23, where the magnitude of S_{11} of the x-polarization excitation prototype is plotted in a small frequency bandwidth of 3.6 – 3.7 GHz. This shift occurs for the strain of 0.04% – 0.88% calculated based on (5.3). The sensitivity in terms of frequency shifts versus the applied strain is plotted in Figure 5.24. The slope of the best fit curve gives a sensitivity of 2.35% frequency shift per 1% strain. This is more than 2 times higher than the sensitivity of the existing passive and chipless RF strain transducers. Apart from the challenges encountered in fabrication, and based on the same design concept,the highest sensitivity observed in simulations (see the black curve in Figure 5.7) was shown to be about 4 times higher than existing passive and chipless strain transducers that give about

a 1% frequency shift per 1% strain. Although the prototype was not operating at the highest sensitive frequency point, these measurements have successfully validated the multi-dimensional sensing concept introduced in this work. The resolution of $|S_{11}|$ value, i.e. minimum detectable change, of the curves in Figure 5.23 depends on the interrogation method, which is discussed in the next section. Figure 5.24 also indicates excellent linearity of the proposed patch-loop RF strain sensor in the measured range of strain, i.e. up to 0.88% of strain. A typical strain level to be monitored in infrastructure and aerospace is up to 1% for structures such as buildings, bridges, and aircrafts.

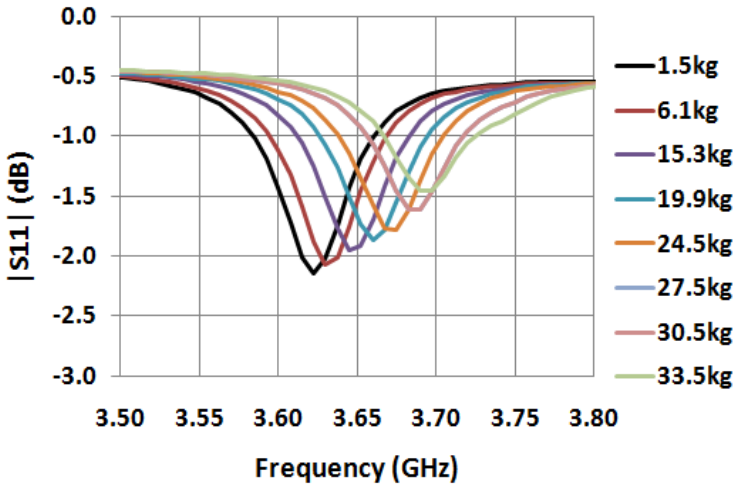

Figure 5.23. Measured $|S_{11}|$ around 3.6 GHz of the fabricated prototype with x-polarization excitation subjected to various attached weights.

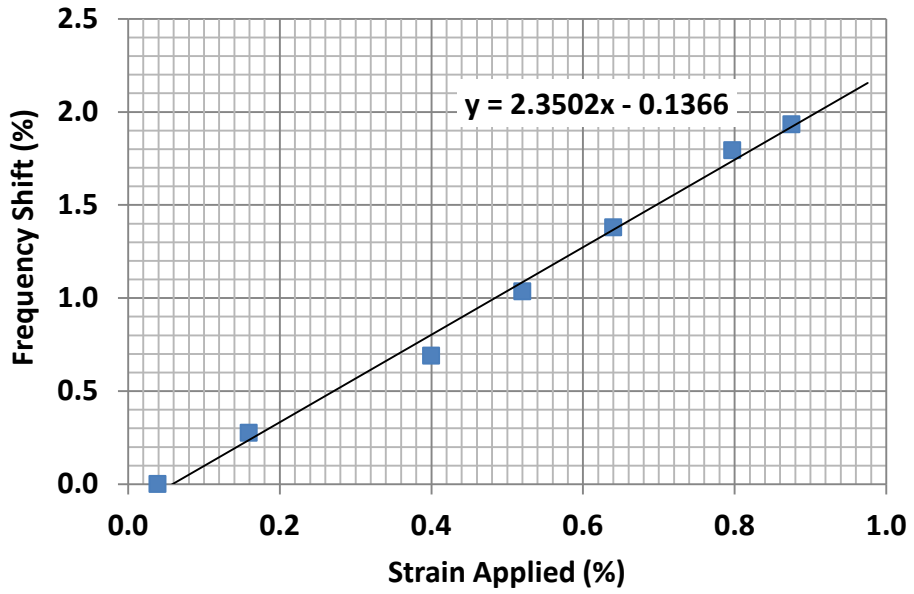

Figure 5.24. Plot of the frequency shift versus the applied strain.

5.5. Remote Sensing Implementation

The passive and chipless RF strain transducer can be interrogated remotely in a long range by an FMCW radar based on the beat frequency level similar to the system demonstrated in Section 3.5 of Chapter 3. The scatterers here are the patches loaded with the open loop rings, i.e. the one-port RF strain transducers. To illustrate the interrogation method that can exploit the frequency shift behavior of the proposed transducer, the single loop loaded patch design (as illustrated in Figure 5.1) is assumed to be integrated in a network configuration like the one shown in Figure 5.25, where a dipole is terminated by the one-port sensor. In this section, no measurements are presented but theoretical calculations are demonstrated for the remote sensing implementation. Therefore, the choice of the dipole as the communication antenna allows higher accuracy

in the analytical estimations due to its simplicity. The well-known expression for the RCS of the loading configuration in Figure 5.25 is shown in (5.4), which is close to the expression (2.7) in Chapter 2 but applied specifically to a dipole [5.23]. Here, at a given operating frequency f ($\lambda = c/f$), G_A is the linear gain of the dipole antenna R_A is the real part of the complex input impedance Z_A of the dipole, and $Z_{LOAD} = R_{LOAD} + jX_{LOAD}$ is the complex input impedance of the patch-loop strain sensor. Thus, the variation in RCS of the dipole is dependent on the variation of the load impedance, i.e. the impedance of the sensor. In this study, S parameters of the single loop loaded patch sensor as analyzed in Section 5.3.2 is employed for the impedance calculations. Specifically, the input impedance corresponding to no strain and 1% strain conditions is derived from the same simulation data set that was shown in Figure 5.7 for L_{cx} of 9759 µm, i.e.the solid and dash black curves. The calculated input impedance, Z_{LOAD}, of the sensor is then presented in Figure 5.26. Additionally, a dipole antenna was designed to resonate at 2.72 GHz (52 mm in length), which is the resonant peak of the lower resonant frequency observed in the solid black curve of Figure 5.7. With the simulated values of G_A, Z_A, and Z_{LOAD}, RCS responses of the network configuration in Figure 5.25 can be estimated and plotted in Figure 5.27. The responses show a RCS variation of about 0.73 dB corresponding to the applied strain of 1%.

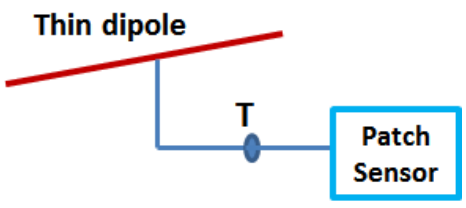

Figure 5.25. Passive sensing network configuration for RCS variation reading.

$$\sigma \approx \frac{\lambda^2 G_A^2}{4\pi} \left| \frac{2R_A}{Z_{LOAD}+Z_A} \right|^2 \tag{5.4}$$

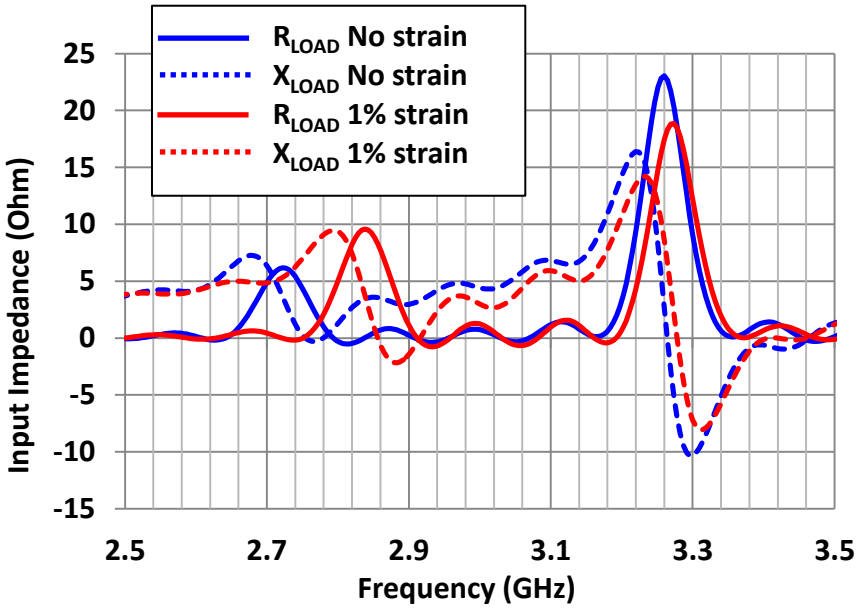

Figure 5.26. Input impedance Z_{LOAD} of the patch-loop strain sensor when no strain (blue lines) and 1% strain (red lines) are applied.

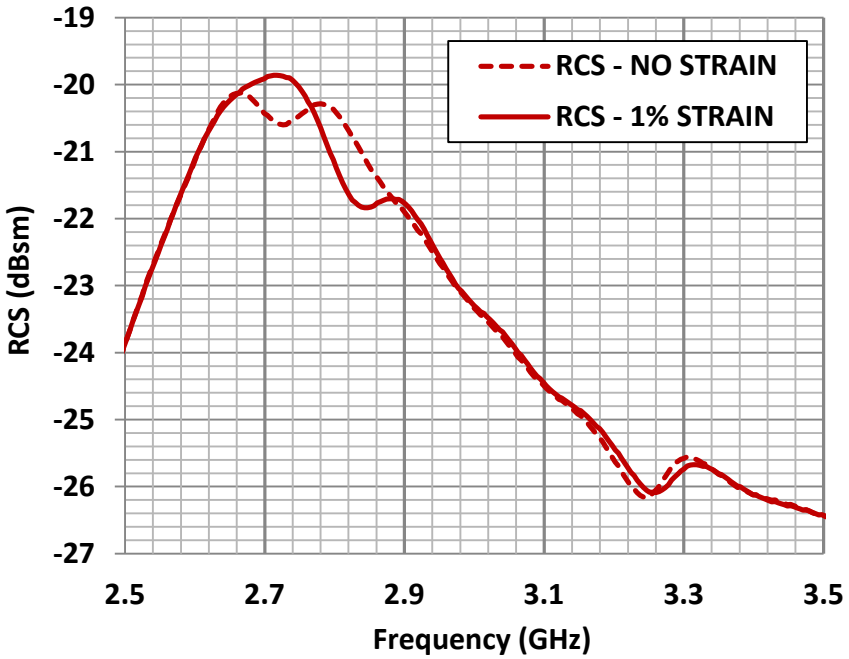

Figure 5.27. RCS variation due to the loading effect of the RF strain transducer (without an impedance transformer).

In order to increase the RCS variation observed in Figure 5.27, an impedance transformer was designed and presented in Figure 5.28, using Advanced Design System (ADS) by Agilent. The resulting input impedance $Z_{IN} = R_{IN} + j\,X_{IN}$ of the patch-loop strain sensor after applying the impedance transformer is shown in Figure 5.29. At the system level, the capacitor in Figure 5.28 is equivalently placed at point *T* in Figure 5.25, where port 1 looks into the thin dipole while port 2 looks into the patch-loop sensor feed point. Therefore, the new transformed input impedance, Z_{IN}, of the load (the patch-loop sensor) is scaled by a complex factor due to the added parallel impedance, $Z_{CAPA} = 1/j\omega C$, where $\omega = 2\pi f$ and $C = 113\ fF$. And the scaling factor itself is also non-linearly proportional to the variations of the load as illustrated in (5.5). The resulting RCS of the

thin dipole was then recalculated and is shown in Figure 5.30 yielding an RCS variation of about 3.8 dB, a detectable level for the radar system in long range interrogation (see Section 3.5.2 of Chapter 3). Consequently, the reading resolution can be improved further with impedance transformers as shown and/or by scaling the design to the millimeter-wave frequency range in which the noise level and thus the minimum detectable level of the FMCW radar can be smaller. In principle, the final sensitivity resolution also depends on the surface deformation of the substrate, i.e. Kapton, for a given applied strain. However, the elasticity of Kapton is much larger than that of the surface materials such as steel and concrete of the monitored structures; consequently, the sensitivity of the transducer is only limited by the frequency shift for a given deformation. Furthermore, such fluctuation of the RCS level can be potentially applied to a passive sensor network as illustrated in Figure 5.31 utilizing delay lines such as those discussed in Section 2.3.4 of Chapter 2. Note that since the design concept employs a ground plane, the sensors can be implemented on any surface without affecting the performance. All sensor nodes can be placed in obscure space and connected to a single communicating high gain planar antenna situated in an open (non-metallic) space for the remote interrogation.

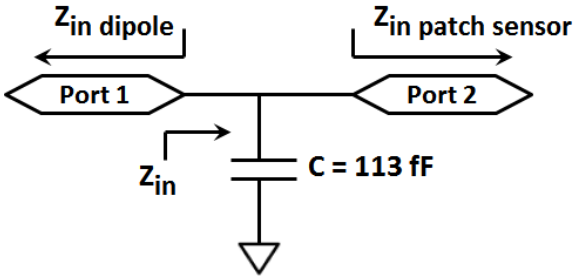

Figure 5.28. An impedance transformer consists of a single parallel capacitor, *C*.

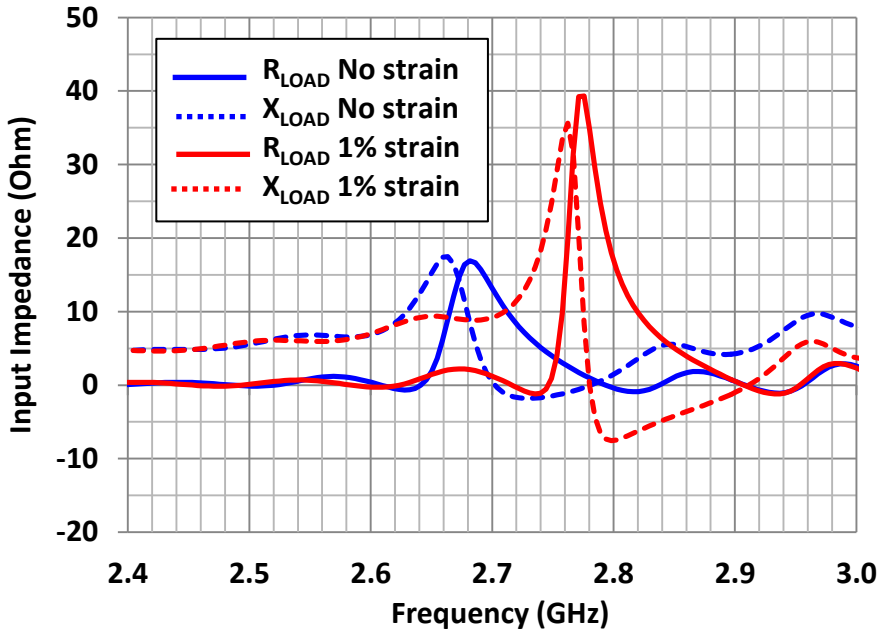

Figure 5.29. Input impedance $Z_{IN} = R_{IN} + jX_{IN}$ of the patch-loop strain sensor after applying the impedance transformer when no strain (blue lines) and 1% strain (red lines) are applied.

$$Z_{IN} = (Z_{CAPA} // Z_{LOAD}) = \frac{R_{LOAD} + jZ_{LOAD}}{1 - \omega C X_{LOAD} + j\omega C R_{LOAD}} \qquad (5.5)$$

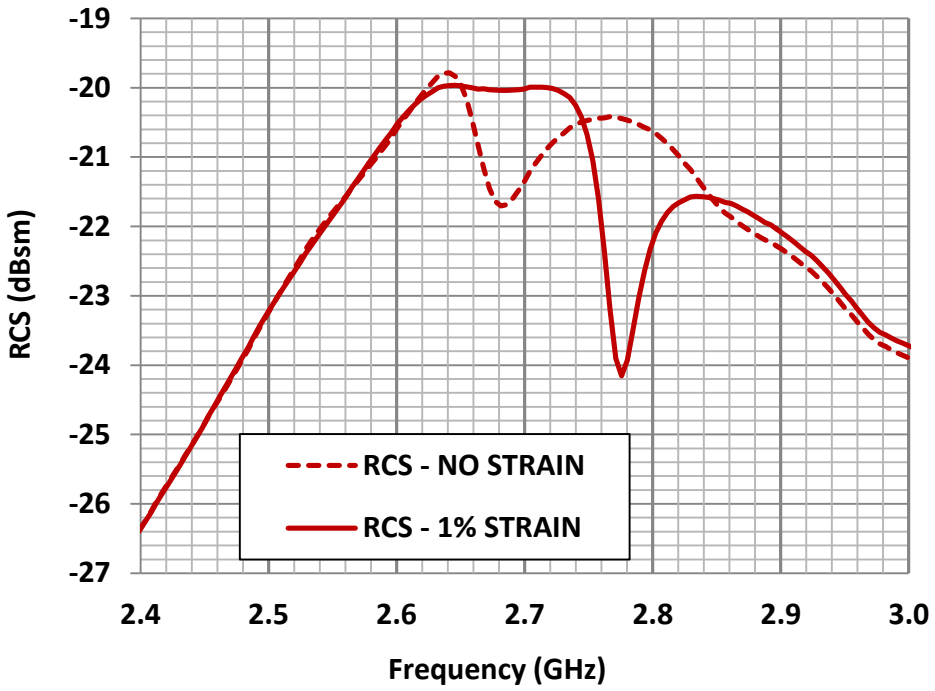

Figure 5.30. RCS responses due to the loading effect of the strain transducer after applying the impedance transformer of a single capacitor to the patch-loop sensor.

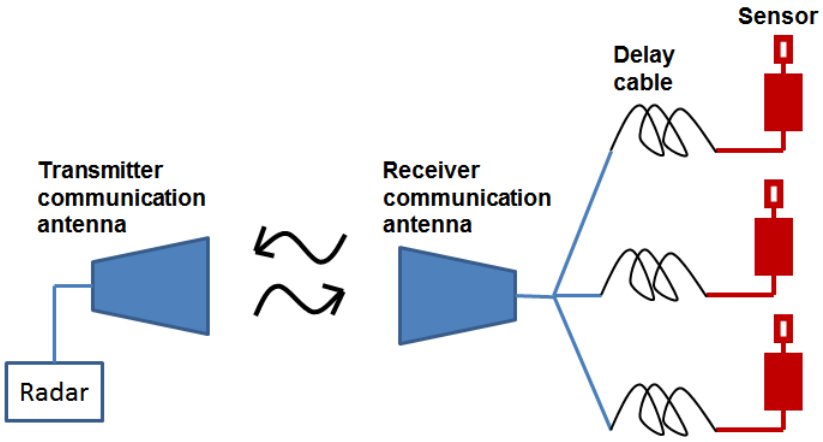

Figure 5.31. RCS measurement system for remote sensing and identification based on an FMCW radar reader.

5.6. Conclusions, Limitations, and Future Work

In general, chipless wireless strain sensors have much lower resolution and sensitivity compared to chip-based strain sensors. Those utilizing MEMS have been shown to have very high precision on the order of nanostrain, i.e. 10^{-9} [5.24 – 5.25]. However, the major advantage of chipless and wireless strain sensors is their possible operation in harsh environments of extremely high temperature applications where chip-based sensors would fail. Furthermore, wireless sensors should enable long range measurement (more than 1 m) and operate independently from the applied surface. As discussed in Section 3.5.4 of Chapter 3, chipless strain sensors based on a SAW-based platform can meet those requirements [5.26 – 5.27], but their operation temperature is also limited up to 1000 ^{o}C due to the limitations of the piezoelectric substrates. Other designs based on radiating resonators yield rather low sensitivity as discussed in Section 5.1. The RF strain sensor design concept introduced in this work provides high sensitivity in long rang remote sensing, operation independent from the applied surface because of the ground plane, and the capability to function in extremely high temperature environments (above 1000 ^{o}C using alumina and platinum). In fact, temperature and strain are dependent physical parameters and usually need to be monitored at the same time. The RF temperature sensor introduced in Chapter 3 can be integrated with the RF strain sensor discussed in this chapter on the same substrate and fabrication process. In theory, they can also be built in the same sensing network with a single wideband high gain communication antenna.

To further compare the performance of the chipless wireless strain sensors, a definition of sensitivity, s_{ε}, was proposed in [5.28]. It is reported again here in (5.6),

where Δf is the resonant frequency shift, f_o is the operating frequency, and ε is the applied strain. The quality factor, Q, is also defined in (5.7), where B is the 3-dB bandwidth of the peaks or notches.

$$S_\varepsilon = \frac{\Delta f}{f_o}\frac{1}{\varepsilon} \tag{5.6}$$

$$Q = \frac{f_o}{B} \tag{5.7}$$

The performance evaluation of six different strain sensors, five of which were reported in [5.14 – 5.16] and is the sixth one being the design introduced in this chapter (referred to as [Thai]), were reported in [5.28] and reproduced here in Figure 5.32 – 5.33. The sensitivity comparison for different sensor designs is shown in Figure 5.32, where the strain sensitivities are plotted versus the maximum strain measured in the linear range of $\Delta f/\Delta L$. Note that the RF strain sensor design of this thesis chapter shows a sensitivity 25 times higher than the least sensitive one. In Figure 5.33, the maximum and minimum quality factor, Q, is given for the six sensors. The presented Q values are mostly close to each other, except for the sensor in 5.14a whose Q value is highly dependent on the environment reflections and the applied calibration. Note that the performance of the RF strain sensor proposed here shows a large dynamic range in linear response from zero strain to 1 % (10^4 microstrain) as seen in Figure 5.23 – 5.24 with respect to not only the resonant frequency shift but also the reflection power level. The precision of strain measurement in this case would depend on the modulation scheme. If the notch

frequency and its backscattering power level are tracked with a wide band scanning from the reader (an FMCW radar), then it is possible to read a strain precision of 0.1 %.

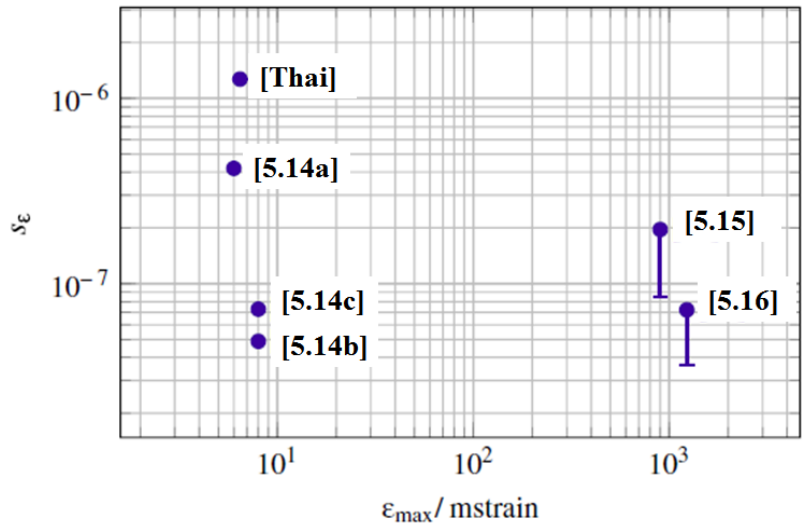

Figure 5.32. Sensitivity comparison between six RF strain sensors. [5.28]

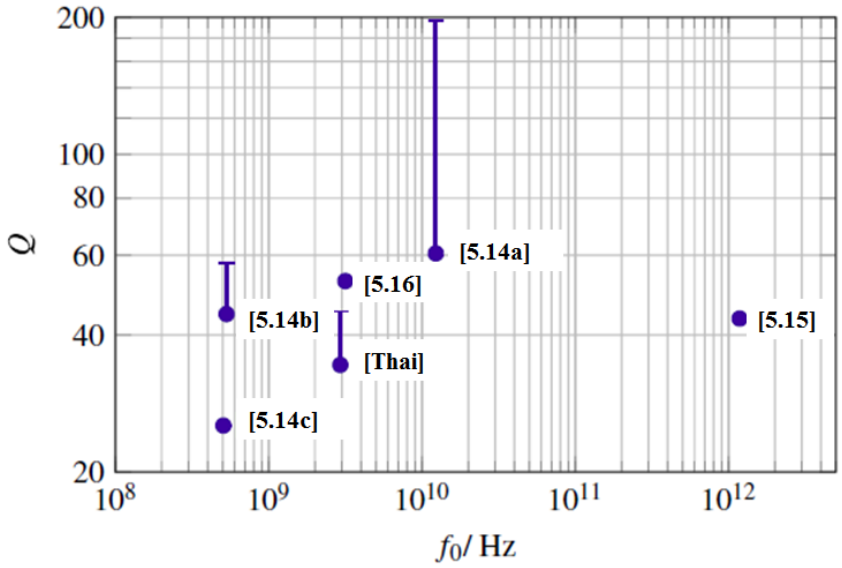

Figure 5.33. Q factor comparison between six RF strain sensors. [5.28]

The major limitation of the design concept here is the construction of the cantilever. The fabrication of the cantilever introduces extra cost and mechanical instability. However, the cantilevers are not free standing and they can be made mechanically stable by packaging a second layer on top of the patch to form an enclosure for the cantilevers. They should only move freely in the x- or y-direction and groves can be utilized for such motion constraints. This design concept also shares the same limitations of delay lines with the RF temperature sensor as discussed in Chapter 3. Future work includes the integration of the RF strain sensor into a sensing network and measurements of the remote interrogation. Additional developments should include the adaptation of alumina and platinum as materials for the sensor and its integration with the temperature sensor for passive chipless long range multi-node multi-physics sensing.

5.7. References

[5.1] D. N. Farhey, "Long-term performance monitoring of the Tech 21 all-composite bridge", *J. Compos. Construct.*, vol. 9, no. 3, pp. 255 – 262, 2005.

[5.2] P. C. Chang, A. Flataus, S. C. Liu, "Review paper: health monitoring of civil infrastructure," *Structural Health Monitoring*, vol. 2, no.3, pp. 257 – 267, 2003.

[5.3] B. Rao, "The need for condition monitoring and maintenance management in industries," in *Handbook of Condition Monitoring*, Amsterdam, Elsevier, 1996, pp 1 – 36.

[5.4] F. Gattiker, F. Umbrecht, D. M¨uller, J. Neuenschwander, "Novel ultrasound read-out for a wireless implantable passive strain sensor (WIPSS)," *Sensors Actuators A: Physical*, vol. 145 – 146, pp. 291 – 298, July-Aug. 2008.

[5.5] K. Stoffel, K. Klaue, S. M. Perren, "Functional load of plates in fracture fixation in vivo and its correlate in bone healing," *Injury*, vol. 31, no. 2, pp. 37 – 86, May 2000.

[5.6] Y. Liu, A. Lacher, G. Wang , A. Purekar, M. Yu, "Wireless fiber optic sensor system for strain and pressure measurements on a rotor blade," in *Proc. Fiber Optic Sensors Appl. V,* vol. 6770, pp. 67700Y.1 – 67700Y.12, 2007.

[5.7] W. Staszewski, "Monitoring online integrated technologies for operational reliability – MONITOR," *Air and Space Europe*, vol. 2, no. 4, pp. 67 – 72, 2000.

[5.8] K. Sun, "Design and characterization of passive wireless strain sensor," M.S. thesis, Dept. of Mech. Eng., Uni. of Puerto Rico, San Juan, Puerto Rico, 2006.

[5.9] J. Wu, S. Yuan, S. Ji, G, Zhou, Y. Wang, Z. Wang, "Multi-agent system design and evaluation for collaborative wireless sensor network in large structure health monitoring," *Expert Systems with Applications*, vol. 37, no. 3, pp. 2028 – 2036, Mar 2010.

[5.10] F. Ansari, "Fiber optic health monitoring of civil structures using long gage and acoustic sensors," *Smart Mater. Struct*., vol. 14, no.3, pp. S1 – S7, 2005.

[5.11] U. Tara, H. Huang, R. Carter, J. Chiao, "Exploiting a patch antenna for strain measurements," *Measurement Science and Technology*, vol. 20, no. 1, pp. 015201, 2009.

[5.12] Z. Qian, Q. Tang, J. Li, H. Zhao, W. Zhang,"Analysis and design of a strain sensor based on a microstrip patch antenna," in *Int. Conf. Microwave and Millimeter Wave Tech. (ICMMT)*, Shenzhen, China, 2012, vol. 5, pp. 1 – 3.

[5.13] A. Daliri, A. Galehdar, S. John, W. Rowe, K. Ghorbani, "Circular Microstrip Patch Antenna Strain Sensor for Wireless Structural Health Monitoring," in *Proc. World Congr. Eng.*, London, UK, June – July 2010, vol. 2.

[5.14] R. Melik, E. Unal, N. K. Perkgoz, C. Puttlitz, and H. V. Demir, "Metamaterial-based wireless RF-MEMS strain sensors," *IEEE Sensors*, Kona, HI, Nov. 2010, pp. 2173 – 2176.

[5.15] J. Li, W. Withayachummankul, S. Chang, D. Abbott, "Metamaterial-based strain sensors," in *Int. conf. Intel. Sensors, Sensor Net. Info. Processing*, Adelaide, SA, Dec. 2011, pp. 30 – 32.

[5.16] C. Mandel, M. Schubler, R. Jakoby, "A wireless passive strain sensor," in *IEEE Sensors*, Limerick, Ireland, Oct. 2011, pp. 207 – 210.

[5.17] T. Thai, H. Aubert, P. Pons, M. Tentzeris, and R. Plana, "Design of a Highly Sensitive Wireless Passive RF Strain Transducer," in *IEEE Int. Microw. Symp*., Baltimore, MD, June 2011, pp. 1 – 4.

[5.18] T. T. Thai, H. Aubert, P. Pons, R. Plana, G. R. DeJean, M. M. Tentzeris, "A newly developed radio frequency wireless passive highly sensitive strain transducer," in *IEEE Sensors*, Limerick, Ireland, Oct. 2011, pp. 211 – 214.

[5.19] T. T. Thai, H. Aubert, P. Pons, G. DeJean, M. Tentzeris, R. Plana, "Novel Design of a Highly Sensitive RF Strain Transducer for Passive and Remote Sensing in

Two Dimensions," *IEEE Trans. Microwave Theo. Tech*., vol. 61, no. 3, pp. 1385 – 1396, Mar. 2013

[5.20] H. Aubert, T. T. Thai, P. Pons, "Strain Sensor," W.O. Patent 2 012 164 191, Dec 7, 2012.

[5.21] A. E. Daniel, G. Kumar, "Tunable dual and triple frequency stub loaded rectangular microstrip antennas," in *IEEE Ant. Prop. Soc. Int. Symp*., Newport Beach, CA, April 2005, vol. 4, pp. 2140 – 2143.

[5.22] E. Erdil, K. Topalli, et. al. "Frequency Tunable Microstrip Patch Antenna Using RF MEMS Technology," *IEEE Trans. Ant. Prop*., vol. 55, no. 4, pp. 1193 – 1196. April 2007.

[5.23] C. Balanis, *Antenna Theory Analysis and Design*, 2nd ed, CA, John Wiley & Sons, 1997, pp. 95 – 96.

[5.24] J. Aebersold, K. Walsh, M. Crain, M. Martin, M. Voor, J. Lin, D. Jackson, W. Hnat, and J. Naber, "Design and development of a MEMS capacitive bending strain sensor," *IOP J. Micromechanics and Microengineering*, vol. 16, pp. 935 – 942, 2006.

[5.25] R. G. Azevedo, D. G. Jones, A. V. Jog, B. Jamshidi, D. R. Myers, L. Chen, X. Fu, M. Mehregany, M. B. J. Wijesundara, and A. P. Pisano, "A SiC MEMS resonant strain sensor for harsh environment applications," *IEEE Sensors J.*, vol. 7, no. 4, pp. 568 – 576, April 2007.

[5.26] J. R. Humphries, D. C. Malocha, "Passive, wireless SAW OFC strain sensor," in *IEEE Freq. Contr. Symp.*, Baltimore, MD, May 2012, pp. 1 – 6.

[5.27] R. Konno, M. Mitsui, H. Kuwano, S. Nagasawa, K. Sano, J. Hayasaka, "A highly sensitive strain sensor using surface acoustic wave and its evaluation for wireless battery-less sensor network," in *IEEE Sensors*, Atlanta, GA, Oct. 2007, pp. 796 – 799.

[5.28] C. Mandel, B. Kubina, M. Schubler, R. Jakoby, "Metamaterial-inspired passive chipless radio-frequency identification and wireless sensing," *Ann. Telecommun., Springer*, vol. 68, no. 7 – 8, pp. 385 – 399, June 2013.

Chapter 6.

RF Pressure Sensor

6.1. Introduction

Pressure sensors are essential for controlling and monitoring thousands of everyday applications, such as in medical technologies (for physiological monitoring), industrial uses (e.g., automotive control with measurements on fluid flow, acceleration, and displacement), and various military applications. Pressure transducers refer to devices that can transform the pressure change in the monitored environment into a change in the properties of an electrical signal. Pressure range varies widely from 10 – 100 mbar for blood pressure and biomedical applications, 1 – 20 bars for car industry, hydraulics and pneumatics applications, and 400 bars for deep sea level applications. Atmosphere has pressure of 1 bar. Common pressure transducer classes include resistive, piezoresistive, and capacitive based sensors, while others are based on inductive-capacitive circuits (LC tanks) whose detection relies on resonant frequency shifts [6.1 – 6.6]. Many of those pressure sensor classes utilize a diaphragm that deflects in response to pressure change, and can be used to measure a wide range of parameters, such as air, liquid pressure and also temperature whose change induces a change in pressure. Most of those require physical wires (to connect to an electronic device for recording and processing information) and/or an antenna (in wireless applications to transmit or receive data). Sensors that were developed for implantable devices such as [6.4 – 6.7] are capable of wireless passive sensing but they are not suitable for long range interrogation because their operation is based on inductive coupling. Pressure sensors based on SAW have been

developed with high accuracy of pressure measurements [6.7 – 6.8], and in principle can be interrogated from a distance but they cannot be applied to extreme temperature environments (1000 ^{o}C and above) due to the material limitations even with Langasite (as discussed in previous chapters). Passive and chipless RF pressure sensors based on EM resonators have also been proposed [6.10 – 6.12]. The design in [6.10] utilizes a membrane integrated with a slot antenna so the slot resonant frequency is modified by the pressure. However, because the slot is inherently a low gain antenna, the RF transducer cannot be implemented in long range. The design cannot be adapted to the impedance load architecture to act as a load to a high gain antenna either. The sensor proposed in [6.11 – 6.12] is based on a dielectric membrane and a half-wavelength resonator (similar to a two-port coplanar filter) situated in a dielectric cavity (Pyrex was used in the design). EM coupling occurs between the resonant mode in the resonator and the transverse stationary waves in the dielectric membrane. As the membrane deflects due to the applied pressure, the air slab thickness is modified and consequently the EM coupling is altered. This device can be interrogated from a long distance when integrated with a high gain antenna [6.12].

This chapter introduced an alternative RF pressure sensor design that has similar advantages to the design in [6.11 – 6.12] such as capacity for long range interrogation. The design presented here is based on a stacked-patch resonator, in which the upper patch is part of the pressure-dependent membrane, designed for millimeter wave frequencies. The resonator operates in two distinct bands between 30 – 55 GHz. Both this sensor design and the design in [6.11 – 6.12] can be adapted to extremely high temperature applications if constructed with alumina and platinum. However, a unique feature of this

design distinctive from the design in [6.11 – 6.12] is the dual frequency response in which one resonance is independent from the membrane deflection (or the pressure change) and the other is pressure-dependent. The advantages of this property are discussed further in later sections. The following discussion is based on [6.13]. In Section 6.2, the design topology and simulations are presented. Its operating principles are discussed in Section 6.3. Without loss of generality, proof-of-concept prototypes operating in the range of 5 – 8 GHz were fabricated to experimentally verify the principles of operation, specifically the correspondence between the membrane position and the frequency shifts. The prototypes and measurements are shown in Section 6.4. To illustrate the robust and adaptable characteristics of the design concept, the design is scaled down in size to operate in the frequency band of 65 – 95 GHz in Section 6.5. The membrane design in this example corresponds to a much lower pressure level. Limitations and future work are discussed in Section 6.6.

6.2. Sensor Design and Simulations

6.2.1. Design Topology

The top view of the new RF pressure transducer, shown in Figure 6.1, features a stacked-patch resonator with a pressure-sensitive variable vertical dimension. The top square patch is mounted to the bottom of a deformable dielectric membrane (silicon is utilized here), and positioned right above a second fixed-position square patch; the two patches are centered on top and bottom, respectively, of a rectangular grounded air cavity. The side view of the RF sensor showing clearly the Si membrane is given in Figure 6.2. The cavity is surrounded by metalized walls that are grounded. The lower

patch is placed on top of the first layer of the LTCC substrate using GL550 (ε_r = 5.6) by Kyocera Corp. The second LTCC layer, with an identical thickness to the first one, is placed underneath the ground plane to support a microstrip line (50 Ω) that feeds the lower patch through a via that passes through a hole with length, g, in the ground plane. In fabrication, the metalized walls can be realized by using via arrays to minimize metal loss, and the Si membrane may be supported by additional LTCC layers as a more mechanically stable frame for the air cavity. Depending on the amplitude of the pressure under observation, the top membrane gets deformed modifying the vertical spacing h_2, thus affecting the resonant frequencies of some cavity modes; that directly translates to the shift of the radiation frequency of the stacked-patch antenna configuration.

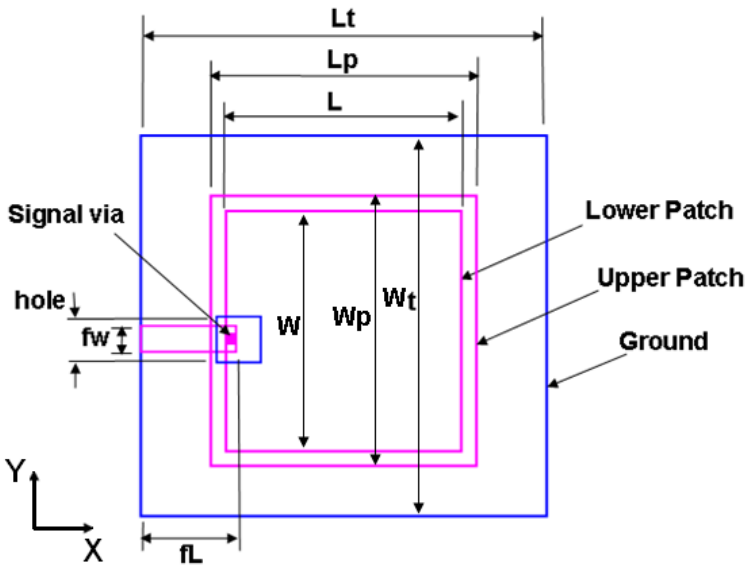

Figure 6.1. Top view of the RF pressure transducer.

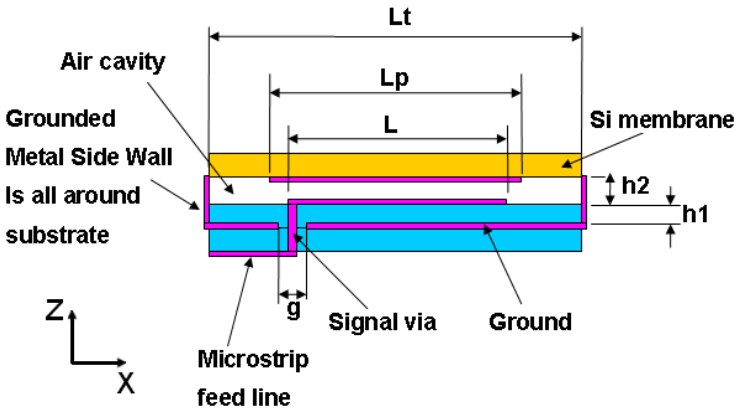

Figure 6.2. Side view of the RF pressure transducer.

6.2.2. Frequency Shift Sensitivity for a 30 – 50 GHz Benchmarking Model

To verify the correlation of the sensed pressure (top membrane deflection) and the resultant frequency shift, various numerical simulations are performed for an RF transducer operating in the 30 – 55 GHz range. The optimized parameters of the stacked-patch sensor are as follows: $L_t = W_t$ = 3340 μm (length and width of the ground), $L_p = W_p$ = 1800 μm (length and width of the upper patch), $L = W$ = 1670 μm (length and width of the lower patch), h_1 = 82 μm (thickness of LTCC substrate), and h_2 = 40 – 100 μm (air gap). The thickness of the membrane was chosen to be 400 μm, and it has the same lateral dimensions as the ground. Observe that the membrane is made four times thicker than the air cavity for two reasons. Firstly, the membrane is also acting as superstrate of the upper patch, so it influences the radiation efficiency of the upper patch at the operating frequency range of 30 – 55 GHz. Thus, the thickness was chosen for the best performance. Secondly, the membrane of 400 μm allows lower cost of fabrication as

opposed to 100 μm choice in the design of 65 – 95 GHz for a different application in a different pressure range.

The stacked-patch resonator was simulated in CST Microstripes [6.14], and S_{11} results are shown in Figure 6.3. Here, a dual-band resonant response is observed. Only the resonant frequency in the higher band shifts from 47.6 to 54.6 GHz as the air gap, h_2, between the two patches decreases from 100 μm to 40 μm. In this work, the deflection is varied from 10% to 25% of the membrane thickness in order to investigate the relationship between the deflection and the frequency shift, to adequately identify and demonstrate the linear variation regions of deflection versus pressure and deflection versus frequency shift. The lower resonant frequency remains almost constant during this range of displacement. It should be noticed that this range of displacement is significantly smaller than the elastic deformation limit of the membrane material, which is silicon (Si) presented here, and also valid for many other materials when the small deflection approximation can be used. As a result, the RF transducer design shows a high sensitivity of about 116 MHz/μm. It is important to note that although the higher resonant frequency shifts as h_2 changes, the lower resonant frequency (32 GHz) is unaffected by the change. If the sensor is treated as a one-port device, i.e. an impedance load, then the fixed frequency can be used for identification and calibration purposes when it is connected to a high gain antenna in a passive sensing network interrogated based on the beat frequency of an FMCW radar similar to the one discussed in Section 3.5 of Chapter 3. The calibration is particularly useful when this sensor is integrated together with the RF temperature sensor of Chapter 3 and/or the RF strain sensor of Chapter 5 on the same substrate layer.

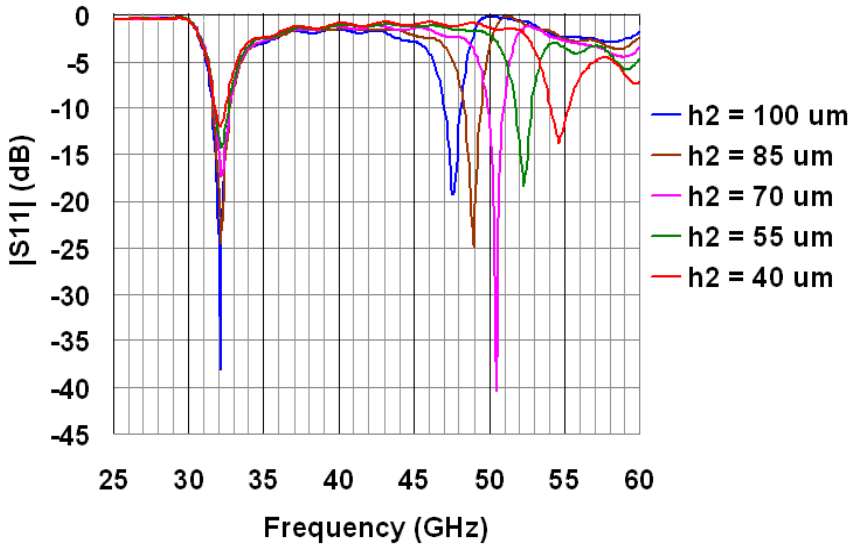

Figure 6.3. Simulated $|S_{11}|$ results of LTCC based RF pressure transducer (30 – 55GHz range) with h_2 = 40 - 100 μm with steps of 15 μm.

The plot of frequency versus deflection is shown in Figure 6.4, where the response is shown to be only slightly non-linear over a large range of deflection. It should be noticed that the non-deflected membrane corresponds to the h_2 value of 100 μm. Therefore, as the deflection increases, the value of h_2 decreases corresponding to an increase in the resonant frequency (Figure 6.3). It can be observed from Figure 6.4 that the linearity assumption is valid up to 30 μm in deflection with a slope of 0.1, i.e. the frequency is increased by 0.1 GHz for every 1 μm of deflection. The frequency response starts to deviate from linearity for larger deflection.

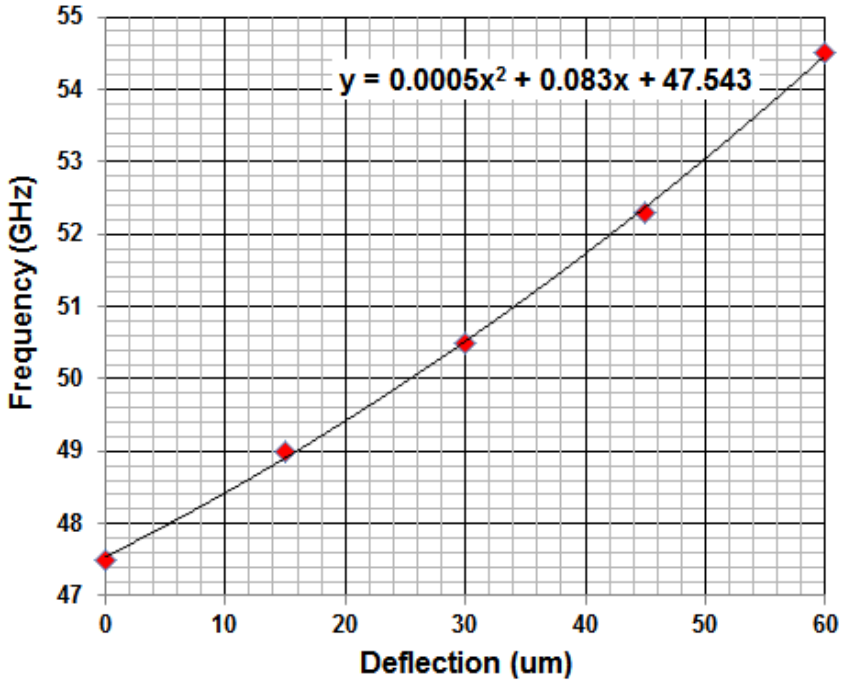

Figure 6.4. Plot of frequency versus deflection for the RF pressure transducer design of 30 – 55 GHz range.

Typically, the small deflection of a square thin plate with both edges clamped can be calculated within an acceptable accuracy according to (6.1), where d_{max} denotes the maximum deflection of the plate (deflection of the center of the diaphragm), υ is the Poisson ratio, P is the applied pressure, L is the plate's side dimension, E is the Young's modulus of the plate's material, and h is the plate's thickness [6.15].

$$d_{max} = 0.01512\,(1-\upsilon^2)\frac{PL^4}{Eh^3} \qquad (6.1)$$

Based on the sensitivity obtained from Figure 6.4 and (6.1) with the Young's modulus of Si equal to 150 GPa and the Poison's ratio of 0.17 [6.16], the frequency shift percentage versus applied pressure is plotted in Figure 6.5. It should be noticed that with an applied pressure of 1500 bars, the deflection is 28 μm which is within the linearity range shown in Figure 6.4. With the narrow band response (high Q) as seen in Figure 6.3, a readable range of 0.1% – 6% frequency shift from a radar allows for the detected pressure from values as small as 25 bars up to values around 1500 bars, i.e. the design enables a highly large dynamic range of pressure sensing utilizing only a single transducer. The plot in Figure 6.5 shows a theoretical sensitivity of 0.004 % frequency shift per bar for this 30 – 55 GHz design.

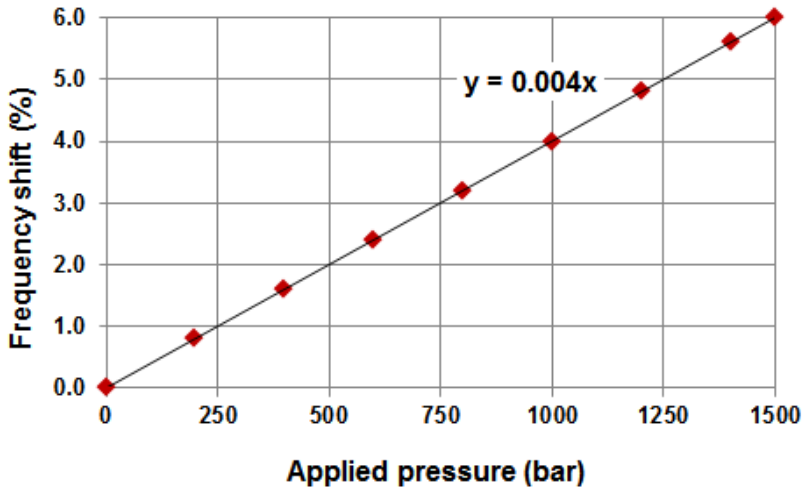

Figure 6.5. Plot of frequency shift percentage versus applied pressure for the RF pressure transducer design of 30 – 50 GHz range.

6.2.3. Radiation Patterns of the Pressure-Independent Frequency

The simulated radiation patterns of the dual band stacked-patch RF sensor at 32 GHz is shown in Figure 6.6. The radiation pattern illustrates the capability of the sensor to provide an effective calibration signal at the pressure-independent resonant frequency. In applications not limited to passive chipless requirements, this resonant peak can serves as a communication link, which may be utilized to send wake-up signal when sensors are in power saving mode, or to send other commands for more complex tasks and retrieve additional information from the sensor nodes. The radiation patterns are similar to that of a single regular patch antenna featuring a gain of 6.1 dBi, which allows for a solid and directive link for the communication channel between the sensing device and the monitoring site. As indicated in Figure 6.3, the worst case of deflection (h_2 = 40 μm) still provides a value of $|S_{11}|$ lower than -10 dB in the 50 GHz band.

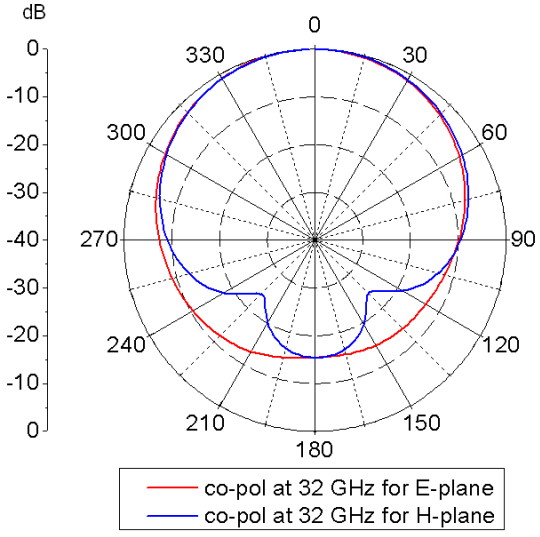

Figure 6.6. Simulated radiation patterns on E-plane (φ = 0° in red), and on H-plane (φ = 90° in blue) at 32 GHz (the constant resonant frequency).

6.3. Principles of Operation

The operation of the RF pressure sensor is based on two uncoupled principles. The first principle is the mechanical deflection of the membrane as it responses to a pressure change. The second principle is the EM response of the stacked-patch resonator, in which the membrane deflection is transformed into a resonant frequency shift. The clear advantage of the two uncoupled principles is that each can be optimized independently depending on the required pressure range and the fabrication constraints. The EM principles are discussed in Section 6.3.1 and 6.3.2, which are followed by the discussion on the mechanical response of the membrane in Section 6.3.3.

6.3.1. Lumped Element Circuit Model

The stacked-patch architecture was originally proposed in [6.17] to provide a wideband patch antenna. In the design of the RF pressure sensor, the stacked-patch antenna was engineered to separate the two resonant frequencies. The dual-band response is due to the presence of the two close resonant frequencies introduced by the two patches. The resonance of the upper patch is influenced by the coupling between the upper and lower patches through the air gap, h_2, which can be modeled by a simplified equivalent circuit topology as shown in Figure 6.7 as proposed in [6.17]. The two patches are modeled as two parallel resonant circuits with (R_1, L_1, C_1) and (R_2, L_2, C_2) representing the radiation resistances and the equivalent inductances and capacitances of the two patches, respectively, while M and C are the mutual inductance and coupling capacitance, respectively. Subscript *1* and *2* refer to the lower and upper patch, respectively. It can be seen from this circuit that the higher frequency resonance shift is a

function of coupling parameter M and C with lumped elements L_1, C_1, and L_2, C_2 remaining the same.

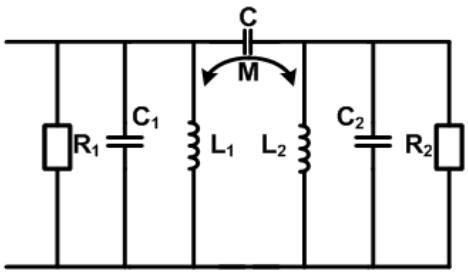

Figure 6.7. Simplified equivalent circuit of the stacked-patch transducer. [6.17]

One of the drawbacks of using this circuit representation is the inaccuracy and uncertainties associated with determining the true values of the parallel *RLC* circuits (resistor-inductor-capacitor). A more accurate alternate circuit approach can be taken from the single-resonance equivalent circuit generated through approximating rational functions and vector fitting, a very effective tool that can accurately fit scattering parameter data to generate an equivalent passive circuit [6.18]. Since there are two resonances that are distinctly separated, one can model the circuit of Figure 6.7 by the circuit of Figure 6.8 and the interaction between the two patches can be represented by the coupling capacitance, *C*, and mutual inductance, *M*. Note that the circuits discussed here provide only a qualitative understanding of the operating principles of the sensor. The specific values of the lumped elements in the circuit are not within the scope of this thesis. Further development of the equivalent circuit models along this direction [6.18 – 6.20] for the stacked-patch resonator can be included in future work.

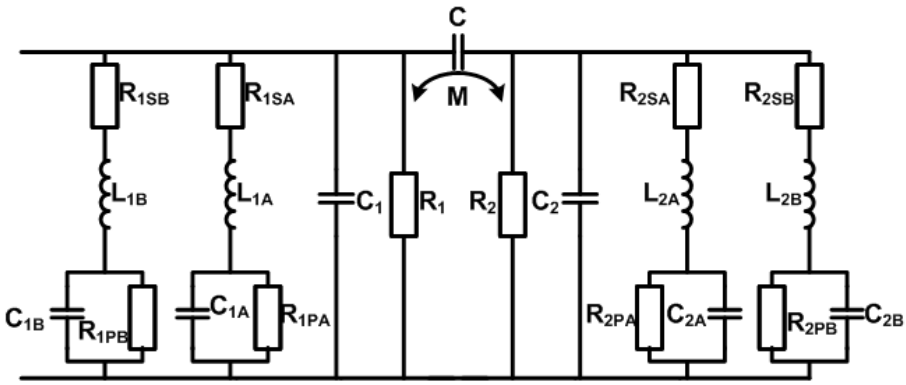

Figure 6.8. Equivalent passive circuit of stacked-patch transducer generated through approximating rational functions through vector fitting.

6.3.2. Surface Current Analysis

The surface current distribution of the two patches of the sensor is shown in Figure 6.9. The fundamental mode surface current, dominant at 32 GHz, is observed to be mainly contributed by the upper patch, while, the fundamental mode surface current, dominant at 48 GHz, is contributed by the combination of the lower and the upper patches together. In terms of the equivalent circuit model shown previously, as h_2 varies, the C_1 parameter is directly affected, which consequently shifts the higher resonant frequency. A change in C is also exhibited, but C_2 stays the same; therefore, this results in a change in $|S_{11}|$ at the lower frequency but not a frequency shift. Since the upper patch is attached to the Si diaphragm, the deflection of the diaphragm due to pressure changes directly corresponds to changes in h_2, which is responsible for the frequency shift. A significant feature of the operation principles presented here is the scalability of design, i.e. designs can be easily modified for any pressure range of various applications based

on the choices of materials. An example of such scalability is demonstrated in Section 6.5.

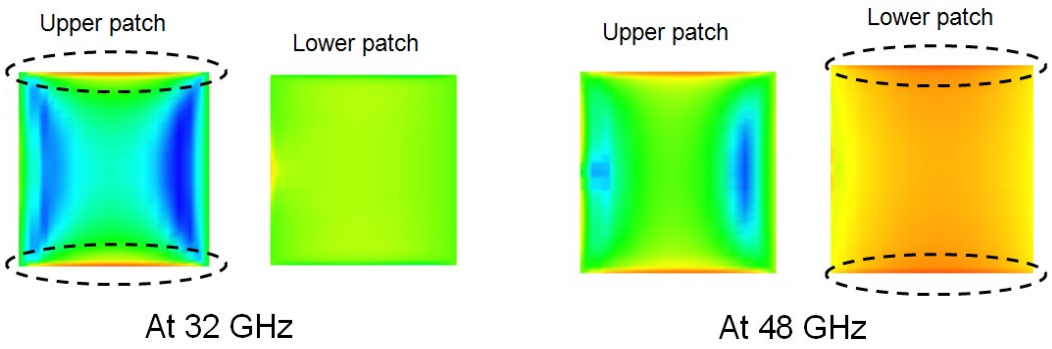

Figure 6.9. Surface currents (RMS values) of the patches at 32 GHz and 48 GHz with dominant currents are circled.

6.3.3. Pressure Effects and the Membrane Deflection Analysis

A sketch of the membrane deflection due to an applied pressure is shown in Figure 6.10. The deflection can be estimated with (6.1).

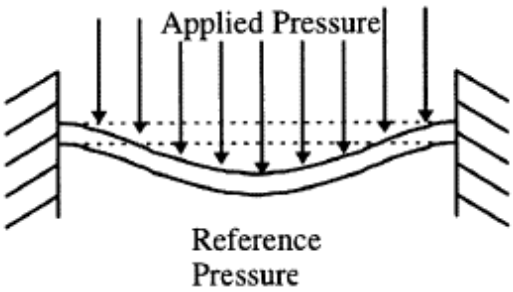

Figure 6.10. Deflection of a diaphragm under applied pressure. [6.21]

It can be observed that the maximum deflection is linearly proportional to the applied pressure, but is proportional to the 4th power of the plate's size, i.e. if the size L is to be reduced, the deflection for a given applied pressure decreases quickly in power of 4. In addition, the maximum deflection is inversely proportional to the Young's modulus and the 3rd power of membrane thickness, therefore different material choices would allow different ranges of pressure and sensitivity required for different applications. For instance, the pressure range applied to hydraulic and pneumatic applications is about 6 – 10 bars, whereas it is about 1 – 5 bars and 20 bars for tires and air conditioning, respectively, in vehicles, 1 – 1000 Pa (0.01 – 10 mbar) for thin film processes, and 10^{-8} Pa in high vacuum. For many biomedical applications, a sensitive pressure range below 500 mmHg (666 mbar or 66.7 kPa) is required. Note that the Young's modulus is the ratio of the stress to strain in the linear elastic region of the material. The materials for any specific application should be chosen such that they are the desired pressure range operating within their elastic region.

6.4. Proof-of-Concept Prototypes at 6 GHz

6.4.1. Electromagnetic and Mechanical Deflection Simulations

Without loss of generality and as a simple experimental proof-of-concept, the stacked-patch resonator is scaled to operate between 5 – 8 GHz. The prototype structure was simplified by replacing the microstrip feed line with a probe feed; hence, the underlying substrate layer below the ground plane (Figure 6.2) was removed. The new scaled design is shown in Figure 6.11 with $L_t = W_t = 32$ mm, $L_p = W_p = 19$ mm, and $L = W = 17$ mm. The feed point was placed at the center along the radiating edge of the lower

patch. The lower-patch LTCC substrate and the upper-patch superstrate Si membrane as the top yellow block in Figure 6.11 are realized by layers of RT/duroid 5880 substrate with a thickness of 787 μm (ε_r = 2.2) [6.22]. The air gap, h_2, between the lower and upper patches is experimentally modified starting from the initial value of 1575 μm.

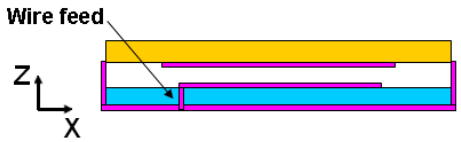

Figure 6.11. Top view of the 6 GHz transducer with coaxial feeding.

Although the flat (uniform) deformation model is first used for the calculation of the pressure-driven deformation, a more realistic approximation of the membrane deflection is modeled by a surface presenting a spherical curvature of radius R as indicated in Figure 6.12. The deflection is denoted by Δh, and $\underline{L_d}$ is the diagonal length of the grounded square cavity. Angle θ is chosen such that the curved surface does not exceed the tensile stress tolerance specified in the material data sheet RT/duroid 5880. The values of the parameters R and θ can be varied to obtain the desired value of Δh. A 3D view illustration of both the uniform surface and the curved surface of the membrane deflection are shown in Figure 6.13. The deformation refers to the value at the center of the patch. In both cases of approximation, the center of the patch experiences the same deflection, i.e. the center of the deflected upper patch in the two approximations have the same height.

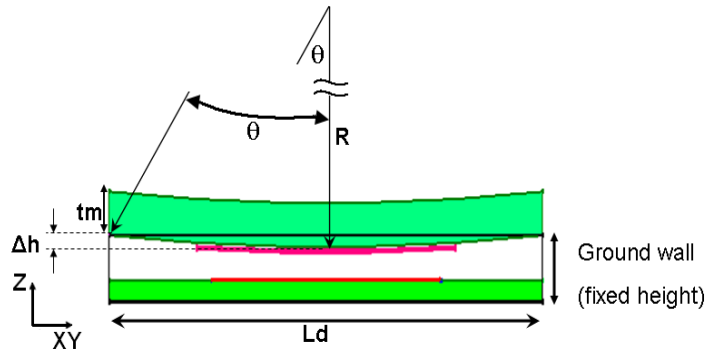

Figure 6.12. Spherical curvature modeling for the improved approximation of membrane deflection.

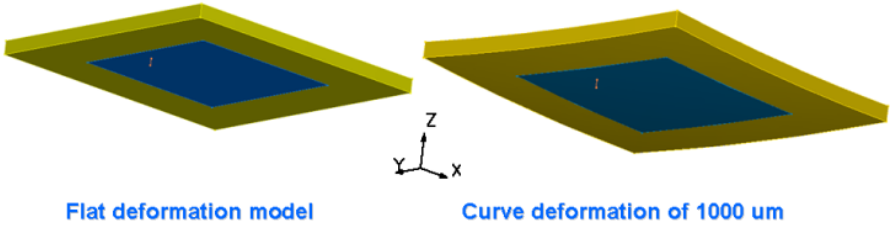

Figure 6.13. Three dimensional illustration of the two approximations to model the deflection of the membrane in the RF pressure transducer.

Plots of the simulated $|S_{11}|$ of the two approximation models are shown in Figs. 6.14 – 6.15, respectively. Those plots indicate that the uniform displacement of the diaphragm is a sufficient approximation to model the EM principle of the stacked-patch RF pressure transducer. Note that the plots show simulations with different deflection intervals of 250 μm and 200 μm for Figure 6.14 and 6.15 respectively. Therefore, without compromising the quality of the RF pressure transducer, this prototype is fabricated in a way that the thickness of the superstrate (supporting the upper patch) is mechanically

adjustable to represent the uniform displacement of the membrane in the transducer. The measurements are essentially static and employed to verify the EM operating principle of the sensor.

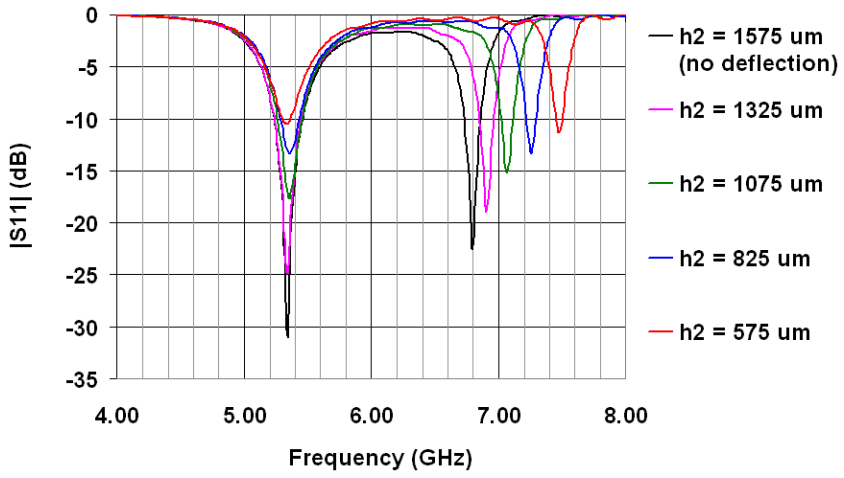

Figure 6.14. Simulated $|S_{11}|$ of 6 GHz scaled RF transducer design of uniform displacement for the membrane deflection with h_2 = 157, 1325, 1075, 825, 575 μm.

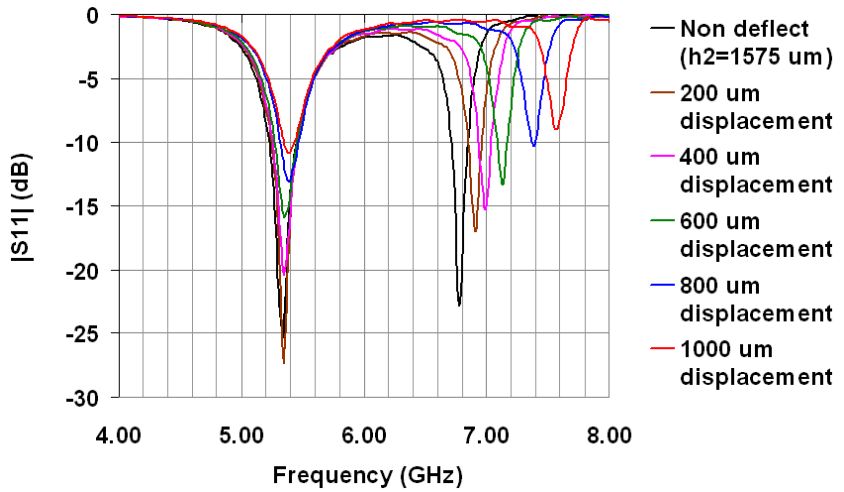

Figure 6.15. Simulated $|S_{11}|$ of 6 GHz RF transducer design of curvature approximation for the membrane deflection with Δh = 0 – 1000 μm with steps of 200 μm.

6.4.2. Prototypes and Measurements

The prototype is fabricated with Quick Circuit Systems of T-Tech Inc. (milling machine systems) [6.23]. The fabricated structure is illustrated in Figure 6.16 indicating how the layers are positioned in the prototype. The resonator prototype was excited with a coaxial probe, and the buffer layers between the upper and the lower patches, made of FR4, were positioned such that an air cavity was formed between the upper and the lower patches. In the prototype, the probe feed introduces additional inductance to L_1 of the circuit in Figure 6.7. Therefore, the length L is shortened by 2 mm with respect to W (Figure 6.1) in order to account for the frequency shift.

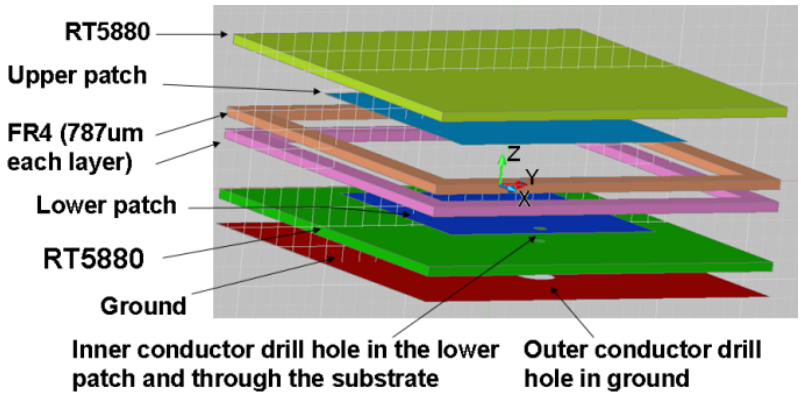

Figure 6.16. The exploded view of the fabricated prototype of the 6 GHz RF transducer scaled design.

Separated layers and the final assembled prototype are shown in Figure 6.17. The layers were held together using plastic fasteners that allow the removal of the FR4 frames. The thickness of the air cavity was determined by the number of FR4 layers stacked between the upper and lower patches. The prototype was assembled with two

different air gap thicknesses, h_2, of 787 μm and 1575 μm. The grounded metalized walls surrounding the air cavity was constructed with copper tape placed the outer edges of the prototype. The measurement results of $|S_{11}|$ of the two mechanically static prototypes are plotted in Figure 6.18. The measured radiation patterns at 5.1 GHz (performed at Satimo [6.24]) are plotted in Figure 6.19 – 6.20.

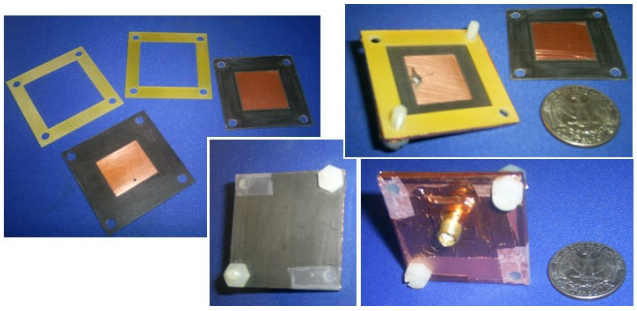

Figure 6.17. Separate fabricated layers and assembled prototype.

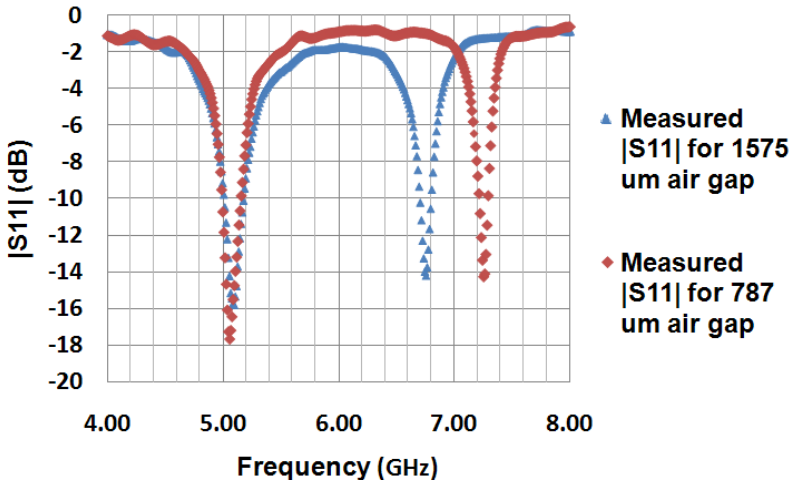

Figure 6.18. Measurement results of $|S_{11}|$ of the 6 GHz prototype of the scaled design.

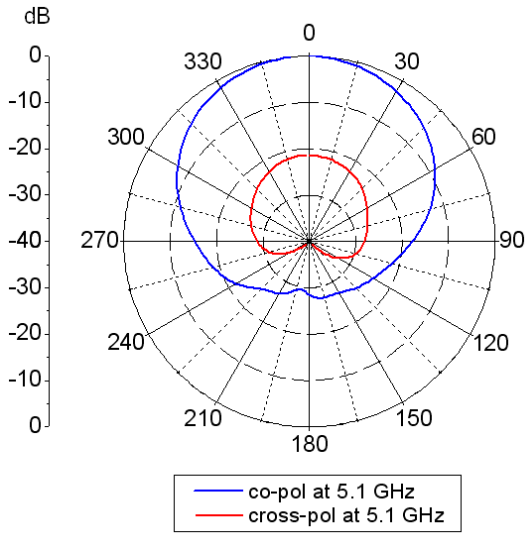

Figure 6.19. Measurements of the radiation pattern of E field on E plane (φ = 0°) at 5.1 GHz (communication channel).

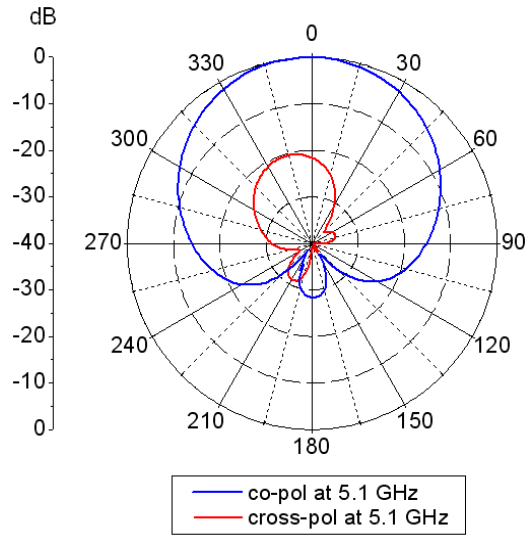

Figure 6.20. Measurements of the radiation pattern of E field on H plane (φ = 90°) at 5.1 GHz (communication channel).

The measurements of $|S_{11}|$ are in excellent agreement with the simulated results shown in Figs. 6.14 – 6.15. A shift of approximately 250 MHz (due to the air gap difference of 787 μm) is observed in the measurements. The radiation patterns recorded at 5.1 GHz are consistent with the simulated results of Figure 6.6, thus verifying the simulation results. As a proof-of-concept, the prototypes have validated the design concept proposed in this work.

6.5. Applications

6.5.1. Example Design for a Small Range of Pressure

To illustrate the adaptability of the RF pressure transducer design concept for both a different operating frequency band and a different pressure range, a different design operating in the range 65 – 95 GHz is presented here as an illustration of how this design can be potentially applied to biomedical and wearable applications with a much smaller pressure range than the one described in Section 6.2. The dimensions are as follows: L_t = 3340 μm, W_t = 4000 μm, L_p = 875 μm, W_p = 1000 μm, L = 835 μm, W = 875 μm, h_1 = 50 μm, and h_2 = 80 – 120 μm. Note that the overall size is relatively the same as the design operating in 30 – 50 GHz range presented in Section 6.2. The thickness of the Si membrane is reduced to 100 μm for a pressure response desirable for biomedical applications. Recall from (6.1) that the deflection at the center of the plate is inverse proportional to the cube of the plate thickness. The 3D model of this rectangular diaphragm is simulated in COMSOL Multiphysics [6.25] (a finite element analysis and solver software package) to derive the sensitivity of pressure, which is plotted against the deflection in Figure 6.21. The pressure is shown for values up to 0.5 bar or 375 mmHg,

which is the typical pressure range required for biomedical applications [6.4 – 6.6]. For most materials including the one utilized in this work, the mechanical limit of the membrane deflection, which is due to tensile stress, is much higher than the electromagnetic limit of the deflection. The electromagnetic limit is defined by two factors: the deflection limit at which the frequency shift no longer remains in a linear relationship with the displacement of the membrane, and the maximum deflection at which the upper metal patch remains in non-contact with the lower patch, which is determined by the air gap between the upper and lower patches. In the design presented here, the maximum deflection at which the mechanical properties of the membrane do not alter is much higher than the maximum deflections allowed by the electrical limits defined earlier. Therefore, the maximum and minimum detectable pressure values are mostly determined by the linear region of the frequency shift. As a design guideline, the maximum dimensions of the sensor should be determined first based on the appropriate frequency ranges of operation, then the choice of material is made based on the relationship of the membrane deflection and the frequency shift. For the specific choices of material and dimensions in this work, the deflection corresponding to the above applied pressure range features a sensitivity of about 1.8 μm/bar. The values of $|S_{11}|$ corresponding to different membrane deflections (h_2 = 80 – 120 μm) are presented in Figure 6.22 showing a linear shift in a wide range of deflection with a sensitivity of 152 MHz/μm. Equivalently, the frequency shift response stays linear within at least 22 bars (atmosphere pressure is 1 bar). This sensitivity corresponds to 274 MHz/bar or 365 kHz/mmHg for the frequency range of 65 – 90 GHz. The direct correlation of the applied pressure and the frequency shift in percentage is shown is Figure 6.23 showing a linear

relationship. The results show that the transducer can be scaled to operate at low pressure limit but still maintain an excellent range of linear response in terms of frequency shift.

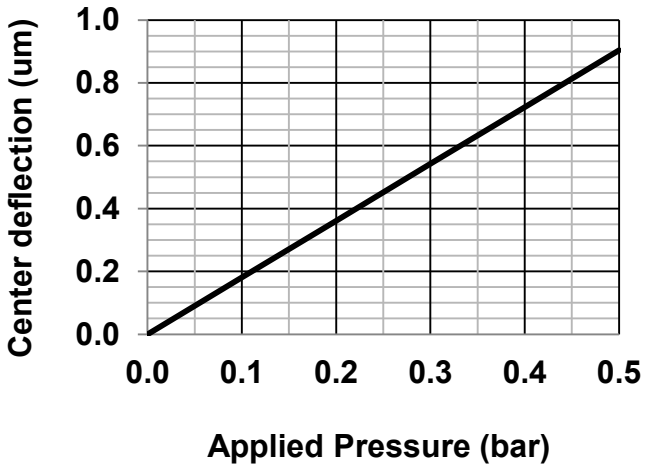

Figure 6.21. Correlation of membrane deflection and applied pressure for a Si diaphragm of 3340 μm x 4000 μm x 100 μm.

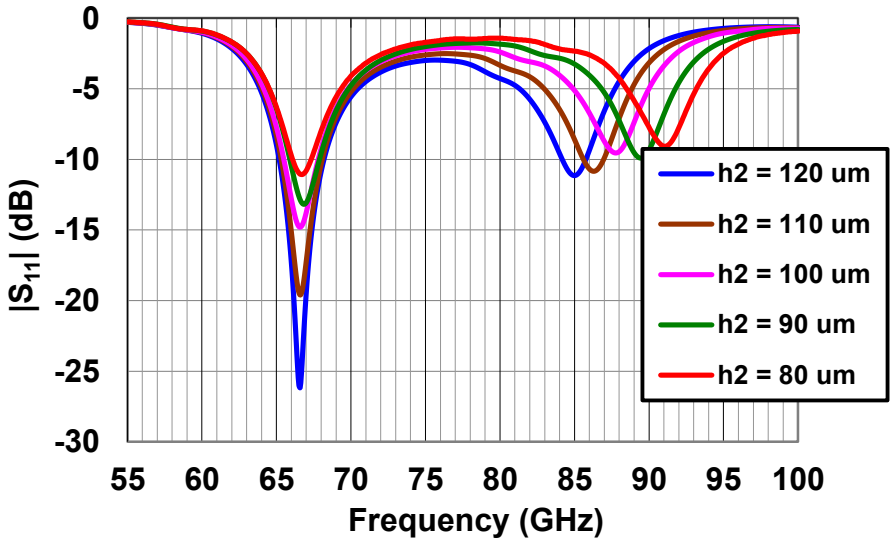

Figure 6.22. Magnitude of S_{11} of LTCC based RF pressure transducer (65 – 95 GHz range) for h_2 = 80 – 120 μm with steps of 10 μm.

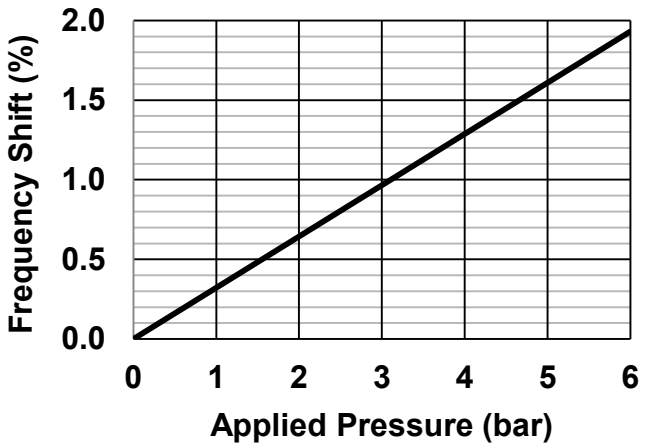

Figure 6.23. Plot of frequency shift versus applied pressure for the RF pressure transducer design at 65 – 95 GHz.

6.6. Remote Sensing, Limitations and Future Work

A new highly sensitive RF pressure transducer was presented in this chapter operating in two frequency bands, one for sensing and one for calibration. This design is simple to produce in a compact form factor and can be used to reduce power consumption of the sensor at device level, providing a sensitivity of 116 MHz/μm or 0.004% frequency shift per bar with respect to the diaphragm deflection due to pressure change, while being easily extended to 65 – 95 GHz for biomedical applications with a sensitivity of 365 kHz/mmHg operating in the range of 0 – 500 mmHg. Furthermore, the operational principles of the transducer design have been successfully demonstrated through a proof-of-concept prototype operating between 5 – 8 GHz that shows a frequency shift of 250 MHz for a deflection of 787 μm, i.e.0.318 MHz/μm . The design can also be modified to the use flexible multilayer organics, such as LCP that allow realization of wireless conformal wearable and implantable sensors. Different designs

presented in the chapter illustrate the adaptability of the design concept to different pressure ranges and operating frequencies keeping the overall dimensions the same. It is possible to implement the design in short range remote sensing where the sensor itself would act as a backscattered antenna without any additional elements, and the interrogation is performed within a few centimeters. However, to implement the design in applications such as an implantable intraocular pressure sensor, a lower frequency would be preferred for longer penetration depth, defined as the travel distance for the waves at which the radiation intensity is dropped by 37 %. The penetration depth at 85 GHz is about 0.3 – 0.4 mm for cornea, blood vessel, and skin, while the penetration depth for the same tissues at 30 GHz is 0.8 – 0.9 mm [6.26].

In long range remote sensing, the passive RF pressure sensor can be implemented as a load with changing impedance that corresponds to the pressure change. Such implementation is configured in the same platform as discussed in Section 3.5 of Chapter 3 and Section 5.5 of Chapter 5. Those chapters have also illustrated how the change of the input impedance of such a load is reflected in the frequency shift observed in the S_{11} frequency response of the load. However, the input impedance analysis of the RF pressure transducer implemented as a load is not included in the work of this Chapter. Note that, the major advantage of this design concept is that it can be implemented on the same substrate and delay-line based sensor network with the RF temperature sensor introduced in Chapter 3 and the RF strain sensor introduced in Chapter 5. All the sensor nodes of all three types of the sensors can utilize the same planar high gain antenna for the communication with the radar. Furthermore, if each sensor cell is composed of a RF temperature sensor node, a RF strain sensor node, and a RF pressure sensor, then the

pressure-independent resonant frequency of the pressure sensor node can be utilize to monitor other factors that can influence the EM resonators beside temperature, strain, and pressure.

6.7. References

[6.1] R. Puers, "Capacitive sensors: when and how to use them," *Sensors and Actuators A*, vols. 37 – 38, pp. 93 – 105, June – Aug. 1993.

[6.2] C. Mastrangelo, X. Zhang, W. C. Tang, "Surface-Micromachined Capacitive Differential Pressure Sensor with Lithographically Defined Silicon Diaphragm," *J. Microelectromechanical Sys*., vol. 5, no. 2, pp. 98 – 105, June 1996.

[6.3] G. Caliano, N. Lamberti, A. Iula, M. Pappalardo, "A piezoelectric bimorph static pressure sensor," *Sensors and Actuators A*, vol. 46 – 47, pp. 176-178, 1995.

[6.4] P.-J. Chen, D. C. Rodger, S. Saati, M. Humayun, Y.-C. Tai, "Microfabricated Implantable Parylene-Based Wireless Passive Intraocular Pressure Sensors," J. Microelectromech. Sys., vol. 17, no. 6, pp. 1342 – 1351, Dec 2008.

[6.5] R. Simons, D. Hall, F. Miranda, "RF Telemetry System for an Implantable Bio-MEMS Sensor," in *IEEE MTT-S Int. Microw. Symp. Digest*, June 2004, vol. 3, pp. 1433-1436,.

[6.6] P. Cong, N. Chaimanonart, W. Ko, D. Young, "A wireless and batteryless 10-bit implantable blood pressure sensing microsystem with adaptive RF powering for real time laboratory mice monitoring," *IEEE J. Solid-state Circuits*, Dec 2009, vol. 44, no. 12, pp. 3631 – 3644.

[6.7] M. Fonseca, J. English, M. Arx, M. Allen, "Wireless micromachined ceramic pressure sensor for high temperature applications," *J. Microelectromech. Sys.*, vol. 11, no. 4, pp. 337 – 343, Aug. 2002.

[6.8] H. Scherr, G. Scholl, F. Seifert, R. Weigel, "Quartz pressure sensor based on SAW reflective delay line," in *IEEE Ultrasonics Symp.*, San Antonio, TX, Nov. 1996, pp. 347 – 350.

[6.9] S. C. Mouslzolf, R. Behanan, R. J. Lad, M. P. Cunha, "Langasite SAW pressure sensor for harsh environments," in *IEEE Int. Ultrasonic Symp. Proc.*, Dresden, Germany, Oct. 2012, pp. 1224 – 1227.

[6.10] H. Cheng, S. Ebadi, X. Gong, "A wireless pressure sensor design using a microwave cavity resonator," in *IEEE Ant. Prop. Soc. Int. Symp.*, Chicago, IL, July 2012, pp. 1 – 2.

[6.11] M. M. Jatlaoui, and P. Pons, H. Aubert, "Pressure Micro-sensor based on Radio-Frequency Transducer," in *IEEE/MTT-S Int. Microw. Symp.,* Atlanta, GA, June 2008, pp. 1203 – 1206.

[6.12] F. Chebila, M. M. Jatlaoui, P. Pons, H. Aubert, "Pressure measurement from the radar interrogation of passive sensors," in *IEEE Ant. Prop. Soc. Int. Symp.*, Toronto, ON, July 2010, pp. 1 - 4.

[6.13] T. T. Thai, G. R. DeJean, M. M. Tentzeris, "A novel front-end radio frequency pressure transducer based on a dual-band resonator for wireless sensing," in *IEEE Microw. Symp. Digest*, Boston, MA, June 2009, pp. 1701 – 1704.

[6.14] 3D Electromagnetic Simulation Software CST (2013) [Online]. Available: http://www.cst.com/ (Accessed: June 2013).

[6.15] S. Gong, and C. Lee, "Analytical Solutions of Sensitivity for Pressure Microsensors," in *IEEE Sensors J.*, vol.1, no. 4, pp. 340 – 344, Dec 2001.

[6.16] V. L. Spiering, S. Bouwstra, R. Spiering, "On chip decoupling zone for package-stress reduction," *Sensors and Actuators A*, vol. 39, no. 2, pp. 149 – 157, 1993.

[6.17] R.L. Li, G. R. Dejean, K. Lim, M. M. Tentzeris, J. Laskar, "Design of Compact Stacked-Patch Antennas in LTCC Multilayer Packaging Modules for Wireless Applications," *IEEE Trans. Advanced Packaging*, vol. 14, no.7, pp. 361 – 363, July 2004.

[6.18] B. Gustavsen, A. Semlyen, "Rational approximation of frequency domain responses by vector fitting," *IEEE Trans. Power Delivery*, vol. 14, no. 3, pp. 1052 – 1061, July 1999.

[6.19] P. Russer, M. Righi, C. Eswarappa, W. J. R. Hoefer, "Lumped element equivalent circuit parameter extraction of distributed microwave circuits via TLM simulation," in *IEEE/MTT-S Int. Microw. Symp.*,San Diego, CA, May 1994, vol. 2, pp. 887 – 890.

[6.20] G. R. DeJean, M. M. Tentzeris, "The application of lumped element equivalent circuits approach to the design of single-port microstrip antennas," *IEEE Trans. Ant. Prop.*, vol. 55, no. 9, pp. 2468 – 2472, Sept. 2007.

[6.21] W. P. Eaton, J. H. Smith, "Micromachined pressure sensors: review and recent developments," *Smart Mater. Struct.*, vol. 6, no. 5, pp. 530 – 539, 1997.

[6.22] Rogers Corporation [Online]. Available: http://www.rogerscorp.com/documents/606/acm/RT-duroid-5870-5880-Data-Sheet.pdf (Accessed: July 2013).

[6.23] T-Tech Inc. [Online]. Available: http://www.t-techtools.com/store/ (Accessed: July 2013).

[6.24] Satimo Inc. [Online]. Available: http://www.satimo.com/ (Accessed: July 2013).

[6.25] COMSOL Inc. [Online]. Available: http://www.comsol.com/ (Accessed: July 2013).

[6.26] Italian National Research Council. *Calculation of the dielectric properties of body tissues in the frequency range 10 Hz - 100 GHz* [Online]. Available: http://niremf.ifac.cnr.it/tissprop/htmlclie/htmlclie.htm (Accessed: July 2013).

PART II.

RF SENSING BASED ON NEAR FIELD

Chapter 7.

RF Proximity Sensor for Non-Touch Human-Computer Interfaces

7.1. Introduction

Human computer interaction (HCI) has emerged as a critical link that has been setting the platform for a new wireless interaction of devices where individuals can act as human computational peripherals (computer mice, keyboards, etc…) or, in some cases, do not need to be present at all when a communication is taking place [7.1]. These platforms have gained increased popularity for use in a wide range of industries. Sensors continue to be the essential bridges that allow these types of interactions to take place. For example, pressure can be sensed remotely by sensors embedded in tires [7.2]. Motion sensors allow intelligent sensing of the human body for security applications [7.3] or for research on individuals with health conditions such as chronic pulmonary disease [7.4]. One particular area, proximity sensing, continues to be the subject of efforts for improved optimization of performance such as sensitivity and sensing range.

Research in proximity sensors has been performed for well over 50 years. Most of these sensors are derived from detecting the change of electromagnetic fields in the presence of a target [7.5 – 7.6]. They fall into two main classes: inductive proximity sensors and capacitive proximity sensors. Inductive proximity sensors have been utilized primarily the detection of metals in machinery or automotive equipment [7.7 – 7.8] or for detection of cars in traffic [7.9]. These sensors offer "non-touch" detection, but the target object has to be magnetic and induce a current in the sensor or the sensor must be

powered to detect materials that interact with the magnetic field. As a result, inductive sensing of humans is difficult to achieve. Capacitive sensors have a wider range of applications from mobile computing devices [7.10] to liquid level sensing [7.11]. A major advantage of capacitive sensors is the ability to sense objects that are in physical contact with electrodes as well as those that are not in physical contact; this is extremely useful for interacting with devices using the human hand and fingers as input tools.

Researchers at MIT expanded greatly on the idea of capacitive sensing by placing electrodes underneath the display of a portable computer [7.12]. In this approach, the electric field between two electrodes is disturbed by the presence of a human finger which facilitates a change in the capacitance. One disadvantage of this approach is the limited amount of information that can be obtained from a scalar capacitive change. This may not be suitable for complex gesture recognition. In addition, this approach operates at low frequencies where the sensitivity of sensing around the electrode can be small. Recently, researchers at Disney Research proposed a new technology called Touche [7.13]. This technology is a capacitive sensor that detects the physical contact of an electrode. It has been utilized in many instances such as with a utensil to correct eating posture and embedded in a couch to signal the presence of a human sitting down. This method expands on the scalar capacitance change of [7.12] by analyzing this change across a small frequency band which creates a signature profile that can change based on the way the electrode is contacted. Here, the electric fields are tightly confined to the electrode direct contact is necessary for sensing to take place. At low frequencies, the fields of such electrodes are mostly quasi-static, and sensing is based on field disturbances. A fundamental limitation of such an approach is that the disturbance

depends on the electrode size relative to the objects. Given a defined object size, the sensitivity and range can be improved with the electrode size, but it also increases the amount of noise in the system. Furthermore, a minimum size limitation on the electrode is highly undesirable in mobile electronics applications [7.14 – 7.15].

A new proximity sensor based on near-field perturbation of an electromagnetic wave at radio frequencies is presented. The concept of near-field sensing in microwave frequencies has been introduced in the past in various forms [7.16 – 7.18]. Electromagnetic signal propagation in the near-field has a distinct behavior from that in the far-field for a radiative element; however, it has not been exploited to extract rich multi-dimensional data through coupling to track objects. With near-field sensing, the limitation on the minimum size of the electrode is greatly mitigated because the electrodes are replaced by radiating elements, or resonators, whose sizes depend on the operation frequencies instead. The following work was developed during my Summer internships at Microsoft Research from year 2010 to year 2012 [7.19 – 7.20].

In the new proximity sensor, a two-port half-wavelength filter loaded with a resonator on the top layer is utilized. The current excited through the filter capacitively couples to a resonator patch above that allows for radiation. At certain frequencies, a small zone of near-field energy allows for a vertical range of human finger detection without physical contact with the sensor. By transmitting an electromagnetic wave over a frequency band instead of a purely capacitive electric field, the amount of information that can be ascertained can allow for complex sensing such as distinguishing a finger from a fist as well as detecting multiple hand gestures. This chapter highlights the topology of the sensor, the operating principles of the sensor, the measurement results

along with discussion, and how this sensor can be integrated into an actual system. The potential applications of this sensor design could open the door to a new class of sensing technology for HCI in ubiquitous electronic platform.

7.2. Topology of the Sensor

The proximity sensor proposed in this chapter is illustrated in Figure 7.1. This sensor consists of a two-port half-wavelength coupled band-pass filter with a resonator patch loaded above. On the bottom of the sensor lies a ground plane. The filter is sandwiched between two RT/duroid 5880 substrates with different thicknesses. The thickness of the substrate between the filter and the ground is h_1 = 31 mils. Moreover, the thickness of the substrate between the filter and the resonator patch above is h_2 = 31 mils (the total substrate thickness is $h_1 + h_2 = h$ = 62 mils). The lengths of the two substrates are also different. This difference was introduced to simplify the measurements of the design. However, in simulations presented in Section 7.3, the two substrates have the same dimensions. The lengths of the h_1 and h_2 thick substrates are represented by the parameters L_{gnd} and L_{upper}, respectively. The resonator patch is square, and the feed lines are designed to excite modes with a 50 Ω impedance. Table 7-1 presents the other parameter values of the final design. The operational frequency range of this sensor is in the C-band between 6 – 8 GHz. The operating principles of the sensor as well as thorough explanations of the design are presented in the next two sections.

TABLE 7-1

Parameter values of Final Sensor Design (in mils)

L_{gnd}	2400	L_{upper}	1400	W_{line}	56
W_{gnd}	1980	L_{patch}	500	$W_{\lambda/2}$	56
L_{strip}	600	L_{slot}	250	s	30
W_{strip}	56	W_{slot}	10	Impedance	50 Ω

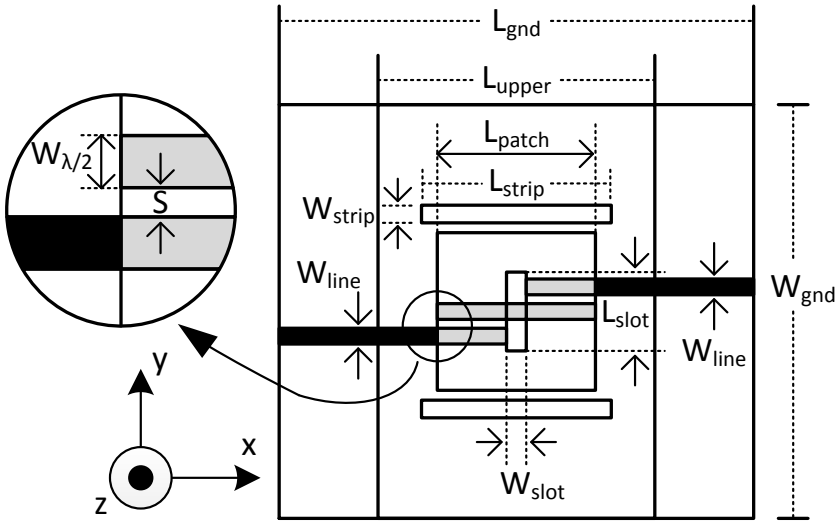

Figure 7.1. Illustration of proximity sensor design. (Dimensions are not drawn to scale.)

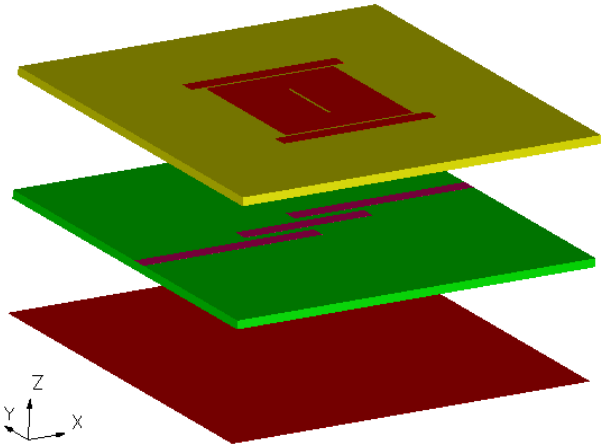

Figure 7.2. Exploded view of the sensor design.

7.3. Operating Principles of the Proximity Sensor

The sensor, a two-port filter, has a band-pass frequency response between 6 – 8 GHz. It is characterized by its S_{21} transfer function, which measures the ratio of voltage exiting *port 2* to the voltage entering *port 1* when the voltage entering *port 2* is equal to zero ($S_{21} = b_2/a_1$ where b_2 and a_1 are the voltage leaving *port 2* and the incident voltage, respectively). The detection mechanism of sensing is fundamentally based on the variations in the transfer function, S_{21}, of the filter when a human finger approaches the sensor. As the finger approaches within 3 cm above the sensor patch, its position relative to the patch induces unique signature S_{21} responses versus frequency of the filter. This uniqueness in their response allows a detection algorithm to correlate a frequency-based response to a specific finger position as well as potentially gesture recognition.

The essential idea of the sensor is to employ the near-field coupling between the human finger and the sensor resonator to influence the loading effect of the sensor, specifically its S_{21}. The filter is constructed from a half- wavelength resonator parallel

coupling filter with a finite radiation loss (a part of the insertion loss). It is this radiation loss that facilitates the coupling of the near-fields with the human finger. The radiation loss and, thus, the near-field coupling are strategically enhanced with the addition of the slotted patch and parasitic strips. The radiation field of any resonator is divided into three regions with respect to the distance, r, away from the resonator. The far-field region (also called Fraunhofer zone) with $r > \lambda_o$ (where λ_o is the free space wavelength) is where the E and H fields are in phase and the power is inverse proportional to r^2. In this region, the absorption or scattering of the radiated power has no effect on the load of the resonator, thus has no influence on the frequency responses of the resonator. The near-field region with $r << \lambda/(2\pi)$ (approximately based on the fields of a dipole antenna) is where the E and H fields are generally not in phase and the power is inverse proportional to r^3. The fields are mostly stored (as opposed to radiated) as in the case of the far-field. Depending on the type of the radiator, the near-field is dominated by either a magnetic component or an electric component, and the field patterns change with r. The intermediate-field region (also called Fresnel zone) has both the stored fields and the radiating fields with comparable distribution in intensity. In both the near-field region and the Fresnel region, the absorption and back scattering of the fields (field coupling) can influence the frequency response of the resonator (the sensor) with the stronger reactions in the near field. Therefore, the frequency of choice (where the wavelength determines the field regions) and the E and H field components are critical factors to be considered in the sensor design [7.21].

The next three subsections present the design evolution of the sensor as shown in Figure 7.3, where the ground (in yellow), the half wavelength resonator parallel coupling

filter layer (in red), and the slotted patch with the parasitic strips layer (in blue) are illustrated (without showing the substrates). The discussion starts with the half wavelength parallel-coupled microstrip line filter (model I), then a slotted patch is added to the filter (model II), and finally the parasitic strips are added to the structure resulting in the final design (model III) as presented in Figure 7.1 of Section 7.1.

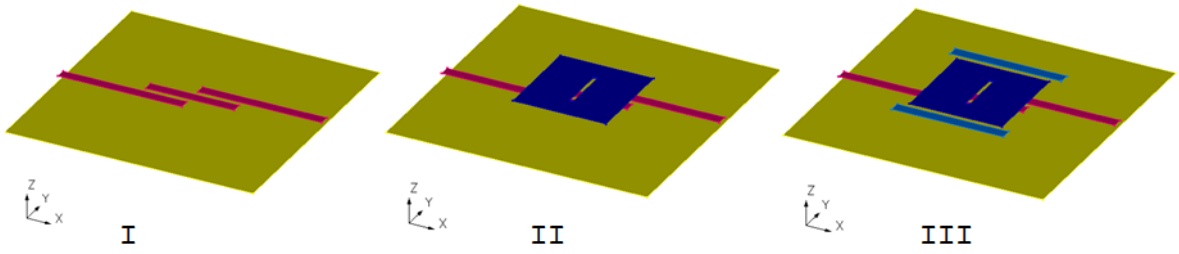

Figure 7.3. Topologies of different models in the design evolution.

7.3.1. Model I: Half-Wavelength Parallel-Coupled Microstrip (HWPCM) Filter

In this subsection, the interaction between the HWPCM filter and a human finger is investigated. A typical HWPCM filter is shown in Figure 7.4 and is based on a half-wavelength microstrip resonator (HWMR), which is the center resonator microstrip line of Figure 7.4. This topology is the same as the one shown in Figure 7.1 excluding the top substrate layer and its metallic elements. The guided wavelength (λ_g) in the designed microstrip transmission line (using a layer of RT/duroid 5880 substrate 62 mil thick [7.22]) is approximately 1300 mils at 6.5 GHz. The HWMR has a length of 590 mils, approximately $\lambda_g/2$. The operation and the design equations of the HWPCM filter are well

documented [7.23 – 7.26]. Due to the discontinuities at the two open ends of the microstrip line, a half-wavelength microstrip line can produce radiation [7.27]. The ratio of the radiated power to the incident power is proportional to the substrate thickness due to the image current on the ground [7.28]. The fundamental mode of its resonance has a maximum electric field at the two open ends. This resonant behavior is utilized to construct the band-pass HWPCM filter through the parallel coupling. The coupling mechanism can be approximately modeled with respect to the insertion loss by the simplified equivalent circuit shown in Figure 7.5, without the phase reversal at coordinates *(0,0,0)*, where Figure 7.5a shows a single coupling segment of the transmission lines and Figure 7.5b shows the equivalent circuit for the coupling line, L_q (Figure 7.4), with electrical length in degree. Detailed analysis of the classical HWPCM filter is discussed in [7.23]. Observe that the near-field power of the HWMR can be adjusted with the coupling gap, *s*, thus influencing the sensitivity of S_{21} of the HWPCM filter in response to the proximity of a finger.

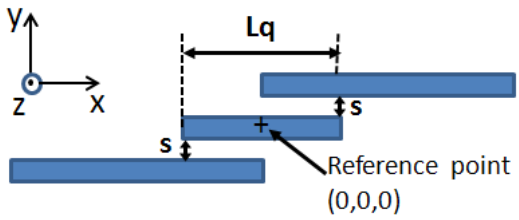

Figure 7.4. Half-wavelength resonator filter.

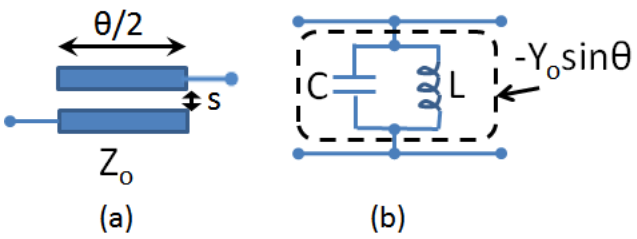

Figure 7.5. Equivalent circuit model of the HWPCM.

To illustrate the S_{21} sensitivity of the HWPCM filter in response to a finger, the finger is modeled by a water block of 400 mils x 400 mils x 400 mils (or 1 cm x 1 cm x 1 cm as a typical finger size). It is positioned at a distance, d, above the HWMR (Figure 7.6). Plots of simulated S_{21} results are shown in Figure 7.7 corresponding to different coupling gaps, s, in two cases: 1) without a water block and 2) with a water block present at d = 600 mils. Observe that as the coupling gap increases, the insertion loss also increases (e.g. lower $|S_{21}|$ at the resonant frequency) and the variation of $|S_{21}|$ is expected. At s = 50 mils, the peak resonant frequency is shifted from 6.4 GHz (without the water block) to 6.5 GHz (with the water block at d = 600 mils). A similar frequency shift occurs at s = 30 mils. A significantly smaller frequency shift occurs at s = 10 mils. The insertion loss generally consists of the conductor loss, the substrate loss, and the radiation loss. The first two factors are relatively constant for all simulated cases shown in Figure 7.7. So the different insertion loss levels associated with different s values mostly reflect different levels of the radiation loss. Furthermore, as the gap, s, increases more than 30 mils, the sensitivity of HWPCM filter (in terms of S_{21} with respect to the water block) stays relatively the same (the similar variations between the dashed and the solid lines for s = 30 mils and 50 mils in Figure 7.7). This suggests that the radiation loss of the filter,

or equivalently the near-field radiation of the HWMR, approaches its maximum level. It is this near-field radiation that is coupled to the water block and thus influences the filter response.

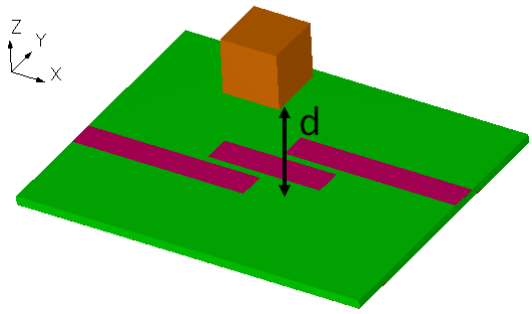

Figure 7.6. 3D view of the HWPCM and a water block positioned above it at a distance *d* in simulations.

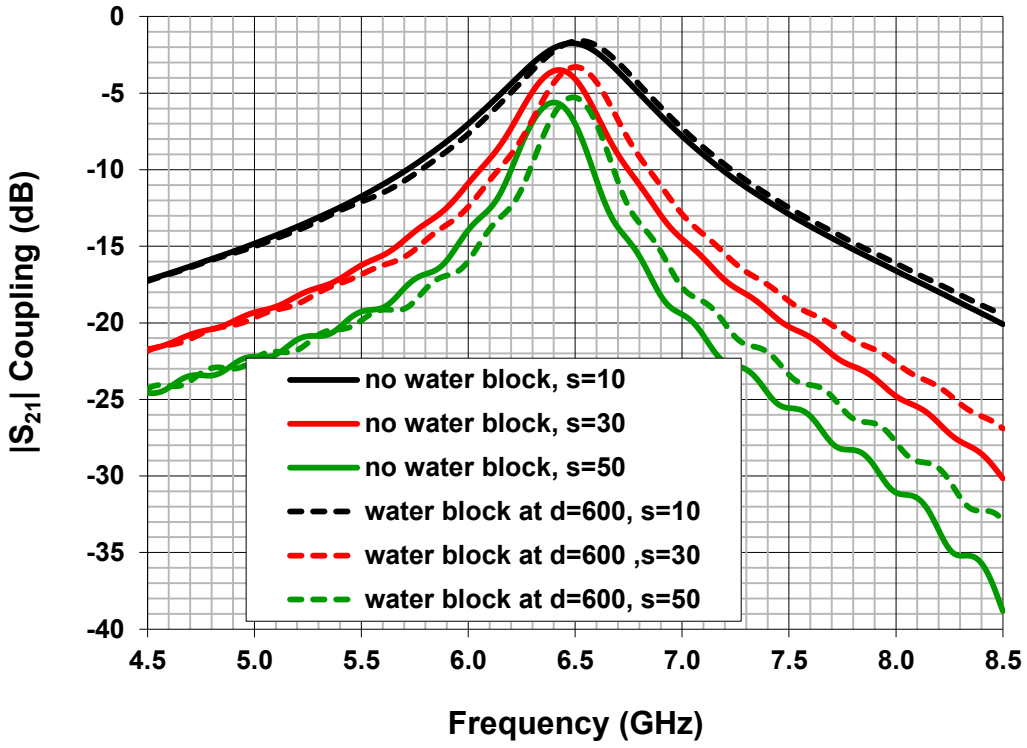

Figure 7.7. Magnitude of S_{21} of the HWPCM with different coupling gaps of s = 10, 30, 50 mils in the case without the water block and in the case with the water block at a distance d = 600 mils.

To further illustrate sensing based on the near-field coupling, the responses of the HWPCM filter operating at 6.5 GHz and at 5 GHz are compared. The water block size is 0.22 λ_o and 0.17 λ_o for 6 GHz and 5.5 GHz, respectively. The HWPCM filter is scaled up in size to operate at 5 GHz while keeping the coupling levels around -3.5 dB of the insertion loss (s is adjusted to 33 mils), which is similar to the insertion loss of the HWPCM filter at 6.5 GHz with s = 30 mil. Plots of $|S_{21}|$ for the HWPCM filter at 5 GHz are shown in Figure 7.8a and compared to those of the HWPCM filter at 6.5 GHz shown in Figure 7.8b. The solid lines represent simulation results with the absence of the water block and the dashed lines represent results with the presence of the water block at 600

mils (or 1.5 cm). The frequency shift of 30 MHz in Figure 7.8a is significantly less than 100 MHz observed in Figure 7.8b. The results show that although both frequency ranges establish the appropriate near-field regions to enable sensing based on coupling (the near-field regions start at 0.7 cm and 0.9 cm for 6 GHz and 5.5 GHz signals, respectively), this coupling also depends critically on the electrical size of the object under detection. With the water block size close to a quarter-wavelength at 6.5 GHz, the near-field can be coupled to the water block better resulting in a larger frequency shift useful for sensing in terms of $|S_{21}|$ variations. The near-field coupling mechanism also suggests a limit on how high the operational frequency can be. Otherwise, the near field region would become too small for a useful sensing range. Additionally, to keep the fabrication cost low (limited by the minimum coupling gap, s), investigations of HWPCM filters operating at higher frequencies are not included in this work.

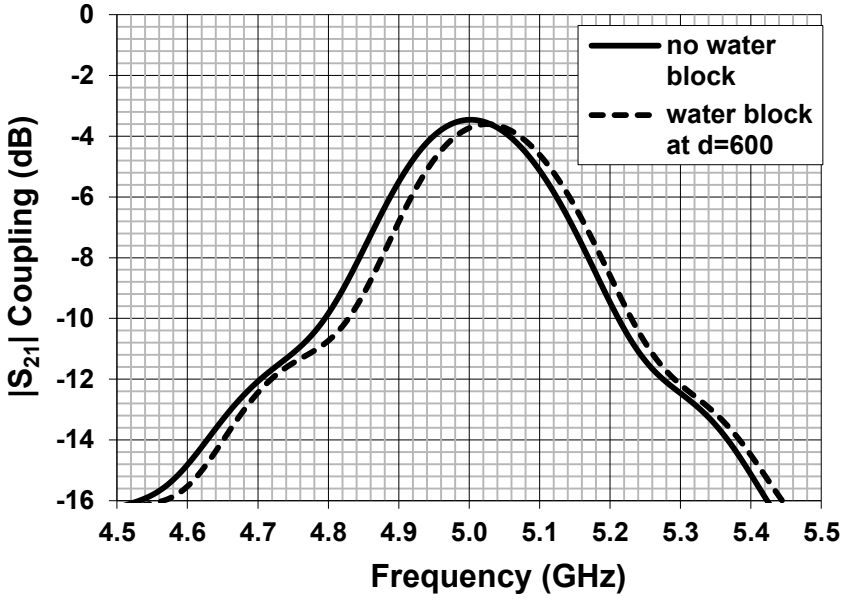

(a) 5 GHz HWPCM

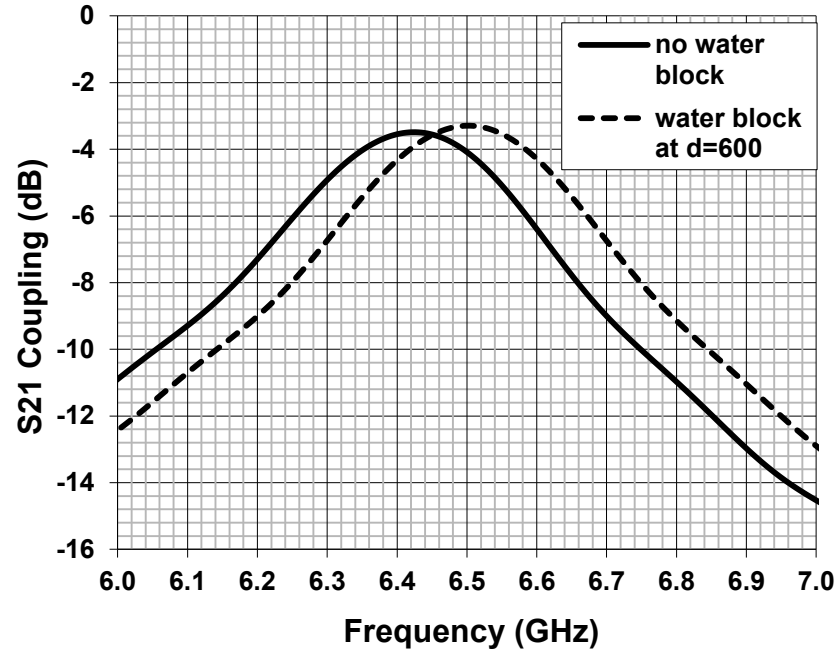

(b) 6.5 GHz HWPCM

Figure 7.8. Magnitude of S_{21} of the HWPCM with different water block settings for the operation frequency of (a) 5 GHz and (b) 6.5 GHz.

To further study the near-fields of the HWPCM filter, plots of the total electric and magnetic fields of the filter are presented in Figure 7.9 (at the resonant frequency of 6.5 GHz and the power is normalized to 1 W). The plots show the first quadrant of the model space. The figure includes the EM fields in hot scale and the surface currents in gray scale revealing one 50 Ω feed line and half of the HWMR. The plots show that the near-field is more dominant by the magnetic field rather than the electric field. Since the water block (or human finger) is a conductive object (non-magnetic), it suggests that an electric field would support the coupling better, hence allowing better sensing. Therefore, a slotted patch is added to the design.

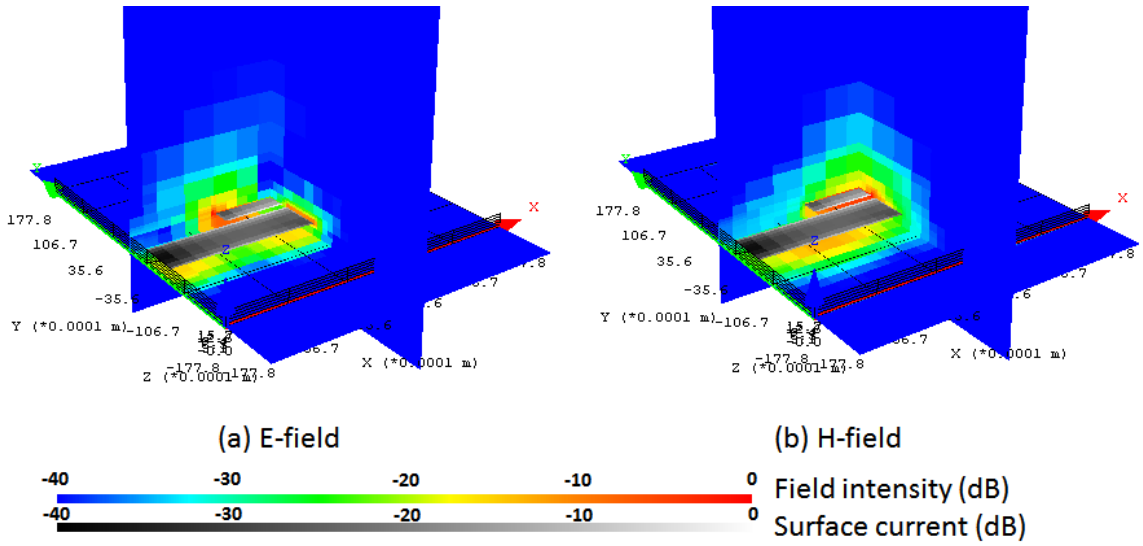

Figure 7.9. Total E-field and H-field at 6.5 GHz (power normalized to 1 W) in x- ,y-, and z-plane located at the origin in spectrum scale with the omission of the ground plane and the substrate for easy visualization (the surface currents of the feed lines and the HWMR are shown in gray scale).

7.3.2. Model II: Coupling of a Slotted Patch to the HWMR

The presence of the strong x-polarized electric field immediately above the HWMR suggests that a slot positioned along the y-axis can effectively couple to the HWMR. Therefore, a slotted patch is introduced and placed above the HWMR filter as shown in Figure 7.3. A top view is presented in Figure 7.10. A second layer of RT/duroid 5880 substrate (same as the lower substrate) separates the HWMR and the signal lines from the slotted patch. In this model, the two substrate layers are each 31 mils thick, and the HWMR is scaled to a length of 500 mils (from 590 mils in model I) to adjust for the impedance change with the presence of the parasitic slotted patch with respect to the operating frequency of 6.5 GHz. The patch is a square patch with a side length of 500 mils.

To illustrate the effects of the slotted patch, frequency responses of models I and II are shown in Figure 7.11a and Figure 7.11b respectively for five cases. Four of the cases represent simulations with the presence of the water block at distances d = 400, 600, 800, and 1000 mils, and the other case represents simulations without the water block. Observe that the sensitivity and dynamic range are greater for model II than for model I. In both models, at around 6.6 GHz, the resonant peaks are shifted both in frequency and in $|S_{21}|$ levels. The behavior of these two types of variations (frequency shift and insertion loss level change) is non-trivial due to the non-linear characteristics of the near-field. Therefore, the detection mechanism mainly relies on simple pattern recognition and the unique signature of each pattern allowing them to be differentiated from one another [7.29 – 7.31]. Besides the fact that pattern recognition is a mature subject in computer sciences, only simple algorithm is required here to differentiate

different non-linear frequency responses and can be implemented with code of size 100 kB or less in a microcontroller (see Section 7.5). In terms of the dynamic range, a good variation of $|S_{21}|$ (1 – 1.5 dB) at the resonant peak is observed in model II for d = 600, 800, 1000 mils (Figure 7.11b). For these distances, d, the variation is much smaller in model I (Figure 7.11a). In the following discussion, the frequency responses of model II are first analyzed; then, a comparison between the two models is presented.

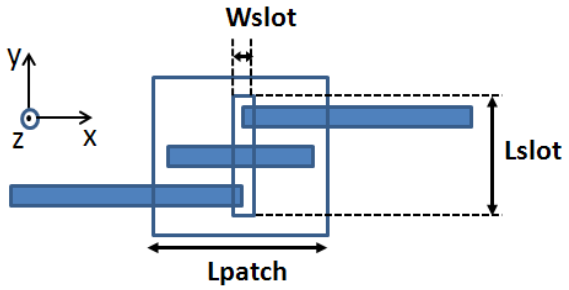

Figure 7.10. Top view of a slotted patch coupled to the HWPCM filter.

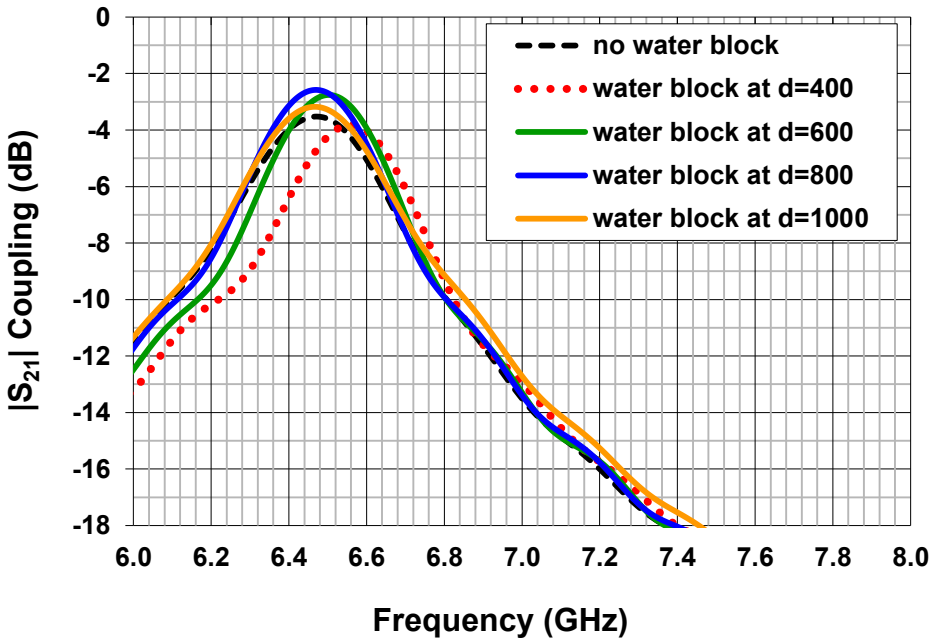

(a) Model I

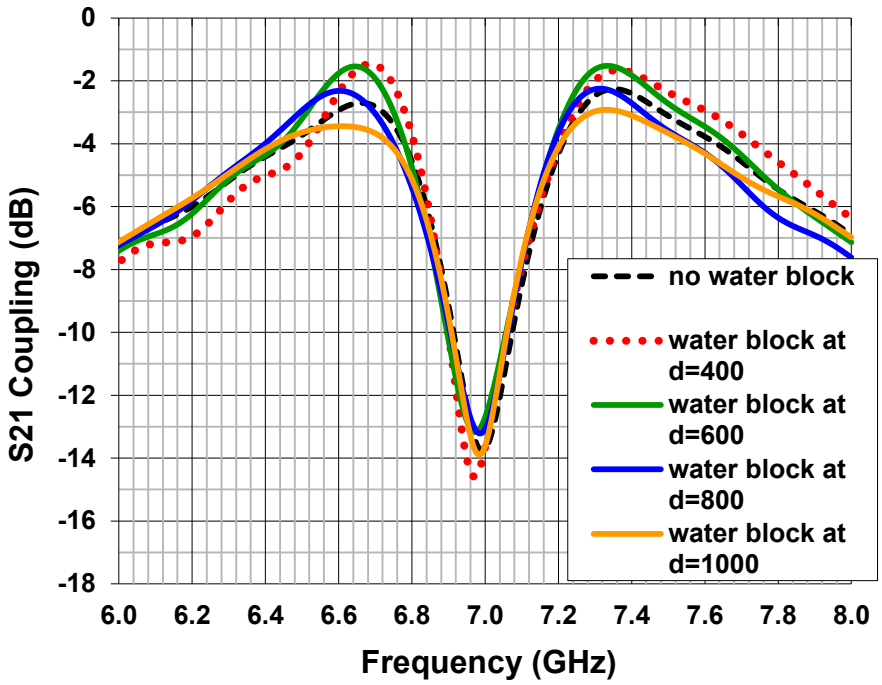

(b) Model II

Figure 7.11. Magnitude of S_{21} of (a) model I and (b) model II in four cases of d = 400, 600, 800, 1000 mils and another case with the absence of the water block.

Observe that model II exhibits two resonant frequency peaks (around 6.6 and 7.4 GHz) as opposed to only one observed in model I. To investigate the resonant mechanism of these two resonant frequencies, the surface currents and total E-field distributions of model II (without the water block) are shown in Figs. 7.12 – 7.14 with *port 1* excited. At both resonant frequencies of model II, the same fundamental mode of the HWMR appears (Figure 7.12), and it is responsible for the excitation of the slotted patch. However, two different modes are excited on the slotted patch. At the lower resonant frequency, the surface currents and the field distribution at the edges of the patch reflect the fundamental mode of a conventional patch antenna (TM_{010}). The E-field is at its maximum and uniform across the radiating edges along the y-direction (Figure 7.13a). Due to the asymmetry of the feed lines, an asymmetric perturbation on the currents is

formed, and the maxima of the E-field are shifted to the two vertices (upper right and lower left of the patch in Figure 7.13b). Thus, the second mode at 7.4 GHz reflects a hybrid mode between TM_{010} and TM_{001} of the conventional patch antenna [7.32]. In this mode, less current appears to flow around the slot resulting in a shorter current path, hence a higher resonant frequency. In terms of the cavity theory, the symmetry and the asymmetry of the E-field distribution in the slots (formed by the edges of the slotted patch with the ground) for frequency 6.64 GHz and 7.37 GHz, respectively, are illustrated in Figure 7.14.

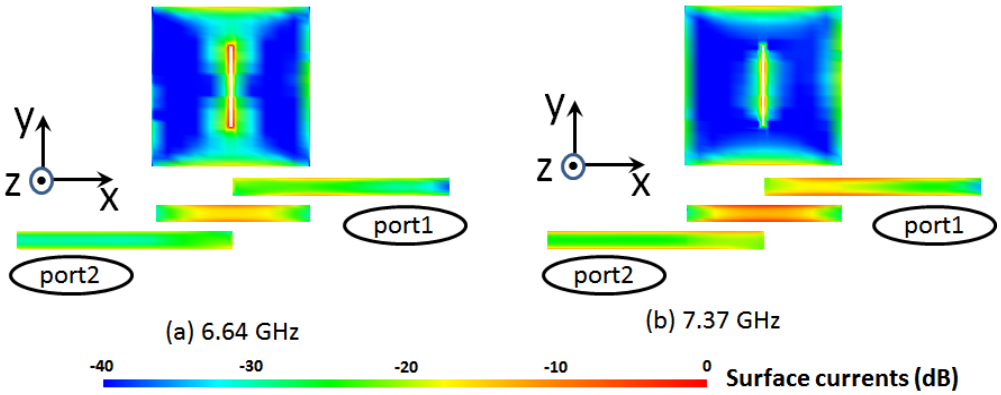

Figure 7.12. Surface currents of the slotted patch, the HWR, and the feed lines are shown for (a) 6.6 GHz and (b) 7.3 GHz with excitation at *port 1* for model II.

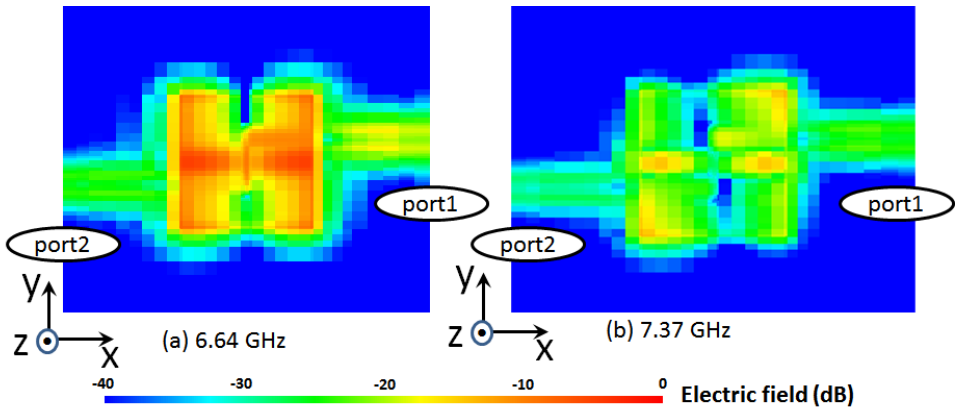

Figure 7.13. Total E-field in the z-plane located between the HWR and the slotted patch with excitation at port 1 for model II.

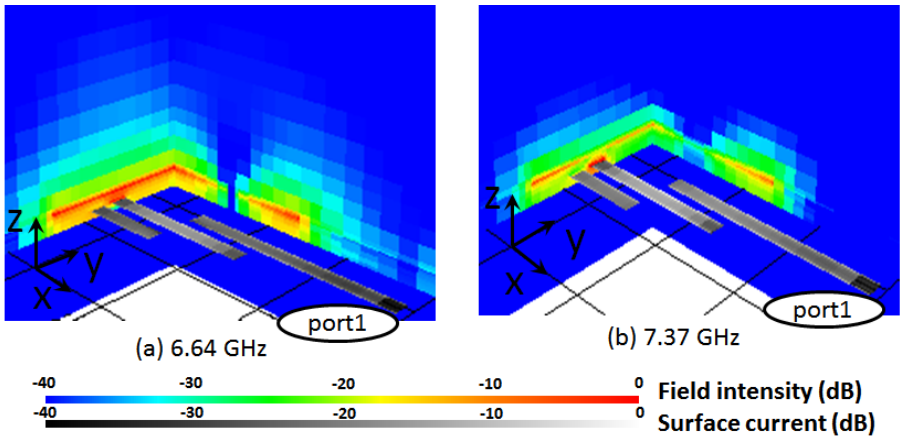

Figure 7.14. Total E-field in the x- and y-plane located at the two edges of the slotted patch in spectrum scale with the omission of the ground plane, the substrate, and the slotted patch for easy visualization for model II (the surface currents of the feed lines and the HWMR are shown in gray scale).

The addition of the slotted patch also transforms the near-field of the sensor from a more magnetic field representation (model I) to a more electric one (model II). The E- and H-field at the lower resonant frequency of model II (6.64 GHz) are displayed in

Figure 7.15. This figure includes the fields in the x-,y-, and z-plane located at the origin (the center of the HWMR in Figure 7.4) in spectrum scale and the surface currents of the slotted patch in gray scale with the omission of the ground, the substrate, the feed lines, and the HWMR. The ratio of the E-field to H-field is significantly higher in model II (Figure 7.15) than in model I (Figure 7.9). The E-field allows the sensor to couple to the water block (or a human finger) more effectively, resulting in better sensitivity and dynamic range.

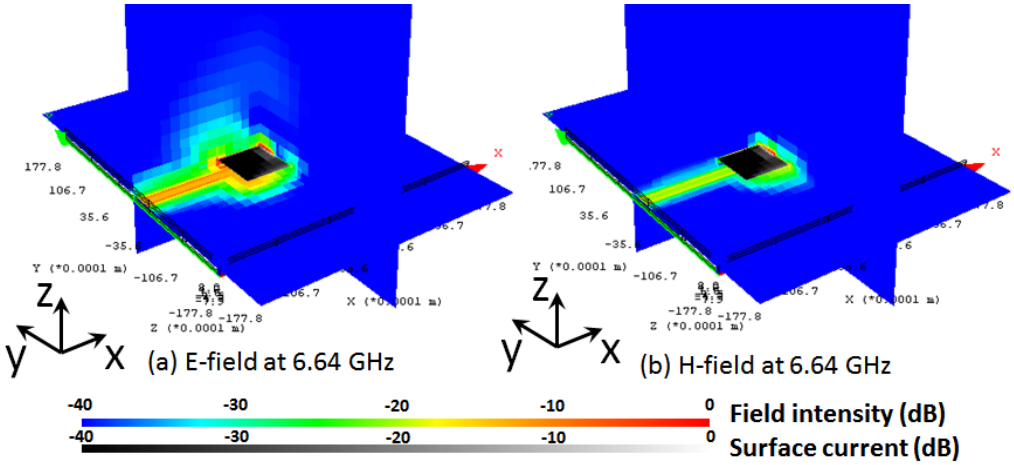

Figure 7.15. Total E-field and H-field (power normalized to 1 W) in x-,y-, and z-plane located at the origin in spectrum scale with the omission of the ground plane, the substrate, the feed lines, and the HWMR for easy visualization for model II (the surface currents of the slotted patch are shown in gray scale).

7.3.3. Model III: Addition of the Parasitic Strips

Plots of $|S_{21}|$ of the sensor of model III with the presence of the water block at various distances (d = 400, 600, 800, and 1000 mils) and without the water block are shown in Figure 7.16. The addition of two parasitic strips, as presented in Section 7.2 (all

other dimensions are the same as those in model II), alters the impedance of the slotted patch. As a result, the first resonant frequency is shifted to a lower value (6.64 GHz in model II to 6.38 GHz in model III) and the second resonant frequency is shifted to a higher value (7.37 GHz in model II to 7.68 GHz in model III). At the lower resonant frequency, the non-radiating edges of the slotted patch induce currents on the strips such that the strips become the main radiators with a high intensity of surface currents (Figure 7.17a). Consequently, the current paths at this mode are also longer, thus shifting the frequency to a lower value. In the higher resonant mode, the new impedance matches the next mode of the slot (Figure 7.17b) which is at a higher frequency than the hybrid mode observed in the upper resonant frequency of model II (Figure 7.12b). Observe that all five curves shown in Figure 7.16 have larger variations than those in Figure 7.11b of model II. Thus, the responses are more distinguishable allowing for a higher sensitivity in detection based on pattern recognition. In addition, the variation between frequency responses of d = 400 mils and d = 600 mils are much greater for model III than those of model II, thus resulting in model III possessing a greater dynamic range in sensing. Such an advantage is achieved because the strips give the sensor a higher directivity across the operating bandwidth. The directivities of the sensor (without the water block) for models II and III are shown in Figure 7.18.

To further study the variations of $|S_{21}|$ between the three models, the standard deviation of the responses shown in Figure 7.11 and Figure 7.16 were investigated. The standard deviation, σ, is a measure of how widely values are dispersed from a reference value in a sample of data. Because the detection for the sensor proposed here is based on the uniqueness of each response, high standard deviation across a frequency band implies

a higher level of uniqueness of responses in that frequency band. In a simplified model, it is assumed that the variation of $|S_{21}|$ has a lognormal distribution such that its standard deviation can be calculated as $\sigma_{dB} = \sqrt{\frac{1}{n} \times \sum_{i=1}^{n} (x_i - x_o)^2}$, where x_o is the $|S_{21}|$ in the case of no water block present (identified as the reference value), x_i is the $|S_{21}|$ value of case i (i = 1…4) corresponding to the four cases of d = 400, 600, 800, and 1000 mils, respectively, and n is the number of data points deviated from the referenced value (here n = 4) [7.33]. The standard deviation (in dB and calculated based on the five curves plotted in Figure 7.11a, 7.11b, and 7.16) is plotted versus frequency for model I, II, and III in Figure 7.19. A higher standard deviation implies a more effective detection that is based on pattern recognition. The larger the bandwidth of the high value standard deviation, the more accurate sensing can be performed in the given bandwidth. Observe that model III offers a significantly higher standard deviation across a large bandwidth than models I and II. Model II exhibits a slightly higher standard deviation consistently over a large continuous bandwidth (6.7 – 7.8 GHz), however, it is not significantly advantageous over model I in terms of offering distinctive variations.

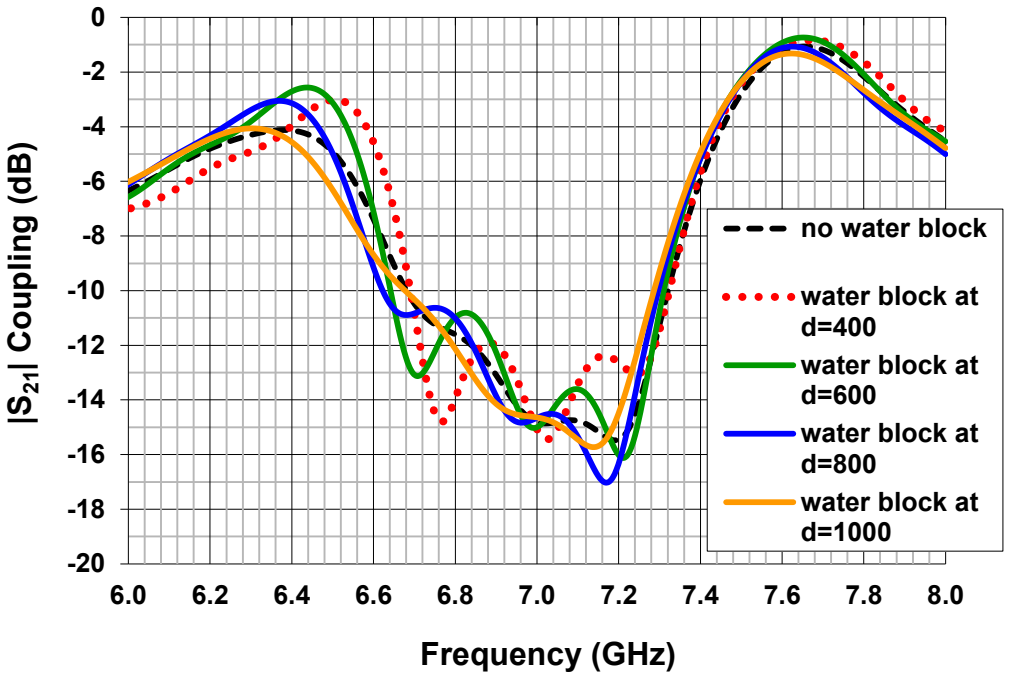

Figure 7.16. Magnitude of S_{21} of model III in four cases of d = 400, 600, 800, 1000 mils (or approximately 1 cm, 1.52 cm, 2 cm, 2.54 cm respectively) and another case with the absence of the water block.

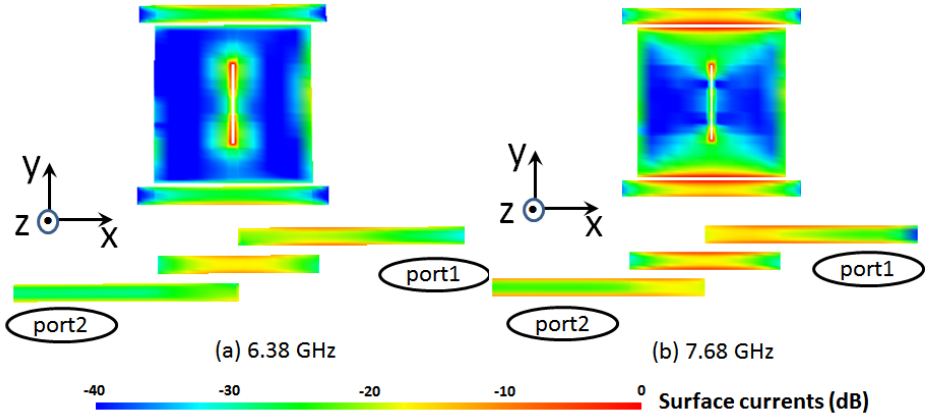

Figure 7.17. Surface currents of the strips and the slotted patch, the HWMR, and the feed lines are shown for (a) 6.38 GHz and (b) 7.68 GHz with excitation at *port 1* for model III.

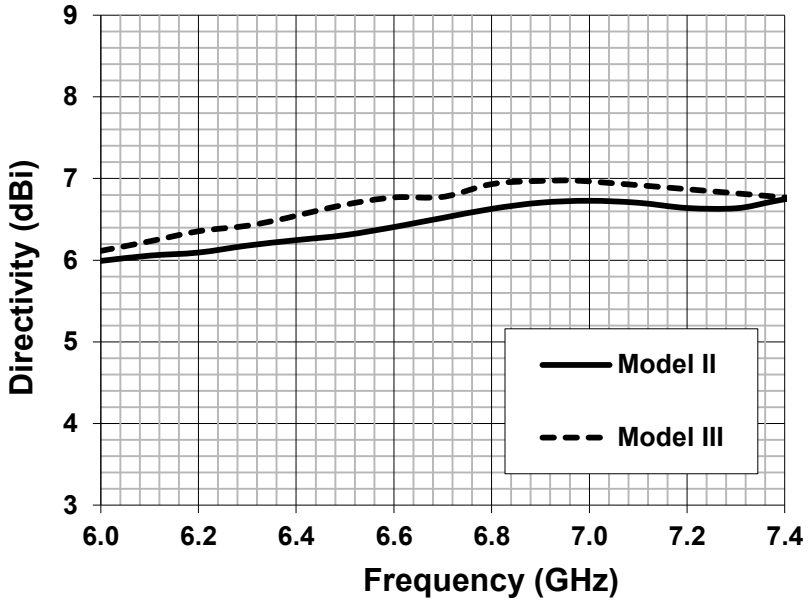

Figure 7.18. Directivities of the sensor (without the water block) for models II and III in the operation bandwidth.

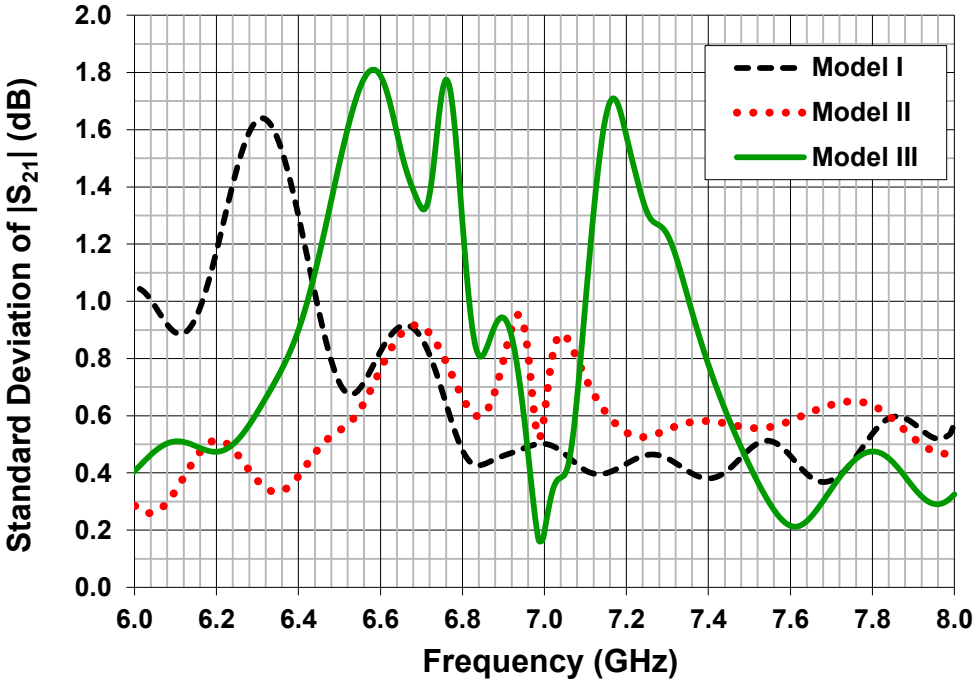

Figure 7.19. Standard deviation of model I, II, and III versus frequency.

7.4. Measurements of the Final Design Prototype

The prototype of the proximity sensor is shown in Figure 7.20a (model III). The samples were fabricated by Prototron Circuits (located in Redmond, WA). The sensor consists of two double-sided copper-clad layers of RT/duroid 5880 substrate. The bottom substrate has the HWR filter lines printed on one side and the ground plane printed on the back side. The top substrate has only the slotted patch printed on the visible side. On the non-visible side, all of the copper has been removed. The top and bottom substrates have different lateral dimensions. This sensor was fabricated in this manner to simplify the measurement procedure by allowing surface mount (SMA) connectors to be directly connected to the circuit without the need for a CPW transition. Each circuit was fabricated as a single two-sided printed circuit board (PCB) using standard fabrication methods that are inexpensive alleviating the need for a more costly multilayer circuit. (Although multilayer circuits are traditionally inexpensive when designed on FR4 materials, the use of RT/duroid 5880 materials increases the complexity of the fabrication which, in turn, can significantly increase the cost.) The boards are brought in contact with each other and held together by four plastic screws and nuts. The length of the screws allows the sensor to be elevated a few centimeters above the surface to further simplify the connection of the measurement cables to the SMA connectors. Note that this fabrication procedure is done solely to prove the concept of the sensor itself and this can only be performed in the absence of vias in the structure. To integrate this circuit into a package, standard multilayer circuit methods would need to be utilized.

The scattering (S-) parameter measurements were taken on an 8510 vector network analyzer (VNA). The calibration is performed to the end of the cables. At around

6.5 GHz, the cable attenuation is less than 0.03 dB. The interface of the cables is 2.4 mm size. Therefore, low loss adapters (maximum VSWR of 1.05:1 at 6.5 GHz) that transform 2.4 mm size to SMA size are placed between the end of the cables and the SMA connectors. The measurement setup is shown in Fig 7.20b, where the fingertip is positioned at different distances above the sensor. Measurements of the coupling of energy from *port 1* to *port 2* (S_{21}) in the presence of a human finger at vertical distances of 2, 5, 10, and 20 mm were taken. Figure 7.20c illustrates the measurement apparatus. Since it is difficult for a human to maintain a steady finger over the sensor without altering the vertical position, styro-foam sheets (with dielectric constant approximately identical to that of air) of 2, 5, 10, and 20 mm thickness were placed above the sensor and used as spacers. Note that careful efforts were performed in placing the fingertip in gentle contact with the styro-foam spacers to exert no extra pressure.

A plot of the S_{21} coupling versus frequency is displayed in Figure 7.21. In this plot, the coupling is recorded when the human finger is displaced by d = 2, 5, 10, and 20 mm above the sensor. Additionally, the case when no finger is present is also recorded. It can be seen in the measurement that each placement of the finger creates a unique signature response of the sensor. It is essential to note that the purpose of this research is to design a proximity sensor to sense different positions of a human finger in close proximity to the sensor. Therefore, the uniqueness of the signature response is the important parameter considered by this plot. In essence, if the intent was to design a filter, this design would be unacceptable mainly because the pass band S_{21} coupling is too low. On the contrary, a proximity sensor is created by utilizing the strong coupling aspects of a HWR filter coupled to a slotted patch, enabling a mechanism for a leakage of

space waves. The minimum threshold value of $|S_{21}|$ in a small band of frequencies centered at around 6.5 GHz is dependent on the minimum detectable level of the power detector discussed in the next section. The maximum $|S_{21}|$ for the vertical placements considered in this plot varies from by as much as 3 dB. Using a small band as opposed to a single frequency helps to distinguish the signature curves from one another. This feature is essential in non-linear sensing and is advantageous when a pattern recognition scheme is employed. For example, the $|S_{21}|$ values at d = 5 and 20 mm are the same at 6.6 GHz, but if a band of frequencies around 6.6 GHz is analyzed, it is evident that the responses at d = 5 and 20 mm are clearly unique to each other. The S_{11} curves exhibit the same uniqueness as the S_{21} curves, but the S_{21} responses are selected to integrate this sensor into a practical system as described in the next section due to the ease of signal reading and lower noise level.

One interesting aspect to note in the measured results of Figure 7.21 is the existence of a spike in the magnitude of S_{21} at around 7.5 GHz. Although this artifact is present in each of the measured responses, it is absent in the simulations. It can be suggested that this spike is due to an imperfection in the device-under-test (DUT) samples used in the measurement. This conclusion is reached after an investigation into the cause of this spike was conducted. During the investigation, the standard short-open-load-thru (SOLT) calibrations were performed and the S-parameters of different two-port circuits were measured between the cables including a simple microstrip line, a phase shifter sandwiched between a microstrip line, and an old band-pass filter that operates between 6 – 9 GHz (that was fabricated some time ago by a different company for a different project). Additionally, the two cables of the VNA were connected directly, and a

direct S_{21} measurement was performed. In all of these samples, it was noticed that no imperfection in the responses. This leads to the belief that the cables and adapters indeed function properly, but imperfections in the samples are the cause of the spike in the S_{21} response at around 7.5 GHz. Obtaining another batch of samples from the manufacturer (or a different one) and performing measurements of those could prove or disprove the suggestion, but increase in manufacturing cost does not justify this approach especially since the spike in the response does not affect the significant information obtained in the unique signature.

A plot of the standard deviation of the measured S_{21} responses is presented in Figure 7.22. It was calculated in the same way as performed for the plots in Figure 7.19. Overall, the plot shows high stand deviation values in the operating band of 6 – 7 GHz, comparable to the green curve (simulated model III) in Figure 7.19. Both curves (from simulation and measurement results of model III) share the same topology in the band 6 – 7 GHz. Note that in measurements, responses for very short distances between the fingertip and the sensor (d = 2 cm, 5cm) are included, which were not investigated in the simulations. At those distances, the inherent non-linearity of the near-field is exhibited stronger in its responses to disturbances (brought forth by the fingertip), resulting in higher standard deviation values for the measured results in the band 7.0 – 7.5 GHz. Consequently, the measurements show support for the near-field sensing concept and detection based on the pattern recognition platform that is proposed here.

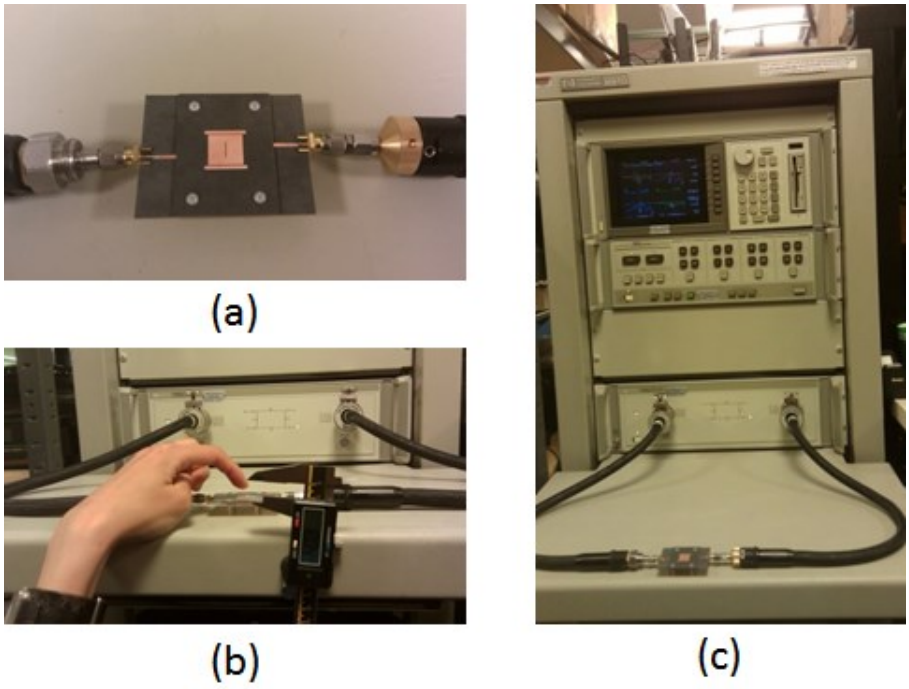

Figure 7.20. Illustration of (a) the proximity sensor, (b) the measurement setup, and (c) the process of the measurement.

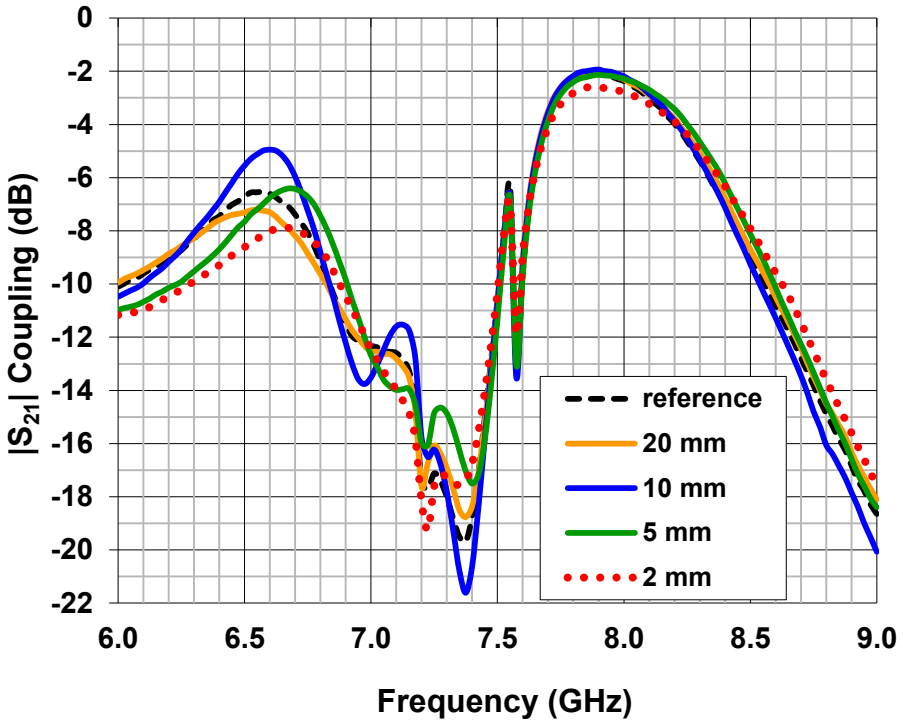

Figure 7.21. Measurements of S_{21} corresponding to a human finger positioned at 2, 5, 10, 20 mm above the sensor and a reference response when no finger is present.

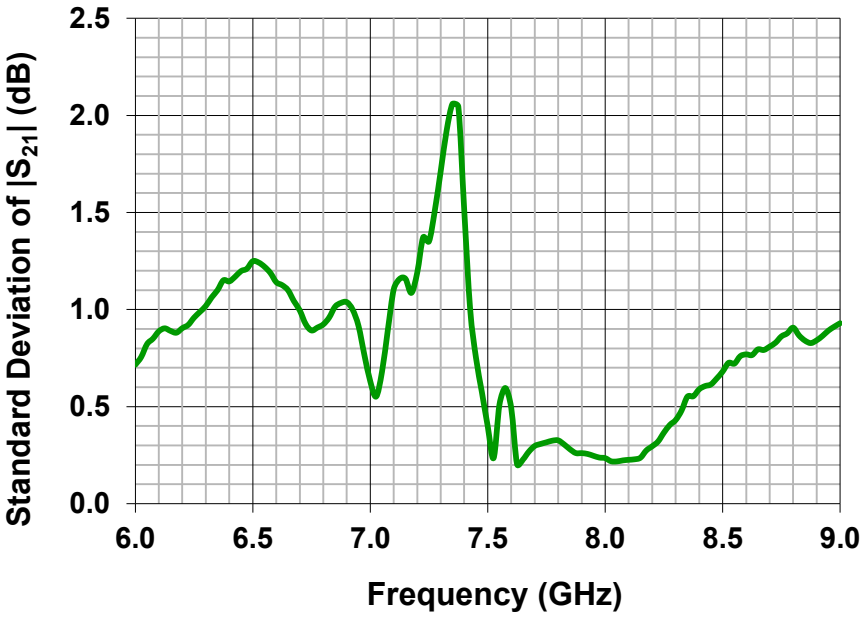

Figure 7.22. Standard deviation of the measured $|S_{21}|$ of model III prototype.

7.5. System Integration

The proximity sensor is integrated into a proof-of-concept system to demonstrate its use. The system diagram is shown in Figure 7.23. The sensor prototype presented in Section 7.4 is excited by a voltage control oscillator (VCO) and the signals are detected by a power detector (PD). A microcontroller (MCU) is used to control the VCO and read and process the output voltage from the PD. An algorithm is implemented on the MCU to decode different positions of the approaching finger and turn on the LED as an indicator (Figure 7.23).

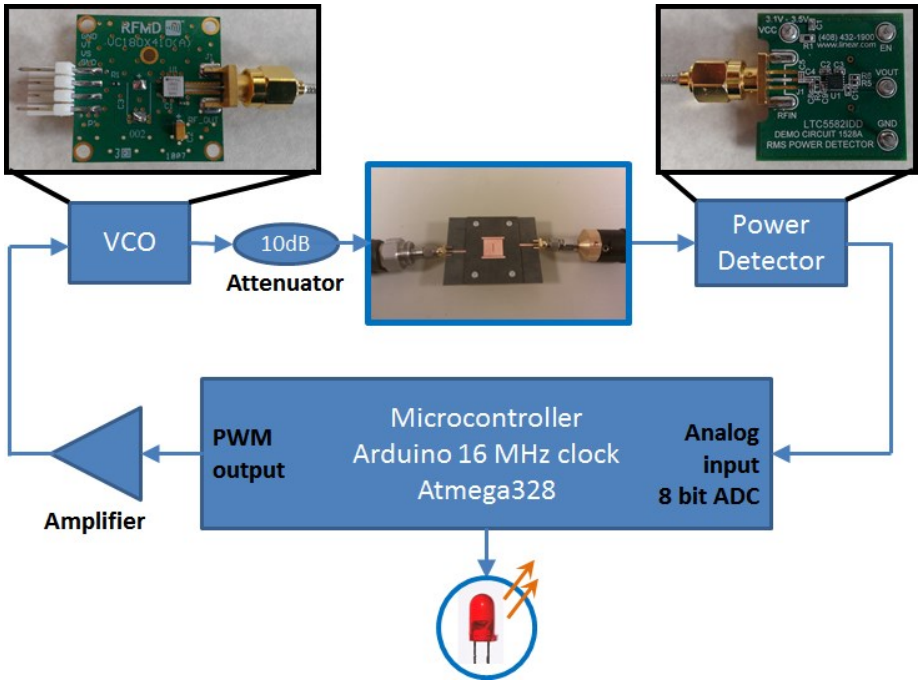

Figure 7.23. Proof-of-concept system integration for the HWR proximity sensor.

The microcontroller utilized here is the Arduino Uno R3 board based on Atmega328 with clock running at 16 MHz [7.34]. The VCO is the evaluation board for

the chip HMC586LC4B from Hittite, low noise wideband MMIC VCO with buffer amplifier operating from 4 GHz to 8 GHz [7.35]. The PD is the evaluation board for the chip ADL5902 from Analog Devices, having a dynamic range of 65 dB rms-to-dc conversion from 50 MHz to 9 GHz [7.36]. All three boards are powered at +5 V. The VCO input is called Vtune and it accepts 1 – 16 V corresponding with output signals in the frequency range 4 – 8 GHz. In this system, the voltage range from 7 – 13 V was used to generate signals in the range approximately 5.8 – 7.5 GHz range. To correctly tune the VCO, the Arduino board is programmed to output a pulse-width-modulated (PWM) signal. PWM is a technique to obtain analog output voltage with a digital clock. Digital control is used to create a square wave, switching at a rate of 62.5 kHz between on (5 V) and off (0 V) states. The switching rate is found to be fast enough to appear on average as a fixed voltage level at the VCO such that monochromatic output signals can be achieved from the VCO. To achieve varying analog values, the pulse width (duty cycle) is modulated. At the MCU, a call to PWM takes an integer from 0 – 255 that outputs a corresponding duty cycle from 0 – 100 %. The PWM output is then amplified (inverted) with a simple negative feedback loop designed based on the opamp LT1632 (45 MHz) from Linear Tech [7.37]. The MCU sweeps through different duty cycles to map the output PWM into the analog range 7 – 13 V as desired. The PD accepts an input power from -60 dBm to 0 dBm and maps it to the range from 0.5 – 3.5 V linearly. Therefore, an attenuation of 10 dB is used at the output of the VCO. Output signals from the PD are fed into an analog input of the Arduino board, which converts an input voltage range, 0 – 5 V, to a digital value between 0 and 1023 (10 bit ADC). Raw data received at the MCU is presented in Figure 7.24, with different responses corresponding to the reference state (no

finger presence), the presence of the finger at 2 cm and 1cm above the slotted patch, and when the finger touches the center of the slotted patch. The PWM duty cycle index (on the scale of 0 – 255) of the x-axis corresponds to the frequency range of approximately 6.2 – 7.2 GHz. The analog input reading, which is represented in digital values after the conversion done by the ADC on the Arduino board as mentioned, is shown on the y-axis of Figure 7.24.

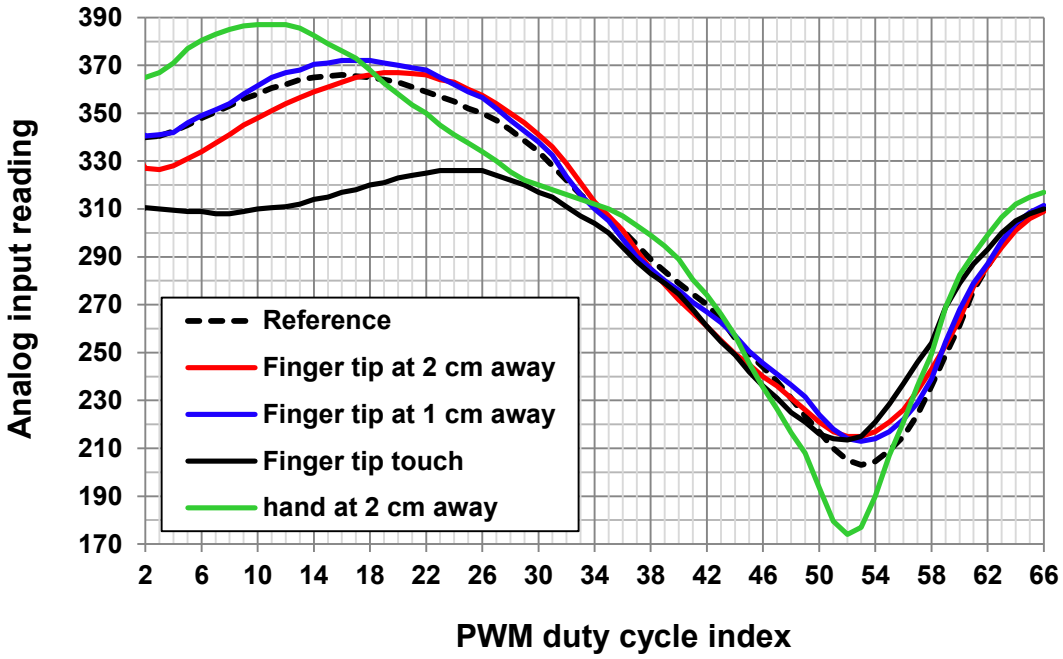

Figure 7.24. Raw data at the ADC input of the Arduino board.

Data shown in Figure 7.24 is recorded and processed in the MCU according to the state machine summarized in Figure 7.25. First, the MCU sweeps through the bandwidth. If calibration is initiated by the user's input, then the output array (represented by the dashed line in Figure 7.24) is recorded and stored as the reference (average of 50

sweeps). The reference appears to be stable with negligible variations over different calibrations. Characteristics of the curve such as the maximum, the minimum, the slopes, and others are calculated and stored. If calibration is not initiated, every 10 sweeps is recorded, averaged, and compared to the reference with respect to the characteristics derived during the calibration. The distinction between unique signatures of the reference state, fingertip positioned at 1 cm and at 2 cm, fingertip touching the surface, and hand palm positioned at 2 cm away allows us to reliably differentiate those states. The significantly unique patterns of the black and the green curves (fingertip touching and hand palm gesture) illustrates that a deliberate pointing gesture can be easily differentiated from a hand palm gesture or a touch. The state machine can also reject the presence of the palm instead of the finger. Further machine learning may be applied to differentiate different finger gestures such as approaching with a finger at a 90° angle to the sensor surface as opposed to approaching with a finger at 30° angle to the sensor surface. Arduino code for the state machine is included in Appendix A.

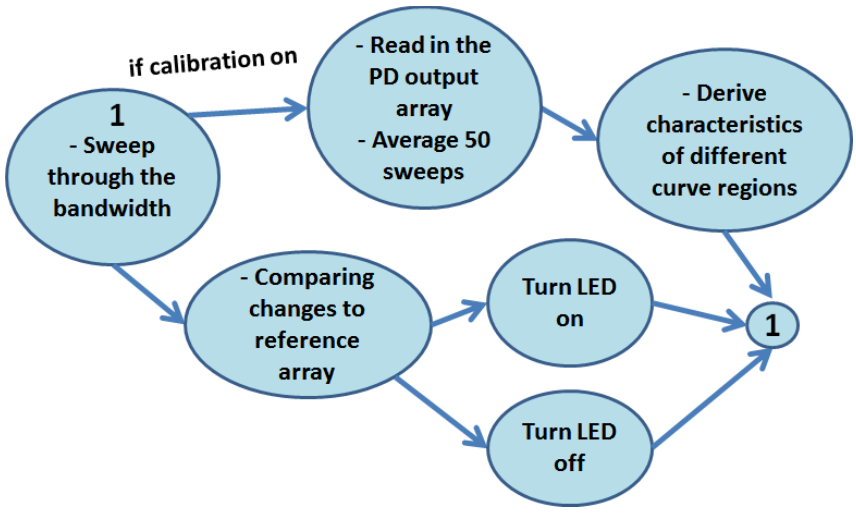

Figure 7.25. State machine in detection.

7.6. Development of Multiple sensor Board

Due to the confinement of the near-field that results in small interference, a multiple sensor board was developed that could potentially enable high sensitivity of detection in lateral directions. To scale up the sensor cells for big panel/display applications, the circuit portion between the VCO and PD in Figure 7.23 is replaced by the following network of components, where switches are used for a single pair of VCO/PD to connect an array of 4 x 8 sensor cells (32 sensors total). The RF switches are SP4T and SP8T [7.38 – 7.39], which are broadband non-reflective switches covering from DC to 8 GHz with high isolation and low insertion loss. With this new topology, the MCU in Figure 7.23 is replaced by a TI MSP430 that features ultralow power consumption with a clock running at 16 MHz [7.40]. The switch network allows a single cell to be turned on and read data over the desired frequency band of 6 – 8 GHz. The microstrip lines that are composed by the ground plane and the filter layer as shown in Figure 7.2 are replaced by the coplanar waveguide here to reduce two metal layers to one layer. The final layout is shown in Figure 7.27, where the blue color shows the top metal layer consisting of the slotted patches, the yellow color shows the middle metal layer consisting of the filters and the RF traces, and the red color shows the bottom metal layer consisting of DC traces. The substrates are Rogers materials [7.22] with a thickness of 32 mils each. The proof-of-concept prototype of the sensor array is presented in Figure 7.28. With the switch topology as presented, each sensor cell is scanned through the operating bandwidth, which takes about 550 ns accounting for delays due to VCO, MCU, ADC, and PD. For a single reading of the entire board, the total delay time is less than 2.5 ms, which is five times less than the current latent time of a capacitive sensing grid (10 – 15

ms). The detection of this board is based on a pattern-recognition and machine-learning algorithm written by Ran Gilad-Bachrach in the machine learning group of Microsoft Research in Redmond [7.19]. Therefore, the detection and measurements of the board are excluded from this thesis, whose objectives are to show the development of the hardware platform. Nevertheless, the detection is based on the same concept presented in Section 7.5.

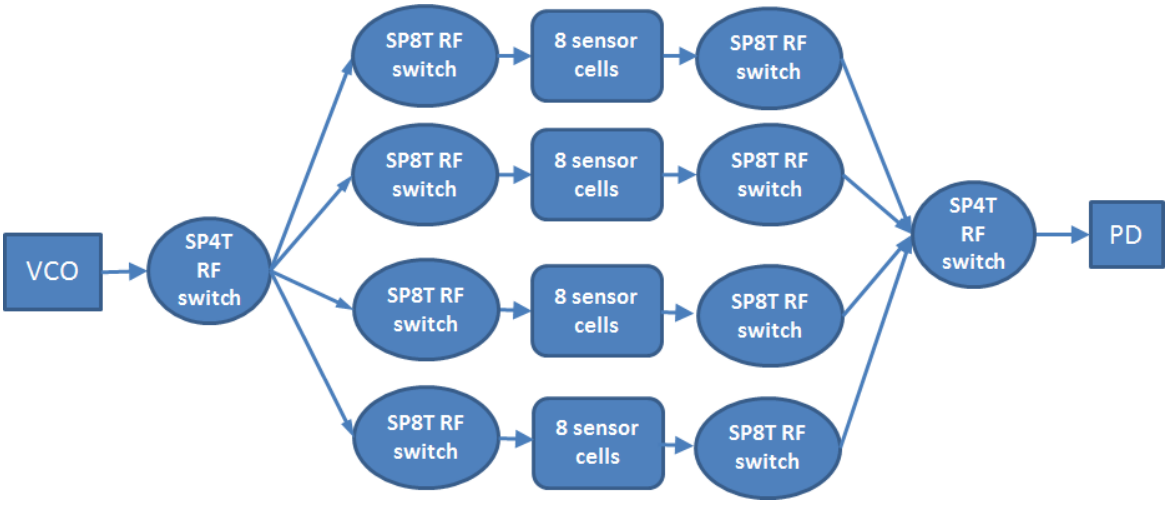

Figure 7.26. RF network for the 4 x 8 sensor array.

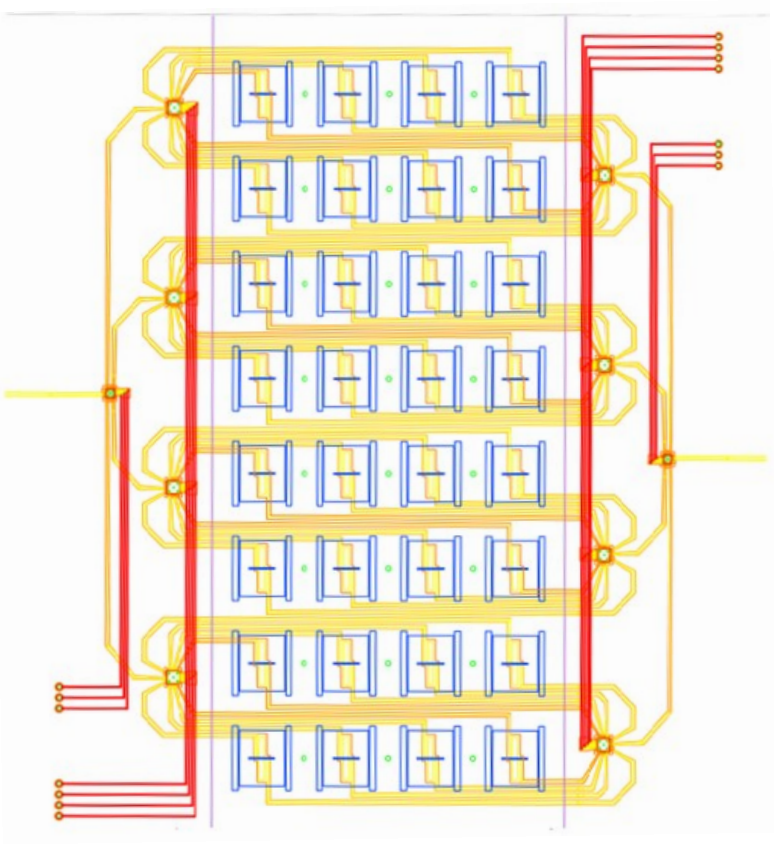

Figure 7.27. Layout of multiple proximity sensor cells using a single pair consists of a VCO and a PD.

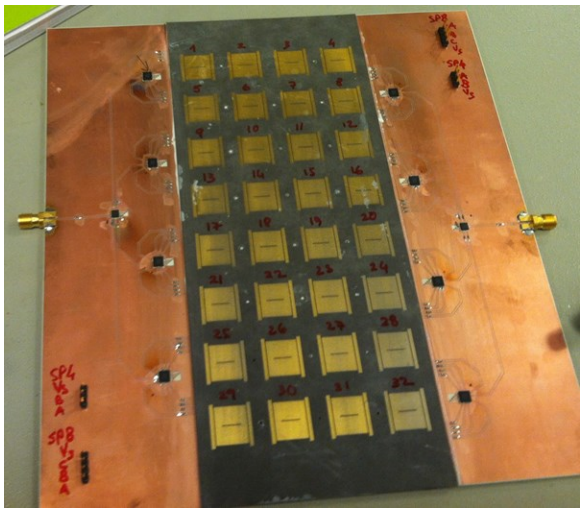

Figure 7.28. Proof-of-concept prototype for 4 x 8 sensor board.

7.7. Conclusions and Future Work

A new proximity sensor based on near-field perturbation of an electromagnetic wave at radio frequencies is presented. This sensor can sense the vertical position of a human finger above the device. This device utilizes a slotted patch with accompanying parasitic strips suspended above a two-port half-wavelength parallel-coupled microstrip (HWPCM) filter. The sensing is performed by examining the coupling responses of the filter versus frequency as a human finger approaches the interrogation zone. Each finger position produces a different response that can be used to create a unique signature over a defined frequency band. Thorough explanations of how this sensor functions along with measured results, discussions, and a specific method of integrating this sensor into a system-level architecture have all been covered. This sensor is a proof-of-concept, and research into these methods can be implemented into several practical applications such as a component which enables transparent displays for mobile devices allowing a high capacity of sensing data or a non-touch interface for medical equipment where sanitation can be significantly improved for communicating with devices in surgical rooms. The current touch technology of capacitive electrodes has been improved with faster chips so the low SNR of the small capacitive change of the electrodes was improved to track fingers 1 – 3 cm above the sensor surface [7.41]. However, the technology is limited by its operating principle in scaling up to big displays or panels. The major difference between the current capacitive technology and the proximity sensor proposed in this thesis is that the former relies on current level changes while the latter utilizes the voltage ratio (S_{21}) over a broad band of frequencies. The threshold limited by Ohmic loss in the metal traces would dominate any signal processing algorithm performed by the chips in a

large area of sensors. The voltage ratio is more immune to the Ohmic loss and can be improved through different stages of amplification. The response time and latency of the capacitive technology is also limited by the capacitive charging time because the electrode size has a lower limit for the capacitive change to be detected. Latency in the new proximity sensor depends on the switching speeds of the VCO, MCU, ADC, and PD which are improved at a constant pace. The sensor, the first of its kind, offers a large amount of data close to that offered by a camera, yet it carries the thin planar form of a touch capacitive surface. Learning-machine algorithm implemented in signal processing allows non-linear characteristics of the sensor to be an advantage, where rich multi-dimensional information encoded in the responses can become informative. For example, it is possible to recognize finger gestures besides registering fingertip positions based on a single sensor cell. The disadvantage is the complexity to be implemented in the signal processing stage. Future work will focus on investigation of the sensitivity of sensing at smaller intervals of human finger placement along with statistical analysis that can assist in the development of more robust machine learning algorithms. Further characterization and optimization can be performed for the multiple sensor board, which potentially may allow for a full three-dimensionally implemented sensing platform. Transparent electrodes based on indium-tin oxide currently utilized in touch displays can be adapted to construct the multiple sensor board for display applications.

7.8. References

[7.1] T. Saizmaa, H. -C. Kim, "A holistic understanding of HCI perspectives on smart home," in *Int. Conference on Network Computing and Advanced Inform.* Manage, Gyeongju, 2008, pp. 59 – 65.

[7.2] A. Pohl, F. Seifert, "Wirelessly interrogable surface acoustic wave sensors for vehicular applications," *IEEE Trans. Instrum. Meas*., vol. 46, no. 4, pp. 1031-1038, Aug. 1997.

[7.3] B. Song et al., "Surveillance tracking system using passive infrared motion sensors in wireless sensor network," in *Int. Conference on Inform. Networking,* Busan, South Korea, 2008, pp. 1 – 5.

[7.4] E. Jovanov et al., "A wireless body area network of intelligent motion sensors for computer assisted physical rehabilitation," *J. Neuroengineering and Rehabilitation*, vol. 2, no. 6, pp. 1 – 10, Mar. 2005.

[7.5] J. L. Carr et al., "Development of a method to determine operator location using electromagnetic proximity detection," in *Int. Workshop on Robotic and Sensors Environments*, Phoenix, AZ, 2010, pp. 1 – 6.

[7.6] K. Koibuchi et al., "Loss estimation and sensing property enhancement for eddy-current-type proximity sensor," *IEEE Trans. Magn.*, vol. 42, no. 4, pp. 1447-1450, Apr. 2006.

[7.7] Balluff Inc. Untitled [Online]. Available: http://www.balluff.com/balluff/MUS/en/products/Inductive-Sensors.jsp (Accessed: 16 Oct 2013).

[7.8] Pepperl+Fuchs Inc. Untitled [Online]. Available: http://www.pepperl-fuchs.com/global/en/classid_142.htm (Accessed: 16 Oct 2013).

[7.9] *Anonymous. It's go time. How do traffic light sensors work?* [Online]. Available: http://www.curiousread.com/2008/01/its-go-time-how-do-traffic-light.html (Accessed: 16 Oct 2013).

[7.10] F. Aezinia et al., "Touchless capacitive sensor for hand gesture detection," in *IEEE Sensors*, Limerick, Ireland, 2011, pp. 546 – 549.

[7.11] C. -T. Chiang, Y. -C. Huang, "A semicylindrical capacitive sensor with interface circuit used for flow rate measurement," *IEEE Sensors J.*, vol. 6, no. 6, pp. 1564 – 1570, Dec. 2006.

[7.12] T. Zimmerman et al., "Applying electric field sensing to human-computer interfaces," in *Proc. of CHI: ACM Conference on Human Factors in Computing Syst.*, Denver, CO, 1995, pp. 280 – 287.

[7.13] M. Sato et al., "Touche: enhancing touch interactions on humans, screens, liquids, and everyday objects," in *Proc. of CHI: ACM Conference on Human Factors in Computing Syst.*, Austin, TX, 2012, pp. 483 – 492.

[7.14] O. Camacho, E. Viramontes (Mar. 2011). *Designing touch sensing electrodes: electrical considerations and recommended layout patterns* [Online]. Available:

http://www.freescale.com/files/sensors/doc/app_note/AN3863.pdf (Accessed: 16 Oct 2013).

[7.15] B. Osoinach (2008). *Proximity capacitive sensor technology for touch sensing applications* [Online]. Available: http://www.freescale.com/files/sensors/doc/white_paper/PROXIMITYWP.pdf (Accessed: 16 Oct 2013).

[7.16] M. Shinagawa et al., "A near-field-sensing transceiver for intrabody communication based on electrooptic effect," *IEEE Trans. Instrum. Meas.*, vol. 53, no. 6, pp. 1533 – 1538, Dec. 2004.

[7.17] A. Razavi et al., "Investigation of penetration ability of UWB antennas in near-field sensing applications," in Euro. Conf. Ant. Prop., Prague, Czech Republic, 2012, pp. 791 – 795.

[7.18] Z. Ren et al., "Near-field probes for subsurfaces detection using split-ring resonators," *IEEE Trans. Microw. Theo. Tech.*, vol. 59, no. 2, pp. 488 – 495, Feb 2011.

[7.19] Microsoft Research Redmond. [Online] Available: http://research.microsoft.com/en-us/labs/redmond/ (Accessed: 16 Oct 2013).

[7.20] Gerald DeJean, Trang Thai, "RF Proximity Sensor," U.S. Patent 20 120 319 760, Dec 20, 2012.

[7.21] R. Schmitt, *Electromagnetics Explained: A Handbook for Wireless/RF, EMC, and High-Speed Electronics*, Boston, MA: Elsevier, 2002.

[7.22] Rogers Corporation. RT/duroid 5880 laminates [Online]. Available: http://www.rogerscorp.com/acm/products/32/RT-duroid-5880-Laminates.aspx (Accessed: 16 Oct 2013).

[7.23] S. B. Cohn, "Parallel-coupled transmission-line resonator filters," *IEEE Trans. Microw. Theory Tech*., vol. 6, no. 2, pp. 223 – 231, Apr. 1958.

[7.24] E. G. Cristal, "New design equations for a class of microwave filters," *IEEE Trans. Microw. Theory Tech.*, vol. 19, no. 5, pp. 486 – 490, May 1971.

[7.25] C. Y. Ho, J. H. Weidman, "Improved design of parallel coupled line filters with trapped input/output," *Microwave J.*, vol. 26, pp. 127 – 130, Oct. 1983.

[7.26] J. -S. Hong, M. J. Lancaster, *Microstrip Filters for RF/Microwave Applications*. New York, NY: John Wiley & Sons, Inc, 2001.

[7.27] L. Lewin, "Radiation from discontinuities in strip-line," *Proc. IEE*, vol. 107, no. 12, pp. 163 – 170, Sept. 1960.

[7.28] B. Easter, R. J. Roberts, "Radiation from half-wavelength open-circuit microstrip resonators," *Electronics Letters*, vol. 6, no. 18, pp. 573 – 574, Sept. 1970.

[7.29] R. Gutierres-Osuna, "Pattern analysis for machine olfaction: a review," *IEEE Sensors J.*, vol. 3, no. 2, pp. 189 – 202, June 2002.

[7.30] A. K. Jain, "Statistical pattern recognition: a review," *IEEE Trans. Pattern Anal. Mach. Intell.*, vol. 22, no. 1, pp. 4 – 37, Jan. 2000.

[7.31] P. H. Swain, *Pattern recognition: a basis for remote sensing data analysis* [Online]. LARS Technical Reports. Paper 129. Available: http://docs.lib.purdue.edu/larstech/129 (Accessed: 16 Oct 2013).

[7.32] C. Balanis, *Antenna Theory: Analysis and Design*, New York, NY: John Wiley & Sons, Inc, 1997.

[7.33] A. Goldsmith, *Wireless Communications*, New York, NY: Cambridge University Press, 2005.

[7.34] Arduino [Online]. Available: http://arduino.cc/en/Main/arduinoBoardUno (Accessed: 16 Oct 2013).

[7.35] Hittite Microwave Corporation. HMC586LC4B [Online]. Available: http://www.hittite.com/content/documents/data_sheet/hmc586lc4b.pdf (Accessed: 16 Oct 2013).

[7.36] Analog Devices, Inc. ADL5902 [Online]. Available: http://www.analog.com/static/imported-files/data_sheets/ADL5902.pdf (Accessed: 16 Oct 2013).

[7.37] Linear Tech Corporation. LT1632 [Online]. Available: http://cds.linear.com/docs/en/datasheet/16323fs.pdf (Accessed: 16 Oct 2013).

[7.38] *Hittite Microwave Corporation. HMC344LC3 SP4T Non-Reflective Switch SMT, DC – 8 GHz.* [Online] Available: http://www.hittite.com/content/documents/data_sheet/hmc344lc3.pdf (Accessed: 16 Oct 2013).

[7.39] *Hittite Microwave Corporation. HMC344LC3 SP8T Non-Reflective Switch SMT, DC – 8 GHz.* [Online] Available: http://www.hittite.com/content/documents/data_sheet/hmc321lp4.pdf (Accessed: 16 Oct 2013).

[7.40] *Texas Instruments MSP430 Ultra-Low Power 16-bit MCUs* [Online]. Available: http://www.ti.com/lit/ds/symlink/msp430f47176.pdf (Accessed: 16 Oct 2013).

[7.41] Cypress Proximity Sensor [Online]. Available: http://www.cypress.com/touch/#Solutions (Accessed: 16 Oct 2013).

Chapter 8.

Contributions, Patents, and Publications to dates

8.1. Contributions

The work presented in this thesis is among the pioneering efforts to develop passive and chipless RF sensors especially for remote sensing in harsh environments such as extreme temperatures rom 1000 ^{o}C to 1500 ^{o}C, in which current technologies are highly limited and not feasible due to their operating principles. In far-field based sensing, the thesis presented designs and developments for RF sensors for temperature, strain, and pressure, all of which can be integrated into a single passive sensor network to be implemented on planar surfaces. In practice, all of those physical quantities (temperature, stress/strain, and pressure) are interdependent and crucially to be monitored simultaneously for any structure in many environments. The solution of such passive sensing platform provided in this thesis offers practical approach for passive remote sensing. The developed sensors have high sensitivity, high adaptation and flexibility in the design concepts, and/or unique features, all of which are first time reported. The sensors can be adapted to more than one interrogation platforms, however in this thesis they are specifically illustrated for long range remote sensing with ID based on the beat frequency of an FMCW radar. An extensive theoretical circuit study was also developed for the temperature sensor. Based on the theory, new sensor types such as humidity or gas operating in similar platforms can also utilize the same design concept. In near-field based sensing, the thesis pioneers a new design for proximity sensing that allows new human interface for mobile electronics. The proximity sensor has a planar platform with

rich multi-dimensional data that allow non-touch keying and non-touch finger interactions in display and medical sanitation applications. The sensor also offers solutions to limitations inherited in the operating principles of current capacitive proximity sensing. In summary, the thesis introduces completely original RF sensing design concepts that provide solutions and complementary features to current sensors to address many limitations of current sensing technologies. The designs were demonstrated with prototypes, system integration, and circuit models with both breadth and depth for completeness of the research.

8.2. Patents and Publications to dates

Achievements are as follows: two granted U.S. patents, one granted W.O patent (international), three published journal papers as first author and one invited magazine article, 15 published conference papers as first author. All publications (more than 30 papers including the co-authored ones) have approximately 90 citations. The patents, the journal papers, and the selective conference papers are listed below.

8.2.1. Patents

1. R. Gilad-Bachrach, G. R. DeJean, T. T. Thai, “Biological entity communication channel,” U.S. Patent 20 130 149 965, June 13, 2013.
2. G. R. DeJean, T. T. Thai, “RF Proximity Sensor,” U.S. Patent 20 120 319 760, Dec 20, 2012.
3. H. Aubert, T. T. Thai, P. Pons, “Strain Sensor,” W.O. Patent 2 012 164 191, Dec 7, 2012.

8.2.2. Journal Papers

1. Trang Thai, Herve Aubert, Patrick Pons, Gerald DeJean, Manos Tentzeris, Robert Plana, “Novel Design of a Highly Sensitive RF Strain Transducer for Passive and Remote Sensing in Two Dimensions,” *IEEE Transactions on Microwave Theory and Techniques*, vol. 61, no. 3, pp. 1385 – 1396, Feb. 2013.
2. Trang T. Thai, J. Mehdi, F. Chebila, H. Aubert, P. Pons, G. DeJean, M. Tentzeris, R. Plana, “Design and Development of a Novel Passive Wireless Ultrasensitive RF Temperature Transducer for Remote Sensing,” *IEEE Sensors Journal*, vol. 12, no. 9, pp. 2756 – 2766, Sept. 2012.
3. T. T. Thai, G. R. DeJean, M. M. Tentzeris, “Design and Development of a Novel Compact Soft-Surface Structure for the Front-to-Back Ratio Improvement and Size Reduction of a Microstrip Yagi Array Antenna,” *IEEE Antennas and Wireless Propagation Letters*, vol.6, pp. 244 – 248, 2007.
4. Trang T. Thai, Li Yang, Gerald R. DeJean, and Manos M. Tentzeris, "Wireless/Microwave Passive Gas Sensors based on Carbon Nanotube Technologies," Invited paper *IEEE Microwave Magazine*, vol. 12, no. 4, pp. 84 – 95, June 2011.

8.2.3. Conference Papers

1. Trang Thai, Gerald DeJean, Ran Gilad-Bachrach, “Confined Intra-Arm Communication for Medical Applications,” Wireless Health 2012 conference, La Jolla, CA, Sept. 2012.

2. T. Thai, H. Aubert, P. Pons, M. Tentzeris, and R. Plana, "Design of a Highly Sensitive Wireless Passive RF Strain Transducer," in *IEEE Int. Microw. Symp*., Baltimore, MD, June 2011, pp. 1 – 4.

3. T. T. Thai, H. Aubert, P. Pons, R. Plana, G. R. DeJean, M. M. Tentzeris, “A newly developed radio frequency wireless passive highly sensitive strain transducer,” in *IEEE Sensors*, Limerick, Ireland, Oct. 2011, pp. 211 – 214.

4. Trang T. Thai, Franck Chebila, Jatlaoui M. Mehdi, Patrick Pons, Herve Aubert, Gerald R. DeJean, Manos M. Tentzeris, and Robert Plana, "Design and development of a millimetre-wave novel passive ultrasensitive temperature transducer for remote sensing and identification," in *European Microwave Conference*, Paris, France, Oct. 2010, pp. 45 – 48.
5. Trang T. Thai, Jatlaoui M. Mehdi, Herve Aubert, Patrick Pons, Gerald R. DeJean, Manos M. Tentzeris, and Robert Plana, "A Novel Passive Wireless Ultrasensitive Temperature RF transducer for Remote Sensing," in *IEEE Int. Microwave Symp*., Anaheim, CA, May 2010, pp. 473-476,.
6. Trang T. Thai, F. Chebila, J. Mehdi, P. Pons, H. Aubert, G. DeJean, M. Tentzeris, and R. Plana, "A Novel Passive Ultrasensitive RF Temperature Transducer for Remote Sensing and Identification Utilizing Radar Cross Sections Variability," in *IEEE Antennas and Propagation Society International Symposium*, Toronto, Ontario, Canada, July 2010, pp. 1 – 4.
7. T. T. Thai, G. R. DeJean, M. M. Tentzeris, "A Novel Front-End Radio Frequency Pressure Transducer based on a Millimeter-Wave Dual-band Resonator for Wireless Sensing," in *IEEE International Microwave Symposium*, Boston, MA, June 2009, pp. 1701 – 1704.
8. T. T. Thai, G. R. DeJean, M. M. Tentzeris, "A Novel Ultrasensitive Millimeter-Wave Pressure Transducer Utilizing a Si Membrane and a Stacked-Patch Configuration," in *IEEE Antennas and Propagation Society International Symposium,* Charleston, SC, June 2009, pp. 1 – 4. **Second Prize Winner of Student Paper Contest.**
9. Trang Thai, Justin Ratner, Wenhua Chen, Tushar Thrivikraman, Gerald DeJean, Manos Tentzeris, "First Generation of Ultrathin Polarized NanoMaterials for Millimeter-Wave (26-40 GHz) Textile Antenna Applications," in *IEEE Antennas and Propagation Society International Symposium*, Charleston, SC, June 2009, pp. 1 – 4.
10. Trang Thai, Justin Ratner, Wenhua Chen, Gerald DeJean, Manos Tentzeris, "Characterization and Testing of Novel Polarized Nanomaterial Textiles for

Ultrasensitive Wireless Gas Sensors," in *IEEE Electronic Components and Technology Conference*, San Diego, CA, May 2009, pp. 1049 – 1052.

11. Trang Thai, Justin Ratner, Gerald DeJean, Anya Traille, Li Yang, and Manos Tentzeris, "Ultrasensitive Wireless Gas-Sensor Utilizing Carbon Nanotubes on Paper, Liquid and Organic Substrates," Invited talk at *National Radio Science Meeting*, Boulder, CO, 2009.
12. T. T. Thai, A. Haque, G. R. DeJean, M. M. Tentzeris, "A Novel Ultrasensitive Gas Detector System Based on Carbon Nanotube Mixtures and Antenna Radiation Variation," in *IEEE Antennas and Propagation Society International Symposium*, San Diego, CA, July 2008, pp. 1 – 4.
13. T. T. Thai, A. Haque, J. Ratner, G. DeJean, M. Tentzeris, "Development of a Fully-Integrated Ultrasensitive Wireless Sensor Utilizing Carbon Nanotubes and Surface Plasmon Theory," in *IEEE Electronic Components and Technology Conference*, Orlando, FL, May 2008, pp. 436 – 439.
14. T. T. Thai, A. Traille, and M. M. Tentzeris, "Design and Development of Carbon-Nanotube EBG's Sensors," Invited talk at *PIERS 2007*, Prague, Czech Republic.
15. T. T. Thai, G. R. DeJean and M. M. Tentzeris, "Design and development of a novel compact soft-surface structure for the front-to-back ratio improvement and size reduction of microstrip Yagi antenna arrays," Proceedings of the 2007 IEEE Antennas and Propagation Society International Symposium, Honolulu, Hawaii, June 2007, pp.1193 – 1196.

Appendix A

Arduino Code for Non-Touch Finger Gesture Detection

```
// Copyright: Trang Thai 03/05/2012
// Executed in Arduino environment
const byte mask = B11111000; // mask bits that are not prescale values

int pinLED = 9;

int prescale = 1;
int dutyLow = 75; // scale of 0-255
int dutyHigh = 140; // scale of 0-255
int arraylength = 66;
int timedelay = 20;
int duty = dutyLow;

double PDout[66];
double PDout_update[66];
double Pmin = 0;
int imin = 0;
double Pmax = 0;
int imax = 0;
int ind = 0;

double refPDout[66];
double refPmin = 0;
int refimin = 0;
double refPmax = 0;
int refimax = 0;

double DiffPDout[65];
double DiffPDout_update[65];
double DiffPmin = 0;

int iDiffzero = 0;

double refDiffPDout[65];
double refDiffPmin = 0;
int refindC1 = 0; //lower limit of inflection region
int refindC2 = 0; //upper limit of inflection region
```

```
int refiDiffzero = 0;

int brightness1 = 20; //2cm
int brightness2 = 100; //1cm
int brightness3 = 200; //touch

void setup()
{
  Serial.begin(9600);
  analogWrite(6,dutyLow); //timer 0 out at pin 6 at ~50% duty cycle
  TCCR0B = (TCCR0B & mask) | prescale; //~62.5 kHz
  pinMode(pinLED, OUTPUT); // setting up output LED pin as the detection indicator
}

void loop()
{
       char ch = Serial.read();
       for (int i=1; i<4; i++) // averaging over i samples for each point in the sweep
          {

            ind = 0;
            Pmin = PDout[0];
            Pmax = PDout[0];

            for (int duty = dutyHigh; duty > (dutyLow - 1); duty--)
                  // for each command 'n', sweep through the band
             {
               analogWrite(6,duty);
               delay(timedelay);
               PDout_update[ind] = analogRead(A1); // READ PD in at A1

               if (i==1)
               {
                 PDout[ind] = PDout_update[ind];
               }
               else
               {
                 PDout[ind] = (PDout_update[ind] + PDout[ind]) /2;
                 if (PDout[ind] < Pmin)
                 {
```

```
            Pmin = PDout[ind];
            imin = ind;
          }
          if (PDout[ind] > Pmax)
          {
            Pmax = PDout[ind];
            imax = ind;
          }
          if (PDout[ind] == Pmax)
          {
            imax = (imax + ind)/2;
          }
        }
        ind++;
      }
    }

  iDiffzero = 0;
  for (int i = 1; i < arraylength; i++)    // loop for the derivative arrays
    {
      DiffPDout[i-1] = PDout[i]-PDout[i-1];
    }


  ///**************************************************************************///
  // Desicion making: imin, indC1, indC2, sumC1C2, and corresponding REF values
  ////////////////////////////////////////////////////////////////////////////////

  analogWrite(pinLED, 0);

  if (((abs(refimin-imin-3)<3)) && (imax < 4))
    {
      analogWrite(pinLED, brightness3);
      Serial.println("near touch 1");
      Serial.print("PDout min = "); Serial.print(PDout[imin]); Serial.print(" @");
Serial.println(imin);
      Serial.print("PDout max = "); Serial.print(PDout[imax]); Serial.print(" @");
Serial.println(imax);

    }
```

```
      if (((abs(refimin-imin-4)<2)) && ((refPDout[refimin]-PDout[imin])>5))
         {
          analogWrite(pinLED, brightness3);
          Serial.println("near touch 2");
          Serial.print("PDout min = "); Serial.print(PDout[imin]); Serial.print(" @");
Serial.println(imin);
          Serial.print("PDout max = "); Serial.print(PDout[imax]); Serial.print(" @");
Serial.println(imax);
         }

      if (abs(refimin-imin-2)<3)
       {
        if ((abs(imax-refimax-5)<2) && (abs(refPDout[refimax]-PDout[imax]-12)<12))
         {
          analogWrite(pinLED, brightness2);
         }
        else if ((abs(imax-refimax-5)<2) && (abs(refPDout[refimax]-PDout[imax]-32)<8))
         {
          analogWrite(pinLED, brightness3);
         }
       }
      if ((abs(refimin-imin-2)<3) && (abs(refPDout[refimin]-PDout[imin]-10)<25))
       {
        if ((abs(imax-refimax-9)<3) && (abs(refPDout[refimax]-PDout[imax]-48)<10))
        {
          analogWrite(pinLED, brightness3);
        }
       }
      if (abs(refimin-imin-3)<3)
       {
        if ((abs(refimax-imax-4)<2) && (abs(refPDout[refimax]-PDout[imax]-30)<2))
        {
          analogWrite(pinLED, brightness3);
        }
       }

      if ((abs(refimin-imin-4)<2) && ((PDout[imin]-refPDout[refimin])>25))
       {
        if (((imax-refimax)>5) && ((refPDout[refimax]-PDout[imax])<28))
         {
          analogWrite(pinLED, 0);
```

```
            Serial.println("off");
            Serial.print("PDout min = "); Serial.print(PDout[imin]); Serial.print(" @");
Serial.println(imin);
            Serial.print("PDout max = "); Serial.print(PDout[imax]); Serial.print(" @");
Serial.println(imax);
          }
        }


///// **** MAIN LOOP REPEATS FROM HERE UNLESS CALIBRATION HIT ****


      ////////////////////////////////////////////////////////////////////////////////////////////
       //                                  CALIBRATION with key 'c'                \\
      ////////////////////////////////////////////////////////////////////////////////////////////

       if (ch == 'c')
 // to obtain at REF : arrays of PDout[] and DiffPDout[], and  pointers to global mins of 2
arrays
      {
        Serial.println("Calibration begins");
        for (int i=1; i<20; i++) // averaging over i samples for each point in the sweep
            {

              ind = 0;
              Pmin = refPDout[0]; //Pmin is recycled variable

              for (int duty = dutyHigh; duty > (dutyLow - 1); duty--)
                  // for each command 'n', sweep through the band
               {
                 analogWrite(6,duty);
                 delay(timedelay);
                 PDout_update[ind] = analogRead(A1); // READ PD in at A1

                 if (i==1)
                 {
                   refPDout[ind] = PDout_update[ind];
                 }
                 else
                 {
                   refPDout[ind] = (PDout_update[ind] + refPDout[ind]) /2;
                   if (refPDout[ind] < Pmin)
```

```
                {
                  Pmin = refPDout[ind];
                  refimin = ind;
                        // Global min of REF PD array pointer saved to 'refimin' index
                }
                if (refPDout[ind] > refPmax)
                {
                   refPmax = refPDout[ind];
                   refimax = ind;
                }
                if (refPDout[ind] == refPmax)
                {
                   refimax = (refimax + ind)/2;
                }
               }
               ind++;
             }
           } // after loop refPmin, refimin, and refPDout[] obtained

        refiDiffzero = 0;
        for (int i = 1; i < arraylength; i++)    // loop for the derivative arrays
           {
             refDiffPDout[i-1] = refPDout[i]-refPDout[i-1];
           } // after the loop 1st global min of Diff array found => refDiffPDout[]



        ////////////////////////////////////////////////////////////////////////////////////
        //         got refPDout[], refDiffPDout[], refimin, refindC1, refindC2
        ////////////////////////////////////////////////////////////////////////////////////

        Serial.print("REF PDout min = "); Serial.print(refPDout[refimin]); Serial.print("
@"); Serial.println(refimin);
        Serial.print("REF PDout max = "); Serial.print(refPDout[refimax]); Serial.print("
@"); Serial.println(refimax);

    }
    ////////////////////////////////////////////////////////////////////////////////////
    //                                DONE CALIBRATION              //
    ////////////////////////////////////////////////////////////////////////////////////

    if (ch == 'r')
```

```
      {
        Serial.print("PDout min = "); Serial.print(PDout[imin]); Serial.print(" @");
Serial.println(imin);
        Serial.print("PDout max = "); Serial.print(PDout[imax]); Serial.print(" @");
Serial.println(imax);
      }

      if (ch == 'R')
       {
        for (int i = 0; i < arraylength; i++) // print out the PDout array
         {
          Serial.println(PDout[i]);
         }
       }

      if (ch == 'D')
       {
        for (int i = 0; i < 70; i++) // print out the PDout array
         {
          Serial.println(DiffPDout[i]);
         }
        Serial.print("index at slope zero = "); Serial.println(iDiffzero);
       }

      if (ch == 'u')
       {
        timedelay += 10;
        Serial.println(timedelay);
       }

      if (ch == 'd')
       {
        timedelay -= 10;
        Serial.println(timedelay);
       }

} // VOID LOOP END
```